

# Measurement of Nuclear Effects in the Production of $J/\psi$ Mesons with the HERA-B Detector

DISSERTATION

zur Erlangung des akademischen Grades eines  
Doktors der Naturwissenschaften,

vorgelegt von

**Diplom-Physiker Ulrich Husemann**

aus Lippstadt,

genehmigt vom Fachbereich Physik  
der Universität Siegen.

Siegen  
Januar 2005

Gutachter der Dissertation: Univ.-Prof. Dr. P. Buchholz  
Univ.-Prof. Dr. C. Grupen

Datum der Disputation: 02. Februar 2005

Internetpublikation der Universitätsbibliothek Siegen: [urn:nbn:de:hbz:467-972](https://nbn-resolving.org/urn:nbn:de:hbz:467-972)

## Abstract

Using data recorded with the HERA-B detector at DESY, nuclear effects in the production of  $J/\psi$  mesons are investigated in proton-nucleus interactions at a center-of-mass energy of 41.6 GeV. HERA-B is a fixed-target spectrometer in which protons from the HERA accelerator are collided with thin wire targets of different materials. Leptonic decays of  $J/\psi$  mesons are enriched by a multi-level trigger system. From approximately 90,000  $J/\psi \rightarrow \mu^+ \mu^-$  decays collected in the 2002/2003 data-taking period using a carbon and a tungsten wire simultaneously, the nuclear suppression parameter  $\alpha$  ( $\alpha < 1$  stands for the suppression of  $J/\psi$  production in nuclear matter) is derived as a function of the  $J/\psi$  kinematics. The measurement of  $\alpha$  is performed by measuring three ratios: the ratio of the  $J/\psi$  yields on the wires, the ratio of the  $J/\psi$  detection efficiencies, and the ratio of luminosities. A small constant suppression of  $J/\psi$  production is measured as a function of Feynman's scaling variable  $x_F$  in the HERA-B range of  $-0.375 < x_F < 0.125$ . An average suppression of  $\bar{\alpha} = 0.969 \pm 0.003(\text{stat.}) \pm 0.021(\text{syst.})$  is found in this range. The measured distributions of  $\alpha(x_F)$  and  $\alpha(p_T)$  agree well with the results of previous measurements. For the first time,  $\alpha(x_F)$  is measured for negative values of  $x_F$  smaller than  $-0.1$ . The measured values of  $\alpha(x_F)$  are consistent with theoretical predictions of  $J/\psi$  suppression due to the absorption of final-state  $c\bar{c}$  pairs or the fully formed  $J/\psi$  mesons.

## Zusammenfassung

In der vorliegenden Arbeit wird der Einfluss nuklearer Effekte auf die Produktion von  $J/\psi$ -Mesonen in Proton-Kern-Wechselwirkungen bei einer Schwerpunktsenergie von 41,6 GeV untersucht. Dazu werden Daten verwendet, die in der Datennahmeperiode 2002/2003 mit dem HERA-B-Detektor am DESY aufgezeichnet wurden. Im HERA-B-Detektor werden Protonen aus dem HERA-Beschleuniger mit dünnen Drahttargets zur Kollision gebracht. Leptonische Zerfälle von  $J/\psi$ -Mesonen werden mittels eines mehrstufigen Triggersystems in den Daten angereichert. Der Unterdrückungsparameter  $\alpha$  ( $\alpha < 1$  bedeutet Unterdrückung der  $J/\psi$ -Produktion in Kernmaterie) wird aus Datensätzen bestimmt, in denen gleichzeitig je ein Kohlenstoff- und ein Wolframdraht als Targets benutzt wurden. Die Messung basiert auf etwa 90.000 rekonstruierten Zerfällen  $J/\psi \rightarrow \mu^+ \mu^-$ . Der Parameter  $\alpha$  hängt von der  $J/\psi$ -Kinematik ab und wird durch die Messung dreier Verhältnisse zwischen den beiden Targetdrähten ermittelt: der Verhältnisse der Zahl produzierter  $J/\psi$ -Mesonen, der  $J/\psi$ -Nachweiseffizienzen und der Luminositäten. Die Messung ergibt eine konstante geringe Unterdrückung der  $J/\psi$ -Produktion als Funktion der Feynman-Skalenvariable  $x_F$  in dem von HERA-B abgedeckten kinematischen Bereich zwischen  $x_F = -0,375$  und  $x_F = 0,125$ . Die mittlere Unterdrückung in diesem Bereich beträgt  $\bar{\alpha} = 0,969 \pm 0,003(\text{stat.}) \pm 0,021(\text{syst.})$ . Die Verteilungen des Unterdrückungsparameters  $\alpha$  als Funktion von  $x_F$  und  $p_T$  stimmen gut mit den Ergebnissen früherer Messungen überein. Erstmals wird in dieser Arbeit  $\alpha(x_F)$  im Bereich negativer  $x_F$ -Werte kleiner als  $-0,1$  bestimmt. Die Messung von  $\alpha(x_F)$  stimmt mit theoretischen Berechnungen überein, die eine Unterdrückung der  $J/\psi$ -Produktion aufgrund der Absorption von  $c\bar{c}$ -Paaren im Endzustand der Proton-Kern-Wechselwirkung oder des voll ausgebildeten  $J/\psi$ -Mesons vorhersagen.



# Contents

<b>1</b>	<b>Introduction</b>	<b>1</b>
1.1	The Standard Model of Particle Physics . . . . .	1
1.2	The Discovery of the Charm Quark . . . . .	2
1.3	Heavy Quarkonia . . . . .	3
1.4	Scope of this Thesis . . . . .	4
<b>2</b>	<b>The HERA-B Experiment</b>	<b>7</b>
2.1	The HERA Storage Ring . . . . .	7
2.2	Subdetectors of the HERA-B Detector . . . . .	8
2.2.1	Target . . . . .	10
2.2.2	Vertex Detector System . . . . .	10
2.2.3	Tracking System . . . . .	11
2.2.4	Particle Identification Devices . . . . .	14
2.3	Pretriggers and First Level Trigger . . . . .	18
2.3.1	Muon Pretrigger . . . . .	18
2.3.2	ECAL Pretrigger . . . . .	18
2.3.3	RICH Multiplicity Veto . . . . .	19
2.3.4	First Level Trigger . . . . .	19
2.4	Data Acquisition System . . . . .	22
2.4.1	Data Flow in the Data Acquisition System . . . . .	22
2.4.2	Second Level Trigger Algorithm . . . . .	22
2.4.3	Fourth Level Trigger and Event Reconstruction . . . . .	24
2.4.4	Trigger Strategies . . . . .	26
2.5	Physics Goals of the HERA-B Experiment . . . . .	27
2.5.1	Heavy Quark Production . . . . .	28
2.5.2	QCD Studies . . . . .	29
<b>3</b>	<b>Charmonium Production and Suppression: Theory and Experiments</b>	<b>31</b>
3.1	The Charmonium Spectrum . . . . .	31
3.1.1	Charmonium Quantum Numbers . . . . .	31
3.1.2	Potential Models . . . . .	32
3.2	Charmonium Production and Decays . . . . .	33
3.2.1	Charmonium Decays . . . . .	33
3.2.2	Color Evaporation Model . . . . .	34
3.2.3	Color Singlet Model . . . . .	35

3.2.4	Nonrelativistic QCD . . . . .	36
3.3	The Glauber Model . . . . .	41
3.3.1	Basic Assumptions . . . . .	42
3.3.2	Parametrizations of Nuclear Densities . . . . .	42
3.3.3	Inelastic Cross Section in the Glauber Model . . . . .	43
3.3.4	Nuclear Absorption in the Glauber Model . . . . .	44
3.3.5	Measuring Nuclear Suppression in HERA-B . . . . .	46
3.4	Nuclear Effects in Charmonium Production . . . . .	47
3.4.1	Initial State Effects . . . . .	48
3.4.2	Final State Effects . . . . .	51
3.4.3	Combination of Nuclear Effects . . . . .	53
3.4.4	Coherent Effects . . . . .	53
3.5	Results of Previous Experiments . . . . .	56
3.5.1	The CERN Experiments . . . . .	56
3.5.2	The FNAL Experiments . . . . .	58
3.5.3	HERA-B Commissioning Run 2000 . . . . .	59
3.6	Summary . . . . .	61
<b>4</b>	<b>Signal Extraction, Efficiencies, and Differential Distributions</b>	<b>65</b>
4.1	Data Selection . . . . .	65
4.1.1	Run Selection and Data Quality Assessment . . . . .	65
4.1.2	Data Reprocessing . . . . .	66
4.1.3	Selection of $J/\psi$ Candidate Events . . . . .	67
4.2	Extraction of $J/\psi$ Signals . . . . .	72
4.2.1	Determination of the $J/\psi$ Yield . . . . .	72
4.2.2	$J/\psi$ Kinematic Distributions . . . . .	75
4.2.3	Wire Configurations and Wire Assignment . . . . .	75
4.3	Monte Carlo Simulation . . . . .	77
4.3.1	Calibration Periods and Monte Carlo Event Statistics . . . . .	79
4.3.2	Reweighting of Kinematic Distributions . . . . .	80
4.3.3	Trigger Simulation . . . . .	81
4.3.4	Detector Resolutions in the Kinematic Variables . . . . .	82
4.3.5	Comparison of Data and Monte Carlo Simulation . . . . .	84
4.3.6	Efficiency Determination . . . . .	89
4.4	Differential Distributions . . . . .	91
4.4.1	Analysis Method . . . . .	91
4.4.2	Results and Discussion . . . . .	92
4.5	Summary . . . . .	101
<b>5</b>	<b>Luminosity and Target Rate Sharing</b>	<b>103</b>
5.1	Luminosity Measurements at HERA-B . . . . .	103
5.2	Vertex Counting Method . . . . .	104
5.2.1	Vertexing Efficiency . . . . .	105
5.2.2	Determination of the Number of Interactions . . . . .	106
5.2.3	Luminosity Ratios for All Runs . . . . .	107

5.3	Systematic Uncertainties . . . . .	107
5.3.1	Uncertainties of the Vertex Counting Method . . . . .	108
5.3.2	Luminosity Ratios from the Track Counting Method . . . . .	108
5.3.3	Uncertainty of the Minimum-Bias Cross Section . . . . .	112
5.3.4	Combination of Systematic Uncertainties . . . . .	112
5.4	Summary . . . . .	113
<b>6</b>	<b>Measurement of Nuclear Effects</b>	<b>115</b>
6.1	Ratios of $J/\psi$ Yields . . . . .	115
6.1.1	Efficiency Ratios . . . . .	116
6.1.2	Strategies to Extract Systematic Uncertainties . . . . .	117
6.1.3	Systematic Uncertainties of the Efficiency Ratios . . . . .	118
6.1.4	Systematic Uncertainties of $J/\psi$ Yield Ratios . . . . .	121
6.1.5	Summary of Systematic Uncertainties . . . . .	124
6.2	Nuclear Effects in $J/\psi$ Production . . . . .	125
6.2.1	Combination of Data Samples . . . . .	126
6.2.2	Control Sample . . . . .	128
6.2.3	Nuclear Suppression Parameter . . . . .	129
6.2.4	Comparison to Previous Experiments . . . . .	134
6.2.5	Scaling with the Momentum Fraction of the Target Parton . . . . .	136
6.2.6	Comparison to Theoretical Predictions . . . . .	137
6.2.7	Absorption Cross Section in the Glauber Model . . . . .	138
6.3	Summary . . . . .	139
<b>7</b>	<b>Summary and Conclusions</b>	<b>141</b>
<b>A</b>	<b>Monte Carlo Simulation of the HERA–B Detector and Trigger</b>	<b>145</b>
A.1	Physics Generators . . . . .	145
A.1.1	Reweighting of Kinematic Distributions . . . . .	146
A.1.2	Multiplicity Reweighting for the Underlying Event . . . . .	150
A.2	Detector Simulation and Hit Preparation . . . . .	150
A.2.1	GEANT Simulation . . . . .	150
A.2.2	Hit Preparation in the Muon Detector . . . . .	151
A.3	Trigger Simulation . . . . .	153
A.3.1	Muon Pretrigger and RICH Multiplicity Veto . . . . .	154
A.3.2	Second Level Trigger Simulation . . . . .	158
A.3.3	Efficiency Map of the First Level Trigger . . . . .	159
<b>B</b>	<b>Kinematic Variables in Fixed-Target Experiments</b>	<b>161</b>
B.1	Transverse and Longitudinal Momentum . . . . .	161
B.2	Angular Distributions . . . . .	163
<b>C</b>	<b>Run Selection</b>	<b>165</b>
<b>D</b>	<b>Plots and Tables</b>	<b>169</b>

<b>List of Figures</b>	<b>190</b>
<b>List of Tables</b>	<b>192</b>
<b>List of Acronyms</b>	<b>193</b>
<b>Bibliography</b>	<b>195</b>
<b>Danksagung</b>	<b>211</b>



---

## Introduction

---

This introductory chapter describes the context in which this thesis is written. The chapter commences with a brief introduction to the Standard Model of particle physics, followed by an overview of the physics of heavy quarkonia and a guide to this thesis.

### 1.1 The Standard Model of Particle Physics

The current knowledge of our universe on the level of the smallest known particles is summarized in the Standard Model of particle physics. The Standard Model, based on quantum mechanics and the special theory of relativity, is the most successful description of nature on the fundamental level so far. The Standard Model was formulated in the 1960's and 1970's, and no experimental evidence for physics beyond the Standard Model has been found since.

In the framework of the Standard Model, there are two kinds of elementary particles, fermions and bosons. All matter is built from fermions. The interactions between fermions are mediated by gauge bosons. The fermions, summarized in Table 1.1, form three generations with similar properties. For each of the fermions, there is an antiparticle with the same properties as the fermion's, except that all charge-like quantum numbers have opposite signs. The fermions can be further divided into quarks and leptons according to the forces which act on them. The forces of the Standard Model include the electromagnetic force, responsible e.g. for the binding of atoms and molecules to liquids and solids, the weak force, which governs for example the radioactive  $\beta$ -decay, and the strong force, by which the quarks and gluons inside nucleons are bound. Gravitational forces are not described within the framework of the Standard Model.

The basic theoretical formalism used to build the Standard Model is relativistic quantum field theory. In relativistic quantum field theory, local gauge symmetries determine the structure of the interactions between the constituents of matter. The two theories which form the Standard Model are the theories of electroweak and strong interactions. The electroweak theory is based on the combined symmetry  $SU(2) \times U(1)$  of the weak isospin components  $I_1$  and  $I_2$  and the hypercharge  $Y = Q + I_3$ ,  $Q$  being the electric charge. Hence, the electroweak theory is the unified theory of weak and elec-

**Table 1.1:** The fundamental fermions in the Standard Model of particle physics. The fermions are arranged in three generations, which are formed by two quarks and two leptons.

Generation	Quarks	Leptons
1	up quark (u) down quark (d)	electron neutrino ( $\nu_e$ ) electron (e)
2	charm quark (c) strange quark (s)	muon neutrino ( $\nu_\mu$ ) muon ( $\mu$ )
3	top quark (t) bottom quark (b)	tau neutrino ( $\nu_\tau$ ) tau ( $\tau$ )

tromagnetic interactions. The gauge bosons mediating electroweak interactions are the massless photon, and three massive bosons, the  $W^\pm$ , and the  $Z$ .

The theory of strong interactions, quantum chromodynamics (QCD), is based on a  $SU(3)$  symmetry of an additional quantum number called color. Quarks carry one of three different colors, and interactions between quarks are mediated by eight massless bi-colored gluons. These two theories are summarized in Table 1.2.

## 1.2 The Discovery of the Charm Quark

An important milestone in establishing the Standard Model was the discovery of the charm quark in 1974. A set of three new fundamental particles had been proposed by Gell-Mann [GM64] and Zweig [Zwe64b]. The quarks, as they were called by Gell-Mann, were introduced as a classification scheme for the “zoo” of particles discovered in the decade before. All known hadrons could be described as composed of a quark-antiquark pair or three quarks, using quarks of three different flavors: u, d, and s. Quarks were considered as useful theoretical constructions to describe experimental data, but there was no evidence for the existence of these particles as the basic constituents of mesons and baryons. In 1970, Glashow, Iliopoulos, and Maiani showed that a fourth quark is needed in order to suppress neutral currents that change strangeness in the theory of electroweak interactions (“GIM mechanism”) [Gla70a].

In November 1974, a narrow resonance at an invariant mass of approximately  $3.1 \text{ GeV}/c^2$  was discovered at about the same time in  $e^+e^-$  annihilation at the Stanford Linear Accelerator Center (SLAC) [Aug74] and in proton-beryllium interactions at Brookhaven National Laboratory (BNL) [Aub74]. While the SLAC group called the new particle “ $\psi$ ”, it was dubbed “ $J$ ” by the BNL group, hence it is widely referred to as the “ $J/\psi$ ” particle. Two weeks later, the discovery of another resonance at  $3.7 \text{ GeV}/c^2$ , the  $\psi'$ , was reported [Abr74]. These discoveries, sometimes called the “November Revolution”, and the subsequent interpretation of the  $J/\psi$  as “charmonium”, i.e. a bound state of a  $c$  and a  $\bar{c}$  quark [App75, DR75], are considered the single most important step to establish quarks as the basic building blocks of matter.

**Table 1.2:** Theories in the Standard Model of particle physics. The dynamical theories in the Standard Model are listed along with the bosons mediating the forces and the fermions on which the forces act. Interactions between the gauge bosons are not shown.

Dynamical Theory	Gauge Bosons	Force Acts On
Electroweak Theory	Photon ( $\gamma$ )	Charged Fermions
	$W^\pm, Z$	All Fermions
Quantum Chromodynamics	8 Gluons (g)	Quarks

### 1.3 Heavy Quarkonia

Charmonia are representatives of a class of particles called “quarkonia”. Quarkonia are bound states of quarks and antiquarks, and can be viewed as the “atoms of strong interaction”. Quarkonia are bound by a potential given by QCD. The potential allows bound states with specific binding energies as well as free states. Thus quarkonium spectroscopy is an important technique in studying the QCD potential. Measuring the properties of quarkonia provides stringent tests of QCD as the theory of strong interactions. The following discussion is restricted to the production and decays of charmonia. A recent overview of the field of heavy quarkonium physics is contained in [Bra04].

Studying the production and decay mechanisms for charmonia reveals new insights in QCD. In hadroproduction, a  $J/\psi$  meson cannot be formed by a simple combination of a  $c\bar{c}$  pair, because the  $c\bar{c}$  pair bears the wrong quantum numbers to form a  $J/\psi$ . Early production models were guided by the idea that every  $c\bar{c}$  pair with a mass below the threshold to produce two charmed mesons has an equal probability to form a charmonium state. Later models noticed that in perturbative QCD, the  $c\bar{c}$  pair has to neutralize its color by radiating gluons before forming a charmonium state. Since these models predicted too small production cross sections, especially at large transverse momenta, they were replaced by models that take into account the approximately nonrelativistic nature of  $c\bar{c}$  bound states, allowing for both colored and color-neutral states to form charmonia. Still these models are not well-tested in fixed-target hadroproduction of charmonia. In addition, the models rely on experimental input to fix non-perturbative parameters.

An interesting field in studying the properties of charmonium states is in-medium production. Due to the presence of color fields and other strongly interacting particles in the nuclear medium, charmonia can dissolve or recombine depending on the medium. Several competing mechanisms to explain these effects can be found in the literature. Suppression of charmonium production has been proposed as a signature for the discovery of a new state of matter, the quark-gluon plasma [Mat86]. However, charmonium suppression can also be caused by conventional suppression mechanisms, such as energy loss of the partons that form the charmonium or absorption of  $c\bar{c}$  states in nuclear matter. In order to understand the suppression of charmonium production in nucleus-nucleus collisions at current experiments at the CERN Super Proton Synchrotron (SPS)

and the Relativistic Heavy-Ion Collider (RHIC) at BNL, and planned experiments at the Large Hadron Collider (LHC) at CERN, a better knowledge of charmonium suppression in proton-nucleus collisions is mandatory. The HERA-B experiment is capable of contributing to this endeavor.

## 1.4 Scope of this Thesis

The HERA-B experiment had been designed to measure CP-violation in the system of neutral B mesons. After it became evident that the competitors in this field, *BABAR* and *Belle*, reached this goal before the HERA-B data-taking commenced, HERA-B was approved for a new physics program based on heavy quark production and QCD studies. One of the main new topics is the nuclear dependence of quarkonium production. During a five-month data-taking period from October 2002 to February 2003, a data sample of approximately 300,000  $J/\psi$  mesons decaying into lepton pairs has been collected, approximately 170,000 of which in the decay channel  $J/\psi \rightarrow \mu^+ \mu^-$ . Based on data from this period, the dependence of the  $J/\psi$  production cross section in proton-nucleus collisions,  $\sigma_{pA}$ , on the target material is studied in this thesis. The dependence of  $\sigma_{pA}$  on the atomic mass  $A$  of the target nucleus is commonly parametrized by the power law

$$\sigma_{pA} = \sigma_{pN} A^\alpha. \quad (1.1)$$

Here,  $\sigma_{pN}$  is the cross section for  $J/\psi$  production in proton-nucleon collisions. In general, the suppression parameter  $\alpha$  is a function of the kinematics of the production process,  $\alpha = \alpha(x_F, p_T, \dots)$ . A value of  $\alpha = 1$  indicates a scaling of the cross section with  $A$ , while values of  $\alpha < 1$  imply  $J/\psi$  suppression.

In HERA-B, charmonium production is studied for two different target materials at the same time. During the data-taking period 2002/2003, several data sets with different combinations of target materials have been recorded. The cross section  $\sigma_{pA}$  in (1.1) can be expressed by the number  $N$  of detected  $J/\psi$ , the detection efficiency  $\varepsilon$ , and the luminosity of the particle beam,  $\mathcal{L}$ :

$$\sigma_{pA} = \frac{N}{\varepsilon \mathcal{L}}. \quad (1.2)$$

Inserting Eq. (1.2) into (1.1) for two different materials with atomic numbers  $A_1$  and  $A_2$ , the set of equations can be solved for  $\alpha$ :

$$\alpha = \frac{1}{\log(A_2/A_1)} \log \left( \frac{N_2 \mathcal{L}_1 \varepsilon_1}{N_1 \mathcal{L}_2 \varepsilon_2} \right). \quad (1.3)$$

Eq. (1.3) suggests a strategy for measuring  $\alpha$  in HERA-B:  $\alpha$  depends on three ratios, the ratio of the number of  $J/\psi$  mesons in different materials,  $N_2/N_1$ , the ratio of luminosities,  $\mathcal{L}_1/\mathcal{L}_2$ , and the ratio of efficiencies,  $\varepsilon_1/\varepsilon_2$ . Hence, the measurement of  $\alpha$  is a relative measurement in which only relative efficiencies and luminosities have to be determined and many systematic effects cancel.

This thesis is organized as follows.

- In Chapter 2, the design and performance of the HERA–B detector and trigger system are described.
- Chapter 3 reviews the most important aspects of the theory of charmonium production and key results from previous experiments.
- The extraction of charmonium signals from the HERA–B data, the determination of detector and trigger efficiencies, and a measurement of  $J/\psi$  differential distributions are described in Chapter 4.
- A measurement of the luminosity ratio can be found in Chapter 5.
- In Chapter 6, the measurement of nuclear effects in  $J/\psi$  production is presented. Systematic uncertainties of the measurement are discussed, and the results are compared to previous experiments and to theoretical predictions.
- The central results of this thesis are summarized in Chapter 7.



---

# The HERA–B Experiment

---

In this chapter, the HERA–B experimental apparatus is described. After a short overview of the experimental environment at the HERA storage ring, the HERA–B subdetectors, their technological challenges and their performance during the 2002/2003 data-taking period are discussed. As the HERA–B dilepton trigger is essential for the analysis presented in this thesis, it is described in detail. Finally, the physics program based on the 2002/2003 run is described.

## 2.1 The HERA Storage Ring

The HERA accelerator (HERA: Hadron-Elektron-Ringanlage) is an electron-proton storage ring situated at the Deutsches Elektronen-Synchrotron (DESY) in Hamburg, Germany. An overview of the DESY accelerator facilities is given in Fig. 2.1.

In the HERA ring, protons are accelerated to 920 GeV and brought into collisions with electrons or positrons with energies of 27.5 GeV at two interaction points covered by the experiments H1 [Abt97] and ZEUS [Hol93]. In these experiments, the internal structure of the proton is probed in deep-inelastic scattering processes. In the HERMES experiment [Ack98], the HERA electron/positron beam is brought into collision with a gas target. Both beam and target can be polarized to study the spin structure of the proton. For the HERA–B experiment, protons from the halo of the HERA proton beam interact with the nuclei of a multi-wire target. Thus in HERA–B, the production and decay of heavy particles in proton-nucleus interactions at a center-of-mass energy of  $\sqrt{s} = 41.6 \text{ GeV}$  are investigated.

The protons are stored in the HERA ring in bunches. With a circumference of 6335.8 m, HERA provides space for 220 proton bunches, and the time interval between two bunch crossings at the interaction points is 96 ns. In the usual filling scheme of the HERA proton ring, only 180 of the 220 bunches are filled. The average rate of proton bunches crossing the HERA–B target thus amounts to  $180/220 \times 1/(96 \text{ ns}) = 8.52 \text{ MHz}$ .

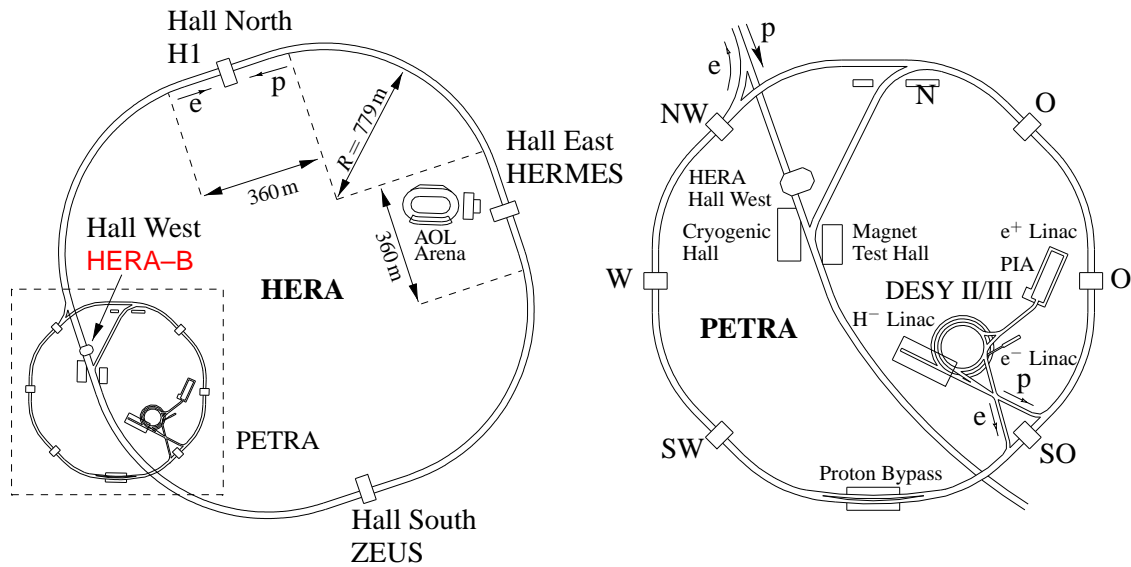


**Figure 2.1:** Sketch of the HERA storage ring (after [DES00]). The HERA ring with the four experimental areas and their respective experiments is shown on the left-hand side. On the right-hand side, a magnified view of the DESY accelerator complex (dashed box in the left picture) is shown.

## 2.2 Subdetectors of the HERA-B Detector

The HERA-B experiment has been proposed and designed to study CP-violation in the system of neutral B mesons [Loh94, Har95]. Planned as a competitor to the experiments operating at asymmetric  $e^+e^-$  colliders, Belle [Aba02] and *BABAR* [Aub02], HERA-B should explore the rich field of B physics in proton-nucleus collisions. However, operating a particle physics detector in the harsh hadronic environment introduces substantial challenges not only in detector and trigger design, but also in their performance.

After a commissioning run in 2000, it became clear that these challenges could not be met in time to compete with the excellent performance of Belle and *BABAR*. Hence, the HERA-B collaboration developed a new physics program making use of the advantages of the HERA-B detector, i.e. large angular acceptance, good primary and secondary vertex resolutions, and a trigger sensitive to lepton pairs. This new physics program covers mainly the fields of heavy quark production and QCD studies [HER00a, HER00b, HER01]. It was approved for a data-taking period of eight months after the HERA luminosity upgrade in 2000/2001. The most important topics of the HERA-B physics program are discussed in Section 2.5. Due to technical problems related to the HERA luminosity upgrade, the data-taking period was reduced to five months, from October 2002 to February 2003.

The HERA-B detector is a forward spectrometer with large angular acceptance. A schematic view of the detector is shown in Fig. 2.2. The aperture of the HERA-B detector of 15–220 mrad in the bending plane of the magnet and 15–160 mrad in the non-bending plane corresponds to approximately 90% of the solid angle in the center-of-mass frame of the primary interactions. Particles are produced by interactions of protons from the halo of the HERA proton beam with an internal wire target. The HERA-B



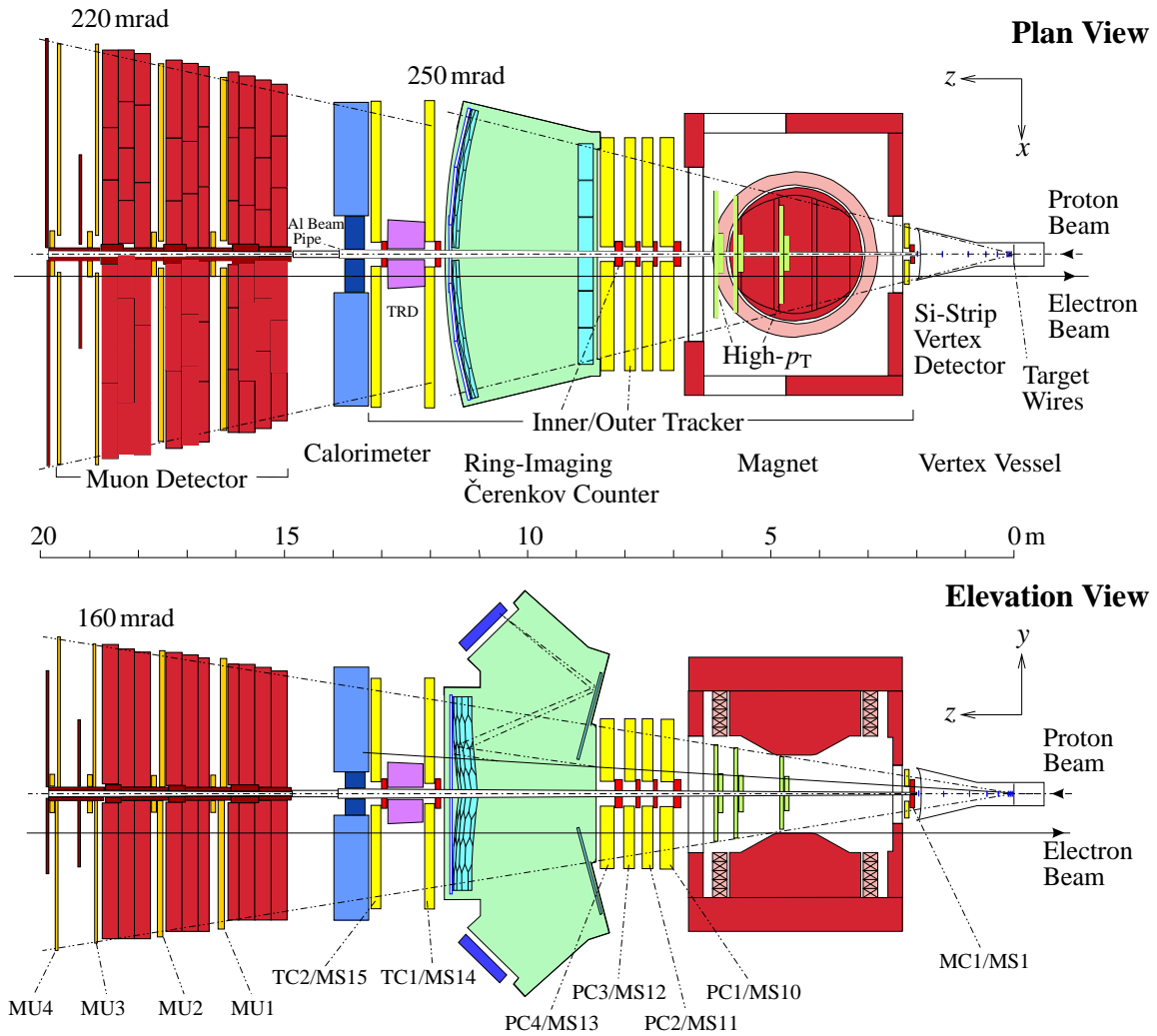


**Figure 2.2:** Schematic views of the HERA-B detector [Spe02]: plan view (above) and elevation view (below). The subdetectors are described in the text.

tracking system consists of a silicon vertex tracker (VDS: Vertex Detector System), a spectrometer magnet, and a multi-layer tracking system, which is divided into an inner part (ITR: Inner Tracker) and an outer part (OTR: Outer Tracker). Particle identification is performed with a ring-imaging Čerenkov counter (RICH), an electromagnetic calorimeter (ECAL), a transition radiation detector (TRD), and a muon detector. The following description of subdetectors is restricted to the parts of the detector which have been in operation during the data-taking period 2002/2003. Unless indicated otherwise, all performance figures are taken from [HER04] and references therein.

The following coordinate system will be used throughout this thesis: The  $z$ -direction is oriented parallel to the proton flight direction. The  $x$ -axis is perpendicular to the  $z$ -axis and points towards the center of the HERA ring. The axis pointing upwards is called the  $y$ -axis.

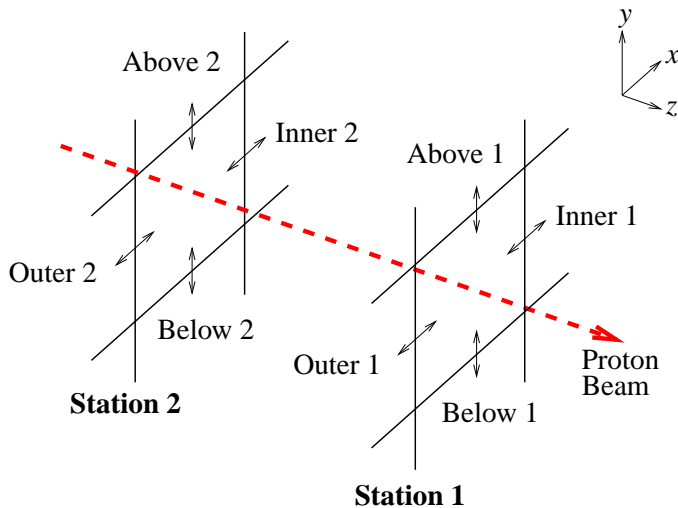


**Figure 2.3:** Sketch of the target wire configuration (after [Sym04]). The wire stations are separated by approximately 4 cm in proton flight direction. The moving directions of the target wires are indicated by arrows.

### 2.2.1 Target

The HERA-B target consists of eight thin wires of materials with different atomic mass numbers  $A$ : carbon ( $A = 12.01$ ), aluminum ( $A = 26.98$ ), titanium ( $A = 47.87$ ), palladium ( $A = 106.42$ ), and tungsten ( $A = 183.84$ ). The target wires are grouped in two stations of four wires each, separated by approximately 4 cm in  $z$ -direction. The wire arrangement and naming scheme is depicted in Fig. 2.3. During the data-taking period 2002/2003, the wire configuration was changed several times, as summarized in Table 2.1.

The target wires are inserted into the halo of the HERA proton beam and can be moved transversely to the beam to adjust the average number of interactions per proton bunch crossing the target. The total interaction rate is measured independently by hodoscope counters mounted at the exit window of the RICH. The automatic target steering allows operation of more than one wire at a time. In this case, the interaction rate for each individual wire is determined utilizing the emission of  $\delta$ -electrons in the interactions of protons with the target wires. For this purpose, each wire is equipped with a charge integrator device to collect the electrical charges on the wire after  $\delta$ -electron emission. This allows to share the interaction rate equally among the target wires.

### 2.2.2 Vertex Detector System

The VDS [Bau03] is a combined vertexing and tracking device based on silicon strip detectors. Located from  $z = 9$  cm to  $z = 220$  cm behind the target, the angular coverage of the VDS reaches from 10 mrad to 250 mrad. The VDS consists of eight superlayers, each containing four quadrants. In the first seven superlayers, the four quadrants are mounted inside a vacuum vessel in a Roman pot system. Hence the quadrants can be moved in transverse direction to the beam axis to avoid radiation damage during proton injection. The last superlayer is mounted at the exit window of the vacuum vessel. An overview of the VDS is shown in Fig. 2.4.

Each quadrant consists of two layers of (mostly double-sided) silicon strip sensors with sensitive areas of  $50 \times 70$  mm<sup>2</sup>. The sensors have a pitch of approximately 50  $\mu$ m and are mounted at stereo angles of  $(0 \pm 2.5)^\circ$  and  $(90 \pm 2.5)^\circ$ . The double-sided sensors are made out of 280  $\mu$ m thick n-doped silicon and include strips on their p- and n-sides.

**Table 2.1:** Target wire configurations during the data-taking period 2002/2003 [Tar03]. Note the changes in material and geometries of some wires due to the replacement of several broken wires during the running.

Wire Name	Abbreviation	Material	Geometry
Inner I	I1	Tungsten <sup>a,b</sup>	Circular, Diameter 50 $\mu\text{m}$
Outer I	O1	Titanium	Circular, Diameter 50 $\mu\text{m}$
Above I	A1	Aluminum	Ribbon, 50 $\mu\text{m} \times 500 \mu\text{m}$
Below I	B1	Carbon	Ribbon, 100 $\mu\text{m} \times 500 \mu\text{m}$
Inner II	I2	Carbon	Ribbon, 100 $\mu\text{m} \times 500 \mu\text{m}$
Outer II	O2	Carbon <sup>c</sup>	Ribbon, 100 $\mu\text{m} \times 500 \mu\text{m}$
Above II	A2	Palladium	Circular, Diameter 50 $\mu\text{m}$
Below II	B2	Titanium <sup>b</sup>	Circular, diameter 50 $\mu\text{m}$

<sup>a</sup>wire replaced on December 3, 2002 and January 2, 2003

<sup>b</sup>wire material changed to tungsten-rhenium alloy (circular, diameter 100  $\mu\text{m}$ ) on February 6, 2003

<sup>c</sup>wire material changed to tungsten (ribbon, 50  $\mu\text{m} \times 500 \mu\text{m}$ ) on January 2, 2003, wire deformed (“banana shape”) since January 4, 2003, broken after January 28, 2003

The VDS provides information on primary and secondary vertices as well as precise track reconstruction in front of the magnet. In more than 85% of the sensors, the measured hit efficiency was better than 95%. A spatial vertex resolution of 31–42  $\mu\text{m}$  in transverse direction to the beam axis has been determined from a Monte Carlo simulation of proton-nucleus interactions. The measured longitudinal distribution of  $J/\psi$  vertices in the data shows a width of 750  $\mu\text{m}$  [Bau03, Abt03d]. This value is a good measure of the decay length resolution of the VDS. It is much smaller than the average decay lengths of 9 mm for neutral B mesons and 2.4 mm for neutral D mesons in HERA–B.

### 2.2.3 Tracking System

#### Spectrometer Magnet

The HERA–B magnet is a dipole magnet with a magnetic field integral of  $\int B dz = 2.13 \text{ T}\cdot\text{m}$  built from normal-conducting copper coils. Charged particles are deflected by the magnetic field in the  $xz$ -plane proportional to the inverse of their momenta.

#### Outer Tracker

The outer part of the HERA–B tracking system—from 80 mrad to 220 mrad—is covered by the OTR. In its original design, the OTR consisted of 13 layers of drift chambers: Seven layers of magnet chambers, denoted MC1–MC7, were placed inside the spectrometer magnet to facilitate the reconstruction of  $K_S^0$  decays downstream of the VDS.

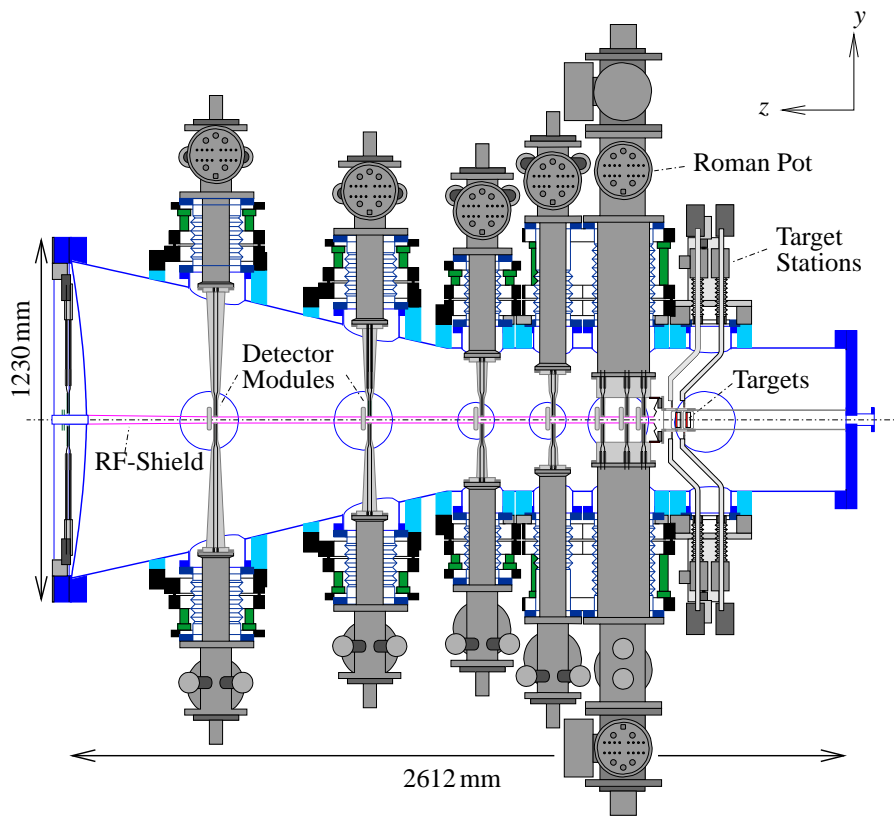


**Figure 2.4:** Schematic drawing of the VDS. The drawing shows the vacuum vessel with the VDS modules mounted in Roman pots and the target stations [Brä01].

However, due to a redesign of the tracking system, the amount of material in front of the calorimeter including these chambers was significantly larger than originally planned, resulting in a lower ECAL resolution. Hence, during the HERA shutdown in 2000/2001, the HERA-B collaboration decided to remove the magnet chambers MC2–MC7, which had not been fully commissioned for tracking and track matching before the HERA shutdown. The remaining material in front of the calorimeter amounts to 0.75–1.5 radiation lengths.

Track reconstruction in the OTR starts from the pattern chambers. In the four layers behind the magnet, PC1–PC4, seeds for the track reconstruction are produced using pattern recognition techniques. The trigger chambers (TC1–TC2), situated in front of the ECAL, are mainly used in the First Level Trigger (FLT). In addition, these chambers are utilized in the tracking to extrapolate tracks downstream the detector. While in the FLT, only the hit information of the OTR is used, drift time information is available in addition for the higher trigger levels and in the offline reconstruction. Each superlayer of the OTR is composed of three stereo layers with orientations of  $0^\circ$  and  $\pm 5^\circ$  to the  $y$ -axis. The superlayers used for the FLT, i.e. PC1, PC4, TC1, and TC2, are designed as double layers in order to provide a larger hit efficiency for the trigger.

The OTR detector consists of drift chambers with a hexagonal “honeycomb” profile, as shown in Fig. 2.5. The cathode material is gold-coated carbon-loaded polycarbonate foil, and the anode wire is a gold-plated tungsten wire with a diameter of  $25\ \mu\text{m}$ . In the

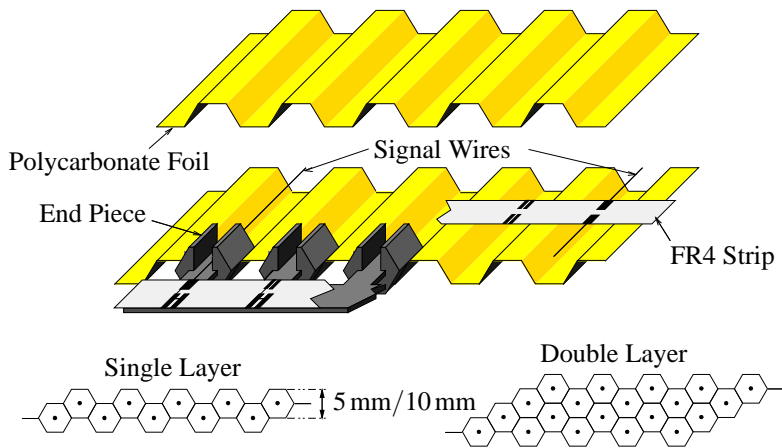


**Figure 2.5:** Illustration of the honeycomb drift cells of the OTR. The lower part of the figure shows cross sections of single and double layer OTR modules [Alb03].

inner part of the OTR, the diameter of the drift cells is 5 mm, while cell sizes of 10 mm have been chosen for the outer part. The drift gas for the OTR is a mixture of argon,  $\text{CF}_4$ , and  $\text{CO}_2$  (65:30:5), and a gas gain of approximately  $3 \times 10^4$  is reached at nominal high voltage.

For tracks with momenta larger than  $20 \text{ GeV}/c$ , i.e. for tracks for which multiple scattering can be neglected, the hit resolution of the OTR cells has been determined to  $320 \mu\text{m}$ . The single cell efficiency measured over the cross section of the cell reaches average plateau values of 94% for the 5 mm cells and 97% for the 10 mm cells.

### Inner Tracker

The ITR [Bag02] constitutes the inner part of the HERA-B tracking system, 5–25 cm from the proton beam pipe, hence covering 10–100 mrad. Initially, the ITR included 10 superlayers, each of which consists of four quadrants of chambers mounted at angles of  $0^\circ$  and  $\pm 5^\circ$  with respect to the  $y$ -axis. As for the OTR, chambers inside the magnet have been removed during the HERA shutdown, such that the ITR setup for the 2002/2003 data-taking period consists of the superlayers MS01 and MS10–MS15, mounted close to the superlayers MC1, PC1–PC4, and TC1–TC2 of the OTR.

The detector technology chosen for the ITR is GEM-MSGC, i.e. micro-strip gaseous chambers (MSGC) with a gas electron multiplier (GEM) foil. A sketch of a GEM-MSGC is shown in Fig. 2.6. MSGCs are a drift chamber variant in which anodes and cathodes are realized as strips on a glass substrate. Ionizing particles crossing a MSGC deposit a primary ionization charge which induces an avalanche of charged particles in the detector volume between the substrate and the drift electrode. In HERA-B, MSGCs with anode pitches of  $300 \mu\text{m}$  and  $350 \mu\text{m}$  are utilized.

Due to the large size of the of the MSGCs used in HERA-B ( $25 \times 25 \text{ cm}^2$ ), a gas amplification of approximately  $10^5$  is needed to achieve an acceptable signal-to-noise ratio in the chambers. Operating MSGCs at this gas gain in hadronic environments leads to serious damage of the chambers, because discharges induced by heavily ionizing particles destroy the anode strips of the chambers. Therefore, GEM foils have been introduced to add an additional gas amplification step. A GEM foil is a perforated polyimide foil that is coated with  $50 \mu\text{m}$  thick copper layers on both sides. A difference of the potential between the copper layers gives rise to additional gas amplification.

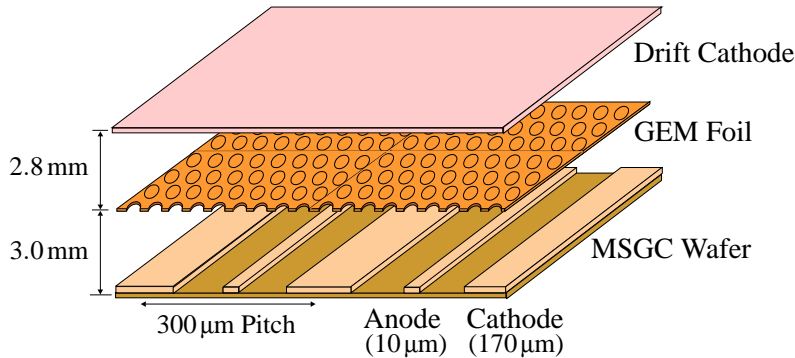


**Figure 2.6:** Sketch of a GEM-MSGC detector of the ITR [Bag02]. The MSGC wafer includes anode and cathode strips. Between the wafer and the drift cathode, a GEM foil is introduced to achieve additional gas amplification.

In the ITR, a mixture of argon and  $\text{CO}_2$  (70:30) is used as the counting gas. The hit efficiencies reached in the ITR are above 90%, and the spatial resolution is better than  $110\ \mu\text{m}$ .

### High- $p_T$ Chambers

Three layers of high- $p_T$  chambers are installed inside the magnetic field of the spectrometer magnet. In the outer part, they consist of straw-tube chambers with cathode pad readout, while the inner part is realized by gas pixel chambers. The high- $p_T$  chambers were planned to be used for the high- $p_T$  pretrigger, sensitive to hadrons with large transverse momenta [Bal00]. This trigger mode was not utilized to acquire data for the modified physics program of 2002/2003. However, data from the gas pixel chambers have been recorded to provide additional tracking information inside the magnet.

## 2.2.4 Particle Identification Devices

### Ring-Imaging Čerenkov Counter

The ring-imaging Čerenkov counter (RICH) [Ari04] is a device to separate protons and kaons from lighter particles, e.g. pions and muons, on the basis of the Čerenkov effect. Charged particles moving through a medium of refractive index  $n$  with velocities  $\beta > 1/n$  radiate photons at a characteristic angle with respect to their flight direction, the Čerenkov angle  $\theta_C = \arccos(1/\beta n)$ . Particles with known momenta and Čerenkov angles can therefore be identified via the mass dependence of  $\beta$ , as shown in Fig. 2.7 (b).

In the HERA-B RICH, the photons are reflected by a system of spherical and planar mirrors to a focal plane outside the detector acceptance that is equipped with photomultipliers. A schematic view of the RICH is shown in Fig. 2.7 (a). All Čerenkov photons which are emitted at the same polar angle from a particle form a ring in the focal plane.

Perfluorobutane ( $\text{C}_4\text{F}_{10}$ ) is used as the radiator gas, resulting in a Čerenkov angle of  $\theta_C = 52.4\ \text{mrad}$  for particles with  $\beta = 1$ . Given the radiator gas and the thickness of the radiator of 2.82 m, a RICH ring is expected to be formed of an average number of 32 photons. In HERA-B, the momentum threshold for the emission of Čerenkov photons is  $2.7\ \text{GeV}/c$  for pions,  $9.6\ \text{GeV}/c$  for kaons and  $18.0\ \text{GeV}/c$  for protons. The RICH efficiency and misidentification probability depend strongly on the considered particles and their momenta. For example, kaons with momenta in the range of  $10\text{--}60\ \text{GeV}/c$

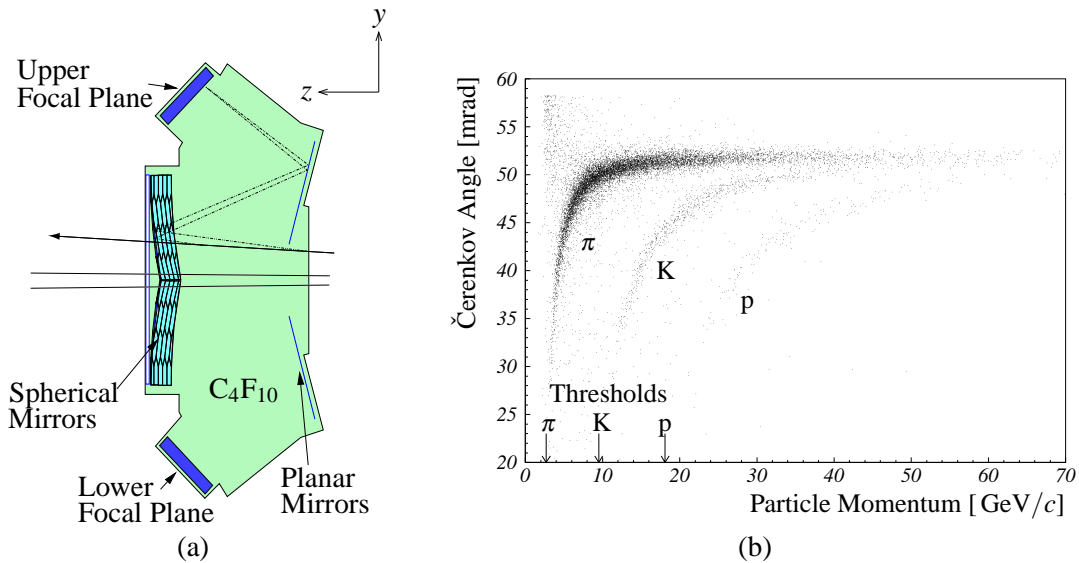


**Figure 2.7:** (a) Schematic drawing of the RICH. Photons emitted from charged particles are deflected to the focal planes by planar and spherical mirrors. (b) Čerenkov angles of pions, kaons, and protons as a function of the particle momentum [Ari04].

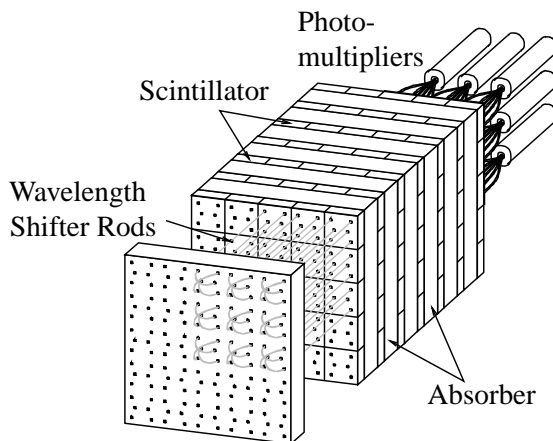


**Figure 2.8:** Illustration of the shashlik calorimeter used in the ECAL [Har95]. Absorber layers are interleaved with layers of scintillator material. The scintillation light is guided to photomultipliers by wavelength shifter rods.

can be identified with 60–80% probability, with less than 5% pion misidentification probability [Ari04].

### Electromagnetic Calorimeter

The HERA-B ECAL [Zoc00] is designed as a sampling calorimeter with a shashlik-type readout: layers of absorber and scintillator materials are staggered, and wavelength shifter rods guide the scintillation light to photo-multipliers, see Fig. 2.8.

The ECAL is divided into three parts to account for the radial dependence of particle densities. The inner ECAL consists of cells with a size of  $2.2 \times 2.2 \text{ cm}^2$ . The absorbers in the inner ECAL are made of a tungsten-nickel-iron alloy. Due to the large flux of particles in the inner part, the scintillator consists of radiation-hard polystyrene-based material. The middle and outer ECAL, employing lead absorbers and standard plastic scintillators, have cell sizes of  $5.6 \times 5.6 \text{ cm}^2$  and  $11.2 \times 11.2 \text{ cm}^2$ .



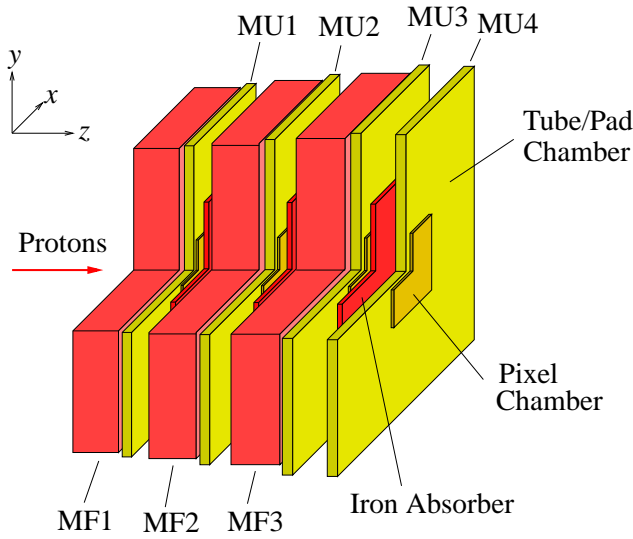


**Figure 2.9:** Sketch of the muon detector. The picture shows the four detector layers MU1–MU4, each consisting of an inner part with gas pixel chambers and an outer part with multi-wire proportional chambers, and the three absorber layers MF1–MF3. The upper right quadrant in beam direction is omitted for the sake of a better view of the inner part of the detector.

The ECAL is used to identify electrons, positrons, and photons by measuring their positions and energies. The spatial resolution  $\sigma_{xy}$ , as determined by comparing the position of clusters of ECAL cells in which energy has been deposited with the extrapolation of electron tracks to the ECAL, is

$$\sigma_{xy} = \frac{(1.10 \pm 0.05) \text{ cm}}{\sqrt{E[\text{GeV}]}} \oplus (0.04 \pm 0.03) \text{ cm},$$

where the symbol “ $\oplus$ ” stands for the quadratic sum of the resolutions. The energy resolution  $\sigma_E$  of the ECAL is determined by studying electrons from photon conversions. Since the rest mass of an electron is much smaller than the electron’s energy, the cluster energy  $E$  measured by the ECAL is approximately equal to the momentum  $p$  measured by the main tracker. Hence, the width of the measured  $E/p$  distribution is a measure of the ECAL energy resolution, combined with the uncertainty of the energy measurement due to the amount of material in front of the ECAL and the momentum resolution of the tracking chambers. For the middle ECAL, the measured energy resolution amounts to

$$\frac{\sigma_E}{E} = \frac{0.103}{\sqrt{E[\text{GeV}]}} \oplus 0.061,$$

close to the expectation from Monte Carlo simulations of  $0.085/\sqrt{E[\text{GeV}]} \oplus 0.06$ . Information on ECAL clusters is used as the starting point of the HERA-B dielectron trigger chain, the ECAL pretrigger.

### Muon Detector

Muons are identified using the fact that they penetrate more material than other particles before being absorbed. Hence, in the muon system [Buc99, Are01, Eig01], three layers of concrete and iron absorbers, MF1–MF3, filter out hadrons. The absorber layers are interleaved with the four superlayers of particle detectors, MU1–MU4, as shown in Fig. 2.9. Between the superlayers MU3 and MU4, there is only very little absorber in



order to minimize the uncertainties of the tracking introduced by multiple scattering in the absorber. This allows to precisely measure track directions behind the absorber and to employ these superlayers for the muon pretrigger, which provides starting points for the higher trigger levels based on coincidences of hits in MU3 and MU4.

Similar to the tracking detectors, the muon system is separated into an inner and outer part. The inner part, built from gas pixel chambers, covers the high-occupancy region from 9 mrad to 40 mrad. The outer part covers 20–220 mrad in the  $x$ -direction and 16–160 mrad in the  $y$ -direction. It is equipped with multi-wire proportional chambers with tubular cells, called “tube chambers” in the following.

The superlayers MU1 and MU2 consist of three stereo layers of tube chambers with orientations of  $0^\circ$  and  $\pm 20^\circ$  with respect to the  $y$ -axis. The last two superlayers, MU3 and MU4, comprise only a single  $0^\circ$  layer of tube chambers. These chambers feature an additional cathode pad readout used for the muon pretrigger, hence they are referred to as “pad chambers”. A muon superlayer of tube or pad chambers is divided into a top and a bottom half, both equipped with 28–34 chambers per stereo layer.

The tube chambers are built of closed aluminum profiles,  $1.4 \times 1.2 \text{ cm}^2$  in size, in which gold-plated tungsten wires with diameters of  $45 \mu\text{m}$  are stretched. To avoid inefficiencies due to the walls of these cells, a chamber consists of two layers of 16 cells each, which are shifted by half a cell size. In the pad chambers, an open aluminum profile of the same size as in the tube chambers is used. The open side of the profile is covered by cathode pads of  $12 \times 10 \text{ cm}^2$ ,  $2 \times 30$  pads in MU3 and  $2 \times 29$  pads in MU4. Similar to the tube chambers, a chambers consists of two layers. In the readout, the two adjacent pads are combined by a logical OR to increase the signal efficiency.

Each cell of the pixel chambers is built from a signal wire of gold-plated tungsten (diameter:  $25 \mu\text{m}$ ) and four potential wires (copper, diameter:  $500 \mu\text{m}$ ), oriented along the beam direction. The cell size amounts to  $0.9 \times 0.9 \text{ cm}^2$  in MU1–MU3 and  $0.94 \times 0.94 \text{ cm}^2$  in MU4. In the superlayers MU1 and MU2,  $2 \times 2$  pixels are connected to a single channel in the readout, while in MU3 and MU4, columns of four pixels form a readout channel. A 65:30:5 mixture of argon,  $\text{CF}_4$ , and  $\text{CO}_2$  is used as counting gas, sufficiently fast for the bunch crossing rate of 96 ns, while showing only small aging effects [Dan01].

The chamber signals are processed by the ASD8 chip [New93], a device that includes a signal amplifier, a shaper and a discriminator, before they are transmitted to the front-end drivers (FED) via flat cables. For the pad signals, an additional pre-amplifier is mounted directly to the pad. The discriminator threshold of the ASD8 can be set for each readout channel individually.

Test beam studies have shown average double layer efficiencies of 99% for the tube chambers [Tit00]. The efficiencies of the pad chambers have been measured in special test runs, and working pads show average efficiencies of 92% [Fom04]. Using the muon detector as a particle identification device requires a good suppression of background, which mainly consists of muons from decays in flight of charged pions and kaons and hadrons passing the muon absorbers. The misidentification probability depends on the particle momenta and the exact criteria to identify muons. Misidentification probabilities of less than 4% for pions and less than 2% for kaons and protons have been measured [Bel02].

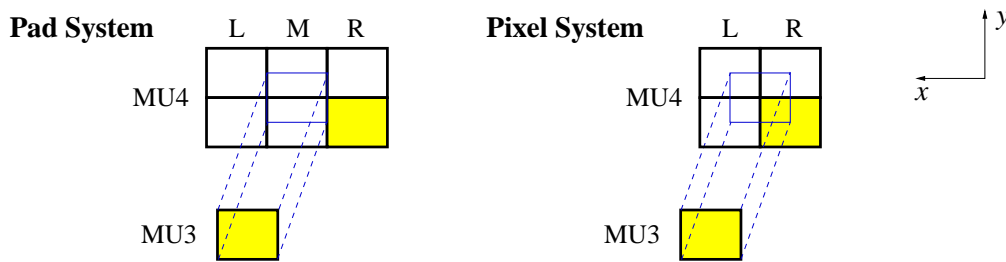


**Figure 2.10:** Muon pretrigger coincidence schemes for the muon pad system (left) and the muon pixel system (right) [Sch01]. The labels “L”, “M”, and “R” correspond to the hit patterns in MU4 that are stored in the pretrigger message, “L” denoting the least significant bit of a pattern.

## 2.3 Pretriggers and First Level Trigger

The key idea of the First Level Trigger (FLT) is to select events with dilepton candidates by a fast message-driven tracking trigger. The higher trigger levels require a FLT rate reduction from 5 MHz to 30 kHz. The maximum allowed time for this reduction step is given by the FED system, which stores events from the last 128 bunch crossings, thus the FLT decision must be taken within  $128 \times 96 \text{ ns} = 12.28 \mu\text{s}$ . In order to meet these requirements, the FLT is implemented as a modular system of custom-made electronics devices. Starting points for the FLT tracking, so-called “Regions of Interest” (RoI), are defined by the pretrigger systems, separately for electron pairs and muon pairs.

### 2.3.1 Muon Pretrigger

The muon pretrigger is the first step of the HERA-B trigger chain for events with at least two muons. In the muon pretrigger, muon candidates are defined by hit coincidences in the last two layers of the muon detector, MU3 and MU4. In the outer part of the muon detector, a 1-to-6 coincidence is required between the pad chambers in MU3 and MU4, as shown in Fig. 2.10. In the inner part, a 1-to-4 coincidence is calculated between “pseudo-pads” composed out of six readout channels of the pixel chambers.

The muon pretrigger hardware comprises three types of electronics boards. The Pretrigger Link Boards receive digitized data from the FED system of the muon detector. Via the Pretrigger Optical Links, the data are transmitted to the Pretrigger Coincidence Units, on which the coincidence calculations are performed using programmable logic. The resulting coincidence data are sent to the Pretrigger Message Generators. The coincidence data are translated into pretrigger messages and transmitted to the FLT, for which they serve as starting points of the search for muon tracks. Detailed descriptions of the design and performance of the muon pretrigger system can be found in [Sch97, Cru98, Ada99, Sch00b, BÖc01, Kla00, Bec01, Sch01, Ada01, Sip04b].

### 2.3.2 ECAL Pretrigger

The ECAL pretrigger [Avo01, Fla01] defines candidates for electrons from leptonic and semi-leptonic decays of heavy particles and for “hard photons”, i.e. photons with large transverse momenta. The pretrigger algorithm forms clusters from  $3 \times 3$  matrices

of readout cells around a cell with large energy deposition. In order to increase the efficiency of  $J/\psi$  detection, the ECAL pretrigger comprises an algorithm to recover the energy loss of electrons due to bremsstrahlung in front of the magnet.

On the ECAL readout boards, cells with energies above an adjustable threshold are flagged, and on the pretrigger board, the energies of the eight surrounding cells are extracted. For this  $3 \times 3$  matrix of ECAL cells, the total cluster energy and the center of gravity of the cluster are calculated. The transverse energy  $E_T = \sum_i E_i \sin \theta_i$  ( $E_i$  energy deposit,  $\theta_i$  angle of particle  $i$  with respect to  $z$ -axis) of the cluster is compared with an adjustable threshold, and the coordinates of a possible bremsstrahlung photon cluster are determined. A trigger message is formed and transmitted to the FLT, as a starting point for the electron tracking in the FLT.

### 2.3.3 RICH Multiplicity Veto

The RICH multiplicity veto [Cru02] is a device to reject events with large track multiplicities before they reach the FLT. By rejecting these events, the trigger chain is better protected against dead-time caused by pile-up of messages. The number of photons in the RICH is strongly correlated with the track multiplicity [Ada01]. Therefore, in the RICH multiplicity veto, a veto signal is generated based on a fast digital sum of the number of photons in some parts of the RICH.

The RICH multiplicity veto is implemented as a modular system, employing three types of electronics boards. The Base Sum Cards of the RICH multiplicity veto receive digitized hits from the RICH FED. The subtotals of 15 Base Sum Cards are summed on two FED Sum Card and transmitted to the Veto Board. On the Veto Board, the final sum is compared to a programmable threshold, and a veto signal is generated. The veto signal is transmitted to the pretriggers to inhibit message transmission to the FLT. Details of the RICH multiplicity veto system are discussed in [Cru02, Brü02a, Hus03].

### 2.3.4 First Level Trigger

#### Trigger Algorithm

Starting from pretrigger messages obtained by the muon detector or the ECAL, the FLT searches for tracks in the superlayers MU4, MU3, and MU1 of the muon detector and TC2, TC1, PC4 and PC1 of the main tracker. Tracks are followed from superlayer to superlayer by an iterative algorithm inspired by the Kalman filter algorithm [Frü87]. The algorithm starts from an RoI defined by a pretrigger message. If a hit is found within the RoI, the weighted mean of the RoI center and the hit is used to construct an RoI in the next superlayer. In order to achieve a sufficient rate reduction, the algorithm requires hits in all three stereo views of the superlayers.

#### Implementation

To fulfill the latency requirements for the pretrigger-FLT chain, the track search algorithm of the FLT is implemented using a network of custom-made electronics boards. See Fig. 2.11 for a schematic view of the FLT.

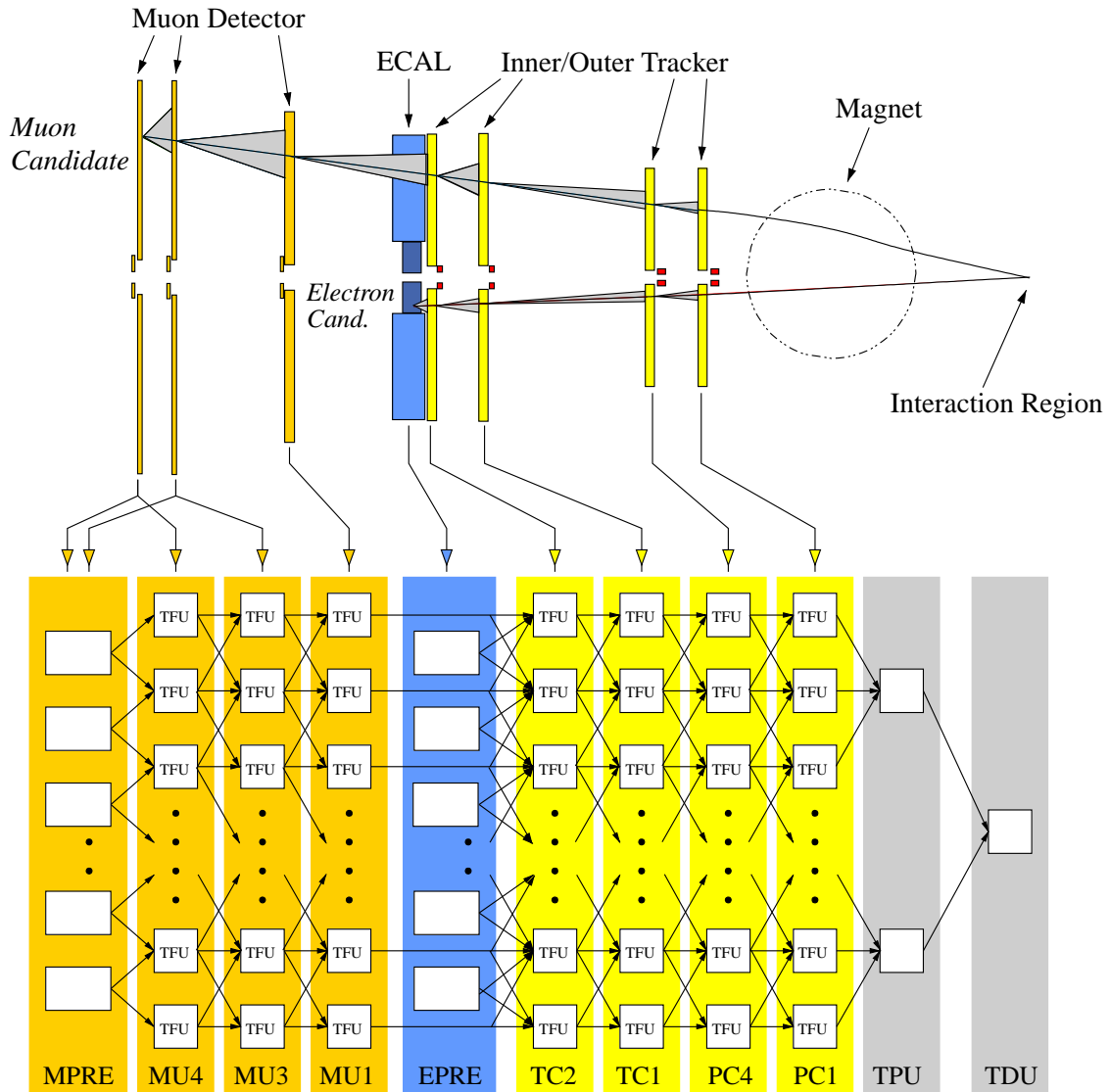


**Figure 2.11:** The network of FLT processors (after [Nör03]). Track candidates from the pre-triggers in the muon detector (MPRE) and the ECAL (EPRE) serve as starting points for a network of TFUs in three superlayers of the muon detector and four superlayers of the OTR. The estimates of the track parameters of track candidates are refined from superlayer to superlayer and finally sent to the TPUs and the TDU.

The track reconstruction algorithm of the FLT is performed by a network of Track Finding Units (TFU). The detector hits are received by the Trigger Link Boards, transmitted via optical links to the TFUs, and stored in so-called wire memories. Starting from an RoI provided by a trigger message from a TFU in a detector superlayer further downstream or from the pretriggers, hits from the wire memory are added to calculate a new RoI for the next superlayer. The trigger message is updated and transmitted to a TFU of the next superlayer or one of the Track Parameter Units (TPU).

The momentum of a track is estimated in the TPU, based on the track parameters behind the magnet and assuming that the track originates from the target region. By comparing the track parameters, track clones can be removed in the TPU.

In the Trigger Decision Units (TDU), the results of the FLT tracking, as received from the FLT network, are translated into trigger signals. A TDU includes two trigger modes, the “count trigger” and the “pair trigger”. In the count trigger mode, the trigger decision is based on the number of tracks which survived the FLT tracking. For the pair trigger mode, the invariant masses of track pairs are calculated. An invariant mass threshold can be set.

During the data-taking period 2002/2003, a second TDU has been introduced, which receives trigger messages directly from the pretriggers. The second TDU allows to bypass the FLT chain and provides the original pretrigger messages for the SLT. Furthermore, the input parts of all TFUs have been modified such that copies of the received pretrigger messages are forwarded to the first TDU in addition to the FLT messages. Hence, the first TDU contains both the result of the FLT tracking and the unmodified pretrigger messages.

### **Fast Control System**

During the FLT processing, data of the last 128 bunch crossings are stored in pipelines at the detector front-end drivers (FED). Events that are accepted by the hardware triggers have to be transferred to the higher trigger levels. For this purpose, the Fast Control System (FCS) [Ful99] distributes the FLT decisions and the corresponding FLT pipeline cell numbers to all FEDs. The FLT pipeline cell number is the address of an event in the FED pipeline and serves as the unique tag for the event within the depth of the FED pipeline. The FCS hardware comprised the FCS mother board and FCS daughter boards in the FED crates of the subdetectors. After a trigger signal arrives at the FCS mother, it is distributed to the daughter boards via optical data-transmission. The daughter boards initiate the transfer of the corresponding event to the event buffer for the higher trigger levels, the Second Level Buffer (SLB). The FCS is capable of generating a trigger signal to select one out of the 220 bunch crossings at random. This “random trigger” is used to select minimum-bias events.

## 2.4 Data Acquisition System

While pretriggers and FLT are built from custom-made electronics, all higher-level trigger algorithms in HERA-B are implemented as software running on PC farms. The data acquisition system (DAQ) [Dam04] provides the hardware needed to perform the triggering, logging and archiving of data, as well as hardware and software for the interconnection between the different trigger components.

### 2.4.1 Data Flow in the Data Acquisition System

After an event has been accepted by the FLT, the data-processing of the DAQ is initiated. The FED data of the accepted event are transferred to the SLB, a buffer system built from Digital Signal Processors (DSP), where they are stored during the SLT processing. Boards based on the same type of DSP are used as a switching network between the SLB and the SLT farm. The SLT farm consists of 240 standard single-CPU PCs with custom-made interface cards to the SLB. SLT farm computers request data for specific RoIs in the event from the SLB and execute the SLT trigger algorithm. The communication between SLB and SLT is managed by an event controller process.

Events that pass the SLT are transported to the Fourth Level Trigger (4LT) farm via a switched Fast Ethernet network. The 4LT farm consists of 100 dual-CPU PCs. After event reconstruction on the 4LT farm, events are collected on up to three dedicated logging computers. The events are buffered on large hard-disks and finally archived on tape.

To optimize the throughput of the DAQ during the 2002/2003 run, only an adjustable fraction of the events was reconstructed online. This is sufficient for a reliable online monitoring of the data quality. The remaining events were reconstructed on the 4LT farm in periods without usable beam, making these events available for analysis with a delay of several days.

The maximum achieved input rate to the SLT during the 2002/2003 data-taking was 25 kHz, mainly limited by the SLB switch throughput. The average logging rate was 100 Hz for data recorded employing a dilepton trigger with maximum event sizes of 150 kB and 1 kHz for data taken with minimum-bias triggers (15 kB per event).

Since data-taking with the HERA-B experiment has been finished, the computing power of the SLT and 4LT farms is also used for offline data processing, i.e. reprocessing of data and production and reconstruction of Monte Carlo simulated data. For the offline processing, the same run control system is utilized that has been used during the data-taking to boot, control and monitor the DAQ system [Her03].

### 2.4.2 Second Level Trigger Algorithm

In the original design of the HERA-B trigger chain, the purpose of the SLT was to perform a full reconstruction of the two tracks which issued the FLT. The SLT tracking is seeded by RoIs provided by the FLT. To allow for more flexible trigger schemes, algorithms to allow seeding from other sources were introduced later.

### Main SLT Algorithm

The trigger algorithm starts from RoIs defined by the FLT or by the pretriggers and comprises the following steps [NPdV03]:

**Slicer:** The Slicer tracking algorithm uses hits from the OTR superlayers PC2 and PC3 in addition to the superlayers already used in the FLT, but is restricted to hits in the  $0^\circ$  layers. The FLT RoIs at the two ends of the main tracker are divided into eight slices, which are combined in all possible ways to check if the hits are consistent with a straight track hypothesis. The algorithm requires at least 9 hits distributed on at least five of the six superlayers. The amount of ghost tracks, i.e. tracks formed from wrong combinations of hits in the detector, is reduced by Slicer.

**RefitX:** Based on a simplified Kalman filter algorithm, i.e. ignoring process noise introduced by multiple scattering, the tracks are refitted using only the hits from the  $0^\circ$  layers. The algorithm starts from TC2, and in each step only the five track candidates with the best qualities are extrapolated to the next superlayer.

**RefitY:** An algorithm identical to RefitX is performed, using only the hits from the  $\pm 5^\circ$  stereo layers and the  $x$ -positions calculated by RefitX. The quality of the tracks is evaluated from a  $\chi^2$  statistic based on the hits on the track and on the number of empty layers in the tracking. Only the best track candidate per input RoI is kept after RefitX and RefitY.

**L2Magnet:** Fast track following through the magnet is realized by a parametrization of the magnetic field integral as a function of the track slope, assuming that the track originates from a box around the active targets. In addition, hits from MC1 and superlayer 8 of the VDS can be utilized to confirm extrapolated tracks in front of the magnet.

**L2Sili:** Tracking in the VDS is also based on a Kalman filter algorithm, applied separately in the  $xz$ - and  $yz$ -views. L2Sili uses hits from the VDS superlayers 1–7. Multiple scattering is taken into account per superlayer rather than per layer to reduce the CPU time consumption.

**L2Vertex:** To trigger an event, a pair of tracks has to originate from a common vertex. The vertex finding in L2Vertex is based on a  $\chi^2$  minimization. Track pairs which form a vertex with  $\chi^2 < 20$  are accepted by the SLT.

### Pretrigger Seeding

Since the FLT was not available during the HERA–B commissioning run in 2000, extensions of the SLT code had been developed to allow SLT tracking based on RoIs defined by the pretriggers or by the SLT itself. For the ECAL, a full reconstruction of clusters was performed to define electron candidates. In the muon SLT code, the FLT tracking in the muon detector was emulated by the SLT, see e.g. [Hus01a].

The muon SLT code used during the 2002/2003 data-taking comprises the following steps: To reduce fake double coincidences, the  $xy$ -positions of muon pretrigger messages in MU3 must be separated by at least 50 cm. The RoI size for hit searching

depends on the position of the RoI in the detector, allowing larger RoIs in the outer parts. A hit clustering algorithm is utilized to increase the hit efficiency for the SLT. If a hit is found within the RoI in the  $0^\circ$  layer of MU2, a straight line defined by the position of the muon pretrigger message and the MU2 hit is extrapolated to MU1. If several hit combinations are found, they are ordered by their quality. The  $x$ -position calculated from the muon SLT code is combined with the  $y$ -position from the muon pretrigger message to define the SLT RoI in TC2. An RoI in PC1 defined by muon tracks would suffer from the large uncertainties introduced by multiple scattering. Therefore, the PC1 RoI is defined for both hypotheses of the charge of the muon and an effective  $p_T$  kick of  $0.7\text{--}2.5\text{ GeV}/c$  resulting from the deflection by the magnetic field.

### Third Level Trigger Algorithm

Due to the rate reduction by the SLT, enough time would be available to run a trigger algorithm which uses information from the entire HERA-B detector. For this task, a Third Level Trigger (TLT) code was foreseen, running on the SLT farm [Sch00a]. Such a trigger is useful to trigger on additional particles which are not seen by the FLT-SLT chain, e.g. single leptons from semi-leptonic decays of B or D mesons. For the physics program of the 2002/2003 data-taking, the TLT has not been employed.

## 2.4.3 Fourth Level Trigger and Event Reconstruction

The 4LT performs full online event reconstruction and classification. Both in the 4LT and in the offline processing, the ARTE framework [ART03] (ARTE: Analysis and Reconstruction Tool) is utilized. ARTE comprises tools for hit preparation, pattern recognition, and reconstruction in the tracking detectors, tools for particle identification, and tools for Monte Carlo simulations. In the following, the main algorithms used for reconstruction and analysis of HERA-B data are described.

### Pattern Recognition and Stand-alone Reconstruction

In the VDS, the CATS package (CATS: Cellular Automaton for Tracking in Silicon) [Abt02a] is used both for pattern recognition and reconstruction. Space points are reconstructed from hits in the VDS, short track segments are built from these space points, and a cellular automaton algorithm is used to combine the track segments to VDS track candidates. The candidates are fitted by a Kalman filter algorithm highly optimized for execution speed.

The main tracker reconstruction comprises two steps: the OTR/ITR-CATS algorithm [Abt02b, Gor04] is used for tracking in the pattern chambers, and RANGER [Man97] is used to propagate tracks to the trigger chambers. OTR/ITR-CATS is similar to the algorithm used for VDS tracking. However, due to the lower hit efficiencies and resolutions in the main tracker compared to the VDS, additional steps have been introduced to allow for dead regions in the detector and to suppress fake tracks. In order to increase the efficiency for the reconstruction of “trigger tracks”, i.e. tracks which issued the SLT, the algorithm allows for using the SLT tracking parameters of these tracks as external seeds for the tracking.



### Matching of Track Segments and Track Refit

The track segments reconstructed by the stand-alone algorithms in the VDS and the sub-detectors behind the magnet are matched by the MARPLE package [Igo98]. From the deflection of the track in the magnetic field, the momentum of the corresponding particle is calculated. MARPLE comprises routines to match track segments from several sub-detector combinations, e.g. VDS–ECAL and VDS–RICH. The most important matching algorithm for track reconstruction and momentum determination connects segments from the VDS and the pattern chambers (PC). Using a Kalman filter technique, the track parameters of the VDS and the PC segments are matched for every combination of track segments, and the quality of the matching is evaluated by calculating the value of  $\chi^2$ . Multiple scattering and fake track segments introduce large tails in the matching  $\chi^2$ , hence only a loose cut of  $\chi^2 < 200$  is required for a matched pair of track segments.

In HERA–B, a track is reconstructed utilizing tracking information from several detector technologies. In addition, the material within the tracking system amounts to 0.75–1.5 radiation lengths. Hence, the track parameters at the beginning and at the end of a particle trajectory are different. Therefore, a global refit of the track parameters is desirable. The refit takes into account the material crossed by the particle trajectory and removes “outliers”, i.e. hits with large contributions to the  $\chi^2$  of the track refit.

### Particle Identification in ECAL, RICH, and Muon Detector

In the ECAL, electrons, photons and strongly interacting hadrons are identified by their energy depositions. The ECAL reconstruction algorithm CARE [Alb97] (CARE: Calorimeter Reconstruction) starts with a search for clusters of cells with energy depositions, followed by the search for electromagnetic showers within the clusters. To distinguish clusters originating from charged and neutral particles, the showers are matched with tracks provided by the tracking detectors. The parameters of clusters, i.e. their energies, spatial positions, and shapes, are evaluated using hits in  $3 \times 3$  matrices of cells around the cell with highest energy deposit. The particle identification code of the ECAL can be applied in the latency-limited SLT environment as well as in the 4LT and offline reconstruction.

The RICH particle identification algorithm RITER [Pes01] uses an extended likelihood method to assign Čerenkov angles to all combinations of tracks and RICH photons. This allows the calculation of particle hypotheses even below their corresponding Čerenkov thresholds. In the case of overlapping RICH rings, an iterative algorithm improves the assignment of photons to tracks. Likelihoods are calculated for six possible particle hypotheses: electron, muon, pion, kaon, proton, and “other”. In the HERA–B RICH, it is difficult to distinguish between light particles such as pions, electrons, and muons. Therefore, the likelihood of light particles is given by the sum of the likelihoods for these particles.

To identify muons, tracks found in the tracking system are matched with hits in all four superlayers of the muon detector [Fom00]. A hit in MU1 and MU2 is defined by a space point formed from hits in the three stereo layers of the superlayers, while a hit in MU3 and MU4 can be a wire or a pad signal. The tracking parameters in the most downstream layer of the tracking system, TC2, are extrapolated to the muon superlayer

MU1. The size of the search window in MU1 is defined by the uncertainties of the track reconstruction in the main tracker, the detector alignment, and uncertainties in the track extrapolation to the muon detector introduced by multiple scattering in the hadron absorber. Every hit found in MU1 in a search window around the extrapolated track is assigned to a muon candidate. All muon candidates are propagated to the next layer, MU2, where again a search window is scanned for hits. Muon candidates without hits in MU2 are discarded, all other combinations are propagated to MU3, where the algorithm tries to link a wire or pad hit to the candidate. Candidates with hits in MU3 are finally propagated to MU4, and again a wire or pad hit is linked to the candidate. This algorithm produces a tree of muon candidates for every main tracker seed. The quality of the candidates is evaluated from a  $\chi^2$  statistic calculated from the distance of the linked hits to the candidate. Missing hits in single stereo views of the superlayers result in an increased value of  $\chi^2$ . The  $\chi^2$  value is transformed into the muon likelihood, and the likelihood for the best candidate is assigned to the track from which the extrapolation started.

### Vertex Reconstruction

The Grover package (Grover: Generic Reconstruction of Vertices) [Abt04a] provides several algorithms for primary and secondary vertex reconstruction. The primary vertex finder starts from an assignment of tracks to target wires using a  $\chi^2$  statistic. The track distribution along the wire is scanned for track clusters, and clusters with at least three tracks are marked as vertex candidates. In a next step, a probabilistic data-association filter, a robust augmentation of the Kalman filter algorithm, is used to refine the determination of the vertex position. In addition, Grover includes user routines for secondary vertex fitting with and without kinematic constraints.

### Event Classification

Fast access to subsamples of the data with specific properties is done by the event classification code. Using standardized selection criteria, subsamples, e.g. of lepton pair or  $K_S^0 \rightarrow \pi^+ \pi^-$  candidates, are built. For dimuon events, three different classes were defined in the 2002/2003 data-taking. The first class requires a pair of clean muon tracks in the event. A common vertex of the muon pair is needed for the second class. For the third class, a minimum invariant mass of the muon pair is required in addition. The precise definitions of these event classes are given in Section 4.1.3.

## 2.4.4 Trigger Strategies

### Dilepton Trigger

The dilepton trigger utilized in the 2002/2003 data-taking is a modified version of the original dilepton trigger strategy in HERA-B, in which the FLT was supposed to be used as a lepton pair trigger while the SLT was seeded by RoIs from the FLT. Due to the limited data-taking time, higher priority was assigned to accumulating a large charmonium data-sample than to optimizing the FLT pair trigger. The trigger mode which meets

these requirements is called “1 FLT/2 SLT\*”. In the 1 FLT/2 SLT\* mode, the FLT is used as a count trigger. The SLT starts again from the pretriggers, independently of the FLT result.

The main hardware modifications needed for the 1 FLT/2 SLT\* trigger was an additional “2<sup>nd</sup> TDU” in the FLT chain and a modification in the input parts of the TFUs. The pretrigger messages are multiplexed and fed into the FLT network and in addition into the 2<sup>nd</sup> TDU, such that the SLT tracking can be performed based on the original pretrigger messages. The changed TFU input allows to forward the pretrigger messages through the FLT network without modifications. Therefore, the pretrigger messages are available to the first TDU in addition. The FLT selection performed by the first TDU is based on counting both the number of FLT tracks and pretrigger messages.

The final trigger decision is a logical AND of two independent trigger chains: at least one track and two pretrigger messages are required to be found by the pretriggers and the FLT, and a track-pair with a common vertex must pass the pretrigger-SLT chain.

### Interaction Trigger

For the minimum-bias data-taking, a trigger was employed that requires minimal activity in the HERA-B detector. Data from the FCS random trigger are fed into the SLT, where, in a first step, events are removed if they originate from empty bunches according to the HERA filling scheme. In events from non-empty bunches, the number of photon hits in the RICH and the energy sum of the ECAL are calculated. Events are accepted if they contain at least 30 RICH photons or at least 1 GeV of energy deposited in the ECAL.

### Hard Photon Trigger

The hard photon trigger is a special trigger setup to enrich events containing photons with large transverse energies. In the ECAL pretrigger, a cluster with a minimum transverse energy of 2.5–3 GeV is required, in which an energy larger than 1.5 GeV is deposited in a single cell. Events selected by the ECAL pretrigger are passed to the SLT, where the cuts imposed in the pretrigger are re-checked in order to suppress hot channels in the pretrigger.

## 2.5 Physics Goals of the HERA-B Experiment

The physics program described in the following is based on the new physics program approved for the time after the HERA luminosity upgrade in 2000/2001 [HER00a, HER00b, HER01]. Some analyses proposed in the new physics program turned out not to be feasible using the limited statistics acquired during the five months of data-taking in 2002/2003. Hence, the description of the program is restricted to a selection of the topics which are actually being analyzed by the HERA-B collaboration.

## 2.5.1 Heavy Quark Production

### Charmonium Production and Nuclear Effects

The theoretical models currently used to describe charmonium production are the color evaporation model (CEM) and models based on nonrelativistic QCD (NRQCD). Details on these models can be found in Chapter 3. The models rely on experimental data to adjust their free parameters. Therefore, a comprehensive test of the model predictions in a broad kinematic range and with good precision is desirable. The HERA-B acceptance for leptonic decays of charmonia extends to fractional longitudinal momenta of  $x_F \approx -0.35$ , a region previously inaccessible to fixed-target experiments. At the same time, a broad range in the transverse momentum, from 0 to 5 GeV/c, is covered by HERA-B.

Data taken with a minimum-bias trigger during the 2002/2003 data-taking period allow a measurement of the  $J/\psi$  production cross section that is not biased by trigger effects. An independent measurement of this cross section by the HERA-B experiment can serve as a normalization for other cross section measurements, for example for  $\psi(2S)$  and  $b\bar{b}$  production.

Using the HERA-B dilepton trigger, several charmonium states are enriched in the data-sample.  $J/\psi$  and  $\psi(2S)$  mesons are detected by their decays into lepton pairs, and the  $\chi_{c1}$  and  $\chi_{c2}$  states undergo radiative decays to  $\ell^+\ell^-\gamma$  final states. The theoretical models of charmonium production can be distinguished by the shapes of the predicted differential cross sections. For example, the dependence of the cross section on the polar angle of the positive lepton with respect to the charmonium state is sensitive to the polarization of the state. In the CEM, no polarization of  $J/\psi$  mesons is expected, while large transverse polarization is predicted in NRQCD.

Measurements of the fraction of  $J/\psi$  produced from radiative  $\chi_c$  decays,  $R(\chi_c)$ , provide a further test of charmonium production models. From the 2000 data-taking, a value of  $R(\chi_c) = 0.32 \pm 0.06(\text{stat.}) \pm 0.04(\text{syst.})$  has been published [Abt03b], which favors production models in the framework of NRQCD. With the data taken in 2002/2003, a more precise measurement of  $R(\chi_c)$  by the HERA-B collaboration will be available.

The HERA-B target has been operated with wires made out of different materials. Therefore, nuclear effects in charmonium production can be analyzed.  $J/\psi$  production in nuclear media is the main subject of this thesis and will be described further in Chapter 3. Furthermore, the ratio of branching fraction times cross section for  $\psi(2S)$  and  $J/\psi$  production is studied within HERA-B. By comparing the ratio to similar measurements at different center-of-mass energies and with different materials, the energy dependence of charmonium production and the different influence of nuclear effects on  $J/\psi$  and  $\psi(2S)$  production are evaluated. An overview of the charmonium studies performed in HERA-B along with preliminary results is given e.g. in [Hus04].

### $b\bar{b}$ Production Cross Section

Measurements of the  $b\bar{b}$  production cross section serve as important tests for perturbative QCD predictions. These predictions are based on the factorization of the production cross sections into perturbatively calculable parton-level cross sections and non-perturbative parton distribution functions and fragmentation functions. Near the

threshold for the production of  $b\bar{b}$  pairs, additional processes contribute to the cross section, e.g. soft gluon emission, which have to be resummed in all orders of perturbation theory [Bon98, Kid01]. The most recent calculations of the  $b\bar{b}$  cross section include next-to-leading-order contributions and systematic treatment of threshold contributions in next-to-next-to-leading-logarithmic order. Still the uncertainties of these predictions are large, and experimental input is needed to constrain the theoretical models.

Previous measurements of  $b\bar{b}$  production in fixed-target experiments were based on very small data sets and bear systematic uncertainties as large as 30%. The measurement by the E789 collaboration using the decay  $b\bar{b} \rightarrow J/\psi X$  resulted in a total production cross section of  $(5.7 \pm 1.5(\text{stat.}) \pm 1.3(\text{syst.}))$  nb/nucleon [Jan95]. The measurement of E771 was based on double semi-leptonic decays of B mesons and yielded  $42_{-21}^{+31}$  nb/nucleon [Ale99]. Due to the limited  $x_F$  range of E789 and E771, both results suffer from uncertainties due to the extrapolation to the full phase space.

Given the good secondary vertex resolution, the larger angular acceptance, and the dilepton trigger, HERA-B is in the position to improve these measurements. Based on data taken during the HERA-B commissioning run in 2000, a  $b\bar{b}$  cross section of  $(32_{-12}^{+15}(\text{stat.}) \pm 8(\text{syst.}))$  nb/nucleon using the decay  $b\bar{b} \rightarrow J/\psi X$  has been published [Abt03c]. A more accurate measurement of the  $b\bar{b}$  cross section will become available from the analysis of the 2002/2003 data. Since HERA-B is capable of reconstructing high- $p_T$  particles in addition to the trigger particles, exclusive B meson decays provide an additional possibility for a measurement of the  $b\bar{b}$  cross section.

Apart from studying B meson production, also the production cross section of  $b\bar{b}$  bound states in proton-nucleus collisions is investigated in HERA-B. The cross section is derived from decays of the  $\Upsilon(1S)$ ,  $\Upsilon(2S)$ , and  $\Upsilon(3S)$  states into lepton pairs.

### Open Charm Production

Apart from studying charmonia, i.e.  $c\bar{c}$  bound states, also the production of open charm mesons is of interest to the HERA-B experiment. Open charm studies in HERA-B are focused on measurements of the production cross sections for charged and neutral D mesons and their ratios. Similar to  $b\bar{b}$  production, both the uncertainties of theoretical predictions and previous experimental results are large. Preliminary results using data from the 2002/2003 data-taking period recorded with the interaction trigger have been reported e.g. in [Bog04].

## 2.5.2 QCD Studies

### Strangeness Production

Particles containing strange quarks, for example  $K_S^0$  and  $\Lambda$  mesons, are produced copiously in proton-nucleus interactions. The HERA-B collaboration has published the production cross sections of  $K_S^0$ ,  $\Lambda$ , and  $\bar{\Lambda}$ , extracted from the 2000 commissioning run [Abt03a]. New measurements based on data taken with the interaction trigger during the 2002/2003 data-taking period are performed in [Gor04]. Another property of  $\Lambda$  and  $\bar{\Lambda}$  hyperons studied in HERA-B is polarization. Several theoretical models for

hyperon polarization exist, but none of them is able to explain the full range of experimental results [Fel99]. Analyses of  $\Lambda$  polarization using data from the 2002/2003 data-taking period are presented in [Böc04, Kli04]. Other hyperons are reconstructed in the HERA-B detector via cascade decays. In the 2002/2003 data, signals of several  $\Xi$  and  $\Omega$  states have been found, e.g. via the decay  $\Xi^- \rightarrow \Lambda\pi^- \rightarrow p\pi^-\pi^-$ , and their production cross sections are being studied. Investigating the production of  $K^*$  and  $\phi$  in proton-nucleus collisions serves as an important input for measurements of strangeness enhancement in nucleus-nucleus collisions, a signature for the formation of a quark-gluon plasma. Differential and total cross sections of  $K^*$  and  $\phi$  production and their nuclear dependence are analyzed in [vE04, Sym04].

### Exotics and Rare Processes

After January 2003, several experiments reported evidence for “pentaquarks”, i.e. particles consisting of five quarks and antiquarks. One of the pentaquark candidates is the  $\Theta^+$  with a mass of  $1540 \text{ MeV}/c^2$ , a hypothetical bound state composed of  $uudd\bar{s}$ . From the non-observation of the decay  $\Theta^+(1540) \rightarrow pK_S^0$  in HERA-B, an upper limit of the production cross section  $\sigma$  times branching fraction  $\mathcal{B}$  at mid-rapidity is derived:  $\mathcal{B}\sigma$  is smaller than  $4\text{--}16 \mu\text{b}/\text{nucleon}$  for  $\Theta^+$  masses between  $1521$  and  $1555 \text{ MeV}/c^2$ . Furthermore, no signal of the  $\Xi^{--}$  pentaquark with the quark content  $ddss\bar{u}$  is observed in the decay  $\Xi^{--}(1862) \rightarrow \Xi^-\pi^-$ , resulting in an upper limit of  $\mathcal{B}\sigma$  of  $2.5 \mu\text{b}/\text{nucleon}$  [Abt04b].

Based on the clean signature of a lepton pair, competitive limits on the branching fractions of the flavor-changing neutral current decay  $D^0/\overline{D^0} \rightarrow \mu^+\mu^-$  are derived. The Standard Model branching fraction of the decay is of the order of  $10^{-19}$ . In extensions of the Standard Model, enhanced branching fractions up to  $3.5 \times 10^{-7}$  are expected [Bur03]. An analysis of the 2002/2003 data yields an upper limit on the branching fraction of  $\mathcal{B} < 2.0 \times 10^{-6}$  at 90% confidence level [Abt04c].

### Direct Photon Production

A measurement of the production cross section of direct photons is an important test of perturbative QCD, and it allows to measure the gluon structure function of the proton. Previous measurements of the direct photon cross section by the FNAL E706 collaboration can only be explained with intrinsic transverse parton momenta larger than  $1 \text{ GeV}/c$  [Apa98], much larger than the value of  $200 \text{ MeV}/c$  expected from the uncertainty principle. By analyzing data taken with the hard photon trigger, an independent check of the E706 result will be available. Preliminary results of the analysis can be found in [Mat04].

---

# Charmonium Production and Suppression: Theory and Experiments

---

Soon after the discovery of the  $J/\psi$  resonance in 1974, the  $J/\psi$  was interpreted as a bound state of a charm and an anti-charm quark,  $c\bar{c}$  [App75, DR75]. In analogy to positronium, a state of matter in which an electron and a positron are bound by the Coulomb force of electrodynamics,  $c\bar{c}$  states were given the name “charmonium”. In the first part of this chapter, theoretical models for the production of charmonium states are reviewed.

In proton-nucleus collisions, as they take place in HERA-B, these models are subject to modifications: charmonium production is suppressed due to interactions with the nuclear medium. The most common parametrizations of nuclear effects are based on the semi-classical Glauber model, which is introduced in this chapter, followed by descriptions of the most relevant suppression mechanisms in the kinematic range of the HERA-B experiment.

The chapter concludes with an overview of previous experiments in the field of fixed-target proton-nucleus interactions in which nuclear effects in charmonium production have been studied.

## 3.1 The Charmonium Spectrum

### 3.1.1 Charmonium Quantum Numbers

Quarks of the same flavor are fundamental representations of the gauge group of QCD, color-SU(3), i.e. a triplet  $q = (q_r, q_g, q_b)$ , where  $r, g, b$  denote the color quantum numbers of the quarks. A quark  $q$  and an anti-quark  $\bar{q} = (\bar{q}_r, \bar{q}_g, \bar{q}_b)$  of the same flavor can be joined in eight colored combinations (“color octet”) and one color-neutral combination (“color singlet”). Since no free quarks or gluons have been observed, color-SU(3) is

an exact symmetry in nature, i.e. all hadrons are color-neutral. Quarkonia are hence color-singlet combinations of  $q\bar{q}$ .

Bound states of  $q\bar{q}$  also satisfy the discrete symmetries of parity and charge conjugation. It follows from Lorentz invariance of the Dirac equation that the wave functions of a particle and its anti-particle have opposite parity. The parity eigenvalue  $P$  of the angular part of the  $q\bar{q}$  wave function is given by the parity of the spherical harmonics  $Y_m^l(\theta, \varphi)$ ,  $P = (-1)^l$ . Here  $l$  and  $m$  are the magnitude and the  $z$ -component of the angular momentum quantum number. Hence the parity of a  $q\bar{q}$  bound state with orbital angular momentum quantum number  $L$  reads

$$P = -(-1)^L. \quad (3.1)$$

Neutral  $q\bar{q}$  systems are eigenstates of the charge conjugation operator. The sign of the corresponding eigenvalue  $C$  is determined from a combination of a factor of  $-1$  from exchanging the quark and the anti-quark,  $(-1)^l$  from  $Y_m^l(\theta, \varphi)$  and  $(-1)^{s+1}$  from exchanging the spin  $s$  of the  $q\bar{q}$  system. For  $q\bar{q}$  bound states with orbital angular momentum  $L$  and spin  $S$ ,  $C$  is therefore given by

$$C = (-1)^{L+S}. \quad (3.2)$$

Heavy quarkonia are nonrelativistic to a good approximation, therefore their spectra are often characterized in spectroscopic notation,  $n^{2S+1}L_J$ , where  $n$  is the principal quantum number of the system, and  $J = L + S$  is the total angular momentum. In this notation, the  $J/\psi$  meson is the  $1^3S_1$  state of the charmonium spectrum. Another common representation of the quantum numbers is  $J^{PC}$ . The quantum numbers of the  $J/\psi$  are  $1^{--}$ , i.e. the  $J/\psi$  is a particle with spin 1 and negative parity and charge conjugation quantum numbers. Particles with these properties are called “vector mesons”, because under Lorentz transformations, their wave functions transform like a vector. Vector mesons bear the same quantum numbers as the photon.

The mass spectrum of charmonium states is shown in Fig. 3.1. If the invariant mass of a  $c\bar{c}$  pair is smaller than twice the mass of the lightest charmed meson, the  $D^0$  meson, the  $c\bar{c}$  pair cannot decay into open charm mesons. Rather, the invariant mass spectrum below threshold consists of discrete  $c\bar{c}$  resonances.

### 3.1.2 Potential Models

The first successful description of the charmonium spectrum has been reached utilizing potential models. In these models, it is assumed that the  $c\bar{c}$  pair is bound by a static potential, i.e. by a flavor-symmetric instantaneous color interaction. Several QCD-inspired potential models for heavy quarkonia have been developed. The asymptotic behavior of the  $c\bar{c}$  potential is Coulomb-like for small distances  $r$ , where strongly interacting particles are asymptotically free, and string-like for large distances, motivated by confinement:

$$V(r) = -\frac{4}{3} \frac{\alpha_S(1/r^2)}{r} + kr. \quad (3.3)$$

Here  $k$  can be viewed as the string tension. Assuming a static potential is only valid if the relative velocity  $v$  of the  $c\bar{c}$  pair satisfies  $v \ll 1$ .<sup>1</sup> It follows from the virial theorem,

<sup>1</sup>In this chapter, “natural units” will be used, i.e.  $\hbar = c = 1$ , unless indicated otherwise.



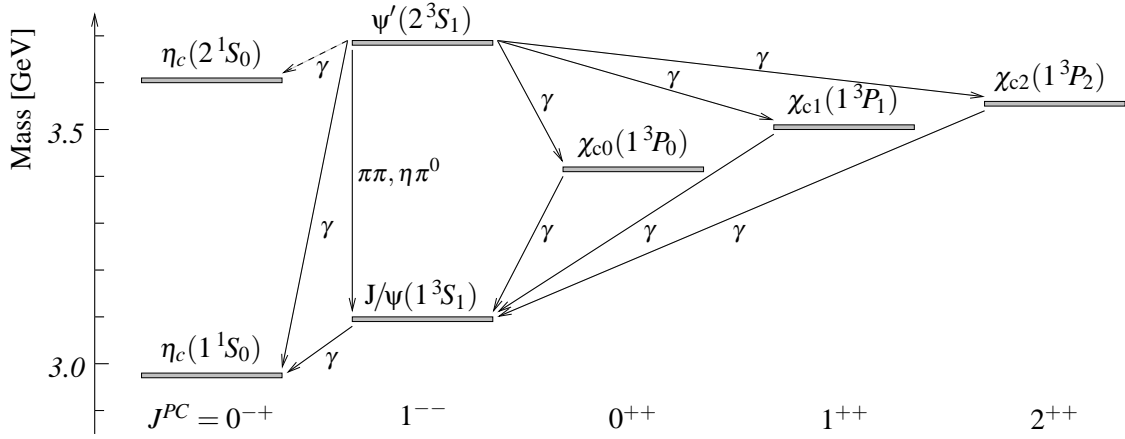


**Figure 3.1:** Invariant mass spectrum of charmonium states below the open charm threshold. The charmonium states are classified according to the spectroscopic notation,  $n^{2S+1}L_J$  ( $n$  principal quantum number,  $S$  spin,  $L$  orbital angular momentum,  $J = L + S$  total angular momentum), and their quantum numbers  $J^{PC}$  ( $P$  parity,  $C$  charge conjugation). The most important transitions between different charmonium states are indicated by arrows.

that in a potential given by Eq. (3.3),  $v$  is proportional to  $\alpha_S(1/r^2)$ . A more detailed evaluation of the relative  $c\bar{c}$  velocity yields  $v^2 \approx 0.25$  [Qui79]. Therefore, for a realistic potential model, relativistic corrections have to be taken into account.

The Cornell potential [Eic78, Eic80] is the prototype of charmonium potentials. In [Buc81], an alternative potential with similar asymptotic behavior is developed, but softening the singularity at  $r = 0$ . In recent years, lattice QCD has become an important tool in hadron spectroscopy, since it allows QCD predictions of the spectrum beyond the non-relativistic approximation. For an overview see e.g. [Ish04] and references therein.

## 3.2 Charmonium Production and Decays

### 3.2.1 Charmonium Decays

A striking feature of the  $J/\psi$  is the narrow total width of the resonance of 91 keV. The reason is the very narrow hadronic width of the  $J/\psi$ . Since the  $J/\psi$  is not heavy enough to decay into other charmed hadrons, allowed  $J/\psi$  decays proceed via the process of  $c\bar{c}$  annihilation. Decays of charmonium states are restricted by the following selection rules:

- According to the Okubo-Zweig-Iizuka (OZI) rule [Oku63, Zwe64a, Iiz66], the rates of decays represented by Feynman diagrams with “unconnected” quark lines, e.g. the annihilation of a  $c\bar{c}$  pair, are suppressed. In the formalism of QCD, the suppression is due to the fact that a color-neutral hadron can only decay into other color-neutral hadrons by exchanging more than one hard gluon.
- Conservation of the charge conjugation quantum number  $C$  allows charmonia with  $C = 1$  to decay into two photons or gluons ( $C = -1$ ). Charmonia with  $C = -1$  are allowed to decay into one virtual or three real photons, or into three gluons.

- The Landau-Yang theorem [Lan48, Yan50] states that massive spin-1 particles cannot decay into two identical massless spin-1 particles. Hence decays of spin-1 charmonia into two gluons are forbidden, even if they are allowed by  $C$ -conservation.

As an example, the  $J/\psi$  meson is color-neutral and has a charge conjugation quantum number of  $C = -1$ , i.e. at least three gluons are produced in hadronic decays of  $J/\psi$  mesons.

An important parameter for the production and decays of charmonia is the radial  $c\bar{c}$  wave function at the production or decay point (chosen to be the origin of the coordinate system),  $R(0)$ . The parameter  $R(0)$  describes the probability of the  $c$  and the  $\bar{c}$  to meet at a point in space and cannot be calculated perturbatively. The leptonic decay width of  $J/\psi$  mesons is given by the overlap of the  $c\bar{c}$  wave functions and the probability of the  $c\bar{c}$  pair to annihilate into a virtual photon. To lowest order, this is summarized in the Van-Royen-Weisskopf formula [vR67],

$$\Gamma(J/\psi \rightarrow \ell^+ \ell^-) = \frac{\alpha^2 q_f^2}{M^2} |R(0)|^2. \quad (3.4)$$

Here  $\alpha$  is the fine structure constant,  $q_f^2$  is the square of the quark charges ( $q_f^2 = 4/9$  for charmonia), and  $M$  denotes the charmonium mass. Hence,  $|R(0)|$  can be extracted by measuring the leptonic decay widths of  $J/\psi$  mesons.

### 3.2.2 Color Evaporation Model

First calculations of charmonium production cross sections emerged soon after the discovery of the  $J/\psi$  meson. As noticed in [Ein75] and further elaborated in [Glü78], the observed large production cross section can be explained by a production mechanism dominated by gluon interactions. The quark sea is a too small source of charm quarks, and fusion of light  $q\bar{q}$  pairs is suppressed by the OZI rule. The sensitivity of the production cross section and the kinematic distributions to gluonic interactions made charmonium production also an interesting probe for the gluon distributions inside hadrons. Calculations of the  $c\bar{c}$  production cross section to lowest order in QCD, including  $q\bar{q}$  and gluon-gluon fusion processes, can be found in [Bab78].

In the Color Evaporation Model (CEM), the prescription to calculate the production cross section  $\sigma^H$  for  $c\bar{c}$  resonances  $H$  arises from a local quark-hadron duality argument [Fri77]: The cross section  $\sigma^H$  represents a fixed fraction  $F^H$  of the total cross section for producing a free  $c\bar{c}$  pair, averaged over masses from twice the  $c$  quark mass to the open charm threshold:

$$\sigma^H = F^H \int_{2m_c}^{2M_{D^0}} \frac{d\sigma(M)}{dM} dM. \quad (3.5)$$

The fraction  $F^H$  for a particular state depends on the details of the transformation from the color-octet  $c\bar{c}$  state to the color singlet state  $H$ , i.e. the charmonium type, the beams,

and the center-of-mass energy of the collision. If the  $c\bar{c}$  pair is produced in an octet state, it can “evaporate” its color by soft gluon emission, circumventing the OZI rule [Hal77].

Since  $F^H$  enters the CEM as a free parameter, the model cannot predict total cross sections. However, cross section ratios between different charmonia are predicted to be constant, and differential cross sections are identical for all charmonia. In the CEM, the final state charmonium is unpolarized, since all spin and color information are randomized by the transition from the octet to the singlet state.

The CEM predictions have been successful in charmonium phenomenology. Therefore, the CEM is used to date as a model for charmonium hadroproduction, see e.g. the calculations presented in [Vog99].

### 3.2.3 Color Singlet Model

The Color Singlet Model (CSM) [Bai81, Ber81] was motivated by the drawbacks of the CEM, namely the arbitrary normalization and the averaging of spin and color degrees of freedom. CSM calculations of charmonium production are carried out in analogy to charmonium decays. It is known from the charmonium model [Eic78], that two energy scales are involved in charmonium decays. Due to the nonrelativistic relative velocity of the  $c\bar{c}$  pair, the binding energy is much smaller than the relevant energy scale for charmonium decays, i.e. the charm quark mass. Therefore, charmonium decays are dominated by processes in which the lowest possible number of gluons is exchanged. The relevant two- and three-gluon contributions are calculable in perturbative QCD.

Similarly, charmonium production cross sections in the CSM are calculated from quark-antiquark and gluon-gluon fusion processes with the following generic form:

$$\sigma(ab \rightarrow n^{2S+1}L_J X) = \hat{\sigma}_{ab} \left| \frac{d^l R_{nl}(0)}{dr^l} \right|^2, \quad (3.6)$$

where  $a$  and  $b$  stand for  $q, \bar{q}$  or  $g$ ,  $\hat{\sigma}_{ab}$  is a process-dependent parton-level cross section convoluted with the appropriate parton distributions, and  $d^l R_{nl}(0)/dr^l$  are derivatives of the universal non-perturbative charmonium wave function. Eq. (3.6) is a factorization formula: it states that the binding of the  $c\bar{c}$  pair at low energies can be treated independently of the production mechanism at higher energies.

An overview of calculations in the framework of the CSM can be found e.g. in [Sch94]. Charmonium states with the quantum numbers  $1^1S_0$  and  $1^3P_J$  can be produced directly as color singlets in gluon-gluon fusion. On the other hand, an additional hard gluon has to be emitted in a perturbative process to form the  $1^3S_1$  state  $J/\psi$  as a color singlet:  $gg \rightarrow 1^3S_1 g$ . The leading contributions are proportional to  $\alpha_s^3$ , see also Fig. 3.2:

$$q\bar{q} \rightarrow n^{2S+1}L_J g, \quad (3.7)$$

$$gg \rightarrow n^{2S+1}L_J g, \quad (3.8)$$

$$gq \rightarrow n^{2S+1}L_J g. \quad (3.9)$$

In addition to the direct production channels,  $J/\psi$  are produced via decays of  $\psi(2S)$  states, e.g.  $\psi(2S) \rightarrow J/\psi \pi \pi$ , and radiative decays of  $\chi_c$  states, i.e.  $\chi_c \rightarrow J/\psi \gamma$ .

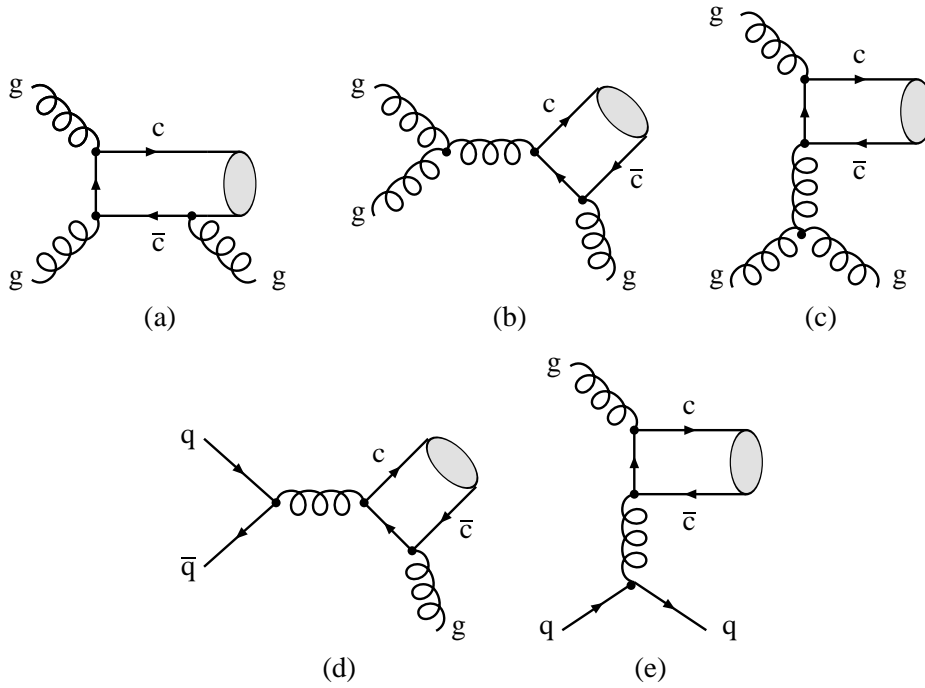


**Figure 3.2:** Contributions of  $\mathcal{O}(\alpha_s^3)$  to charmonium production in the CSM (after [Sch94]). Due to  $C$ -parity conservation, direct  $J/\psi$  production is only possible via process (a).

To adjust the cross sections derived from these processes to experimental data, a large correction factor (“K-factor”) of  $K = 1.7$  has to be introduced, indicating that higher-order corrections to the tree-level cross sections are important [Sch94].

Due to the average velocity of  $v^2 = 0.25$ , relativistic corrections proportional to  $v^2$  add important contributions to the production cross section. However, within the CSM approach, there is no systematic way to include these corrections. The CSM fails to explain the production cross section of charmonia at large transverse momenta, published by the CDF collaboration [Abe97], especially in the case of  $\psi(2S)$  production. As it is known today, important contributions to the cross section from color-octet processes are missing in the framework of the CSM, such that this model has been superseded by models based on nonrelativistic quantum field theory.

### 3.2.4 Nonrelativistic QCD

Charmonium production can be described in the framework of a nonrelativistic quantum field theory. In a nonrelativistic quantum field theory, contributions to production and decay cross sections of bound states are ordered not only by the coupling strengths, e.g. powers of the fine-structure constant  $\alpha$ , but also by the relative velocities of their constituents. This approach has been demonstrated to work for positronium in nonrelativistic QED [Cas86] and has been extended to nonrelativistic QCD (NRQCD) later [Bod95]. The description of NRQCD presented in this chapter follows [Krä01].

### Constructing NRQCD

The basic notion of NRQCD is that three distinct length scales—or equivalently, energy scales—are involved in the production and decays of charmonia:

1. The creation of  $c\bar{c}$  pairs occurs at a length scale comparable to the Compton wavelength of  $c$  quarks,  $r_1 \propto 1/m_c$ .
2. The size of the charmonium is related to the relative velocities  $v$  of the quarks by the uncertainty relation:  $r_2 \propto 1/(m_c v)$ .
3. The kinetic energy of the  $c\bar{c}$  pair defines the binding energy, hence  $r_3 \propto 1/(m_c v^2)$ .

Given that  $v \ll 1$ , the length scale of  $c\bar{c}$  production is well-separated from the other scales and from the hadronization scale  $\Lambda_{\text{QCD}}$ . For charmonium, in which  $v^2 \approx 0.25$ , this assumption is valid to a good approximation. Therefore, compared to the charmonium size, all propagators involved in the creation of  $c\bar{c}$  pairs are contracted to a point and can be treated in perturbative QCD.

For light quarks and gluons, the standard QCD Lagrangian is used, while the heavy quarks are represented by a Schrödinger-Pauli Lagrangian for the two-component heavy quark field  $\psi$  and the heavy antiquark field  $\chi$ :

$$\mathcal{L} = \psi^\dagger \left( iD_0 + \frac{\vec{D}^2}{2m_c} \right) \psi + \chi^\dagger \left( iD_0 - \frac{\vec{D}^2}{2m_c} \right) \chi + \mathcal{L}_{\text{light}} + \mathcal{L}_{\text{glue}} + \delta\mathcal{L}, \quad (3.10)$$

where the covariant derivative is  $D^\mu = \partial^\mu + igA^\mu$ , and  $A^\mu$  is an abbreviation for  $(\lambda^a/2)A_a^\mu$  with the Gell-Mann matrices  $\lambda^a$ , the gluon fields  $A_a^\mu$ , and the QCD coupling constant  $g$ . In the term  $\delta\mathcal{L}$ , all possible operators have to be included that obey the symmetries of QCD. The most important operators are the bilinear and the four-fermion operators. The relevant bilinear operators are

$$\begin{aligned} \delta\mathcal{L}_{\text{bilinear}} = & \frac{c_1}{8m_c^3} \psi^\dagger \vec{D}^4 \psi + \frac{c_2}{8m_c^2} \psi^\dagger (\vec{D} \cdot g\vec{E} - g\vec{E} \cdot \vec{D}) \psi \\ & + \frac{c_3}{8m_c^2} \psi^\dagger (i\vec{D} \times g\vec{E} - g\vec{E} \times i\vec{D}) \cdot \vec{\sigma} \psi + \frac{c_4}{2m_c} \psi^\dagger g\vec{B} \cdot \vec{\sigma} \psi + \text{c.c. terms}, \end{aligned} \quad (3.11)$$

where  $\vec{E}$  and  $\vec{B}$  are the chromoelectric and the chromomagnetic fields and  $\vec{\sigma}$  is the Pauli matrix. Heavy quarks are created and annihilated by local four-fermion operators:

$$\delta\mathcal{L}_{4\text{-fermion}} = \sum_i \frac{d_i}{m^2} (\psi^\dagger \kappa_i \chi) (\chi^\dagger \kappa'_i \psi), \quad (3.12)$$

where  $\kappa_i$  and  $\kappa'_i$  contain spin and color indices and polynomials in the spatial derivative  $\vec{D}$ . The dimensionless coefficients  $c_i$  in Eq. (3.11) and  $d_i$  in Eq. (3.12) are determined by matching NRQCD scattering amplitudes with amplitudes obtained in full QCD.

### NRQCD Factorization and Power Counting

In NRQCD, the inclusive cross section for producing a charmonium state  $H$  is given by

$$\sigma(H + X) = \sum_n \hat{\sigma}(c\bar{c}[n] + X) \langle \mathcal{O}^H[n] \rangle. \quad (3.13)$$

The sum over  $n$  includes both color and angular momentum quantum numbers, which do not have to be identical to the quantum numbers of  $H$ . Specifically, both color singlet and color-octet contributions are included. Eq. (3.13) is the central factorization formula of NRQCD. The process-dependent short-distance coefficients  $\hat{\sigma}(c\bar{c}[n] + X)$  describe the partonic hard process and are calculable in perturbative QCD. The long-distance matrix elements  $\langle \mathcal{O}^H[n] \rangle$  include the hadronization mechanism. The matrix elements are “universal”, i.e. independent of the specific process under study. The matrix elements are given by the vacuum expectation values of the four-fermion operators in Eq. (3.12):

$$\langle \mathcal{O}^H[n] \rangle = \sum_{X,\lambda} \langle 0 | \chi^\dagger \kappa_n \psi | H(\lambda) + X \rangle \langle H(\lambda) + X | \psi^\dagger \kappa'_n \chi | 0 \rangle, \quad (3.14)$$

where the sum is over all possible light hadrons in the final state  $X$  and the charmonium polarizations  $\lambda$ .

Eq. (3.13) represents an infinite series of non-perturbative matrix elements. However, NRQCD provides rules to sort the individual contributions by their relative importance, given by their dependence on the relative  $c\bar{c}$  velocity  $v$ . This method of “power-counting” assumes a hierarchical ordering of the relevant energy scales  $m_c v$ ,  $m_c v^2$ , and  $\Lambda_{\text{QCD}}$ . The power counting rules are derived from a Fock state decomposition of the charmonium state  $|H\rangle$ :

$$|H\rangle = \mathcal{O}(1) |c\bar{c}\rangle + \mathcal{O}(v) |c\bar{c}g\rangle + \dots, \quad (3.15)$$

in which the leading term  $|c\bar{c}\rangle$  describes a  $c\bar{c}$  pair in a color singlet state with the same quantum numbers as  $|H\rangle$ . The importance of sub-leading terms is then derived from “selection rules”, i.e. the probabilities to reach the dominant state by QCD interactions. See [Ben97, Krä01] and references therein for further details of this procedure.

### Comparison to Previous Models and Experimental Data

From the NRQCD point of view, the cross section predictions of the CSM fail to describe the data because important contributions to the cross section are missing. While the color-singlet contributions are properly taken into account, large color-octet contributions are neglected in the CSM.

The CEM shows some similarities with NRQCD: In CEM calculations, charmonium production via color-octet processes is allowed, hence the kinematic dependences of the cross section are similar to NRQCD. However, the power-counting rules are different: Since the spin and color quantum numbers of final states are randomized in the CEM, only the dimension of an operator is relevant in the power-counting.

The theoretical framework of NRQCD has become a standard tool for describing charmonium production in high-energy physics. The universal non-perturbative matrix elements have to be inferred from experimental data and allow stringent tests of

NRQCD. Some decay matrix elements have been determined in lattice QCD [Bod96]. The charmonium wave function needed for the color-singlet matrix elements can be determined from leptonic decays of charmonia or using potential models. All further matrix elements are extracted from experimental data, as shown e.g. in [Cho96a, Cho96b] for quarkonium production at the Tevatron and in [Ben96] for fixed-target quarkonium production.

Predictions of NRQCD, especially the universality of the non-perturbative matrix elements, have been compared with experimental data for several different production processes and kinematic regions. Results on  $J/\psi$  and  $\psi(2S)$  production at the Tevatron,  $J/\psi$  production in  $\gamma\gamma$  collisions at LEP (LEP: Large Electron Positron Collider) and in deep-inelastic scattering at HERA (HERA: Hadron-Elektron-Ringanlage) are in good agreement with NRQCD. However, results on  $J/\psi$  polarization at large transverse momenta and HERA photoproduction data are currently at variance with NRQCD predictions. Therefore more experimental input is desirable to perform decisive tests of NRQCD. Recent overviews of confronting NRQCD with experimental data can be found e.g. in [Krä01, Bod03].

Further developments in the field of NRQCD include the effective field theories of “potential NRQCD” (pNRQCD) and “velocity NRQCD” (vNRQCD). These models address deficiencies of NRQCD in power-counting and the regularization of divergences and will become relevant for heavy quarkonium production at future linear colliders [Hoa02].

### Fixed-Target $J/\psi$ Production in NRQCD

The description of  $J/\psi$  hadroproduction at fixed-target energies includes both the direct  $J/\psi$  production and the production via decays of  $\chi_c$  and  $\psi(2S)$  states:

$$\sigma_{J/\psi} = \sigma_{J/\psi, \text{direct}} + \mathcal{B}(\psi(2S) \rightarrow J/\psi X) \sigma_{\psi(2S)} + \sum_{J=0}^2 \mathcal{B}(\chi_{cJ} \rightarrow J/\psi X) \sigma_{\chi_{cJ}}. \quad (3.16)$$

With their large branching fractions of  $\mathcal{B}(\psi(2S) \rightarrow J/\psi \pi\pi) = 0.505 \pm 0.012$ ,  $\mathcal{B}(\chi_{c1} \rightarrow J/\psi \gamma) = 0.316 \pm 0.033$ , and  $\mathcal{B}(\chi_{c2} \rightarrow J/\psi \gamma) = 0.202 \pm 0.017$ , the corresponding decays contribute significantly to  $J/\psi$  production, whereas the influence of  $\chi_{c0}$  production with  $\mathcal{B}(\chi_{c0} \rightarrow J/\psi \gamma) = 0.0118 \pm 0.0014$  is negligible [Eid04]. HERA-B has measured that  $(32 \pm 6(\text{stat.}) \pm 4(\text{syst.}))\%$  of all  $J/\psi$  come from the radiative decay  $\chi_{cJ} \rightarrow J/\psi \gamma$  [Abt03b]. Approximately 10% of the  $J/\psi$  originate from decays  $\psi(2S) \rightarrow J/\psi X$ .

The leading contributions to fixed-target  $J/\psi$  production are summarized in Table 3.1. Both color-singlet and color-octet processes are included. For  $J/\psi$  and  $\psi(2S)$ , the color-octet processes are one order less in  $\alpha_S$  but suppressed by  $v^4$  relative to the color-singlet processes. In  $\chi_c$  production, both mechanism enter at the same order in  $\alpha_S$  and  $v$ .

A graphical representation of a color-octet process contributing to direct  $J/\psi$  production is shown in Fig. 3.3: A  $c\bar{c}$  pair in a color-octet state is formed by gluon-gluon fusion. It evolves to a pre-resonance  $c\bar{c}$  state which neutralizes color by radiating (or absorbing) a soft gluon. This gluon is collinear to the  $c\bar{c}$  pair, i.e. the gluon emission (absorption) leaves the momentum of the  $c\bar{c}$  pair practically unchanged. Finally, the  $J/\psi$  resonance is formed.

**Table 3.1:** Lowest order processes contributing to  $J/\psi$  production at fixed-target energies. Both direct and indirect production channels are included. For every process, the relevant matrix elements and the order of the cross section in  $\alpha_S$  and  $v$  are given [Ben96]. Note that in  $\chi_c$  production, color-singlet and color-octet contributions enter at the same order in  $\alpha_S$  and  $v$ .

Production Channel	Matrix Elements	Order
$gg \rightarrow J/\psi, \psi(2S)$	$\langle \mathcal{O}^\psi[1, {}^3S_1] \rangle$	$\alpha_S^3 v^3$
$gg \rightarrow J/\psi, \psi(2S)$	$\langle \mathcal{O}^\psi[8, {}^1S_0] \rangle, \langle \mathcal{O}^\psi[8, {}^3P_{0,2}] \rangle$	$\alpha_S^2 v^7$
$q\bar{q} \rightarrow J/\psi, \psi(2S)$	$\langle \mathcal{O}^\psi[8, {}^3S_1] \rangle$	$\alpha_S^2 v^7$
$gg \rightarrow \chi_{c0,2}$	$\langle \mathcal{O}^{\chi_{c0,2}}[1, {}^3P_{0,2}] \rangle$	$\alpha_S^2 v^5$
$q\bar{q} \rightarrow \chi_{c0,2}$	$\langle \mathcal{O}^{\chi_{c0,2}}[8, {}^3S_1] \rangle$	$\alpha_S^2 v^5$
$gg, gq, g\bar{q} \rightarrow \chi_{c1}$	$\langle \mathcal{O}^{\chi_{c1}}[1, {}^3P_1] \rangle$	$\alpha_S^3 v^5$
$q\bar{q} \rightarrow \chi_{c1}$	$\langle \mathcal{O}^{\chi_{c1}}[8, {}^3S_1] \rangle$	$\alpha_S^2 v^5$

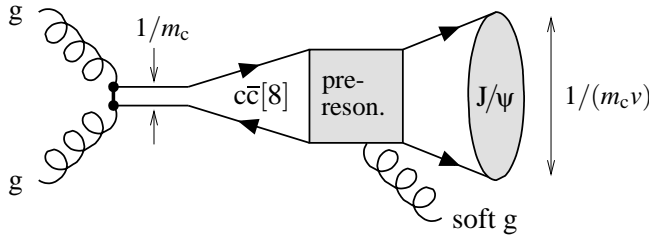


**Figure 3.3:** Sketch of a color-octet contribution to  $J/\psi$  production. A color-octet  $c\bar{c}$  pair is created by gluon-gluon fusion and evolves to a pre-resonance state. A soft gluon is radiated, and the final color-singlet  $J/\psi$  resonance is formed. The typical sizes of the color-octet state and the final  $J/\psi$  are indicated by arrows.

The number of independent matrix elements can be reduced by spin symmetry. The following relations are valid up to corrections of  $\mathcal{O}(v^2)$  [Ben96]:

$$\langle \mathcal{O}^{\chi_{cJ}}[1, {}^3P_J] \rangle = (2J+1) \langle \mathcal{O}^{\chi_{c0}}[1, {}^3P_0] \rangle, \quad (3.17)$$

$$\langle \mathcal{O}^{\chi_{cJ}}[8, {}^3S_1] \rangle = (2J+1) \langle \mathcal{O}^{\chi_{c0}}[1, {}^3S_1] \rangle, \quad (3.18)$$

$$\langle \mathcal{O}^\psi[8, {}^3P_J] \rangle = (2J+1) \langle \mathcal{O}^\psi[8, {}^3P_0] \rangle, \quad (3.19)$$

where  $\psi$  stands for  $J/\psi$  or  $\psi(2S)$ . In addition, only the combination

$$\Delta^\psi[8] = \langle \mathcal{O}^\psi[8, {}^1S_0] \rangle + \frac{7}{m_c^2} \langle \mathcal{O}^\psi[8, {}^3P_0] \rangle \quad (3.20)$$

enters the  $J/\psi$  and  $\psi(2S)$  production cross sections at lowest order in  $\alpha_S$ . Hence for the  $\chi_c$  states, two free parameters remain,  $\langle \mathcal{O}^{\chi_{c0}}[1, {}^3S_1] \rangle$  and  $\langle \mathcal{O}^{\chi_{c0}}[1, {}^3P_0] \rangle$ . For the  $J/\psi$  and the  $\psi(2S)$ , the parameters  $\langle \mathcal{O}^\psi[1, {}^1S_1] \rangle$ ,  $\langle \mathcal{O}^\psi[8, {}^3S_1] \rangle$ , and  $\Delta^\psi[8]$  have to be extracted from experimental data. The color-singlet matrix elements are related to the charmonium wave function, as shown in Eq. (3.6) for the CSM:

$$\langle \mathcal{O}^H[1, {}^3S_1] \rangle = \frac{9}{2\pi} |R(0)|^2, \quad \langle \mathcal{O}^H[1, {}^3P_0] \rangle = \frac{9}{2\pi} \left| \frac{dR(0)}{dr} \right|^2. \quad (3.21)$$



**Table 3.2:** NRQCD matrix elements for fixed-target  $J/\psi$  production [Ben96].  $\langle \mathcal{O}^H[1,^3S_1] \rangle$  and  $\langle \mathcal{O}^H[1,^3P_0] \rangle$  are computed from the wave functions in the Buchmüller-Tye potential [Buc81].  $\langle \mathcal{O}^H[8,^3S_1] \rangle$  are taken from fits to Tevatron data, and  $\Delta^\psi[8]$  are fitted to fixed-target data.  $\Delta_{\text{NLO}}^\psi[8]$  is taken from an evaluation of fixed-target data at next-to-leading order [Mal99].

Matrix Element	$J/\psi$ [GeV <sup>3</sup> ]	$\psi(2S)$ [GeV <sup>3</sup> ]	$\chi_c$ [GeV <sup>3</sup> ]
$\langle \mathcal{O}^H[1,^3S_1] \rangle$	1.16	0.76	–
$\langle \mathcal{O}^H[8,^3S_1] \rangle$	$6.6 \times 10^{-3}$	$4.6 \times 10^{-3}$	$3.2 \times 10^{-3}$
$\langle \mathcal{O}^H[1,^3P_0] \rangle / m_c^2$	–	–	$4.4 \times 10^{-2}$
$\Delta^\psi[8]$	$3.0 \times 10^{-2}$	$5.2 \times 10^{-3}$	–
$\Delta_{\text{NLO}}^\psi[8]$	$1.8 \times 10^{-2}$	$2.6 \times 10^{-3}$	–

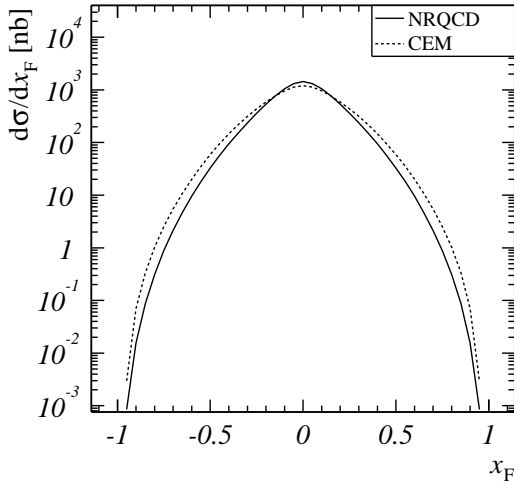


**Figure 3.4:**  $x_F$  distribution of  $J/\psi$  production in NRQCD (solid line) and in the CEM (dashed line) [Vog04]. The CEM prediction is calculated at leading order, using the MRST LO parton distribution functions [Mar98a, Mar98b], and scaled to the proper next-to-leading order value.

All further matrix elements are obtained from fits to fixed-target and collider data [Ben96]. An evaluation of the matrix element  $\Delta^\psi[8]$  beyond leading order can be found in [Mal99]. Numerical values of the relevant NRQCD matrix elements for  $J/\psi$  production in HERA-B are summarized in Table 3.2. The differential cross sections for  $J/\psi$  production in HERA-B, as predicted in the CEM and in NRQCD, are depicted in Fig. 3.4.

### 3.3 The Glauber Model

The charmonium production models introduced in this chapter describe charmonium production by scattering processes among hadrons or between hadrons and photons. However, in most fixed-target experiments either the target or both target and beam consist of atomic nuclei. In addition, heavy ion beams are collided at the Relativistic Heavy-Ion Collider (RHIC) and the future Large Hadron Collider (LHC). Therefore, charmonium production is probed in hadron-nucleus or nucleus-nucleus collisions, and additional effects due to interactions inside nuclei become relevant. The standard framework to evaluate nuclear effects is the Glauber model. Some elementary applications of this model in proton-nucleus collisions are discussed in this section.

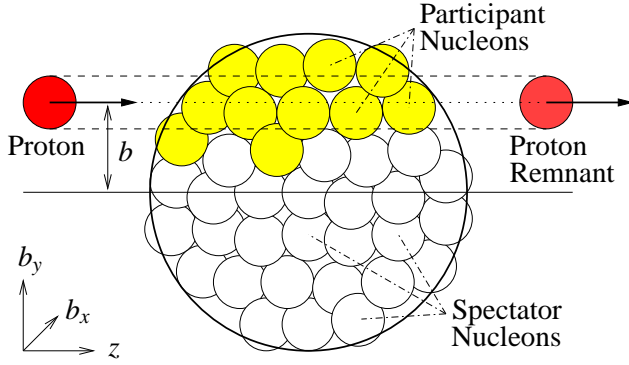


**Figure 3.5:** Schematic illustration of a proton-nucleus collision in the Glauber model. A proton crosses the nucleus at an impact parameter  $b$  and interacts with individual nucleons along the trajectory (after [Bru02b]).

### 3.3.1 Basic Assumptions

In the Glauber model, proton-nucleus collisions are viewed as an incoherent sum of binary proton-nucleon collisions. Coherent effects like baryon excitations are neglected. The original derivation by Glauber [Gla59, Gla70b] is based on a semi-classical approximation to quantum mechanical scattering theory. The derivation presented here is based on a combinatorial approach, as also used in [Sha01]: A proton propagating in  $z$ -direction crosses a nucleus at an impact parameter  $b = |\vec{b}|$  as indicated in Fig. 3.5. Along the trajectory, proton-nucleus interactions may occur, which are assumed to be mutually independent.

### 3.3.2 Parametrizations of Nuclear Densities

The distribution of nucleons inside the nucleus is described by a nuclear density function  $\rho(b, z)$ . For nuclei with an atomic mass numbers of  $A \leq 16$ , a harmonic oscillator model is employed for calculations, resulting in an approximately Gaussian shape of the nuclear density [Pi92]:

$$\rho(r) = \left(1 + \frac{A-4}{6} \frac{r^2}{d^2}\right) \exp\left[-\frac{r^2}{d^2}\right], \quad (3.22)$$

where  $r = \sqrt{b^2 + z^2}$  is the radial distance from the center of the nucleus and

$$d^2 = \left(\frac{5}{2} - \frac{4}{A}\right) (\langle R_{\text{ch}}^2(A) \rangle - \langle R_{\text{ch}}^2(p) \rangle) \quad (3.23)$$

with the mean squared charge radii of the nucleus and of the proton,  $\langle R_{\text{ch}}^2(A) \rangle$  and  $\langle R_{\text{ch}}^2(p) \rangle$ . For all heavier nuclei, the Woods-Saxon distribution [Woo54] is utilized:

$$\rho(r) = \frac{\rho_0}{1 + \exp[(r-R)/a]}, \quad (3.24)$$

where  $R$  is the nuclear radius and  $a$  is the surface thickness of the nucleus. Experimental determinations of the parameters of both models are listed e.g. in [Bar77, DJ87].

The amount of nuclear matter to be crossed by a proton colliding with a nucleus at an impact parameter  $b$  is expressed by the nuclear thickness function

$$T(b) = \int_{-\infty}^{\infty} \rho(b, z) dz, \quad (3.25)$$

which is normalized by the requirement

$$\int \int_{-\infty}^{\infty} \rho(b, z) dz d^2b = \int T(b) d^2b = 1. \quad (3.26)$$

In a cylindrical coordinate system, the two-dimensional integral over the impact parameter,  $\int d^2b$ , is given by  $2\pi \int_0^\infty b db$ . Up to the normalization,  $T(b)$  is equivalent to the effective path length  $L$  of the proton inside the nucleus.

### 3.3.3 Inelastic Cross Section in the Glauber Model

The probability  $P_0$  for a proton to scatter off a single nucleon inside the nucleus is given by the product of the proton-nucleon cross section and the nuclear thickness:  $P_0(b) = \sigma_{pN}T(b)$ . Assuming independent collisions between the proton and the individual nucleons, the probability for  $n$  collisions along a trajectory with an impact parameter  $b$  in a nucleus consisting of  $A$  nucleons is described by a binomial distribution:

$$P(n, A; b) = \binom{A}{n} [\sigma_{pN}T(b)]^n [1 - \sigma_{pN}T(b)]^{A-n}. \quad (3.27)$$

The cross section is obtained as the sum over all probabilities, integrated over all impact parameters:

$$\sigma_{pA}^{\text{inel}} = \int \left( \sum_{n=1}^A P(n, A; b) \right) d^2b = \int (1 - P(0, A; b)) d^2b = \int \left( 1 - [1 - \sigma_{pN}T(b)]^A \right) d^2b. \quad (3.28)$$

Note that for small proton-nucleon cross sections  $\sigma_{pN}$ , this result is equivalent to the original results by Glauber [Gla59],

$$\sigma_{pA}^{\text{inel}} = \int (1 - \exp[-\sigma_{pN}T(b)A]) d^2b \approx \int \left( 1 - [1 - \sigma_{pN}T(b)]^A \right) d^2b. \quad (3.29)$$

Eq. (3.28) is valid for any kind of inelastic scattering. From the extreme cases of very large and very small cross sections, lower and upper bounds on the nuclear dependence of  $\sigma_{pA}^{\text{inel}}$  are obtained as follows:

#### Case 1: Large Absorption Cross Section

If the cross section is so large that the probability for at least one interaction within the radius  $R$  of the nucleus is unity, i.e.  $\sigma_{pN}T(b) = 1$  for  $b < R$ , the inelastic cross section is given by

$$\sigma_{pA}^{\text{inel}} = 2\pi \int_0^R b db = \pi R^2. \quad (3.30)$$

This approximation is sometimes referred to as the ‘‘black disk’’ approximation, since the cross section depends only on the area of the two-dimensional projection of the nuclear surface. Assuming that  $R$  scales with the number of nucleons according to

$R = R_0 A^{1/3}$  and noting that the normalization condition of  $T(b)$ , Eq. (3.26), yields  $\sigma_{pN} = \pi R_0^2$ , the resulting  $A$ -dependence of the inelastic cross section reads

$$\sigma_{pA}^{\text{inel}} = \pi R^2 = \pi R_0^2 \cdot A^{2/3} = \sigma_{pN} \cdot A^{2/3}. \quad (3.31)$$

A recent compilation of inelastic proton-nucleus interactions for HERA-B energies results in a value of

$$\sigma_{pA}^{\text{inel}} = \sigma_{pN} \cdot A^{0.7111 \pm 0.0011}, \quad (3.32)$$

rather close to the black disk approximation [Car03].

### Case 2: Small Absorption Cross Section

In the case of hard scattering processes, the cross section  $\sigma_{pN}$  is small, and the inelastic cross section  $\sigma_{pA}^{\text{inel}}$  in Eq. (3.28) can be expanded in a Taylor series, keeping terms up to  $\mathcal{O}(\sigma_{pN})$ :

$$\sigma_{pA}^{\text{hard}} = \int \left( 1 - [1 - \sigma_{pN} T(b)]^A \right) d^2b \approx \sigma_{pN} A \int T(b) d^2b. \quad (3.33)$$

Using the normalization condition (3.26), a linear scaling behavior of the proton-nucleus cross section with the number of nucleons is obtained:

$$\sigma_{pA}^{\text{hard}} = \sigma_{pN} \cdot A. \quad (3.34)$$

Several different ways to parametrize deviations from this linear scaling of the cross section with  $A$  can be found in the literature. The suppression factor  $S$  is defined as

$$S \equiv \frac{\sigma_{pA}^{\text{hard}}}{\sigma_{pN} \cdot A}. \quad (3.35)$$

Experimental data on nuclear suppression are often parametrized using the power law

$$\sigma_{pA}^{\text{hard}} = \sigma_{pN} \cdot A^\alpha, \quad (3.36)$$

where values of  $\alpha < 1$  indicate suppression of the hard scattering cross section in pA-collisions. The parameters  $S$  and  $\alpha$  are connected by the relation

$$S = A^{\alpha-1}. \quad (3.37)$$

### 3.3.4 Nuclear Absorption in the Glauber Model

The framework of the Glauber model allows to incorporate nuclear suppression of particles produced in hard scattering processes. Keeping the physics picture of proton-nucleus interactions as incoherent sums of binary collisions, a generic absorption cross section  $\sigma^{\text{abs}}$  is defined. The probability  $P_{>}(b, z)$  for a proton at a point  $(b, z)$  to survive the proton-nucleus collision without being absorbed is then given by

$$P_{>}(b, z) = \left[ 1 - \sigma^{\text{abs}} \cdot \int_z^\infty \rho(b, z') dz' \right]^{A-1} \equiv \left[ 1 - \sigma^{\text{abs}} T_{>}(b, z) \right]^{A-1}, \quad (3.38)$$

where the exponent results from the fact that after the collision with one nucleon, only the remaining  $A - 1$  nucleons can still absorb the proton. In the cross section formula (3.33), the nuclear thickness function is replaced by an effective thickness function  $T^{\text{abs}}(b)$ , which takes into account the survival probability  $P_{>}(b, z)$ :

$$T^{\text{abs}}(b) = \int_{-\infty}^{\infty} \rho(b, z) \left[ 1 - \sigma^{\text{abs}} T_{>}(b, z) \right]^{A-1} dz = \frac{1}{\sigma^{\text{abs}} A} \left[ 1 - \left( 1 - \sigma^{\text{abs}} T(b) \right)^A \right], \quad (3.39)$$

where in the last step, the identity

$$\frac{d}{dz} \left[ 1 - \sigma^{\text{abs}} \cdot \int_z^{\infty} \rho(b, z') dz' \right]^A = \sigma^{\text{abs}} A \rho(b, z) \left[ 1 - \sigma^{\text{abs}} \cdot \int_z^{\infty} \rho(b, z') dz' \right]^{A-1} \quad (3.40)$$

has been used. For small absorption cross sections  $\sigma^{\text{abs}}$ , Eq. (3.39) can be expanded in a Taylor series. Keeping terms up to  $\mathcal{O}((\sigma^{\text{abs}})^2)$ , the effective thickness function reads

$$T^{\text{abs}}(b) = \frac{1}{\sigma^{\text{abs}} A} \left[ A \sigma^{\text{abs}} T(b) - (\sigma^{\text{abs}})^2 \frac{A(A-1)}{2} T(b)^2 \right]. \quad (3.41)$$

Inserting this result into Eq. (3.33), and using the normalization of  $T^{\text{abs}}(b)$ , the hard cross section is given by

$$\sigma_{\text{pA}}^{\text{hard}} = \sigma_{\text{pN}} A \left( 1 - \sigma^{\text{abs}} \frac{A-1}{2} \int T(b)^2 d^2b \right) \equiv \sigma_{\text{pN}} A \left( 1 - \sigma^{\text{abs}} \langle \rho L \rangle \right). \quad (3.42)$$

The result of Eq. (3.42) can be interpreted as an approximation to the usual exponential form of an absorption cross section,

$$\sigma_{\text{pA}}^{\text{hard}} = \sigma_{\text{pN}} A \exp \left[ -\sigma^{\text{abs}} \langle \rho L \rangle \right]. \quad (3.43)$$

The suppression factor for hard scattering processes is hence given by

$$S = \begin{cases} 1 - \sigma^{\text{abs}} \langle \rho L \rangle & \text{for } \sigma_{\text{pA}}^{\text{hard}} \text{ as in Eq. (3.42),} \\ \exp \left[ -\sigma^{\text{abs}} \langle \rho L \rangle \right] & \text{for } \sigma_{\text{pA}}^{\text{hard}} \text{ as in Eq. (3.43).} \end{cases} \quad (3.44)$$

In Eq. (3.42), the quantity  $\langle \rho L \rangle$  is defined, i.e. the average product of the nuclear density  $\rho$  and the nuclear path length  $L$ .  $\langle \rho L \rangle$  is a measure of the average amount of matter seen by the proton before leaving the nucleus. The actual nuclear path length is obtained from  $\langle \rho L \rangle$  by:

$$L = \frac{\langle \rho L \rangle}{\rho_0 A}. \quad (3.45)$$

In case of a uniform density,

$$\rho(r) = \rho_0 = \begin{cases} \left( \frac{4\pi}{3} R^3 \right)^{-1} & \text{for } r \leq R, \\ 0 & \text{for } r > R, \end{cases} \quad (3.46)$$

the quantity  $\langle \rho L \rangle$  is given by

$$\langle \rho L \rangle = \frac{A-1}{2} \int T(b)^2 d^2b = \frac{A-1}{2} 2\pi \rho_0^2 R^4 = \frac{9}{16\pi} (A-1) \frac{1}{R^2} \quad (3.47)$$

While a uniform nuclear density is a good approximation for heavy nuclei, a Gaussian shape as in the harmonic oscillator model is more appropriate for light nuclei. An expression for  $\langle \rho L \rangle$  in this case can be found in [Ger92]

$$\langle \rho L \rangle = \frac{3}{8\pi} (A-1) \frac{1}{\langle R_{\text{ch}}^2(A) \rangle}, \quad (3.48)$$

where  $\langle R_{\text{ch}}^2(A) \rangle$  is the mean squared charge radius of the nucleus, as already used in Eq. (3.23).

### 3.3.5 Measuring Nuclear Suppression in HERA-B

In HERA-B, nuclear effects are extracted from data sets for which a tungsten and a carbon wire have been used simultaneously. Therefore, nuclear effects are extracted from ratios of cross sections. Using the power-law parametrization of Eq. (3.36) for two target materials with atomic mass numbers  $A_1$  and  $A_2$ , the parameter  $\alpha$  is determined from

$$\alpha = \frac{\log(\sigma_2/\sigma_1)}{\log(A_2/A_1)}. \quad (3.49)$$

If the  $A$ -dependence of charmonium production is measured using this expression, the functional form of the suppression as a function of  $A$  is fixed by the parametrization. Since the suppression parameter is only extracted from the cross section measured with two materials, the measurement cannot be over-constrained by a fit.

To extract the absorption cross section  $\sigma^{\text{abs}}$ , the ratio of suppression factors for the two materials,  $R = S_2/S_1$ , is utilized:

$$R^S = \frac{S_2}{S_1} = \frac{\sigma_2/\sigma_1}{A_2/A_1}. \quad (3.50)$$

Using Eq. (3.44), this relation is solved for the absorption cross section:

$$\sigma^{\text{abs}} = \begin{cases} \frac{1-R^S}{\langle \rho L \rangle_2 - \langle \rho L \rangle_1 R^S} & \text{for } \sigma_{\text{pA}}^{\text{hard}} \text{ as in Eq. (3.42),} \\ \frac{\log(R^S)}{\langle \rho L \rangle_1 - \langle \rho L \rangle_2} & \text{for } \sigma_{\text{pA}}^{\text{hard}} \text{ as in Eq. (3.43),} \end{cases} \quad (3.51)$$

with the appropriate choices of  $\langle \rho L \rangle_{1,2}$  for the target materials under study, as summarized in Table 3.3. This method is independent of the functional form of the suppression. However, since the nuclear path length  $L$  cannot be measured in HERA-B, model-dependent assumptions on this quantity enter the result.

**Table 3.3:** Summary of nuclear parameters for carbon and tungsten. For the calculations of the path length parameters, a uniform nuclear density is used for tungsten (heavy nucleus), while for carbon (light nucleus), a Gaussian density is employed.

Parameter	Reference	Carbon	Tungsten
Atomic Mass $A$ [u]		12.011	183.840
$R = 1.118A^{1/3}$ [fm]		2.560	6.357
$R = 1.16A^{1/3} - 1.35A^{-1/3}$ [fm]	[Bar77]		6.358
$R = 1.19A^{1/3} - 1.61A^{-1/3}$ [fm]	[DJ87]		6.483
$\langle R_{\text{ch}}^2(A) \rangle$ [fm <sup>2</sup> ]	[Pi92]	5.983	
$\langle \rho L \rangle$ [fm <sup>-2</sup> ]		0.220	0.810
$L$ [fm]		1.286	4.742

### 3.4 Nuclear Effects in Charmonium Production

The suppression of charmonium production in nuclear media could be caused by a large number of different nuclear effects. A priori, it is not obvious if single effects dominate the suppression or which combination of effects accounts for the suppression pattern observed in experimental data. Therefore, nuclear effects are separated into classes which can be distinguished by studying different physics processes and different regimes of the kinematic variables. In the literature, nuclear effects are separated into “initial state effects” related to the partons which participate in the interaction in which the charmonium is produced and “final state effects” due to interactions of the  $c\bar{c}$  pair or the fully formed charmonium state with the nuclear environment. Comprehensive overviews of the most important nuclear effects, with different emphases on the individual effects, can be found in [Ger99] and [Vog99, Vog00]. The following criteria help in disentangling different nuclear effects.

- Initial state effects can be separated from final state effects, because the former influence all charmonia in the same way, while the latter are specific for the produced charmonium state. For other processes with similar partons in the initial state, e.g. dilepton production via the Drell-Yan process, similar initial state effects are expected.
- Effects that depend on the details of the transition from the initial to the final state can be distinguished by their dependence on the kinematics of the production process. For these effects, different results are expected from experiments covering different kinematic regions, and large coverage of phase space is needed to study the time evolution from the  $c\bar{c}$  state to the final charmonium.
- If the final state particles lose energy by interactions with the nuclear medium, their momentum spectra may be partly shifted out of the acceptance of an experiment. Hence, an apparent suppression effect may be due to a rearranged  $x_F$  spectrum.

The discussion of nuclear effects in this chapter is restricted to effects which are potentially interesting for the kinematic range covered by HERA-B, i.e. 920 GeV beam energy and a range in Feynman- $x$  of  $-0.3 \lesssim x_F \lesssim 0.15$ . The main observables described in the literature and accessible to HERA-B are the exponent  $\alpha$  of the power-law parametrization (3.36), measured as a function of  $x_F$  and  $p_T$ , and the absorption cross section  $\sigma^{\text{abs}}$ .

### 3.4.1 Initial State Effects

#### Nuclear Parton Distribution Function

In the quark-parton model, cross sections for high-energy hadronic collisions can be factorized into a cross section for the partonic sub-process and parton distribution functions (PDF). The partonic cross section is calculable in perturbative QCD, and the PDFs are universal functions that describe the parton content of hadrons as a function of the momentum fraction  $x$  carried by the proton and the four-momentum transfer  $Q^2$  in the collision. The PDFs are non-perturbative objects, and only their evolution with  $x$  and  $Q^2$  can be calculated in perturbative QCD.

PDFs of nucleons bound in an atomic nucleus are different from those in isolated protons or neutrons. This effect has been shown in deep-inelastic scattering experiments utilizing nuclear targets. Many models have been developed to explain this deviation. See e.g. [Arn94] for an overview. The modifications of nuclear PDFs are sometimes referred to as “shadowing” effects. Historically, this name arises from an analogy of nuclear shadowing of the hadronic cross section in photon-nucleus collisions: Since photons and vector mesons bear the same quantum numbers, photons can fluctuate into vector mesons and interact strongly with nucleons on the nuclear surface. Hence a shadow is cast on the inner nucleons.

The influence of nuclear effects on PDFs can be illustrated by comparing the ratio of the structure functions  $F_2(x, Q^2)$  for different nuclei. In lowest order of the quark-parton model,  $F_2$  describes the number of partons with momentum fractions  $x$  inside a nucleon, weighted with the parton charge. A sketch of the observed ratio  $F_2^{\text{D}}$  for deuterium and  $F_2^{\text{A}}$  for a nucleus with an atomic mass number  $A$  is shown in Fig. 3.6.  $F_2^{\text{A}}$  is suppressed in the “shadowing” region  $x < 0.1$ . An enhancement (“anti-shadowing”) of  $F_2^{\text{A}}$  is observed for  $0.1 < x < 0.3$ , while for  $0.3 < x < 0.8$  the ratio decreases again, as observed first by the European Muon Collaboration (EMC) [Aub83]. For  $x \rightarrow 1$  the ratio increases again, due to the Fermi motion of the nucleons inside the nucleus. Currently, two sets of nuclear PDFs are available, EKS98 [Esk99] and HKM [Hir01]. These sets parametrize the nuclear effects based on different combinations of experimental data to determine the free parameters, as discussed e.g. in [Acc03].

The kinematic range covered by the HERA-B experiment of  $-0.3 \lesssim x_F \lesssim 0.15$  corresponds to  $0.06 \lesssim x_2 \lesssim 0.6$  for the nuclear PDFs. Here  $x_2$  denotes the momentum fraction carried by the parton inside the target nucleon, see Appendix B for a discussion of the kinematic formulae. This range covers mainly the anti-shadowing regime, such that nuclear PDFs alone would cause an enhancement of charmonium production within the HERA-B acceptance. Suppression due to nuclear PDFs of the target is expected to scale with  $x_2$  when studied at different beam energies.



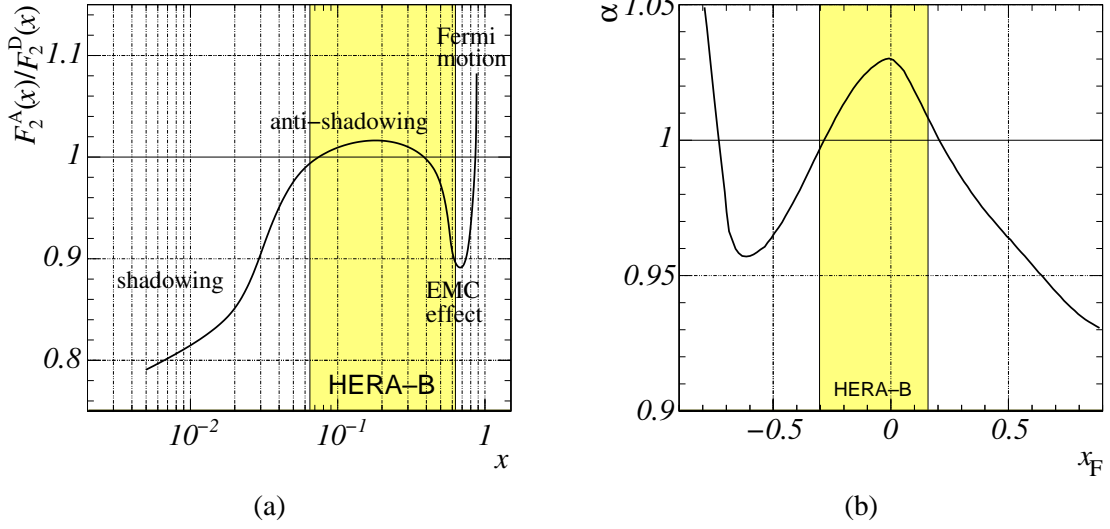


**Figure 3.6:** Illustrations of charmonium suppression by nuclear structure functions: (a) Schematic drawing of the structure function ratio  $F_2^A(x)/F_2^D(x)$  (after [Arn94]). The features of the ratio are explained in the text. (b) Charmonium suppression parameter  $\alpha(x_F)$  due to nuclear PDFs. The calculation is performed for 800 GeV beam energy using the EKS98 set of nuclear PDFs (after [Vog00]). The  $x$ - and  $x_F$ -ranges covered by HERA-B are indicated by the shaded areas.

### Initial State Energy Loss

Before the hard interaction, the partons inside the beam proton can lose energy by multiple scattering with the target nucleons. The net result is a shift  $\Delta x_1$  in the momentum fraction carried by the interacting parton inside the beam proton. In a model formulated in [Gav92], the dependence of the shift on  $x_1$  and  $A$  are given by

$$\Delta x_1 \propto x_1 A^{1/3}. \quad (3.52)$$

The shift  $\Delta x_1$  is proportional to the radius of the nucleus, as expected for multiple scattering with the nucleons. The linear dependence on  $x_1$  is chosen in analogy to the  $x_1$  dependence of the Bethe-Heitler process [Bet34] in QED. Energy loss effects become large for large  $x_F$ , i.e. for large  $x_1$ . The probability of finding e.g. a quark in the proton in the limit of  $x_1 \rightarrow 1$  behaves like  $(1 - x_1)^3$ , therefore small shifts in  $x_1$  are amplified for large  $x_F$ .

An alternative model has been proposed in [Bro93] and further refined in [Bai97]. In this model,  $\Delta x_1$  is proportional to the nuclear path length and to the average transverse momentum of the partons, both proportional to  $A^{1/3}$ . The  $x_1$  dependence is derived from the uncertainty principle [Bro93]:

$$\Delta x_1 \propto \frac{1}{x_1} A^{2/3}. \quad (3.53)$$

This model predicts very large suppression effects for small and negative  $x_F$  [Vog00].

A comparison of the predictions of the two models for 800 GeV beam energy in the framework of NRQCD is presented in Fig. 3.7.

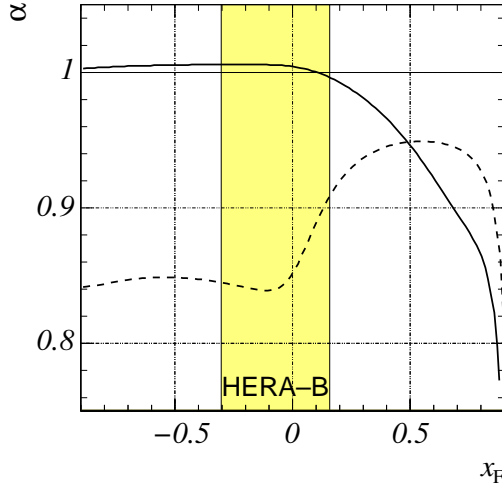


**Figure 3.7:** Charmonium energy loss at 800 GeV in NRQCD (after [Vog00]). In the model of [Gav92] (solid line), mainly large positive  $x_F$  are affected, while in [Bai97] (dashed line), a large effect is observed for small and negative  $x_F$ .

### Transverse Momentum Broadening

Multiple scattering of the partons prior to the hard interaction influences not only the longitudinal momenta of the partons. The transverse momentum spectrum of the initial state partons is also modified [Gav88, Hüf88]. The average transverse momentum  $k_T$  of the partons relative to the proton (“intrinsic  $k_T$ ”) is increased due to multiple elastic interactions. This increase translates into a broadening of the  $p_T$  spectrum of the final charmonium states.

The sequence of elastic rescattering is treated as a random walk. Hence the average transverse momentum of  $J/\psi$  in pA collisions is given by [Ger99]:

$$\langle p_T^2 \rangle_{J/\psi}^{pA} = \langle p_T^2 \rangle_{J/\psi}^{pN} + \sigma_{gN}^{\text{el}} \langle p_T^2 \rangle_{gN} \langle \rho L \rangle. \quad (3.54)$$

Here  $\langle p_T^2 \rangle_{J/\psi}^{pN}$  is the average  $p_T$  in pN collisions. The second term is proportional to the elastic cross section for gluon-nucleon scattering,  $\sigma_{gN}^{\text{el}}$ , and the average transverse momentum for this process,  $\langle p_T^2 \rangle_{gN}$ . The number of scattering processes before the hard interactions is approximated by  $\langle \rho L \rangle$  for small absorption cross sections. The parameter  $\sigma_{gN}^{\text{el}} \langle p_T^2 \rangle_{gN} = 4.5 \pm 0.4 \text{ mb} (\text{GeV}/c)^2$  is extracted from a fit to data from the NA3 and NA38 experiments [Ger99].

The influence of transverse momentum broadening on the nuclear suppression parameter  $\alpha(p_T)$  is explained by the shift of the  $p_T$  spectra towards larger values for heavier materials. Given the approximate shape of the spectra, often parametrized by

$$\frac{dN}{dp_T} \propto p_T \left( 1 + \left( \frac{35\pi}{256} \frac{p_T}{\langle p_T \rangle} \right)^2 \right)^{-6},$$

the parameter  $\alpha$ , i.e. the logarithm of the ratio of these spectra, is smaller than unity for small values of  $p_T$ , while a value of  $\alpha > 1$  is expected for large  $p_T$ .

### Intrinsic Charm

Intrinsic charm models are based on a decomposition of the proton wave function into Fock states. In addition to the state which includes the three valence quarks,  $p = |uud\rangle$ , fluctuations containing additional gluons or quark pairs are produced for short time intervals. A fluctuation containing at least one  $c\bar{c}$  pair,  $|uudc\bar{c}\dots\rangle$ , is called intrinsic charm of the proton.

If intrinsic charm is included in the production mechanism, the fraction of  $c\bar{c}$  pairs which form charmonium states is reduced with respect to  $c\bar{c}$  pairs in which single  $c$  or  $\bar{c}$  quarks bound to open charm mesons. In addition, the intrinsic charm cross section depends on the atomic mass number  $A$  such that intrinsic charm also contributes to the nuclear suppression of charmonium production.

The probability to find intrinsic charm in proton-nucleus collisions is estimated in [Vog00]. The effect on the  $A$ -dependence of charmonium production is symmetric in  $x_F$  since the  $c\bar{c}$  fluctuation can occur both in the target and in the beam nucleons. At an intrinsic charm probability of 0.3%, consistent with available data, and large beam energies, the influence on  $\alpha(x_F)$  is only significant for very large  $|x_F|$ . The central  $x_F$  region covered by HERA-B is only affected in case of an intrinsic charm probability of 1% or larger.

#### 3.4.2 Final State Effects

Final state effects are mechanisms that influence the  $c\bar{c}$  pair after the production process. If  $J/\psi$  suppression due to final state effects is studied, both direct  $J/\psi$  production and production via feed-down from other charmonium states has to be considered. Therefore, the suppression factor calculated for  $J/\psi$  is taken as the sum of suppression factors for all these processes, weighted with the fractions  $f_{\psi_i}$  of  $J/\psi$  produced by decays of the charmonium states  $\psi_i$ :

$$S^{J/\psi} = f_{J/\psi} S^{J/\psi, \text{direct}} + f_{\psi(2S)} S^{\psi(2S)} + f_{\chi_{cJ}} S^{\chi_{cJ}}. \quad (3.55)$$

As an example, in [Vog00], values of  $f_{J/\psi} = 0.58$ ,  $f_{\psi(2S)} = 0.12$ , and  $f_{\chi_{cJ}} = 0.3$  are utilized.

### Nuclear Absorption

Nuclear absorption effects depend on the details of the time evolution of charmonium formation after the production of a  $c\bar{c}$  pair, as sketched in Fig. 3.3. The time scales involved in the process are the time needed to form a color-octet  $c\bar{c}$  pair, the time to produce a color-neutral pre-resonance state and the time to fully form the resonance, schematically written for color-octet gluon-gluon fusion as:

$$gg \xrightarrow{\tau_8} |c\bar{c}\rangle_8 \xrightarrow{\tau_{8 \rightarrow 1}} |(c\bar{c})_8 g_8\rangle_1 \xrightarrow{\tau_\psi} |c\bar{c}\rangle_1, \quad (3.56)$$

where the subscripts indicate color-singlet or color-octet states. The formation time of the color octet,  $\tau_8 = 1/(2m_c) \approx 0.07 \text{ fm}/c$  is much smaller than all other time scales involved in the process. Therefore it is usually neglected in calculations of absorption

cross sections. In [Vog00], a value of the formation time of the pre-resonance state  $\tau_{8 \rightarrow 1}$  is estimated:  $\tau_{8 \rightarrow 1} = 0.3 \text{ fm}/c$ . Assuming that final state absorption is the only nuclear effect, in [Arl00], a fit to the nuclear suppression data of the E866 experiment [Lei00] is performed. The fit yields a very small value of  $\tau_{8 \rightarrow 1} = 0.02 \text{ fm}/c$  which is incompatible with the value of [Vog00] and suggests that the formation of the pre-resonance state cannot be described by a single physics process, like soft gluon emission.

An order-of-magnitude estimate of the lower bound for the formation time  $\tau_\psi$  of the final resonance can be obtained from the uncertainty principle. The formation time is larger than the proper time needed to distinguish different charmonium states,  $\tau_\psi \geq (M_{\psi(2S)} - M_{J/\psi})^{-1} \approx 0.3 \text{ fm}/c$ . A more precise value for  $\tau_\psi$  can be calculated from potential models. For  $J/\psi$ , a value of  $\tau_{J/\psi} = 0.92 \text{ fm}/c$  is obtained [Kar88].

In NRQCD, both singlet and octet processes contribute to charmonium production. The absorption cross sections for both processes are estimated in [Vog00]. Octet production is assumed to be energy- and  $x_F$ -independent, since the formation of the final charmonium is expected after the  $c\bar{c}$  pair has left the nucleus. For color singlet production, the time structure of charmonium formation is taken into account, therefore the absorption cross section becomes time-dependent. In [Bla89, Vog91], the dependence on the proper time  $\tau$  is parametrized by

$$\sigma^{\text{abs}}(\tau) = \begin{cases} \sigma_{\psi N}^{\text{abs}} \left( \frac{\tau}{\tau_\psi} \right)^\kappa & \text{for } \tau < \tau_\psi, \\ \sigma_{\psi N}^{\text{abs}} & \text{otherwise.} \end{cases} \quad (3.57)$$

In the Glauber approach, the absorption cross section is constant, i.e.  $\kappa = 0$ . If  $\sigma^{\text{abs}}$  is proportional to  $\pi R(\tau)^2$ , i.e. the geometric cross section of the nucleus, a value of  $\kappa \approx 2$  is expected. In [Ger00], a value of  $\kappa = 1$  is used instead. Note that  $\tau$  is related to the path length from the production point  $z$  to the charmonium formation point  $z'$  by  $z' - z = \beta\gamma c\tau$ . Hence the formation time introduces a dependence of the absorption cross section on  $x_F$ . The travelling distance as a function of  $x_F$  for HERA-B energies is shown in Fig. B.1. The distances for formation times between 0.1 and 1 fm/c can be compared to the size of a carbon nucleus (approximately 2.5 fm) and a tungsten nucleus (approximately 6.5 fm). For positive  $x_F$ , the final charmonium state is formed after leaving the nucleus. In this case, the absorption does not depend on the charmonium type. For negative  $x_F$ , depending on the actual value of  $\tau_\psi$ , the charmonium formation takes place inside the nucleus. The nuclear suppression due to absorption as expected for HERA-B is shown in Fig. 3.8. Due to the different radii of  $J/\psi$ ,  $\psi(2S)$ , and  $\chi_c$  mesons, the absorption cross sections of these charmonia are different, leading to different dependences of the nuclear suppression on the atomic mass number [Vog02].

A different approach to the calculation of nuclear absorption for small and negative  $x_F$  is discussed in [Kou02, Kou04]. Assuming that a color-singlet pre-resonance is formed quickly, the absorption of the pre-resonance and the final charmonium is studied in a quantum-mechanical model. The Schrödinger equation is solved for a Hamiltonian with a complex potential which describes both the  $c\bar{c}$  binding and interactions with the nuclear medium. In this model, transitions between charmonium states are possible, and interference effects are observed. The predicted nuclear dependence for  $J/\psi$  production is essentially flat, but suppression of  $\psi(2S)$  states is expected for negative  $x_F$ .

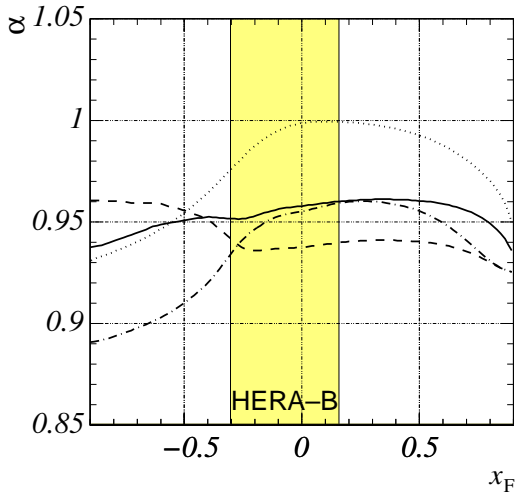


**Figure 3.8:** Nuclear suppression by final state absorption at 920 GeV (after [Vog02]). The suppression is calculated in NRQCD with a singlet absorption cross section of 2.5 mb and an octet absorption cross section of 5 mb. The nuclear suppression is shown for all  $J/\psi$  (solid line), direct  $J/\psi$  (dashed line),  $J/\psi$  from  $\psi(2S)$  decays (dot-dashed line), and  $J/\psi$  from  $\chi_c$  decays (dotted line).

### Final State Energy Loss

Energy loss in the final state can occur via color interactions of the color-octet state  $|c\bar{c}g\rangle_8$ . In [Kha93], it is argued that the lifetime of this state is prolonged by the QCD-equivalent of the Landau-Pomeranchuk-Migdal effect [Lan53, Mig56]: A characteristic time interval  $\tau_c$  is needed for the emission of a soft gluon. If within this interval, the  $|c\bar{c}g\rangle_8$  state scatters with the nuclear medium, the measurement of  $\tau_c$  starts from zero again. Hence the gluon is only emitted after the  $|c\bar{c}g\rangle_8$  state leaves the nucleus. As a consequence, the  $c\bar{c}$  pair traverses the entire nucleus as a color-octet state. Color interactions between the color-octet state and the nuclear medium lead to energy loss of the  $c\bar{c}$  pair. By this effect, the  $x_F$  spectrum is not suppressed but rather shifted to lower  $x_F$  values. A comparison to data shows that final state energy loss alone cannot account for the observed nuclear suppression pattern in proton-nucleus collisions [Vog00].

### 3.4.3 Combination of Nuclear Effects

In [Vog00], the two most important effects discussed above are combined and confronted with preliminary data from E866. Energy loss is seen as the most important initial state effect, while nuclear absorption of the  $c\bar{c}$  is the main final state effect. The resulting prediction of the nuclear suppression parameter  $\alpha$  is depicted in Fig. 3.9. The prediction is adjusted to the E866 data using specific choices of the absorption cross sections and the energy loss model. The gross features of the data are reproduced, however, the details are not described correctly.

### 3.4.4 Coherent Effects

In predictions based on the semi-classical Glauber model, coherent interactions of the beam proton with the entire target nucleus are neglected. This approximation cannot be made for large charmonium energies. Charmonium production can be viewed as a quantum-mechanical fluctuation of the beam particle to a  $c\bar{c}$  pair. Coherence effects are expected to become important if the coherence length of the  $c\bar{c}$  fluctuation is comparable or larger than the size of the target nucleus. For  $J/\psi$  with an energy of  $E \approx 50$  GeV and mass  $M \approx 3$  GeV/ $c^2$ , the coherence length is approximately given by  $l_c \approx E/M^2 \approx 1$  fm.

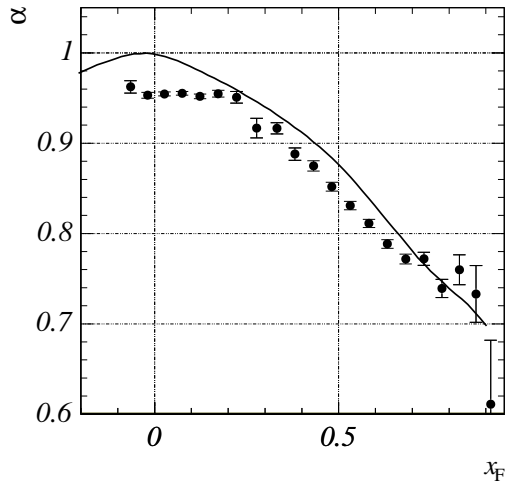


**Figure 3.9:** Nuclear suppression by a combination of nuclear effects at 800 GeV (after [Vog00]). A combination of singlet and octet absorption is calculated in NRQCD. The initial state energy loss is taken from [Gav92]. The resulting suppression parameter  $\alpha$  is compared with data from the E866 experiment [Lei00].

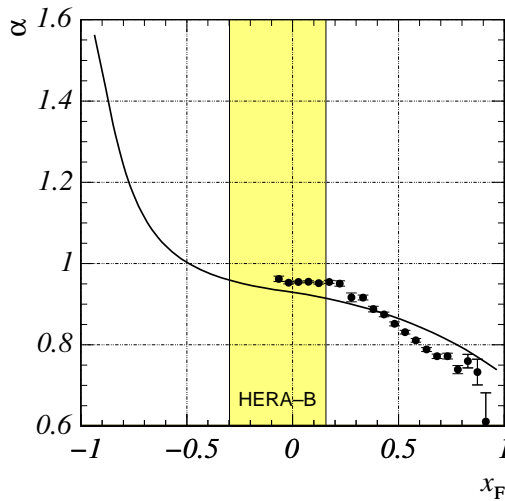


**Figure 3.10:**  $J/\psi$  suppression in the BCKT model (after [Bor03]). The model parameters are adjusted to the experimental values of E866 [Lei00].

### Reggeon-Based Approach

Nuclear suppression by shadowing due to coherence effects is predicted in the BCKT model [Bor93, Bor03], which is based on the Reggeon approach. Due to quantum-mechanical fluctuations, fast beam protons “look” like a cloud of light and heavy partons, which interact with the nuclear matter. Interactions of the soft partons inside the cloud introduce screening effects on the production of charmonia. The nuclear dependence of  $J/\psi$  productions in the BCKT approach features three regimes, as shown in Fig. 3.10. For  $x_F \approx 0$ , the screening effects cancel, and only a small absorption is predicted. Screening is expected for  $x_F > 0.2$ , and for  $x_F < -0.3$ , the BCKT approach predicts antiscreeing. This effect is caused by a redistribution of longitudinal momenta from the screening to the antiscreeing regime. After adjusting the model parameters to the experimental result of E866, the BCKT model describes the main features of the nuclear suppression parameter as a function of  $x_F$ .

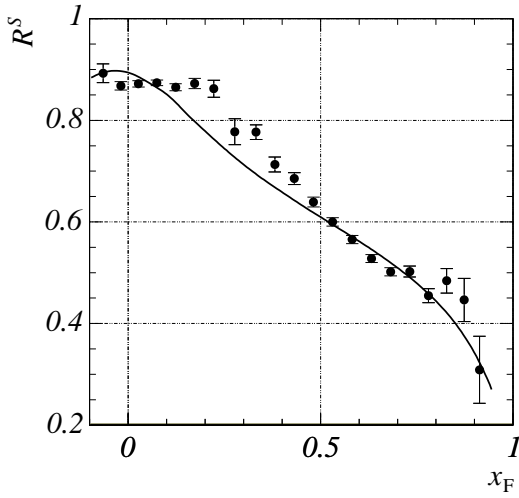


**Figure 3.11:**  $J/\psi$  suppression in the light-cone Green function approach compared to experimental data (after [Kop01]). The nuclear suppression  $R^S(W/\text{Be})$ , see Eq. (3.50), is shown as a function of  $x_F$ . The data points are taken from the E866 experiment [Lei00]. The line represents the full prediction of [Kop01], including corrections for initial state energy loss, gluon enhancement for small  $x_F$ , and contributions from  $\chi_c$  decays.

### Light-Cone Green Function Approach

Another approach to calculating nuclear suppression of charmonia due to coherence effects has been studied in [Kop01]. A full QCD calculation of coherence effects in the framework of light-cone Green functions has been performed, describing charmonia as color dipoles with fixed transverse separation. The calculation yields predictions of charmonium suppression over a broad energy range. The prediction is parameter-free in the sense that all phenomenological parameters are determined from experiments other than fixed-target proton-nucleus collisions.

The intuitive picture behind these calculations is the following: The  $c\bar{c}$  fluctuations lose coherence with the partons in the beam proton by the interaction with the target partons. In the target rest frame, the lifetime of the  $c\bar{c}$  fluctuation increases with energy, and the coherence length may exceed the size of the nucleus. In this case, the  $c\bar{c}$  pair interacts with the whole nucleus, i.e. the individual nucleons compete in interacting with the  $c\bar{c}$  pair. In the formalism of the Glauber model, this effect is described as shadowing of the  $c$ -quarks in the nuclear structure functions. At RHIC energies of 200 GeV/nucleon and energies planned for the LHC (5.5 TeV/nucleon), also the shadowing of gluons within  $c\bar{c}g$  fluctuations becomes important. The resulting suppression of charmonium production by  $c$ -quark shadowing is much larger than the suppression of open charm production in deep-inelastic scattering, hence QCD factorization is violated.

At center-of-mass energies of 200 GeV, final-state absorption of the  $c\bar{c}$  pair is seen as the main suppression mechanism. At HERA-B energies, the coherence length of the  $c\bar{c}$  fluctuation is of the same order of magnitude as the size of the nucleus, and coherence effects start to become important. For energies much larger than 1 TeV, as relevant for RHIC and LHC, coherence effects are predicted to be the main suppression mechanism. The shadowing effects due to coherent interactions is a function of the fractional momentum of the target partons,  $x_2$ , only. On the other hand, data taken at energies between 200 and 800 GeV show scaling of nuclear suppression with  $x_F$  rather than with  $x_2$ . See Section 3.5 for an overview of experimental results on charmonium suppression. This is explained by an interplay of coherence effects with initial state energy loss. In Fig. 3.11, the prediction of [Kop01] is compared to results of the E866 experiment [Lei00]. Although the model parameters are not adjusted to the E866 result, the data are described rather well by the model.

## 3.5 Results of Previous Experiments

The nuclear dependence of charmonium production has been studied prior to HERA-B in several fixed-target experiments using various primary and secondary beams. The following discussion is restricted to experiments using proton beams. The most important  $A$ -dependence results of previous experiments are summarized in Table 3.4. Compilations of results on the suppression parameter  $\alpha$  as a function of  $x_F$  and  $p_T$  can be found in Figs. 3.14 and 3.15.

### 3.5.1 The CERN Experiments

#### NA3

The NA3 experiment [Bad80] was a spectrometer optimized for the detection of Drell-Yan dimuons with invariant masses above  $4 \text{ GeV}/c^2$ , which also provides good acceptance for charmonium decays into muon pairs. An unseparated secondary beam, composed of pions, kaons, and protons, was delivered by the CERN Super Proton Synchrotron (SPS) and collided with a liquid hydrogen and a platinum target simultaneously. Proton-nucleus collisions were recorded at beam energies of 200 GeV. A “beam-dump” configuration was used, in which almost all hadrons were filtered by a 150-cm-thick absorber of steel and tungsten. The absorber was followed by a spectrometer, consisting of a dipole magnet and 38 layers of multi-wire proportional chambers (MWPC) for muon tracking. A hodoscope counter behind an additional 180 cm thick iron wall was used to identify the muons.

The nuclear dependence of  $J/\psi$  production has been studied in NA3 in the context of  $J/\psi$  hadroproduction in pion-nucleus and proton-nucleus interactions [Bad83]. A decrease of  $\alpha(x_F)$  with increasing  $x_F$  and an increase of  $\alpha(p_T)$  with increasing  $p_T$  was observed. Hence, the NA3 collaboration claimed evidence for a new “diffractive” production mechanism for low  $p_T$  and large  $x_F$ , in which charmonium suppression by initial state interactions is possible. An average value of the nuclear suppression parameter of  $\alpha = 0.94 \pm 0.03$  was extracted. However, the nuclear suppression has been determined with only two target materials, one of which made out of hydrogen. Using a hydrogen target and interpreting the data using the  $A^\alpha$  parametrization introduces a systematic shift towards lower values of  $\alpha$ , as also observed for inelastic interactions [Gei91].

#### NA38

The NA38 experiment [Bag89] was designed to study dimuon production in collisions of heavy-ion beams from the SPS with nuclear targets. NA38 was the first experiment to report evidence for charmonium suppression by the formation of a quark-gluon plasma in heavy-ion collisions [Abr97a]. In addition to the heavy-ion program, dedicated runs with proton beams on nuclear targets have been recorded, employing targets out of beryllium, carbon, aluminum, copper, silver, and tungsten. While in proton-nucleus runs, the NA38 target was followed by a hadron absorber of carbon and uranium, in nucleus-nucleus runs, an electromagnetic calorimeter to measure the transverse energy was added. The muon spectrometer of NA38 had previously been used in the NA10



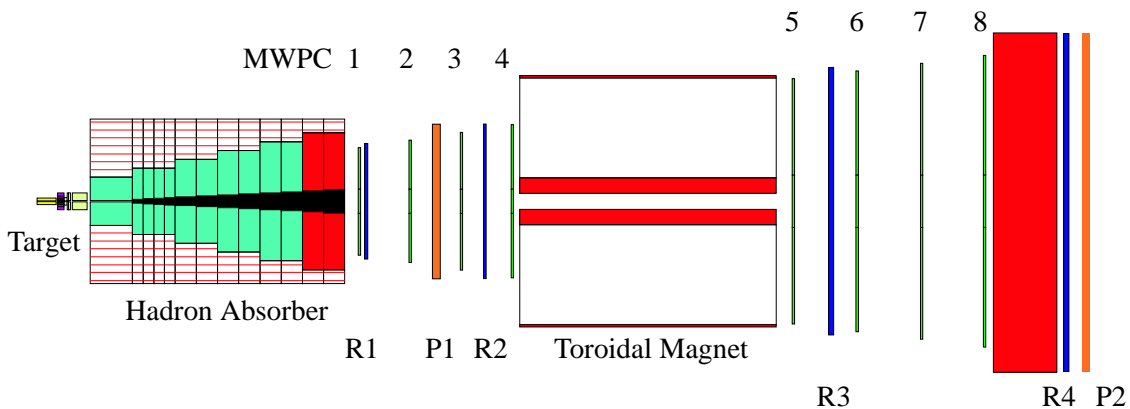


**Figure 3.12:** Schematic drawing of the CERN NA50 experiment (after [Sha01]). The target area is followed by a hadron absorber and eight layers of multi-wire proportional chambers (MWPC 1–8). Trigger signals are provided by the trigger hodoscopes R1–R4 and P1–P2.

experiment [And84]. It consisted of eight layers of MWPCs, four in front of and four behind a toroidal magnet. Four hodoscope counters, one of which behind a 120 cm thick iron wall, provided the trigger signal.

The NA38 collaboration measured the nuclear dependence of  $J/\psi$  production in collisions of protons with carbon, aluminum, copper, and tungsten, resulting in a suppression parameter of  $\alpha = 0.919 \pm 0.015$  [Abr98a]. The value has been obtained from a fit to measurements of the production cross sections per nucleon for the different target materials. The fit combines the production rate results measured in NA38 with results from hydrogen and deuterium targets in the NA51 experiment [Abr98b].

## NA50

For the successor of NA38, the NA50 experiment [Abr97b], the spectrometer was extended by a silicon-strip multiplicity detector. Inside the hadron absorber, a zero-degree calorimeter was added. Together with the electromagnetic calorimeter, these detectors were utilized for a precise measurement of charmonium suppression as a function of the collision centrality. A schematic drawing of the NA50 experiment is shown in Fig. 3.12. In dedicated runs with proton beams, data were recorded with targets out of beryllium, carbon, aluminum, copper, silver, and tungsten.

The NA50 collaboration has published the results of their nuclear suppression studies in three different representations [Ale04]: Apart from the suppression parameter  $\alpha = 0.925 \pm 0.015$ , the absorption cross section is given both for fits to the full Glauber model and to the path length approximation (see Section 3.3). The Glauber model absorption amounts to  $(4.4 \pm 0.7)$  mb, while in the path length approximation, a value of  $(4.9 \pm 0.8)$  mb is determined. Within the  $x_F$  acceptance of the spectrometer,  $-0.1 < x_F < 0.1$ , the NA50 collaboration found no indication for an onset of strong  $J/\psi$  suppression for small and negative  $x_F$ , where the  $J/\psi$  is fully formed inside the nucleus.

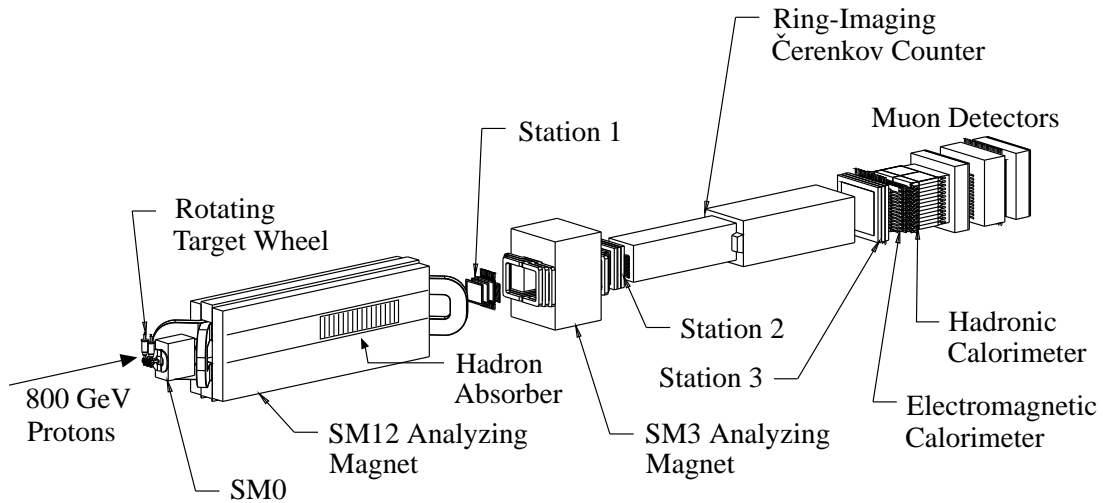


**Figure 3.13:** Schematic drawing of the FNAL Meson East spectrometer as utilized in the E866 experiment (after [Lee99]). The detector consists of three dipole magnets (SM0, SM12, SM3), three tracking stations, a ring-imaging Čerenkov counter, electromagnetic and hadronic calorimeters, and muon detectors.

### 3.5.2 The FNAL Experiments

The FNAL Tevatron provided an 800-GeV proton beam for the experiments located at the FNAL Meson East beam line. The Meson East spectrometer used in the E772, E789, and E866 experiments had been employed by the E605 experiment before. The layout of the spectrometer as utilized in E866 is depicted in Fig. 3.13. The target area was followed by two dipole magnets, the second of which containing a beam dump made of copper, graphite, and polyethylene. Behind the absorber, the spectrometer consisted of three stations composed of six planes of MWPCs, situated in front of and behind a third dipole magnet and after a ring-imaging Čerenkov counter. The spectrometer was completed by electromagnetic and hadronic calorimeters and a muon detector of scintillation counters and proportional tubes behind a shielding wall.

#### E772

The E772 experiment [Jaf89] was constructed to study the nuclear dependence of Drell-Yan,  $J/\psi$ ,  $\psi(2S)$ , and  $\Upsilon$  production in proton-nucleus interactions. Muon pairs were produced by collisions of protons with nuclear targets of liquid deuterium, carbon, calcium, iron, and tungsten.

The E772 collaboration published a suppression parameter of  $\alpha = 0.920 \pm 0.008$  [Ald91]. With the E772 measurement, the NA3 result of decreasing  $\alpha$  with increasing  $x_F$  was confirmed with better precision, while no strong increase of  $\alpha$  is observed for increasing  $p_T$ . If the E772 result, taken at 800 GeV beam energy, is compared to the 200-GeV result of NA3, the nuclear suppression parameters shows a scaling behavior as a function of  $x_F$ , but not as a function of the fractional momentum  $x_2$  of the struck parton in the target nucleon. From this finding, the E772 collaboration concluded that the contribution of nuclear shadowing to  $J/\psi$  suppression is small.

**E789**

The E789 experiment [Pri00] was designed to study the production and decays of B and D mesons. Therefore, the first magnet of the Meson East spectrometer was replaced by eight layers of silicon strip detectors to identify decays of these long-lived particles downstream of the target.

A first result on the  $J/\psi$   $A$ -dependence was obtained in a configuration in which the copper beam dump or a beryllium block in front of the beam dump were used as targets [Kow94]. With this configuration, the forward direction of the collision was covered:  $0.3 < x_F < 0.95$ . The result on the suppression factor  $\alpha$  as a function of  $x_F$  is compatible with the previous result of E772 within the systematic uncertainties.

Another measurement [Lei95] was performed with beryllium, carbon, and tungsten targets placed downstream of its nominal position. Hence the acceptance of the spectrometer was in the range of  $-0.1 < x_F < 0.1$ . In this range, a value of  $\alpha \approx 0.88$  is observed, lower than the values previously published by E772 for larger  $x_F$ . Therefore, contrary to NA50, evidence for increasing  $J/\psi$  suppression for  $x_F < 0$  is reported.

**E866/NuSea**

The main objective of the E866/NuSea experiment was a measurement of the asymmetry in the  $\bar{u}$  and  $\bar{d}$  quark content of nucleons. For this purpose, the trigger and data acquisition systems of the Meson East spectrometer were modernized [Gag98], and new MWPCs and hodoscopes with larger acceptances were added to the first tracking station. The new trigger system allowed for a larger maximum  $p_T$  compared to E772 of  $> 4 \text{ GeV}/c$ . In order to cover the large  $x_F$  range of  $-0.10 < x_F < 0.93$ , data have been recorded with three different combinations of magnetic field configurations and target positions, providing good acceptance for small  $x_F$  (SXF), intermediate  $x_F$  (IXF), and large  $x_F$  (LXF) respectively.

As a result, the E866 collaboration published the most precise measurement of the suppression factor  $\alpha$  in fixed-target hadroproduction of  $J/\psi$  mesons available to date [Lei00], covering wide ranges of  $x_F$  and  $p_T$ . The target materials utilized in E866 were beryllium, iron, and tungsten. For  $x_F \approx 0$ , the suppression parameter  $\alpha$  is larger, i.e. the suppression is smaller than previously reported by E772 and E789. The explanation for this discrepancy is seen in the limited  $p_T$  acceptances of these experiments, which introduce large correction factors for small  $x_F$  due to the correlation between the  $x_F$  and  $p_T$  acceptances.

**3.5.3 HERA-B Commissioning Run 2000**

Based on data taken during the HERA-B commissioning run in 2000, a feasibility study of a  $J/\psi$  suppression measurement has been performed [Bru02b]. From the runs in which a carbon wire (Inner II) and a titanium wire (Below I) were operated simultaneously, approximately 1,800  $J/\psi \rightarrow \mu^+ \mu^-$  decays and 2,500  $J/\psi \rightarrow e^+ e^-$  decays were reconstructed. The suppression parameter  $\alpha$  was determined following Eq. (1.3), i.e. by measuring the ratios of  $J/\psi$  yields, luminosities and efficiencies. The choice of target materials results in a small ratio of atomic mass numbers and hence in a small “lever

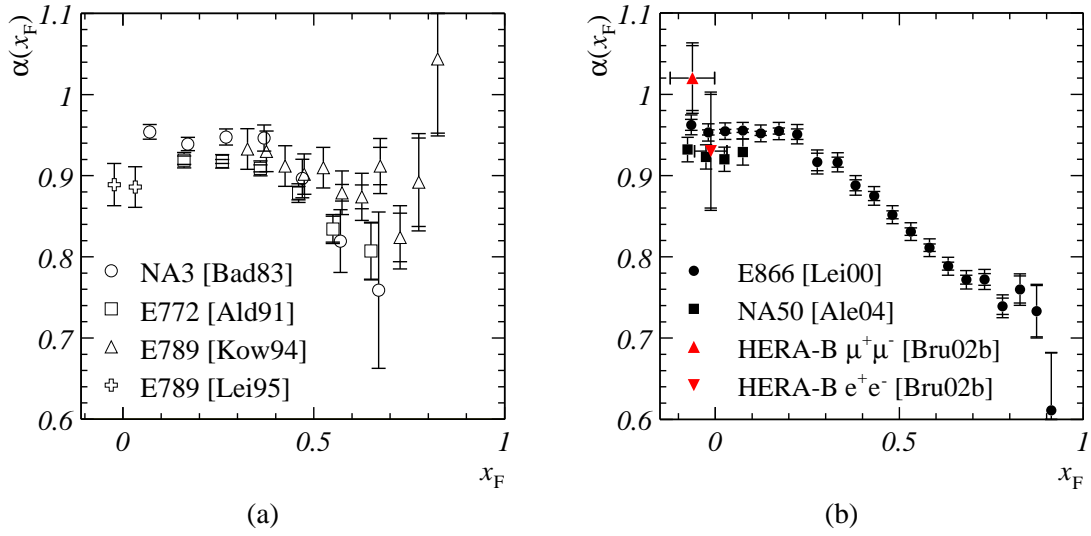


**Figure 3.14:** Previous measurements of  $\alpha$  as a function of  $x_F$ . (a) Early measurements. (b) Recent results. The error bars indicate the statistical uncertainties and the quadratic sum of the statistical and the systematic uncertainties of the measured values. A discussion of the experimental setups and the results can be found in the text.

arm” for the measurement of  $\alpha$  compared to measurements with one heavy material, for example tungsten.

The luminosity ratio was determined from counting the numbers of primary vertices on the two wires. The result was cross-checked with two methods: The average response of different subdetectors is proportional to the detector response for a single inelastic interaction. Therefore, the number of interactions can be extracted from the average number of hits in the VDS, OTR, and RICH and the energy deposited in the ECAL. Assuming that the number of interactions follows a Poisson distribution, the number of interactions can also be obtained by counting the number of empty events.

At the time of the measurement, no realistic simulation of all efficiencies in the HERA-B detector and trigger chain was available. However, detector and trigger efficiencies were expected to cancel out if the ratios of  $J/\psi$  yields, luminosities and efficiencies are calculated, except for the different geometrical acceptance of the wires. Therefore, the efficiency ratio was determined from the data by migrating tracks from one wire to the other and evaluating the difference in the acceptance.

In the dimuon channel, a clean  $J/\psi$  signal could be observed by loose cuts on the RICH likelihood of the muon tracks, the number of hits in the VDS, the OTR and the muon detector, the  $\chi^2$  probability of the dimuon vertex and the angle of the positive muon in the  $J/\psi$  rest frame. However, in the dielectron channel, either hard cuts on the ratio of the ECAL energy and the track momentum or the reconstruction of an additional bremsstrahlung photon were required to obtain a visible  $J/\psi$  signal.

The low number of  $J/\psi$  recorded during the commissioning runs allowed only for a measurement of  $\alpha$  integrated over  $x_F$  and  $p_T$ . The results are compatible with no nuclear suppression in the accessible kinematic range of HERA-B, but also with the high-

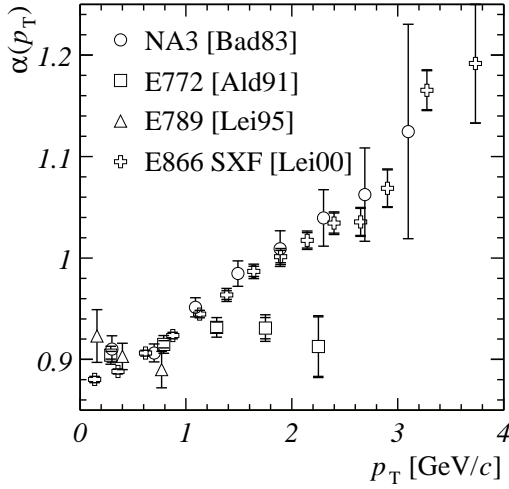


**Figure 3.15:** Previous measurements of  $\alpha$  as a function of  $p_T$ . The error bars indicate the statistical uncertainties and the quadratic sum of the statistical and the systematic uncertainties of the measured values. The E866 result is only shown for the SXF (small  $x_F$ ) spectrometer configuration, which covers the  $x_F$  range closest to the HERA-B acceptance. The experimental setups and a discussion of the results can be found in the text.

precision measurement of E866, in which a small suppression is observed [Bru02b]:

$$\begin{aligned}\alpha(\text{J}/\psi \rightarrow \mu^+ \mu^-) &= 1.02 \pm 0.04(\text{stat.}) \pm 0.02(\text{syst.}) && \text{for } -0.105 < x_F < 0.017, \\ \alpha(\text{J}/\psi \rightarrow e^+ e^-) &= 0.93 \pm 0.07(\text{stat.}) \pm 0.02(\text{syst.}) && \text{for } -0.056 < x_F < 0.032.\end{aligned}$$

The main systematic uncertainties of this result originate from the relative acceptance of the two target wires (1.5%) and the luminosity ratio (1%).

## 3.6 Summary

NRQCD provides a well-founded theoretical framework for calculations in the field of charmonium production. However, several predictions of NRQCD, e.g. the universality of the NRQCD matrix elements and the large transverse polarization of charmonia, remain to be tested experimentally. In addition to NRQCD, the CEM is a valuable tool for phenomenological calculations.

The domain of nuclear effects in charmonium production reveals a complex pattern of theoretical predictions and experimental results. Many theoretical models distinguish between initial and final state effects. The absorption in nuclear matter is usually evaluated in the framework of the Glauber model. Other models are based on coherent interactions between the beam proton and the target nucleus. The current status of the models and the perspectives of HERA-B to test the models can be summarized as follows.

- A comparison of previous experiments at different beam energies shows that nuclear effects scale with  $x_F$  rather than with  $x_2$ . Therefore, the influence of nuclear parton distribution functions on the nuclear suppression is small. The kinematic range covered by HERA-B allows for a further test of  $x_2$  scaling by the comparison with previous results from NA3 and E866.
- The effects of intrinsic charm and initial state energy loss as predicted in [Gav92] become important for the large- $|x_F|$  regions which are inaccessible to HERA-B. The

initial state energy loss predicted by [Bai97] is disfavored by the measurements of E866 and NA50. HERA-B can provide additional constraints on this model.

- The large acceptance of the HERA-B spectrometer and the choice of one light and one heavy target material allow a measurement of transverse momentum broadening in HERA-B. The energy and material dependence of transverse momentum broadening can be studied by comparing the HERA-B result with results from previous experiments obtained at different beam energies and with different materials.
- Different theoretical models of the charmonium formation process predict vastly different values of the formation time of the pre-resonance  $c\bar{c}$  state. Independently of this discrepancy, the predicted nuclear absorption effects are small and require a high-precision measurement of the absorption of  $J/\psi$ ,  $\psi(2S)$ , and  $\chi_c$  states at the same time.
- The BCKT model based on coherent proton-nucleus interactions predicts a large antiscreening effect for negative  $x_F$ . With an  $x_F$  coverage of  $x_F < -0.1$ , HERA-B could discover first indications for antiscreening.
- The light-cone Green function approach is compelling in that its predictions agree well with the results of E866 without tuning phenomenological parameters to fixed-target data. Unfortunately, no predictions for negative  $x_F$  are available at HERA-B energies.

In summary, the HERA-B data allow to extend measurements of nuclear effects to the previously unexplored kinematic range of  $x_F < -0.1$  and to impose more stringent constraints on several of the theoretical predictions. Unfortunately, the limited size of the HERA-B data set results in small significances for some measurements, as will be discussed in Section 6.2.6.

**Table 3.4:** Compilation of measurements of nuclear effects in the production of  $J/\psi$  in proton-nucleus collisions. For all measurements, the center-of-mass energies, target materials,  $x_F$  and  $p_T$  ranges, the  $J/\psi$  statistics and (if available) the average values of the suppression parameter  $\alpha$  are listed. A discussion of the experimental setups and a discussion of the results can be found in the text.

Experiment	Reference	$\sqrt{s}$ [GeV]	Target Materials	Min./Max. $x_F$	Max. $p_T$	$J/\psi$	$\alpha$
CERN NA3	[Bad83]	19.4	H <sub>2</sub> , Pt	0.0 <sup>a</sup> 0.95 <sup>a</sup>	4.0 GeV/ $c$ <sup>a</sup>	83,000 <sup>b</sup>	0.94±0.03 <sup>c</sup>
FNAL E772	[Ald91]	38.8	D, C, Ca, Fe, W	0.1 <sup>a</sup> 0.7 <sup>a</sup>	3.0 GeV/ $c$ <sup>a</sup>	100,000	0.920±0.008
FNAL E789	[Kow94]	38.8	Be, Cu	0.3 0.95	5.0 GeV/ $c$	245,000	$\alpha(x_F)$
FNAL E789	[Lei95]	38.8	Be, C, W	-0.1 0.1	1.5 GeV/ $c$ <sup>a</sup>	2,000	0.887 <sup>d</sup>
CERN NA38	[Abr98a]	29.1	C, Al, Cu, W	-0.09 <sup>b</sup> 0.14 <sup>b</sup>	5.0 GeV/ $c$ <sup>a</sup>	49,000	0.919±0.015
FNAL E866	[Lei00]	38.8	Be, Fe, W	-0.1 0.93	4.0 GeV/ $c$	> 3,000,000	$\alpha(x_F, p_T)$
HERA-B ( $\mu^+\mu^-$ )	[Bru02b]	41.6	C, Ti	-0.105 0.017	5.0 GeV/ $c$	1,800	1.02±0.04
HERA-B ( $e^+e^-$ )	[Bru02b]	41.6	C, Ti	-0.056 0.032	5.0 GeV/ $c$	2,500	0.93±0.07
CERN NA50	[Ale04]	29.1	Be, Al, Cu, Ag, W	-0.1 0.1	5.0 GeV/ $c$ <sup>a</sup>	3,600,000 <sup>e</sup>	0.925±0.015

<sup>a</sup>number estimated from publication

<sup>b</sup>derived from rapidity range for  $p_T < 1$  GeV/ $c$

<sup>c</sup>for proton beam at  $\sqrt{s} = 19.4$  GeV

<sup>d</sup>weighted average of published values

<sup>e</sup>number not given in publication, compiled from [Sha01]





---

# Signal Extraction, Efficiencies, and Differential Distributions

---

This chapter introduces two important parts of the measurement of nuclear effects in  $J/\psi$  production, i.e. measurements of the  $J/\psi$  yields and efficiencies of the HERA-B detector and trigger. The chapter commences with a discussion of the selection of “good” runs for the analysis. The list of runs used in the analysis comprises only runs which have been recorded operating two target wires simultaneously. Next, the extraction of  $J/\psi$  signals and measurements of the distribution of  $J/\psi$  mesons as a function of the kinematic variables are described. Corrections for the detector acceptance and efficiencies based on a Monte Carlo (MC) simulation are required to obtain the “true” kinematic distributions of  $J/\psi$  mesons from these raw distributions. The chapter closes with a discussion of the differential distributions for  $J/\psi$  production and a comparison of the results to previous experiments.

## 4.1 Data Selection

The data sample analyzed for this thesis has been taken with the HERA-B detector during a five-month data-taking period between October 2002 and February 2003. During this time period, approximately 150 million events have been recorded using the dilepton trigger. The selection of  $J/\psi$  candidate events in this data sample is described in this section.

### 4.1.1 Run Selection and Data Quality Assessment

As a first step, a list of runs is compiled, which contains only runs taken with the dilepton trigger. For these runs, the quality of the data is checked, and only “good” runs are used in the analysis. The resulting list of runs is shown in Appendix C.

The quality of the data is evaluated in several steps. The data quality of a run is first assessed by the shift crew, to exclude runs with known problems in the subdetectors

or in the data acquisition (DAQ) system. During the run, important control parameters are continuously monitored by the data quality (DQ) system in the HERA-B DAQ and checked by the shift crew on a regular basis. The parameters are saved every 30 minutes in the form of ROOT histograms, and a collection of histograms containing the most important control parameters is compared with a reference set of histograms at the end of each run [Brä03]. The control parameters include

- occupancies of the subdetectors and the trigger components to identify defective readout channels,
- the number of hits in the subdetectors as a function of the bunch crossing number and hit correlations between different subdetectors to check their synchronization,
- figures of merit of the vertexing and the tracking performance, both subdetector-specific and for the global track reconstruction, and
- invariant mass distributions of  $J/\psi$ ,  $K_S^0$ ,  $\Lambda$ ,  $\bar{\Lambda}$ , and  $\pi^0$  to monitor the particle yields and their time evolution.

The data quality summary is saved in the DQ database together with the most important DAQ parameters and can be accessed via a WWW-interface [Nör02] (WWW: World Wide Web). In a second step, the persons responsible for the subdetector DQ evaluate the subdetector performance on the basis of additional monitoring information and enter their DQ assessments into the DQ database. After these steps, runs with “bad” DQ assessment by the shift crew or severe subsystem problems are excluded from the analysis.

The DQ of the muon detector was re-evaluated based on the recorded DQ information in [Sip04a]. The occupancies of all chambers of the muon detector were scanned for “hot” readout channels, which were not masked during the data-taking. In a Monte Carlo (MC) simulation, additional hits were artificially added to some of the muon chambers. Adding hits at the observed level of hot channels resulted in a negligible influence on the number and the quality of reconstructed muons. Therefore, no additional runs were excluded due to hot channels in the muon detector. However, several runs were deleted from the run list due to wrong trigger settings or problems with the threshold settings of the ASD8 chip in the muon detector readout. A small fraction of runs revealed a mis-synchronization of two front-end drivers (FED) in the pad systems of MU3 and MU4. Due to the coincidence scheme of the muon pretrigger, the trigger rate in the detector area covered by these FEDs was decreased to the level of random coincidences. Runs showing this “missing quadrant” problem are treated separately in the comparison of data with the MC simulation.

#### 4.1.2 Data Reprocessing

A variable fraction of the events in a run were already reconstructed online during the data-taking. The remaining events were reconstructed in periods without usable beam, using the same calibration constants as in the online data-taking. The calibration constants include calibration and alignment of the subdetectors, and masks for problematic readout channels. The quality of the reconstructed data could be improved by additional offline corrections, based on better knowledge of the detector and reconstruction per-

**Table 4.1:** Classification of dimuon candidate events. The criteria applied to tracks and vertices are explained in the text. An event class contains all selection criteria from the previous class, and further criteria are added.

ARTE Event Class	Bit	Comment
ECLASS_DIMUON	19	at least two muon candidates (standard cuts, see Table 4.2)
ECLASS_JPSIMM	2	additionally: vertex prob( $\chi^2, n_{\text{dof}} > 10^{-5}$ , mass $M < 20 \text{ GeV}/c^2$ )
ECLASS_JPSIMMH	24	additionally: vertex invariant mass $M > 2.3 \text{ GeV}/c^2$

formance. In two reprocessing efforts, the entire data set was re-reconstructed with an updated version of the reconstruction software and refined calibration constants. The most important improvements include

- more realistic hit preparation and run-by-run alignment of the VDS,
- new alignments of the target wires and the OTR,
- new track matching and clone removal procedures,
- an optimized track refit which includes the removal of “outliers”, i.e. hits with large contributions to the  $\chi^2$  of the track refit.

### 4.1.3 Selection of $J/\psi$ Candidate Events

After a brief overview of the framework in which the data analysis is performed, the procedure of selecting  $J/\psi$  candidate events is described in this section. In runs accepted for the analysis, candidate events are selected using three different classes of selection criteria. As a first step, a selection based on global properties of the events is performed. The second selection step comprises cuts on the properties of muon tracks, since  $J/\psi$  mesons are reconstructed by their decays into muon pairs. The properties of vertices formed by combinations of the muon tracks serve as a third set of selection criteria. Note that most of the criteria are standard cuts used in all dimuon analyses within HERA-B.

Events are selected according to the standard cuts already during the reprocessing. The events are flagged with a combination of event classification bits to facilitate the access to subsamples of events. The event classification scheme used for dimuon events is shown in Table 4.1. For certain analyses, further specialized cuts are added.

### Analysis Framework

For the analysis presented in this thesis, data are preselected using ARTE [ART03], the standard analysis framework in HERA-B. The events are provided in two different formats: The DST format (DST: Data Summary Tape) contains both the raw detector data and the full result of the reconstruction. The typical size of a dilepton-triggered event in the DST format amounts to 135–150kB. In the mini-DST format (MINI), most of the raw data and intermediate results of the hit preparation and track reconstruction

are omitted. Thus, the event size is reduced to approximately 30–40 kB. The MINI format contains all information needed for this analysis. Therefore, the analysis is based on events in the MINI format. The events are accessed via a run catalogue from which the events are selected by their run numbers and their event classification bits.

To become independent of the large ARTE framework, which depends on many external software packages and databases, the information required for the analysis is extracted to an  $n$ -tuple in the TTree format provided by the ROOT package [Bru97]. The definition of the  $n$ -tuple structure, together with rules to fill the  $n$ -tuple and additional control histograms are given in the XML format (XML: Extensible Markup Language). The C++ code to create and fill the  $n$ -tuple is generated automatically from the XML definitions.

The analysis of the  $n$ -tuple is performed in a stand-alone program, which uses elements of the ROOT analysis framework. For fits to kinematic distributions, the corresponding ROOT functions are used, which internally utilize minimization routines from the MINUIT package [Jam75]. Unbinned and binned maximum likelihood (ML) fits are performed by employing the RooFit package [Ver04]. RooFit is a C++ class library for data-modelling based on ROOT, which has been developed within the BABAR collaboration.

### Event-based Selection Cuts

Events with large multiplicities are rejected in the reprocessing. High-multiplicity events contain several superimposed interactions, and most of them are triggered by random combinations of muon candidates. In addition, their reconstruction is time-consuming, and the events are rather difficult to analyze. Therefore, an event is only reconstructed if the hit multiplicity in the OTR does not exceed 13,000 hits. The fraction of events rejected by the cut on the number of OTR hits is obtained from the DAQ database: For the runs in which high-multiplicity events were already rejected by the RICH multiplicity veto, approximately 2–5% of the events are discarded. The rejection factor is increased to approximately 10–15% in runs taken without the RICH multiplicity veto.

An additional event-based cut is required if the data is compared to the MC simulation of the HERA–B trigger chain: Instead of using a bit-level simulation of the First Level Trigger (FLT), the FLT efficiency is parametrized in the simulation. The efficiency can only be measured in events in which one of the SLT tracks is matched with a FLT track. A FLT and a SLT track are matched if their distance  $\Delta r$  is less than 2 cm (see Eq. (A.16)). Events without an FLT–SLT match are not considered in the analysis. By using this cut on all dimuon events with the classification bit #24, the number of reconstructed  $J/\psi$  is reduced by approximately 6.0%. If only two-wire runs are considered, the reduction amounts to approximately 5.2%. A more detailed description of the HERA–B trigger simulation and the treatment of the FLT efficiency therein can be found in Appendix A.

**Table 4.2:** Selection criteria for muon candidates. The cut values correspond to cuts imposed on the elements of the ARTE table RTRA or quantities derived from RTRA elements. The first group of cuts are standard cuts already used in the event classification. The second group comprises additional cuts specific for this analysis.

	Criterion	Cut Value
<b>Standard Cuts</b>	Track is “long” track	<code>fit == 0</code>
	Track belongs to clone-free subset	<code>cmp &amp; Rsegc::clonerm</code>
	Track produced hits in VDS	<code>hsi ≥ 5</code>
	Track produced hits in main tracker	<code>hin + hou ≥ 9</code>
	Track produced hits in muon detector	<code>hmu ≥ 4</code>
	Momentum of particle	$5 \text{ GeV}/c \leq p \leq 460 \text{ GeV}/c$
	Muon likelihood of track	<code>lmmu &gt; 0.01</code>
<b>Additional Cuts</b>	$\chi^2$ probability of track refit	$\text{prob}(\chi^2, n_{\text{dof}}) > 0.003$
	Transverse momentum of particle	$p_T > 0.7 \text{ GeV}/c$

### Track-based Selection Cuts

If an event passes the event-based selection, it is scanned for muon candidates. Muon tracks are selected according to the following criteria (see Table 4.2 for a summary).

- In the clone removal procedure, the best track out of a list of tracks with very similar parameters is flagged. The figure of merit to evaluate the track quality is a combination of the numbers of hits in several subdetectors. A track is assigned a very large value of the figure of merit and hence kept in most cases if it is built from a VDS segment linked to exactly one segment in the PC area of the OTR [Ple01, Ple03].
- The track is required to be reconstructed from a minimum number of five hits in the VDS, nine hits in the main tracker, and four hits in the muon detector.
- The momentum must be in the range of 5–460 GeV/ $c$ , where the lower cut reflects the momentum cutoff due the muon absorber, and the upper cut removes tracks with momenta larger than half the beam energy, which are likely to be wrongly reconstructed. Note that the nominal lower limit for the track momentum was 4 GeV/ $c$ . However, hits in the muon detector are only reconstructed for tracks with momenta larger than 5 GeV/ $c$ .
- A very low cut on the muon likelihood of the track of 0.01 is imposed to select tracks which could be matched to hits in the muon detector.

In addition to these standard selection criteria, two further cuts have been applied in the analysis. The transverse momenta of the tracks are required to be larger than 0.7 GeV/ $c$ . This cut is motivated by the intrinsic transverse momentum cutoff of the trigger chain. An additional cut on the  $\chi^2$  probability of the track refit results in a lower fraction of fake tracks and tracks from decays in flight of pions and kaons, which show a smaller  $\chi^2$  probability because of the “kink” in the particle trajectory due to the decay. The cut value chosen in this analysis has been shown to reduce the number of back-

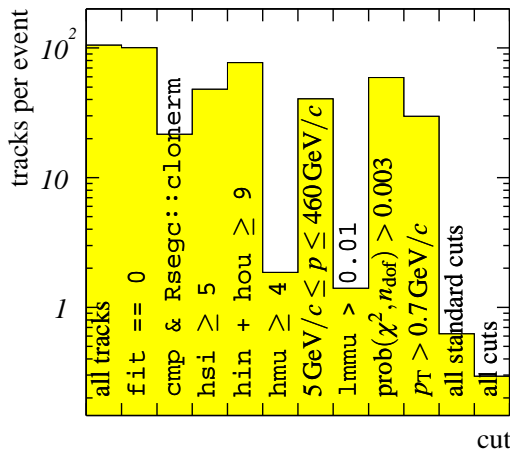


**Figure 4.1:** Influence of the track selection cuts on the number of tracks per events. Each cut is first applied separately, then all cuts are combined by a logical AND. The figure is based on 100,000 events from run #20505.

ground events in the data by 36% in the mass range in which 95% of the signal is found. At the same time, the reduction of the  $J/\psi$  signal is comparable within 3% between the data and the MC simulation. In addition, by using the cut on the  $\chi^2$  probability of the tracks, a better agreement between the kinematic distributions in the data and the MC simulation is achieved [Spi04c].

The reduction of the number of tracks per event by these cuts is illustrated in Fig. 4.1, which is based on 100,000 events from run #20505, taken with the wire combination I1I2. After all standard cuts, on average 0.62 muon track candidates per event remain. The additional cuts reduce this number to 0.29.

The efficiency of the cuts on reconstructed muons from  $J/\psi$  decays is evaluated based on 100,000 reconstructed MC events for the wire combination I1I2 in which the  $J/\psi$  is produced on the wire Inner I and 100,000 events using the wire Inner II. The cut efficiencies for  $J/\psi$  from both wires agree within less than 1%. In order to link a reconstructed track to a “true” track from the MC generator, the tracks are matched by the “70%-criterion”: A reconstructed track is matched to a true track if more than 70% of the hits from which the track is reconstructed are matched to true hits, and a maximum of four non-matched hits is tolerated [Hul02]. Due to the wrong assignment of MC hits to tracks in the track reconstruction, this criterion underestimates the total number of reconstructed tracks. However, the relative change in the number of tracks by applying the selection cuts is expected to be well-reproduced. Out of the reconstructed muons from  $J/\psi$  decays, 63% satisfy the standard selection criteria. The additional cuts reduce this number to 60%. Note however that the clone removal cut is independent of the 70%-criterion and may remove a track which is matched to a true track. The fraction of tracks remaining after solely applying the clone removal cut amounts to 75%.

### Vertex-based Selection Cuts

The selection criteria for vertices are summarized in Table 4.3. Each oppositely charged combination of muon candidates in an event is fitted to a two-prong vertex. The vertex fit is performed by a Kalman filter algorithm provided by the Grover package (Grover: Generic Reconstruction of Vertices) [Abt04a]. A vertex is accepted if the  $\chi^2$  probability of the vertex fit is larger than  $10^{-5}$ . To reduce the large number of track pairs with low

**Table 4.3:** Selection criteria for dimuon vertices. The cut values correspond to cuts imposed on the result of a two-prong vertex fit using Grover.

Criterion	Cut Value
Unlike-sign combination of tracks	Track charges $Q_2 = -Q_1$
$\chi^2$ probability of vertex fit	$\text{prob}(\chi^2, n_{\text{dof}}) > 10^{-5}$
Dimuon invariant mass	$2.3 \text{ GeV}/c^2 < M < 20 \text{ GeV}/c^2$

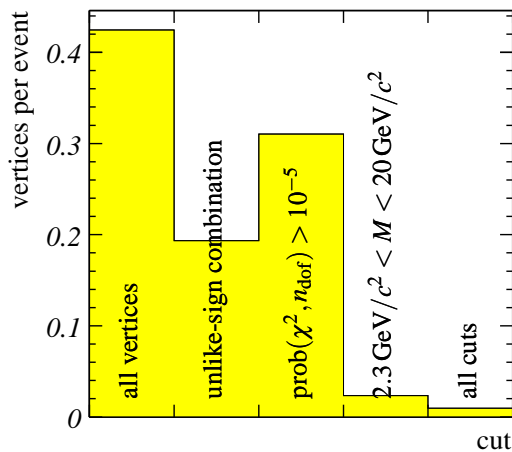


**Figure 4.2:** Influence of the vertex selection cuts on the number of vertices per events. Every cut is first applied separately, then all cuts are combined by a logical AND. The figure is based on 100,000 events from run #20505.

invariant masses which are not used in the analysis, only vertices with invariant masses in the range of  $2.3\text{--}20 \text{ GeV}/c^2$  are accepted. In approximately 3% of the events, more than one vertex passes the selection criteria. Since there is no unique way to select the “best” vertex in an event, all vertices are kept. The influence of the vertex-based cuts on the number of vertices per event is shown in Fig 4.2. After applying all cuts, 0.017 vertices per event are found on average. Applying the vertex-based criteria on successfully reconstructed muon pairs from the decays of  $J/\psi$  in the MC simulation by employing the “70%-criterion”, the number of vertices is reduced by only 1.5–1.6%.

### Fiducial Volume Cuts

Areas of the HERA–B detector are excluded from the analysis, if the efficiencies of the subdetectors or parts of the trigger chain are not well-described by the MC simulation. A muon track from a  $J/\psi$  candidate event is removed if a straight-line extrapolation of the track from its endpoint to the  $z$ -position of the affected superlayers crosses the  $xy$ -position of one of the excluded areas. The fiducial cuts applied in this analysis originate from three sources, as summarized in Table 4.4.

- Since the Inner Tracker (ITR) was not used in the trigger, the inner acceptance of the HERA–B detector for dimuon events is limited by the inner edges of the Outer Tracker (OTR). In the innermost region, projections of muon tracks from  $J/\psi$  decays to the superlayers of the OTR show different inner acceptance edges in data and MC, as exemplified in Fig. 4.3. Due to the large effort that would have been required to

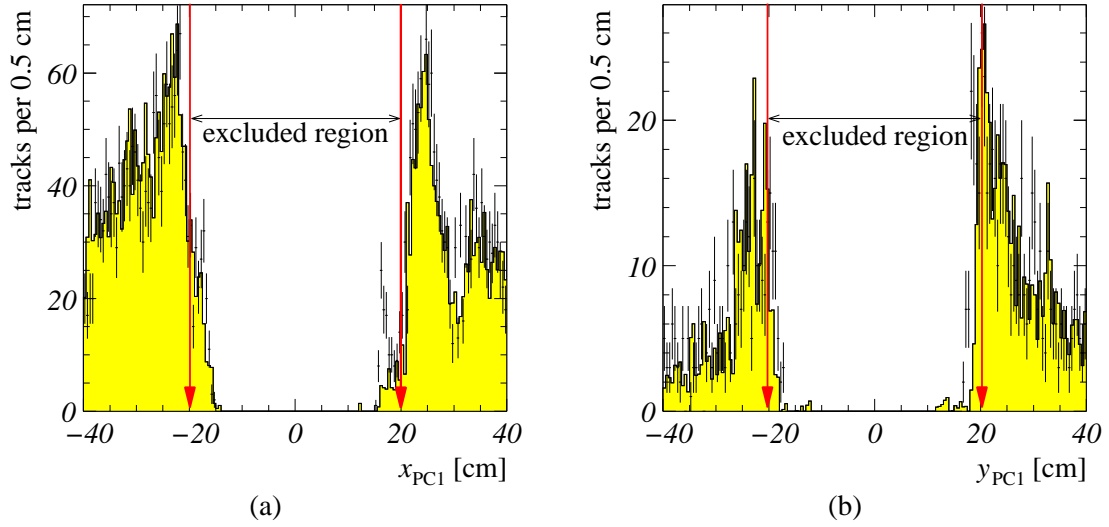


**Figure 4.3:** Fiducial cuts in the OTR superlayer PC1. Muon tracks from  $J/\psi$  candidates which could be fitted to a vertex with an invariant mass in the range of  $3.0\text{--}3.2\text{ GeV}/c^2$  are extrapolated to the  $z$ -position of PC1. The data points are taken from all runs with the wire combination I1I2 in November 2002, and the histograms show the corresponding results from the MC simulation, scaled to the integral of the data. (a)  $x$ -positions of all tracks in the range of  $|y_{\text{PC1}}| < 10\text{ cm}$ . (b)  $y$ -positions of all tracks in the range of  $|x_{\text{PC1}}| < 10\text{ cm}$ . The cut values are indicated by the arrows.

improve the MC description of the OTR, a cut of  $|x| > 19.9\text{ cm}$  and  $|y| > 20.25\text{ cm}$  at the  $z$ -position of the OTR superlayer PC1 is placed instead. The superlayer PC1 is chosen because it has the largest influence on the inner acceptance of the OTR.

- Comparisons of the muon pretrigger messages found in the data with messages generated by the muon pretrigger simulation MUPRESIM operated on the same data show that the response of the first circle of muon pad detector cells around the proton beam pipe is systematically underestimated in the simulation. Therefore, tracks crossing the area of these pads in the superlayer MU3 are excluded from the analysis.
- In all superlayers of the muon detector, the area above the electron beam pipe is covered by a special chamber, the so-called “chamber 99”. This chamber was unstable during the entire data-taking period. Therefore, tracks crossing the area covered by this chamber in the superlayer MU3 are rejected.

## 4.2 Extraction of $J/\psi$ Signals

### 4.2.1 Determination of the $J/\psi$ Yield

Throughout this thesis, the number of  $J/\psi$  mesons in a given kinematic range is determined by a maximum likelihood fit to the invariant mass spectrum of all  $J/\psi$  candidates in this range. In order to obtain a precise measure of the number of  $J/\psi$ , the functional form used to describe the shape of the invariant mass spectrum must reflect the most important features of the measured spectrum.



**Table 4.4:** List of fiducial volume cuts. The endpoints of muon tracks from  $J/\psi$  candidates are extrapolated to a given superlayer, and a rectangular cut on the  $xy$ -position of the track is performed.

Superlayer	$z$ [cm]	Cut in $x$ [cm]	Cut in $y$ [cm]	Reason
PC1	705	$\notin [-19.9;19.9]$	$\notin [-20.25;20.25]$	OTR edge
MU3	1888	$\notin [-52.4;52.4]$	$\notin [-45.80;45.80]$	first circle of pads
MU3	1888	$\notin [39.3;65.5]$	$\notin [-117.00;5.10]$	muon chamber 99

### Core of $J/\psi$ Signal

Since the mass resolution of the HERA-B detector at the  $J/\psi$  mass of approximately  $30 \text{ MeV}/c^2$  is much larger than the total decay width of the  $J/\psi$  of  $91 \text{ keV}/c^2$  [Eid04], the core of the  $J/\psi$  signal is described by a Gaussian function:

$$s_0(M; \mu, \sigma) \propto \exp \left[ -\frac{(M - \mu)^2}{2\sigma^2} \right]. \quad (4.1)$$

Here, the independent variable is the invariant mass  $M$ ;  $\mu$  and  $\sigma$  are the mean value and the width of the Gaussian function.

### Non-Gaussian Tails

As a result of multiple scattering in the HERA-B detector material, the momentum resolution of muon tracks shows non-Gaussian tails. Since the momentum resolution enters directly into the invariant mass resolution, non-Gaussian tails are also visible in the invariant mass spectrum. To model these tails, two additional Gaussian functions  $s_2$  and  $s_3$  with the same mean value  $\mu$  but larger widths are added to the original Gaussian shape of Eq. (4.1).

The widths of  $s_2$  and  $s_3$  are obtained by separating the multiple scattering fraction of  $\sigma$  from the other contributions:  $\sigma^2 = \sigma_0^2 + \sigma_{\text{MS}}^2$ . A value of  $\sigma_{\text{MS}} = 22 \text{ MeV}/c^2$  is determined from a MC simulation. The widths are then given by  $\sigma_2^2 = \sigma_0^2 + (2\sigma_{\text{MS}})^2$  and  $\sigma_3^2 = \sigma_0^2 + (7\sigma_{\text{MS}})^2$ . The contributions of  $s_2$  and  $s_3$  to the signal,  $C_2$  and  $C_3$ , are determined from a MC simulation and fixed in the fit function. The values used in the analysis are  $C_2 = 0.239$  and  $C_3 = 0.030$ . The full signal shape is then given by [Spi04b]

$$s^{\text{MC}}(M; \mu, \sigma) \propto (1 - C_2 - C_3) \exp \left[ -\frac{(M - \mu)^2}{2\sigma^2} \right] + C_2 \exp \left[ -\frac{(M - \mu)^2}{2\sigma_2^2} \right] + C_3 \exp \left[ -\frac{(M - \mu)^2}{2\sigma_3^2} \right]. \quad (4.2)$$

The invariant mass distribution of  $J/\psi$  in the MC simulation is well-described using the non-Gaussian tails. On the other hand, at the expense of a more complicated signal shape, the improvement of the signal description in real data results in a slightly better  $\chi^2$  value of the mass fit [Spi04b]. Therefore, the signal shape of Eq. (4.2) is used only for fits to the invariant mass spectrum in the MC simulation.

### Radiative Tail

In the data, the invariant mass spectrum shows a feature which is not taken into account in the MC simulation, an asymmetry in the shape of the  $J/\psi$  signal. This asymmetry is caused by the radiative decay  $J/\psi \rightarrow \mu^+ \mu^- \gamma$ . For a  $J/\psi$  decaying into this final state, the  $\mu^+ \mu^-$  system carries only a fraction of the  $J/\psi$  four-momentum, hence its invariant mass is smaller than the  $J/\psi$  mass, resulting in a radiative tail towards lower invariant masses. The additional photon is not reconstructed.

A parametrization of the invariant mass distribution including the radiative tail is derived in [Spi04a]. To avoid divergent contributions from very small photon energies, a cutoff for the minimum photon energy of 10 MeV is introduced. The differential cross section  $d\sigma/dM$  of this process calculated in quantum electrodynamics is used to fix the shape of the radiative tail and the fraction of events contained in the tail of approximately 4.5%, stable over a range of photon energy cutoffs of  $10^{-3} - 10^2$  MeV. To take into account resolution effects, a convolution of the cross section function with the Gaussian signal function has been performed numerically and is parametrized by a 10th order polynomial function  $r(M)$ . See [Spi04a] for the explicit form of  $r(M)$ . The combined signal function used for fits to the real-data spectrum,  $s^{\text{RD}}(M; \mu; \sigma)$ , reads:

$$s^{\text{RD}}(M; \mu, \sigma) = s_0(M; \mu, \sigma) + r(M). \quad (4.3)$$

### Combinatorial Background

The main background in the dimuon spectrum arises from combinations of muons from decays in flight of pions and kaons. Additional small contributions result from semi-leptonic decays of  $c$  and  $b$  quarks and the Drell-Yan process. Since the number of random combinations available decreases approximately exponentially with the invariant mass, an exponential function is chosen to describe the background below the  $J/\psi$  signal,

$$b(M; a) = \exp[-aM]. \quad (4.4)$$

The exponential model for the background is checked with a MC simulation: Random momenta and transverse momenta for two particles are drawn according to distributions similar to the observed momentum distributions. Independent of the exact choice of the shape of the distributions, the local shape of the invariant mass spectrum of the two particles in the range of  $2.5 - 3.5 \text{ GeV}/c^2$  is described well by an exponential distribution.

Since the amount of background events and the shape of the invariant mass distribution influences the invariant mass fits, it is desirable to extract the number of  $J/\psi$  in the MC simulation under similar background conditions as in the data. The probability for pions with momenta of  $10 \text{ GeV}/c$  to decay before the HERA-B calorimeter (13 m downstream of the target) and hence to contribute to the combinatorial background is approximately 2%. However, the rate at which minimum-bias interactions are produced is larger than the  $J/\psi$  production rate by six orders of magnitude. Therefore, to model the combinatorial background in the MC simulation, approximately 10,000 inelastic MC events would be required for each  $J/\psi$  event, corresponding to approximately 5000 CPU years for a sample of  $10^6$   $J/\psi$  on a standard PC. As a less time-consuming alternative to this approach, the background is added to the invariant mass distribution separately.

The number  $N_b$  of background events and the slope  $a$  of the background distribution are extracted from fits to the real data and scaled to the number of reconstructed J/ψ in the MC simulation. A random sample of  $N_b$  values for the invariant mass distributed according to the shape of the background is generated and added to the MC events.

### Fitting Procedure

The combination of the signal and the background shapes is implemented in an extended ML fit. The fit function reads

$$f(M; N_s, N_b, \mu, \sigma, a) = \begin{cases} N_s s^{\text{RD}}(M; \mu, \sigma) + N_b b(M; a) & \text{for real data,} \\ N_s s^{\text{MC}}(M; \mu, \sigma) + N_b b(M; a) & \text{for MC simulation.} \end{cases} \quad (4.5)$$

The free parameters in this fit are the number of signal events  $N_s$ , the number of background events  $N_b$  in the fit range, the mass  $\mu$  and the width  $\sigma$  of the J/ψ, and the slope  $a$  of the background function. A low number of events in some bins of the kinematic distributions leads to unstable fits if all parameters are left free. Systematic studies of the influence of fixing the J/ψ mass and width on the analysis are discussed in Section 6.1.4. The mass range of the fit includes  $2.5 \text{ GeV}/c^2 < M < 3.5 \text{ GeV}/c^2$ . The fit is performed as an unbinned ML fit if the number of events in the fit range is smaller than 1,000. Otherwise, a binned ML fit is performed which saves computing time and leads to identical results in the limit of large samples. The bin width utilized in histograms of invariant mass distributions throughout this analysis is  $25 \text{ MeV}/c^2$ . Binned ML fits to the full J/ψ data sample and to MC-simulated data for the wire combination I1I2 for the calibration period of November 2002 using the fit functions of Eq. (4.5) are presented in Fig. 4.4.

### 4.2.2 J/ψ Kinematic Distributions

To study the influence of the J/ψ kinematics on the production process, the J/ψ are separated into intervals of the following kinematic variables: Feynman- $x$  ( $x_F$ ), transverse momentum ( $p_T$ ), rapidity ( $y$ ), polar angle of the outgoing positively charged muon ( $\cos \theta_{\text{GJ}}$ ), and azimuthal angle of the outgoing positively charged muon ( $\phi_{\text{GJ}}$ ). The rapidity distribution is evaluated as a cross-check of the  $x_F$  results, since by measuring the rapidity, the kinematic region of  $x_F \approx 0$  can be resolved better. The subscript ‘‘GJ’’ of the angular variables indicates the choice of the reference frame for the evaluation of  $\cos \theta$  and  $\phi$ , the Gottfried-Jackson frame [Got64]. The exact definitions of the kinematic variables and the Gottfried-Jackson frame are explained in Appendix B.

### 4.2.3 Wire Configurations and Wire Assignment

The dilepton-triggered data sample recorded during the 2002/2003 data-taking period consists of runs with different single- and double-wire target configurations. Table 4.5 shows the number of runs and events recorded with different wire configurations along with the number of reconstructed J/ψ in the respective data samples. For the measurement of the nuclear dependence of J/ψ production, only the two-wire runs are considered. A detailed list of all two-wire runs used in the analysis can be found in Appendix C.

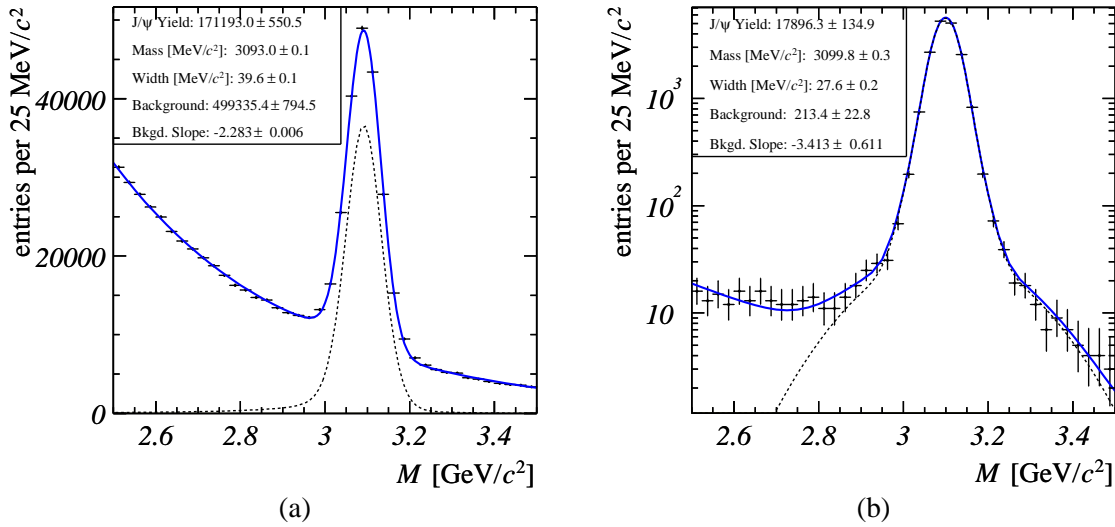


**Figure 4.4:** Fits to the invariant mass spectra in the data and in the MC simulation. (a) Fit to the full  $J/\psi \rightarrow \mu^+\mu^-$  data set, selected by the event classification bit #24. (b) Fit to MC-simulated data for the wire combination III2 in the calibration period of November 2002 (see Section 4.3). The figure shows the invariant mass spectrum in the MC simulation before adding background events. The solid curves represent the full fit result while the dashed curves show the signal shape only.

To measure the influence of the nuclear medium on  $J/\psi$  production,  $J/\psi$  mesons produced on target wires of different materials have to be separated. Different assignment criteria are used for wire combinations from the same target station and from different stations. If the two target wires are located in different target stations, the separation of the two stations in the  $z$ -direction of approximately 4 cm is much larger than the vertex resolution of 750  $\mu\text{m}$ . Therefore, a cut on the difference of the  $z$ -positions of the wire and the vertex of  $|\Delta z| < 300 \mu\text{m}$  is used. The  $z$ -position of the wire is determined from the average  $z$ -position of all dimuon vertices in the calibration period recorded with the same target wire combination. The function used to approximate the distribution of vertices is the sum of two Gaussian functions with the same mean value. The mean value obtained from the fit is used as the wire position.

For target configurations with two wires from the same target station, the wire separation in the  $z$ -direction amounts to approximately 5 mm. Therefore, a different wire assignment method is used, based on a cut on the impact parameters of the tracks to the wires. In the Grover package, a function is provided to calculate the two-dimensional impact parameter of a track with respect to a target wire at the  $z$ -position of the wire. The  $\chi^2$  distance of the track and the wire is calculated by normalizing the square of the impact parameter,  $d^2$ , to the quadratic sum of the tracking uncertainties and the diameter of the target wire,  $\sigma^2$ . The  $J/\psi$  is assigned to the wire for which the sum of the  $\chi^2$  distances of the two muons and the  $J/\psi$  is the smallest [Gia04]:

$$\frac{d^2}{\sigma^2} = \frac{d_{\mu^+}^2}{\sigma_{\mu^+}^2} + \frac{d_{\mu^-}^2}{\sigma_{\mu^-}^2} + \frac{d_{J/\psi}^2}{\sigma_{J/\psi}^2}. \quad (4.6)$$

**Table 4.5:** Run statistics for different wire configurations. The number of  $J/\psi$  is obtained from a binned ML fit to the invariant mass spectrum of all  $J/\psi$  candidates selected by the event classification bit #24. Several runs with non-satisfactory data quality are excluded from the list of analyzed two-wire runs with carbon and tungsten targets.

Wire Configuration	# Runs	# Events	# $J/\psi$
Inner I	5	1,477,785	$1,163 \pm 48$
Below I	50	10,594,188	$11,132 \pm 135$
Inner II	55	20,743,719	$32,306 \pm 238$
Outer II	5	6,259,085	$4,284 \pm 97$
Below II	9	5,899,127	$9,369 \pm 133$
Inner I / Below I (I1B1)	33	22,430,992	$17,948 \pm 181$
Inner I / Inner II (I1I2)	44	16,764,315	$19,436 \pm 186$
Below I / Inner II (B1I2)	16	10,059,122	$20,373 \pm 181$
Below I / Outer II (B1O2)	66	41,560,860	$44,439 \pm 281$
Below I / Below II (B1B2)	24	13,758,395	$10,220 \pm 136$
Inner II / Below II (I2B2)	5	590,269	$440 \pm 27$
<b>Analyzed C–W Combinations</b>	<b>155</b>	<b>89,551,141</b>	<b><math>87,108 \pm 396</math></b>
<b>Total</b>	<b>312</b>	<b>150,137,857</b>	<b><math>171,193 \pm 551</math></b>

The probability to assign a  $J/\psi$  to the wrong target wire has been estimated using MC simulations for the wire combinations I1B1 and I1I2. For both selection methods, more than 99% of the reconstructed  $J/\psi$  are assigned to the correct wire and less than 0.1% are assigned to the other active wire. The remaining fraction of  $J/\psi$  is assigned to other wires.

Examples for the discriminating power of both wire assignment methods for real data are presented in Fig. 4.5. While no events are rejected by the  $\chi^2$  distance cut, 8.7% of all events are rejected by the cut on  $|\Delta z|$ . However, within the statistical uncertainties, the total number of  $J/\psi$  reconstructed on the two wires is the same as the number obtained from a joint fit without the  $|\Delta z|$  cut. Hence, in both methods, no significant signal loss is observed. For the  $\chi^2$  distance method, the good wire separation at small distances between the wires is obtained at the expense of a slightly higher contamination by background events.

### 4.3 Monte Carlo Simulation

For the analysis presented in this thesis, a detailed MC simulation is used to correct the “raw” detector data for the acceptances and efficiencies of the detector and the trigger. Details on the implementation of the MC simulation chain can be found in Appendix A.

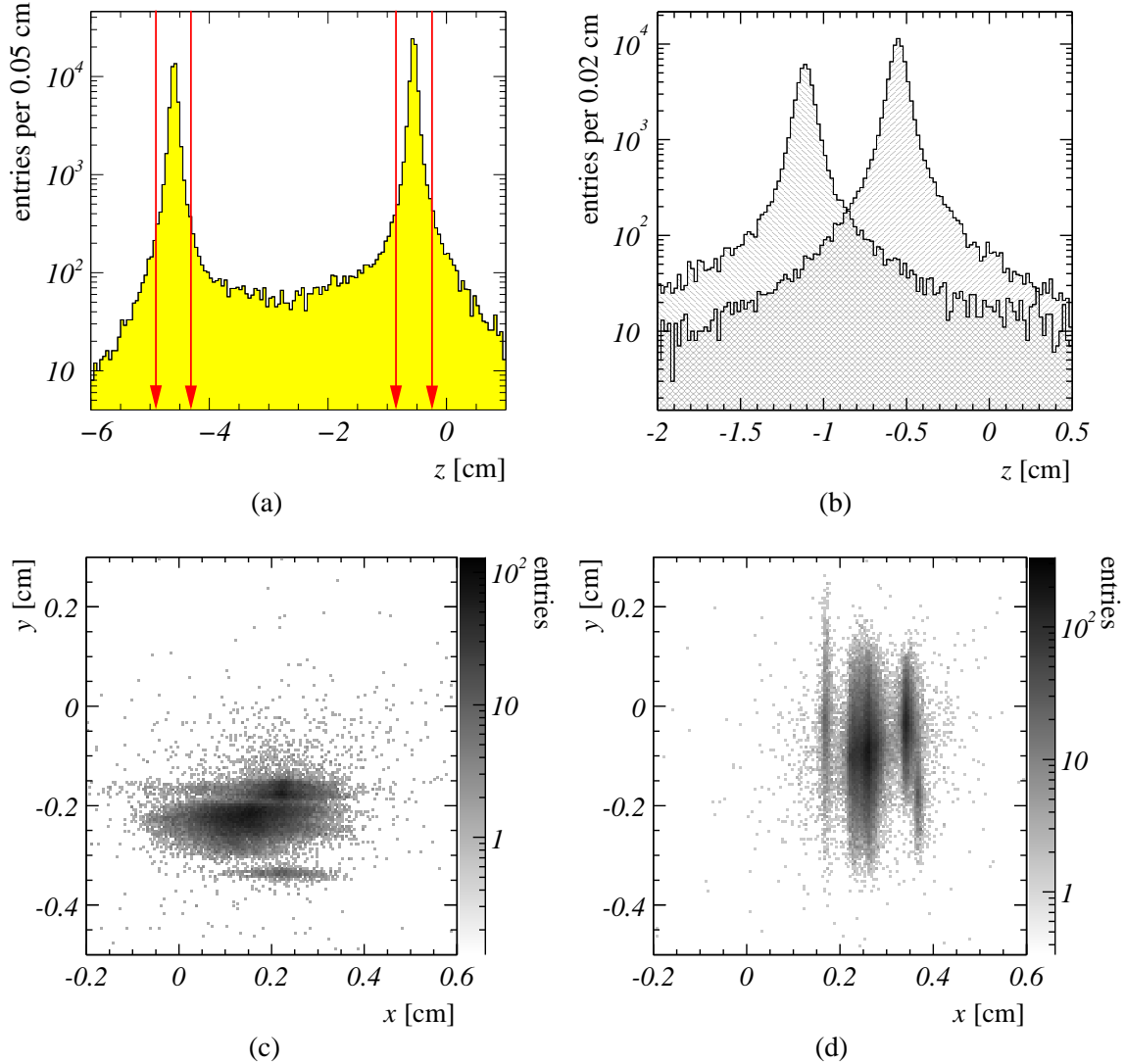


**Figure 4.5:** Illustration of wire separation methods. (a)  $z$ -distribution of dimuon vertices in all runs taken with the wire combination I1I2. The wire separation cuts are indicated by arrows. (b)  $z$ -projections of vertices assigned to the wire Below I (peak at  $z \approx -1.1$  cm) and Inner I (peak at  $z \approx -0.55$  cm) for the wire combination I1B1. (c) I1B1:  $xy$ -projection of vertices assigned to the wire Below I. (d) I1B1:  $xy$ -projection of vertices assigned to the wire Inner I. The vertices are clearly separated. The variations of the beam position for different HERA fills are reflected by several bands in the  $xy$ -projections of vertices. All events are selected according to event classification bit # 24.

### 4.3.1 Calibration Periods and Monte Carlo Event Statistics

In order to reflect the changing conditions of the HERA-B detector during the data-taking between October 2002 and February 2003, the run period was divided into calibration periods with similar detector and trigger performances. The definition of the calibration periods is shown in Table 4.6. Maintenance work in the detector and trigger systems took place during the monthly access days to the detector. Therefore, the calibration periods cover the time intervals between two access days. In addition, two special calibration periods were artificially created: the period of January 2003 is split into two parts due to an improvement of the muon pretrigger which was carried out between two access days. Runs showing the “missing quadrant problem” (see Section 4.1) were distributed over several calibration periods. However, most of these runs were recorded during November 7–13, 2002 (see the run list in Appendix C). Therefore, the MC conditions for this period are the same as those for November 2002, except for the reduced muon pretrigger efficiencies in the detector area affected by the “missing quadrant” problem.

The detector conditions used in the MC simulation are obtained by averaging the conditions in all runs during a calibration period. The exact averaging procedure is different for different subdetectors. As an example, the determination of average calibration constants in the muon detector is discussed in Section A.3.1.

MC events were generated both at the PC farms of the Second Level Trigger (SLT) and the Fourth Level Trigger (4LT) at DESY and at external institutes. Approximately 20% of the MC events which contain the decay  $J/\psi \rightarrow \mu^+ \mu^-$  were generated using the PC cluster of the “Experimentelle Teilchenphysik” group at the University of Siegen. The event reconstruction and trigger simulation requires a large variety of external software and databases; therefore it is performed at DESY only.

In order to cover all important two-wire configurations and all calibration periods with MC events, sets of 1–2.5 million events per wire were reconstructed with 12 different configurations. The  $J/\psi$  signal was simulated in separate MC data sets for the two wires. Before the reconstruction, the events were mixed with inelastic interactions on both wires simultaneously. The track multiplicity in  $J/\psi$  events is reproduced if the number of mixed inelastic events on each wire follows a Poisson distribution with a mean value of 0.5. The number of MC events generated and reconstructed for each of the calibration periods is shown in Table 4.7. Out of the 40 million events passed to the trigger simulation and reconstruction, only about 250,000  $J/\psi$  candidates could be reconstructed. This is due to the low total efficiency of the detector and trigger simulation of less than 1% (see Section 4.3.3). The average number of reconstructed  $J/\psi$  in the MC simulation per reconstructed  $J/\psi$  in the data is 2.5. The actual ratio varies due to changes in the detector efficiencies between the different calibration periods. The size of the MC sample ensures that the statistical uncertainties due to the MC simulation are smaller than the uncertainties from the data. However, the statistical error of the MC simulation cannot be entirely neglected.

**Table 4.6:** Definition of calibration periods during the 2002/2003 data-taking. The run numbers correspond to the first and last runs within a calibration period taken with the dilepton trigger.

Period	Start	End	First Run	Last Run
October 2002	2002-10-02	2002-11-05	19890	20242
November 2002	2002-11-07	2002-12-03	20333	20593
December 2002	2002-12-07	2002-12-20	20612	20763
January 2003 (I)	2003-01-07	2003-01-20	20826	20924
January 2003 (II)	2003-01-21	2003-02-05	20926	21104
February 2003	2003-02-08	2003-03-01	21122	21304
“Missing Quadrant”	several runs from different periods			

### 4.3.2 Reweighting of Kinematic Distributions

The differential distributions of  $J/\psi$  obtained from the PYTHIA event generator do not agree well with the distributions measured in HERA-B and in previous experiments. Especially the  $p_T$  spectrum is distorted by a low- $p_T$  cutoff of 1 GeV/ $c$  to regularize the parton-level cross sections. Therefore, event weights  $w(x_F, p_T)$  are required to adjust the  $x_F$  and  $p_T$  spectra. An early version of these weights, adjusted to parametrizations of the spectra measured in the E789 experiment, is discussed in [Iva99]. The comparison of the weights to the HERA-B data taken in 2002/2003 showed two shortcomings of the reweighting: The parametrization of the  $x_F$  shape used by E789 [Sch95],

$$\frac{dN}{dx_F} \propto (1 - |x_F|)^C, \quad (4.7)$$

is non-differentiable at  $x_F = 0$  and does not describe the theoretical predictions by the color evaporation model (CEM) and nonrelativistic QCD (NRQCD) depicted in Fig. 3.4. In addition, the  $p_T$  shape depends on the wire material. Therefore, a new set of weights has been introduced, based on the  $p_T$  spectra measured by HERA-B and the  $x_F$  spectrum predicted by NRQCD. The resulting  $x_F$  shape is parametrized by [Kol04]:

$$\frac{dN}{dx_F} \propto \frac{f(x_F; x_1, C)}{x_F^2 + x_0^2} \text{ with } f(x_F; x_1, C) = \begin{cases} \exp\left[-\frac{x_F^2}{2\sigma^2}\right] & \text{for } |x_F| \leq x_1, \\ A(1 - |x_F|)^C & \text{for } |x_F| > x_1. \end{cases} \quad (4.8)$$

The values of the parameters  $A$ ,  $C$ ,  $x_0$ , and  $x_1$  are documented in Section A.1.1. The following parametrization of the material-dependent  $p_T$  shape is employed:

$$\frac{dN}{dp_T^2} \propto \left[1 + \left(\frac{p_T}{p_0}\right)^2\right]^{-6} \text{ with } p_0 = \begin{cases} 2.9 \text{ GeV}/c & \text{for carbon targets,} \\ 3.1 \text{ GeV}/c & \text{for tungsten targets.} \end{cases} \quad (4.9)$$

A comparison of the reweighted  $x_F$  and  $p_T$  spectra with the original spectra generated by PYTHIA is shown in Fig. 4.6. The figure is based on 100,000 MC events generated for the carbon wire Inner II. The calculation of the MC weights is detailed in Section A.1.1.



**Table 4.7:** Summary of Monte Carlo simulated events. For every wire combination and calibration period, the number of MC events and the number of  $J/\psi$  for both wires are shown. The number of  $J/\psi$  is determined by a fit to the invariant mass spectrum of muon pairs.  $J/\psi$  candidates are selected by the event classification bit #24. Events with  $J/\psi$  candidates which pass the trigger simulation are weighted with the efficiency of the FLT and the kinematic weight.

Wire Comb.	Period	Events Wire 1	Events Wire 2	$J/\psi$ Wire 1	$J/\psi$ Wire 2
I1B1	October 2002	2,576,248	2,523,459	11,542	11,793
	Nov 2002	1,013,629	1,007,788	5,186	8,833
	“Missing Quadrant”	1,504,104	1,513,178	6,703	4,451
I1I2	October 2002	1,542,044	1,645,078	7,567	8,083
	November 2002	1,542,795	1,646,144	8,506	8,930
	December 2002	1,543,649	1,647,927	9,593	10,223
B1O2	January 2003 (I)	1,322,894	1,278,141	10,826	7,703
	January 2003 (II)	2,625,646	2,547,446	20,814	16,019
	February 2003	1,020,561	1,026,728	7,318	5,670
B1I2	January 2003 (II)	2,020,302	2,243,943	18,478	18,810
B1B2	October 2002	1,509,294	1,498,243	8,308	6,671
	February 2003	2,023,271	2,047,124	15,493	13,083
<b>Sum</b>		<b>20,244,437</b>	<b>20,625,199</b>	<b>130,334</b>	<b>120,269</b>

### 4.3.3 Trigger Simulation

In order to determine the effects of the dilepton trigger chain on the  $J/\psi$  signal, a detailed trigger simulation is required. The simulation chain comprises bit-level simulations of the pretrigger systems and the SLT, and the FLT efficiency map. The FLT efficiency map is a parametrization of the FLT efficiency relative to the SLT efficiency. A sketch of the trigger simulation chain is given in Fig. 4.7. The ordering of the FLT and the SLT are exchanged in the simulation, which is justified by the fact that the triggers work independently in the 1 FLT/2 SLT\* trigger mode, and that the final trigger decision is a logical AND of the FLT and the SLT decisions.

The efficiencies of the single steps of the trigger simulation, i.e. the fractions of events remaining after every step of the trigger chain, are illustrated in Fig 4.8. The figure is based on approximately 3,000,000 events generated in a MC simulation for the wire combination I1I2 in the calibration period of November 2002. The number of events is first reduced by the geometrical acceptance of the detector for the decay of a  $J/\psi$  into an muon pair. An event is geometrically accepted if two muon tracks cross the muon detector superlayers MU3 and MU4. The muon pretrigger efficiency is the efficiency to find at least two muon pretrigger messages in an event. The overall efficiency is further reduced by the SLT algorithm, separated into the muon tracking, the Slicer and Refit algorithms and the propagation of track pairs through the magnet and the VDS to a common vertex. After the SLT algorithm, the FLT efficiency map is applied to the event. The overall efficiency, averaged over particles generated on both wires amounts to approximately 0.9%.

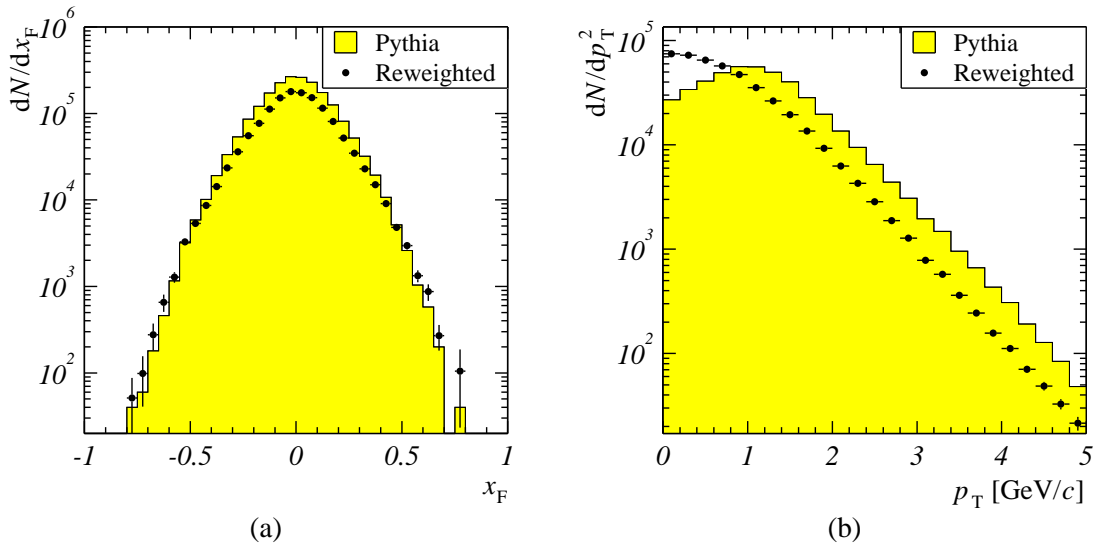


**Figure 4.6:** Comparison of the PYTHIA-generated kinematic distributions (histograms) and reweighted distributions (data points). (a)  $x_F$  distributions. (b)  $p_T$  distributions. The figures are based on 100,000 MC events generated on the carbon wire Inner II.

#### 4.3.4 Detector Resolutions in the Kinematic Variables

The finite resolution of the HERA-B detector for measuring the four-momenta of particles results in finite resolutions of the kinematic variables derived from these four-momenta. The data is represented in intervals of the kinematic variables (“bins”). In order to minimize fluctuations between the intervals, bin sizes much larger than the resolution in the corresponding kinematic variable are required.

The resolution of the detector is mainly determined by multiple scattering, i.e. it depends on the amount of material through which the particles travel in the detector. Since the detector description in the MC simulation is unchanged over the entire data-taking period with respect to the material budget, it is sufficient to study resolution effects in a single calibration period. The wire combination III2 from the November 2002 period has been chosen for the study. Approximately 3,000,000 generated MC events are passed through the detector and trigger simulation. Every event is weighted with the kinematic weight and the FLT efficiency. In the reconstruction, the same cuts are applied as for events from the real data. After all selection steps, a sample of approximately 17,500 events remains.

In addition to multiple scattering, the detector resolution is reduced by misalignment of the detector. As an example, the width of the  $J/\psi$  peak in the invariant mass spectrum in the real data is approximately  $40 \text{ MeV}/c^2$  while it amounts to  $28 \text{ MeV}/c^2$  in the MC simulation. Therefore, a safety margin is incorporated in the choice of the bin sizes. The detector resolutions in the momentum-related variables  $x_F$ ,  $p_T$ , and  $y$  are depicted in Fig. 4.9. The resolutions are shown in two representations: by the difference between the true and the reconstructed values of the variable in an event and by the correlation between the true and the reconstructed values. For both methods, no matching between true and reconstructed tracks is required.

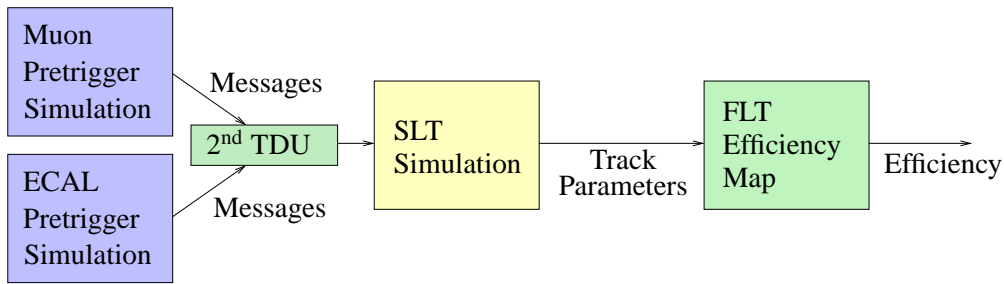


**Figure 4.7:** Sketch of the trigger simulation chain. The messages from the pretrigger simulations are collected in the second Trigger Decision Unit (2<sup>nd</sup> TDU) and transferred to the simulation of the SLT. A weight obtained from the FLT efficiency map is assigned to accepted events. Due to the trigger algorithm, the order of the FLT and the SLT can be exchanged.

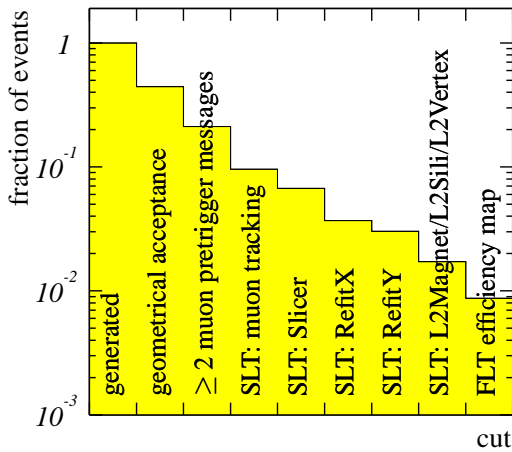


**Figure 4.8:** Efficiencies of the trigger simulation steps. The cuts are applied sequentially from left to right. The graph shows the fraction of events which satisfy a given cut in the trigger simulation chain. The figure is based on approximately 3 million generated MC events for the wire combination I112 in the calibration period of November 2002.

Two different binnings are used in the analysis. For the analysis of differential distributions, small bin sizes (referred to as “binning I” in the following) are required to resolve the details of the shape of the distributions. Larger bins (“binning II”) are used in the analysis of nuclear effects to improve the precision of the measurement of the  $J/\psi$  yield and efficiency ratios. A comparison of the resolutions and the bin sizes shows that the minimum bin sizes are larger than the full width at half-maximum (FWHM) of the resolutions at least by a factor of 6. The purity of the bins, i.e. the fraction of reconstructed events in a bin which have been generated in the same bin is larger than 77% for binning I and larger than 91% for binning II. The fraction of generated events in a bin which are reconstructed in the same bin is a measure of the stability of the reconstruction. It is greater than 81% for binning I and greater than 88% for binning II. A summary of the resolutions, minimum bin sizes, purities, and stabilities is presented in Table 4.8.

**Table 4.8:** Detector resolutions in the kinematic variables. The full width at half-maximum (FWHM) of the difference between the reconstructed and the true values of the variable is used as a measure of the resolution. The resolution is compared with the minimum bin size used in analyzing the variables, and the minimum purities and stabilities of the bins are evaluated. Binning I corresponds to the binning used for the analysis of differential distributions, while binning II is used for the analysis of nuclear effects.

Var.	Resolution	Binning I			Binning II		
		Min. Size	Purity	Stability	Min. Size	Purity	Stability
$x_F$	0.0016	0.02	0.77	0.82	0.05	0.95	0.97
$p_T$	0.038 GeV/ $c$	0.25 GeV/ $c$	0.81	0.81	0.5 GeV/ $c$	0.92	0.91
$y$	0.004	0.25	0.86	0.97	0.25	0.97	0.98
$\cos \theta_{GJ}$	0.019	0.125	0.91	0.88	0.125	0.91	0.88
$\phi_{GJ}$	0.02 rad	0.628 rad	0.93	0.94	0.628 rad	0.93	0.94

#### 4.3.5 Comparison of Data and Monte Carlo Simulation

In this analysis, the MC simulation is used to correct the raw data by efficiencies and ratios of efficiencies of the detector. The standard procedure to perform an efficiency correction is a one-dimensional bin-by-bin correction, in which every bin of the measured kinematic distribution is corrected by the total efficiency for the bin. If the bin sizes are chosen such that the kinematic distributions do not vary strongly within a bin, the total efficiency is independent of the actual shape of the generated distribution, i.e. of the MC model employed to generate the events. However, a bin-by-bin correction only performed in a single kinematic variable implies integrating the efficiencies of all other variables. The procedure of bin-by-bin corrections is therefore only valid if either the efficiencies of the other variables are uncorrelated to the variable under consideration or their shapes and correlations are properly modelled in the MC simulation.

In order to check these preconditions, the kinematic distributions obtained from the MC simulation are compared to corresponding kinematic distributions in the real data. The kinematic distributions are compared for data sets from two different types of wire combinations. A data set with two wires from the same target station (I1B1) is compared to another data set, in which wires from both target stations are utilized (I1I2). For the study, 3,000,000 generated events from the wire configurations I1I2 and 2,000,000 generated events from I1B1, both from the calibration period of November 2002, are examined. MC-simulated events which pass the trigger simulation are weighted with the kinematic weight and the FLT efficiency. To select  $J/\psi$  in the MC sample, the same criteria as in the real data are applied. The study comprises comparisons of properties of the muons from  $J/\psi$  decays and of the  $J/\psi$  reconstructed from the muons.

### Kinematic Distributions of Muons From $J/\psi$ Decays

The kinematic distributions of muons from  $J/\psi$  decays are determined by a statistical method. Due to the background from random combinations of muons, the assignment of muons to a  $J/\psi$  is not always possible on an event-by-event basis. Therefore, the combinatorial background is subtracted via sideband subtraction. Events are sorted into a signal and a sideband sample by the dimuon invariant mass, using the measured  $J/\psi$  mass and width of approximately  $\mu = 3.09 \text{ GeV}/c^2$  and  $\sigma = 40 \text{ MeV}/c^2$ . Events in the mass interval of  $\mu \pm 3\sigma$  are considered signal events. Sideband events contain muon pairs with invariant masses of  $[\mu - 10\sigma; \mu - 5\sigma]$  and  $[\mu + 5\sigma; \mu + 10\sigma]$ . All distributions of the kinematic variable are filled for both, the signal and the sideband intervals. The numbers of events in the sidebands are scaled to the expected number of background events in the signal interval using the background slope from a combined fit to signal and background in the invariant mass spectrum. The scaled sideband distributions are subtracted from the signal distributions. For the comparison of the kinematic distributions in the real data and the MC simulation, the MC distributions are scaled to the integral of the distributions obtained from the data.

Representative examples of the comparison between the data and the MC simulation are depicted in Fig 4.10. The figure shows the momenta of muons from both wires of the wire combination I1I2 and from the wire Inner I of the wire combination I1B1. The overall agreement between the data and the MC simulation is good. However, several discrepancies are observed: For the wire combination I1I2, the MC description of muons from the wire Inner II is better than the description of muons from Inner I. Furthermore, a momentum asymmetry between the positively charged and the negatively charged muon is observed for Inner II, and the momenta are underestimated by the MC in the case of Inner I. In general, the description of the wire combination I1B1 is better than the description of I1I2. The momenta and transverse momenta of muons originating from the wire Inner I—used in both combinations—are better reproduced by the MC simulation of I1B1, and a smaller momentum asymmetry is observed. Since both wires combinations are combinations of a carbon and a tungsten wire, the track multiplicities and the levels of background are similar. Therefore, the observed discrepancies between the data and the MC simulation can only originate from imperfections in the SLT simulation, the only part of the trigger chain in which a target wire is treated differently if used in a different wire combination. Systematic uncertainties introduced by the SLT simulation are discussed in Section 6.1.3. The full result of the comparison of the muon kinematics in the data and the MC simulation is documented in Appendix D, Figs. D.1 and D.2.

### Kinematic Distributions of $J/\psi$

In addition to the muon kinematics, the kinematic properties of the  $J/\psi$  reconstructed from muon pairs are compared for the data and the MC simulation. To reconstruct the kinematic distributions, the data set is separated into intervals of the kinematic variables. The invariant mass spectrum is fitted for each of the intervals individually. Both the number of reconstructed  $J/\psi$  per interval and the statistical uncertainty of the number of  $J/\psi$  are extracted from the fit.

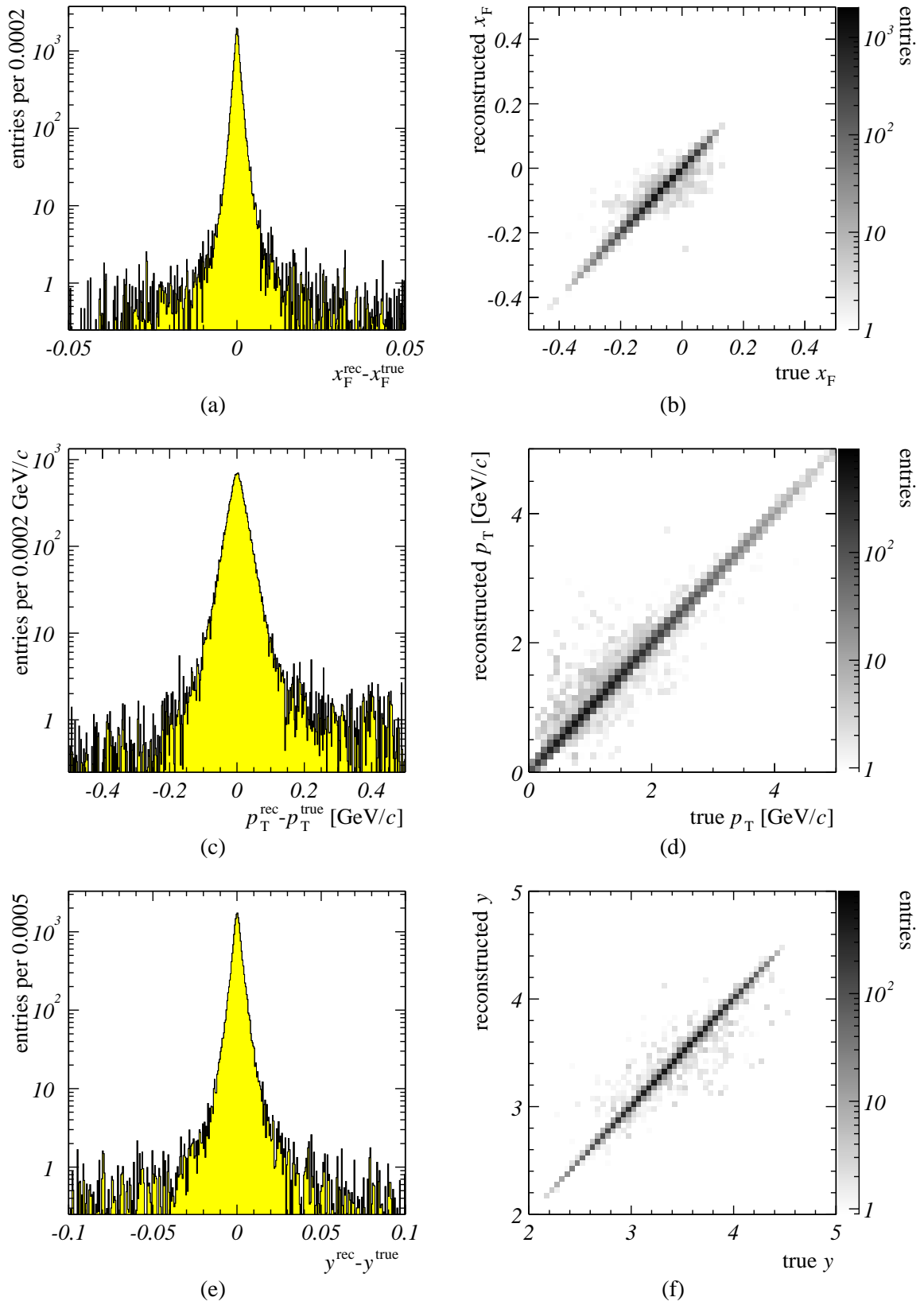


**Figure 4.9:** Detector resolutions in the kinematic variables  $x_F$ ,  $p_T$ , and  $y$ . In subfigures (a), (c), and (e), the differences of the reconstructed and the true values are shown. Subfigures (b), (d), and (f) show the correlation between the true and the reconstructed values. A logarithmic scale is used for the number of entries in all plots.

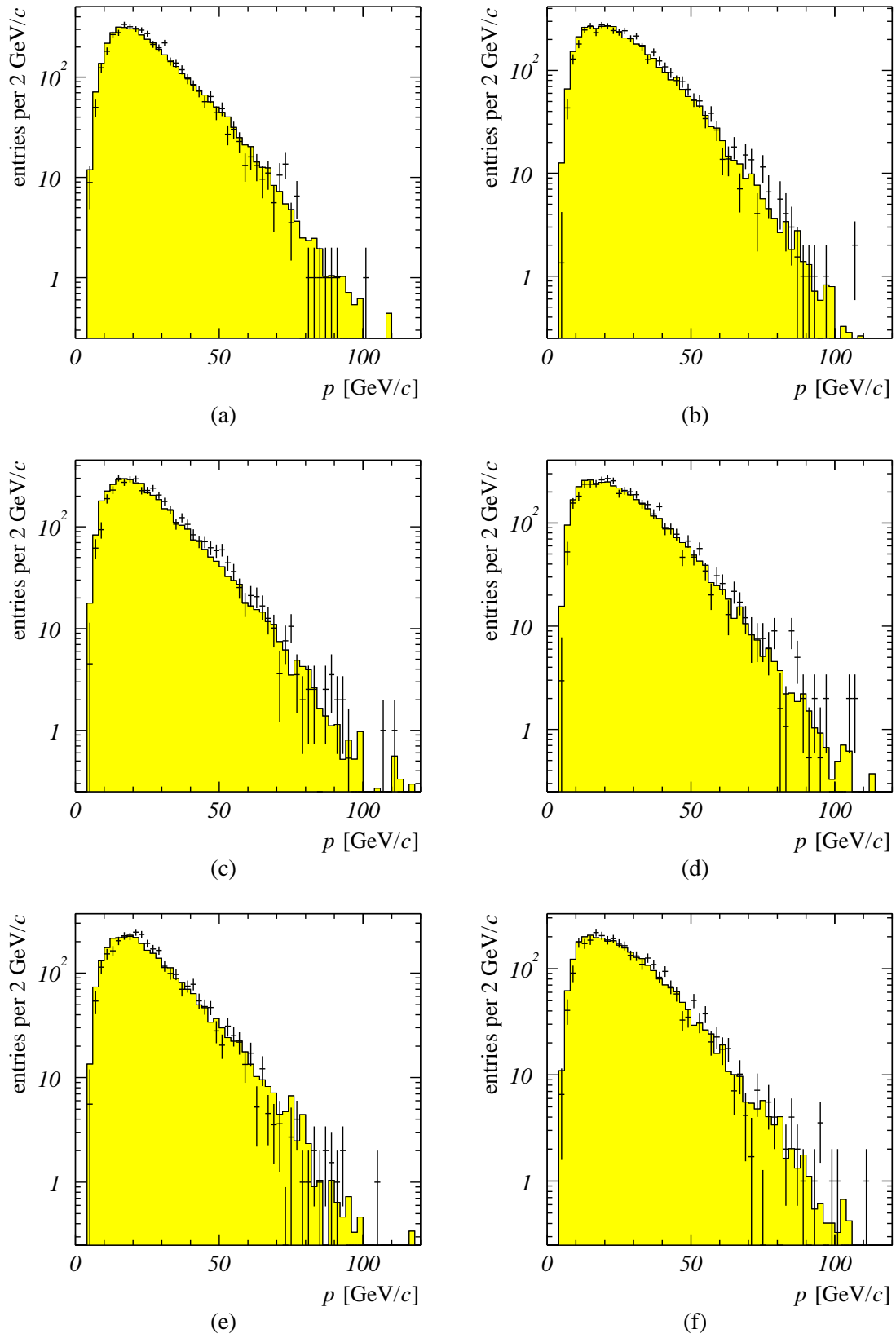


**Figure 4.10:** Comparison of the momenta of muons from  $J/\psi$  decays in the data (points) and the MC simulation (histograms). (a)–(b) Momenta of  $\mu^+$  and  $\mu^-$  from the wire Inner II in the wire combination I1I2. (c)–(d) Momenta of  $\mu^+$  and  $\mu^-$  from the wire Inner I in I1I2. (e)–(f) Momenta of  $\mu^+$  and  $\mu^-$  from the wire Inner I in I1B1. The background is removed via sideband subtraction, and the MC distributions are scaled to the integral of the data distributions.

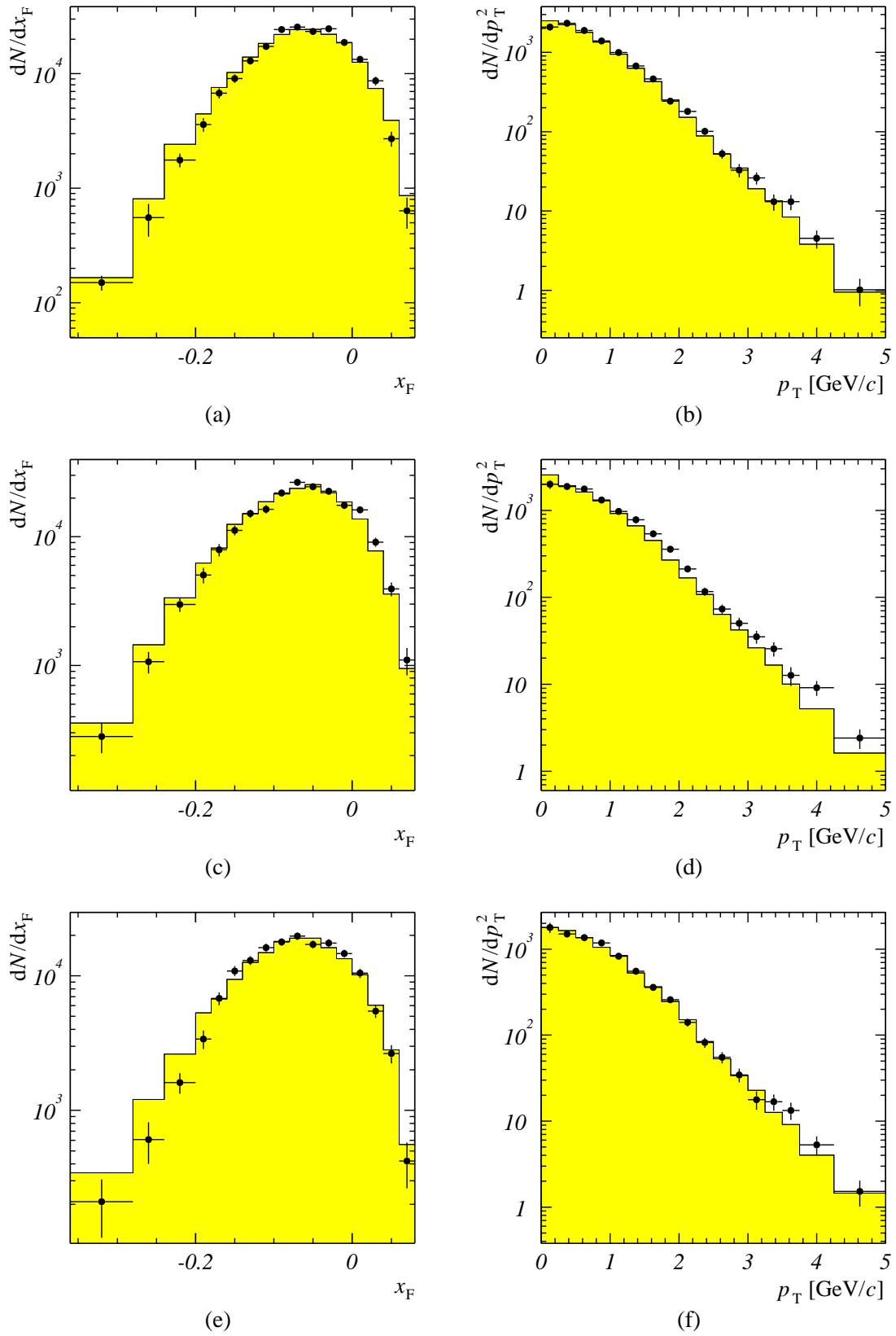


**Figure 4.11:** Comparison of  $J/\psi$  kinematic distributions in the data (points) and the MC simulation (histograms). (a)–(b)  $x_F$  and  $p_T$  distributions of  $J/\psi$  from the wire Inner II in the wire combination I1I2. (c)–(d)  $x_F$  and  $p_T$  distributions of  $J/\psi$  from the wire Inner I in I1I2. (e)–(f)  $x_F$  and  $p_T$  distributions of  $J/\psi$  from the wire Inner I in I1B1. The MC distributions are scaled to the integral of the data distributions.



The study is performed for two data sets recorded in November 2002 with the wire combinations I1I2 and I1B1. For both data sets, the description of the angular variables in the MC simulation is in good agreement with the real data. Several discrepancies are observed for the momentum-related variables. This is illustrated by comparing the  $x_F$  and  $p_T$  distributions from the wires Inner I and Inner II from I1I2 and from the wire Inner I from the wire combination I1B1, as shown in Fig. 4.11. The differences in the quality of the muon momentum description between I1I2 and I1B1 translate into differences in the description of  $x_F$  and  $p_T$ . The agreement between data and MC simulation is satisfactory for I1B1, except for the most positive and the most negative bins in  $x_F$ . However, larger discrepancies are observed for I1I2. Both, the  $x_F$  and the  $p_T$  distributions, are underestimated by the MC simulation, reflecting the underestimated muon momenta. While the observed differences are most probably due to imperfections in the MC simulation, a part of the discrepancies could also be attributed to the influence of nuclear effects. The  $x_F$  distribution in the MC simulation is based on a NRQCD prediction which does not include nuclear effects. A complete documentation of the results of the comparison can be found in Appendix D, Figs. D.3 and D.4.

### 4.3.6 Efficiency Determination

In order to extract the true differential distributions from the data, the raw distributions have to be corrected by the total efficiency  $\varepsilon$  to detect a particle in a given kinematic interval. The total efficiency is extracted from the MC simulation of the HERA–B detector and trigger by calculating the ratio of reconstructed to generated  $J/\psi$ , usually as a function of a single kinematic variable  $u$ :

$$\varepsilon(u) = \frac{N^{\text{rec}}(u)}{N^{\text{gen}}(u)}, \quad \text{where } u = x_F, p_T, \dots \quad (4.10)$$

The total efficiency can be separated into several contributions. The geometrical acceptance of the detector and trigger is defined as the fraction of particles generated in the MC simulation which leaves detectable hits in the detector. The number of detected hits in the detector is influenced by the hit efficiencies of the detector cells and the masking of dead channels. Further contributions to the total efficiency originate from the reconstruction and the trigger algorithms. An example of the interplay of all these factors for the muon pretrigger is given in Section A.3.1. In addition, two types of weights are used in the HERA–B MC simulation. The number of generated events is weighted with the kinematic weight to correct the  $x_F$  and  $p_T$  distributions. In addition, the number of events reconstructed and accepted by the trigger simulation,  $N^{\text{trig}}$ , is reduced by the FLT efficiency  $\varepsilon^{\text{FLT}}$ . The total efficiency is thus given by:

$$\varepsilon(u) = \frac{w(x_F, p_T) \varepsilon^{\text{FLT}}(x_F, p_T, \dots) N^{\text{trig}}(u)}{w(x_F, p_T) N^{\text{gen}}(u)}, \quad \text{where } u = x_F, p_T, \dots \quad (4.11)$$

The quantity  $\varepsilon^{\text{FLT}}(x_F, p_T, \dots) N^{\text{trig}}(u)$ , i.e. the reconstructed number of  $J/\psi$  in the MC simulation as a function of  $u$  is determined by applying the same selection criteria which are used to select  $J/\psi$  candidates in the data to the MC events. The dependence of  $\varepsilon^{\text{FLT}}(x_F, p_T, \dots) N^{\text{trig}}(u)$  on  $u$  is obtained from fits of the invariant mass spectra in

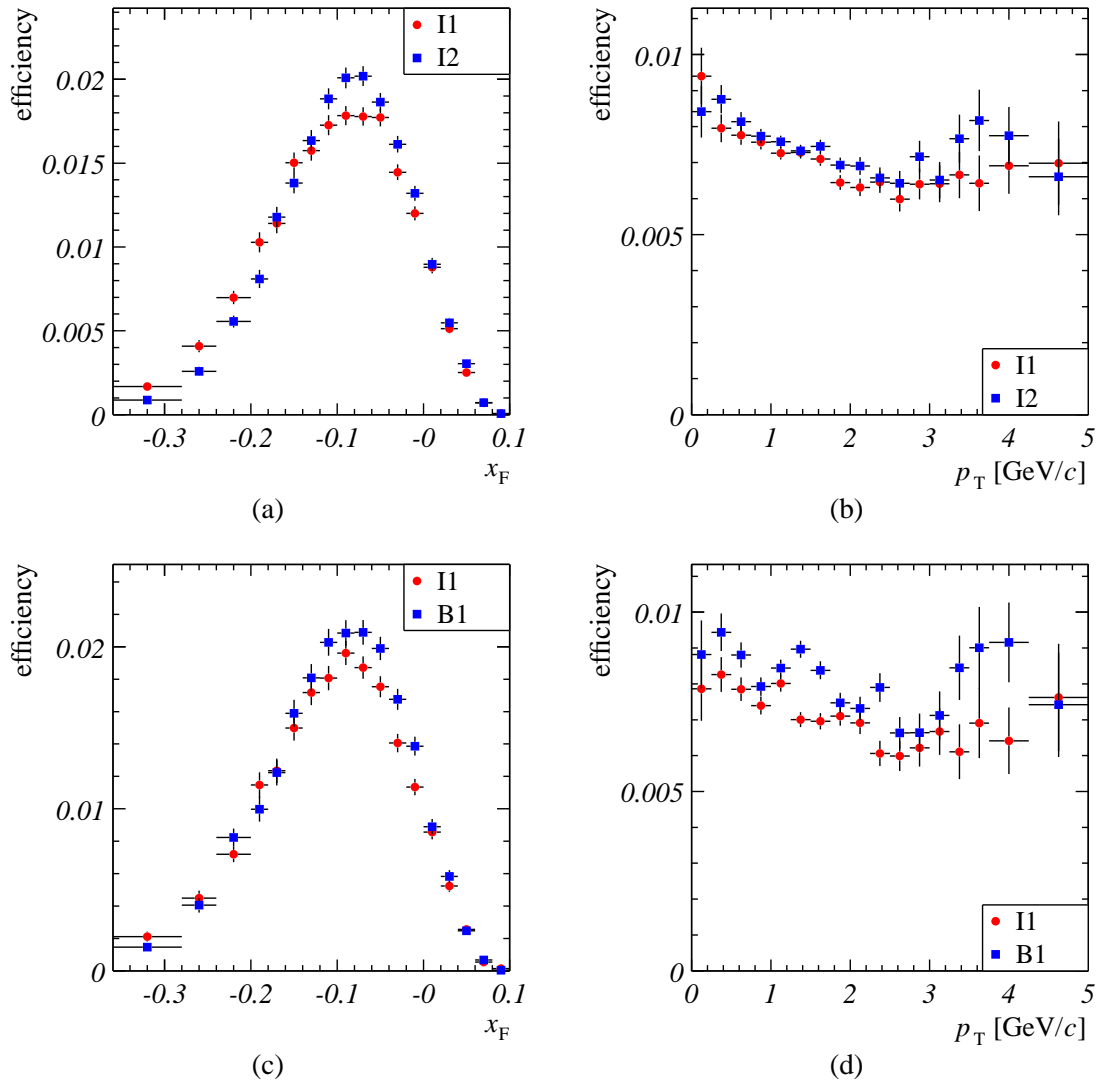


**Figure 4.12:** Total efficiency as a function of  $x_F$  and  $p_T$  for different wire combinations from the calibration period of November 2002. (a)–(b) Wire combination I1I2. (c)–(d) Wire combination I1B1.

intervals of  $u$ . The fits are performed as maximum likelihood fits according to the shape function given in Eq. (4.5).

The total efficiency as a function of the kinematic variables  $x_F$  and  $p_T$  for the wire combinations I1I2 and I1B1 in the calibration period of November 2002 are shown in Fig. 4.12. The shapes of both, the  $x_F$  and the  $p_T$  efficiency distributions, are similar in the wire combination I1B1. For I1I2, the efficiency of the wire Inner II is suppressed for large negative  $x_F$ . This effect is connected to a target constraint in the SLT algorithm and will be discussed in Section 6.1.3. A summary of the total efficiencies for all kinematic variables under study is given in Appendix D, Figs. D.5 to D.6.

## 4.4 Differential Distributions

Insight in the details of the process of charmonium production is gained by analyzing the  $J/\psi$  kinematics. The observables connected with the  $J/\psi$  kinematics are the differential production cross sections, i.e. the  $J/\psi$  yield per luminosity as a function of the kinematic variables. For the analysis of nuclear effects in  $J/\psi$  production, only ratios of the differential cross sections are relevant. Therefore, the differential spectra are presented as intermediate results without normalization to the luminosity and including statistical uncertainties only.

The analysis is restricted to all two-wire data samples since only for these samples, MC events simulated according to the current best knowledge of the detector and trigger chain are available at the time of writing this thesis. A detailed comparison of the differential distributions with theoretical predictions and previous experiments and a discussion of the systematic uncertainties of the differential distributions using a previous version of the MC simulation code is contained in [Vuk04]. Many of the systematic effects described there have entered the improved MC simulation which is employed for this analysis.

### 4.4.1 Analysis Method

The differential distributions are studied separately for each of the two target wires as a function of the momentum-related variables  $x_F$ ,  $p_T$ , and  $y$  and the variables  $\cos\theta_{GJ}$  and  $\phi_{GJ}$ , which describe the angular distributions of muons from  $J/\psi$  decays. In order to resolve the fine-structure of the differential distributions, the small bin sizes of binning I are utilized. The analysis of differential distributions includes the determination of the “raw” differential spectra, efficiency corrections of the raw spectra and fits to the corrected spectra. To obtain differential distributions for the entire data-taking period, the corrected spectra measured in all calibration periods are combined.

### Raw Kinematic Distributions and Efficiency Corrections

The raw  $J/\psi$  spectra are obtained from separate fits to the invariant mass spectra in intervals of the kinematic variables using the shape function (4.5). In order not to be influenced by non-converging fits due to low statistics, bins in which the invariant mass spectrum contains less than 30 events in the range of  $2.9\text{--}3.2\text{ GeV}/c^2$  are excluded from the analysis. For every bin  $i$  of the distribution, the number  $N_i$  of  $J/\psi$  obtained from the fit is corrected by the efficiency  $\varepsilon_i$  of the bin obtained from the MC simulation. The range of bins, for which efficiency corrections are performed, is restricted to bins in which the efficiencies are larger than 0.1% for at least six of the 12 MC configurations. The efficiencies in the excluded bins are smaller than the average efficiency by more than a factor of 10. Systematic uncertainties in the efficiency determination on the  $10^{-3}$  level in these bins result into large correction factors with uncertainties as large as 100%. Since the binning involves variable bin widths, the raw spectra are corrected by the widths  $W_i$  of the bins in addition. For a variable  $u$ , the differential distribution in a bin  $u_i$  is therefore reported as

$$\left. \frac{dN}{du} \right|_{u_i} = \frac{N_i}{\varepsilon_i W_i}. \quad (4.12)$$

Note that all differential distributions presented in this chapter do not include absolute normalizations, since no corrections for the luminosities and for dead-times of the detector and the DAQ system are applied.

A test of the stability of the invariant mass fit as a function of the kinematic variables is presented in Fig 4.13, in which the fitted  $J/\psi$  masses and widths are plotted as functions of  $x_F$  and  $p_T$ , together with the fitted background slope. In the MC simulation (not shown), an increase in the mass of approximately 4% per unit of  $x_F$  and an increase of the width of approximately 2% per unit of  $x_F$  are observed. These shifts are caused by the decreasing momentum resolution with increasing muon momenta. As a function of  $p_T$ , the MC-simulated masses and widths are approximately constant. The fitted  $J/\psi$  masses and widths in the real data do not show these clear trends. As a function of  $x_F$ , the mass is stable but approximately 0.1% lower than the value published by the Particle Data Group of  $(3096.919 \pm 0.011) \text{ MeV}/c^2$  [Eid04]. An increase in the  $J/\psi$  mass by 0.2% per  $\text{GeV}/c$  is observed for increasing  $p_T$ , and the  $J/\psi$  width is approximately constant as a function of both,  $x_F$  and  $p_T$ . These results show that the resolution-related variations of the  $J/\psi$  mass and width are hidden by a larger variation, most probably due to the detector alignment. The influence of the variations of the fitted  $J/\psi$  mass and width on the ratio of particle yields is discussed in Section 6.1.3.

### Combination of Data Sets

The detector conditions and thus the efficiencies vary for the different calibration periods. Therefore, the differential distributions are determined separately for each calibration period. The differential distributions determined for the different calibration periods are combined to the final result in two ways. In a first approach, the corrected differential spectra of all calibration periods are added, and the shape parameters are extracted from a global fit to the sum of all spectra. In this approach, stable fits are obtained due to the large statistics of the summed spectra. On the other hand, systematic differences between the calibration periods are diluted by summing all spectra. Alternatively, the shape parameters obtained from fits to the spectra of single calibration periods are combined by a weighted average to derive the final shape parameters. This method allows to identify the differences in the results from single periods. However, some fits to single-period spectra suffer from instabilities due to the low statistics. For both approaches, results from the two wires in carbon-tungsten combinations are treated separately. In the carbon-carbon combination B1I2, both wires are assigned to the carbon result, and results from the titanium wire Below II in data taken with the combination B1B2 in October 2002 are ignored.

### 4.4.2 Results and Discussion

The final differential distributions are obtained by a combination of data from all calibration periods. The results and their uncertainties are discussed and compared to the results of previous experiments and theoretical models. The results obtained by adding the differential distributions are shown in Fig. 4.14. A summary of the fit results to single calibration periods together with the weighted average of the fit results can be found in Fig. 4.15. In Tables 4.9 and 4.10, the global fit results for carbon and tungsten targets

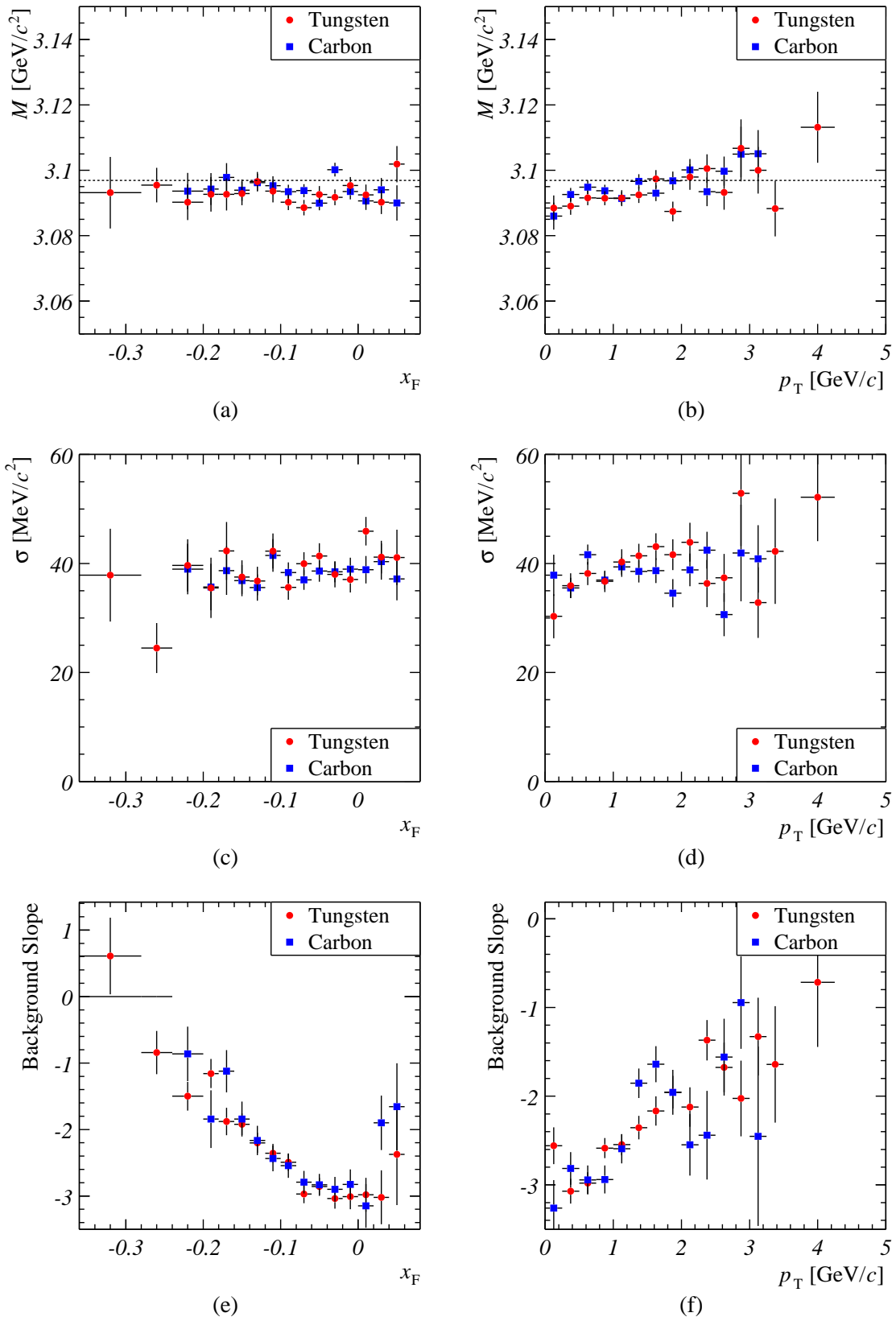


**Figure 4.13:** Mass and width of  $J/\psi$  signal, and background slope as a function of  $x_F$  and  $p_T$ . The figures are based on data taken with the wire configuration I112 from the calibration period of November 2002. The value of the  $J/\psi$  mass published by the Particle Data Group [Eid04] is indicated by the dashed lines. Bins with less than 30 events in the invariant mass range of 2.9–3.2 GeV/ $c^2$  are excluded.

are listed. The differential distributions for all data sets are documented in Appendix D, Figs. D.7 to D.11, and Tables D.1 to D.4. Note that all results are preliminary in the sense that they do not include detailed studies of systematic uncertainties.

### Feynman-x

The differential distribution as a function of  $x_F$  has been measured by many experiments. However, the experiments cover different ranges in  $x_F$ , and the experimental results on the  $x_F$  shape bear large uncertainties. Proton-proton collisions are symmetric in the parton momentum fractions  $x_1$  of the beam proton and  $x_2$  of the proton in the target nucleus. Therefore, parametrizations of the shape of the differential distribution as a function of  $x_F = x_1 - x_2$  are symmetric in  $x_F$ . The most common parametrization found in the literature is (see e.g. [Sch95])

$$\frac{dN}{dx_F} \propto (1 - |x_F|)^C. \quad (4.13)$$

However, this shape is non-differentiable at  $x_F = 0$ , and it describes neither the HERA-B data nor theoretical predictions well [Vuk04]. Therefore, the  $x_F$  shape is not compared to Eq. (4.13), but rather to two other parametrizations of the  $x_F$  distribution. The first parametrization has been proposed by the E705 collaboration [Ant92]. It is motivated by the asymptotic  $(1 - x_{1,2})^C$  behavior of the parton distribution functions of the colliding partons:

$$\frac{dN}{dx_F} \propto \frac{[(1 - x_1)(1 - x_2)]^C}{x_1 + x_2}, \text{ where } x_{1,2} = \frac{1}{2} \left( \sqrt{x_F^2 + 4M^2/s} \pm x_F \right). \quad (4.14)$$

As an alternative test of the  $x_F$  distribution, the shape is compared to the NRQCD prediction of the  $x_F$  shape for 920 GeV/ $c$  proton-proton collisions [Vog04]. For the fit, the same parametrization is used as for the reweighting of the  $x_F$  shape in the MC simulation. The  $x_F$  shape is depicted in Fig. 3.4.

A comparison of the measured  $x_F$  shape shows poor agreement both with the NRQCD prediction and E705 parametrizations of the shape. The deviations from a symmetric shape are especially large for positive  $x_F$ . The kinematic regime of positive  $x_F$  is populated with events in which both muons are reconstructed in the inner part of the HERA-B spectrometer. In the inner part, the chamber occupancies are the largest, and the detector and trigger performance is not well-reproduced in the MC.

These discrepancies have already been reduced by introducing the fiducial cuts on the inner edges of the detector. However, the efficiencies for the positive  $x_F$  bins are also reduced by the fiducial cuts, leading to large uncertainties in the efficiency correction. Therefore, the confidence in fits to the  $x_F$  spectrum is improved if only the part of the spectrum with  $x_F < 0$  is fitted.

Due to the limited statistics, most fits to single calibration periods are rather unstable. Therefore, the method of a global fit to the  $x_F$  spectrum is chosen to extract the shape parameter  $C$ . The fit is restricted to  $x_F < 0$  to circumvent the uncertainty for positive  $x_F$ . The resulting value of the shape parameter is

$$C = \begin{cases} 4.78 \pm 0.16(\text{stat.}) & \text{for carbon targets,} \\ 5.22 \pm 0.21(\text{stat.}) & \text{for tungsten targets.} \end{cases} \quad (4.15)$$

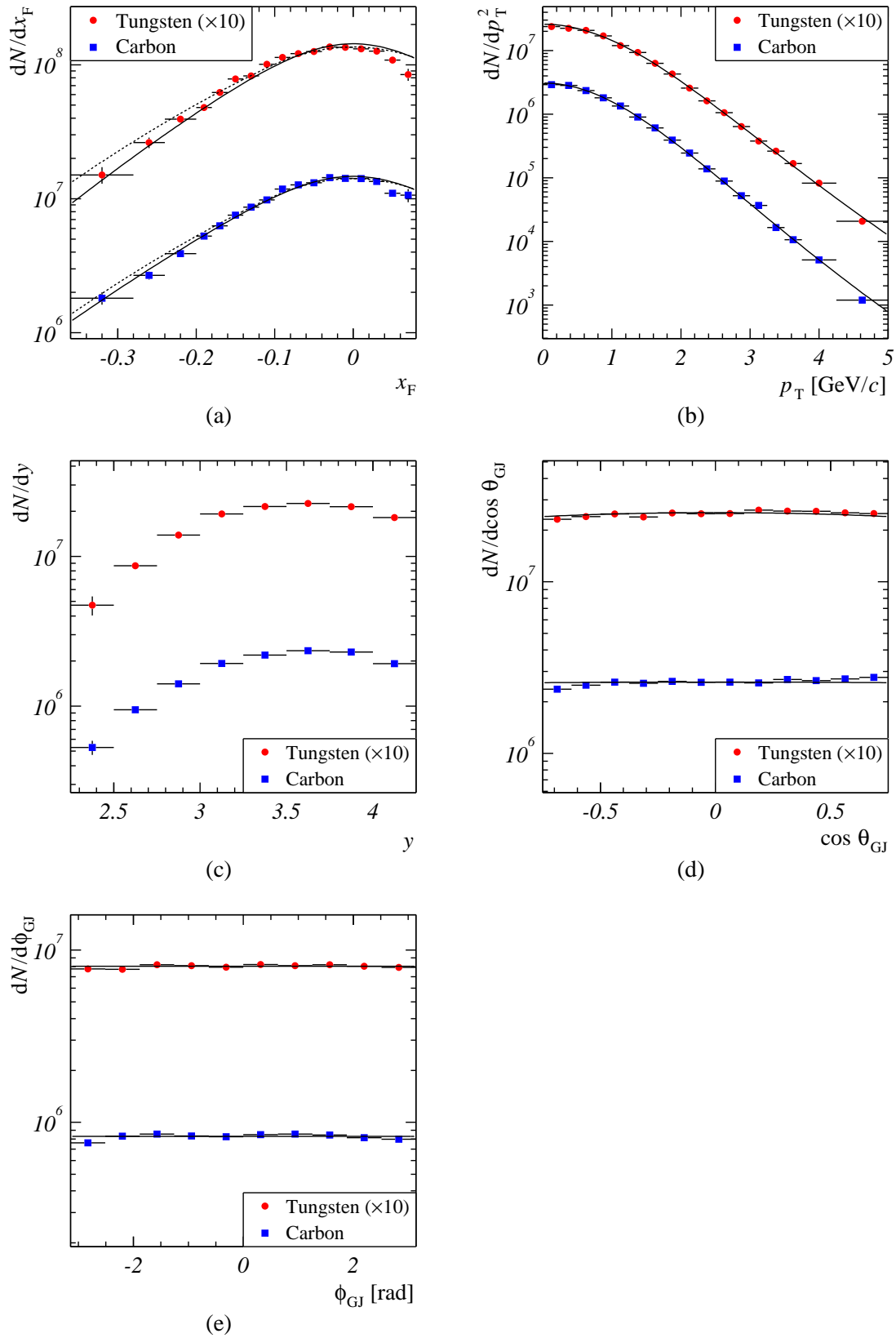


**Figure 4.14:**  $J/\psi$  differential distributions summed over all data sets. (a)  $x_F$  distributions fitted with a parametrization of the E705 fit (solid line) and the NRQCD prediction (dashed line). (b) Fit to  $p_T$  distributions. (c)  $y$  distributions. (d) Fit to  $\cos \theta_{GJ}$  distribution. (e) Fit to  $\phi_{GJ}$  distribution. All distributions obtained from tungsten wires are scaled by a factor of 10. The fit results are summarized in Tables 4.9 and 4.10.

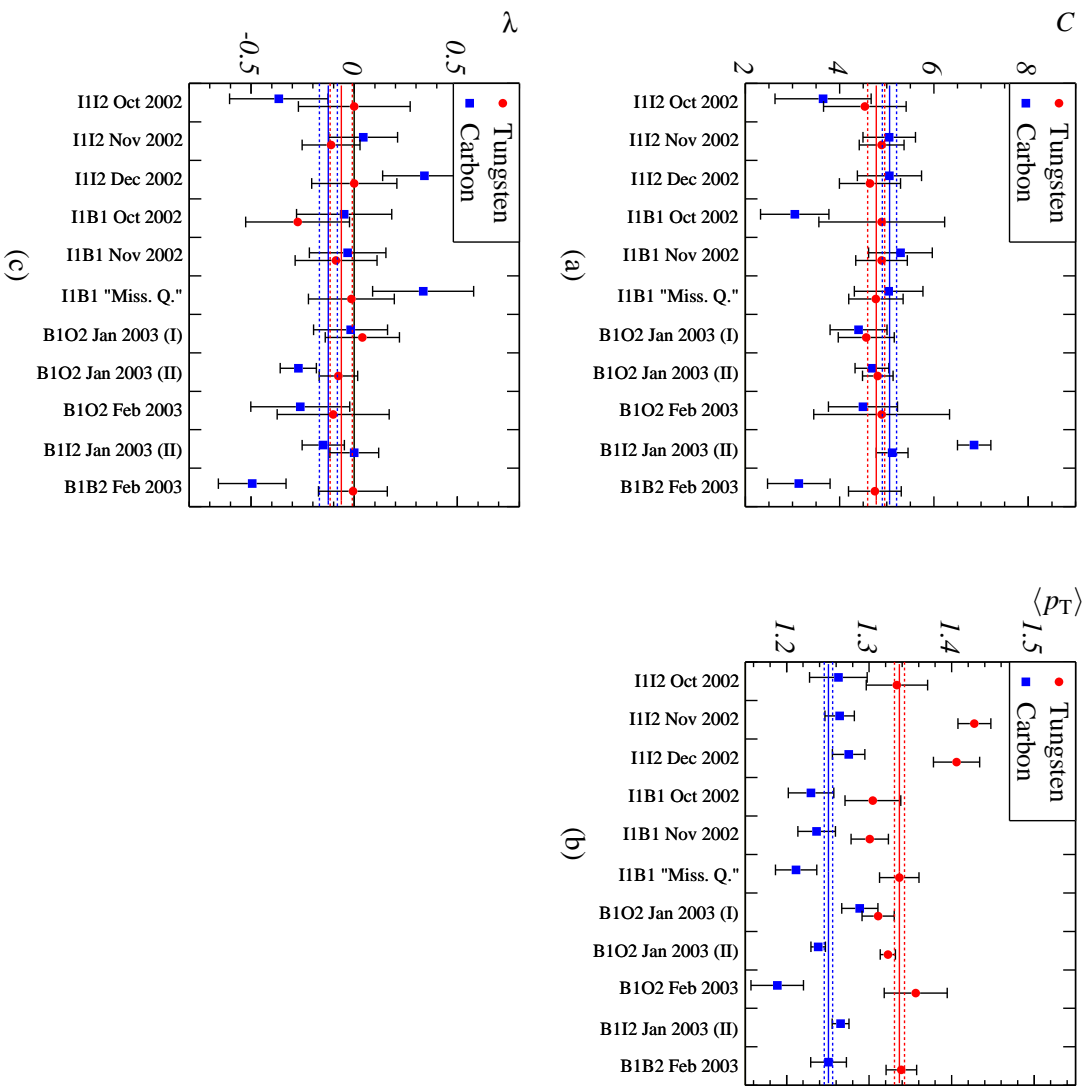


**Figure 4.15:** Fit parameters for the  $x_F$ ,  $p_T$ , and  $\cos \theta_{GJ}$  distributions for all data samples. The fit values and their uncertainties are plotted separately for the carbon and the tungsten wires of each data sample. (a) Parameter C of E705 fit. (b) Average transverse momentum. (c) Polarization parameter  $\lambda$ . The solid and dashed horizontal lines indicate the weighted mean of the parameter values and the uncertainty of the weighted mean. “Miss. Q.” refers to the calibration period “Missing Quadrant”. The fit results are summarized in Tables 4.9 and 4.10.



**Table 4.9:** Fit parameters of  $J/\psi$  differential distributions for carbon targets. The different fit methods are explained in the text.

Variable	Parameter	Method	Value	$\chi^2/n_{\text{dof}}$
$x_F$	$C$ (E705)	Global Fit	$4.65 \pm 0.15$	58.3/15
$x_F$	$C$ (E705)	Global Fit ( $x_F < 0$ )	$4.78 \pm 0.16$	26.7/11
$x_F$	$C$ (E705)	Weighted Average	$4.77 \pm 0.18$	46.9/11
$x_F$	Norm (NRQCD)	Global Fit	–	76.9/16
$p_T$	$\langle p_T \rangle$ [GeV/ $c$ ]	Global Fit	$1.2443 \pm 0.0044$	33.2/15
$p_T$	$\langle p_T \rangle$ [GeV/ $c$ ]	Weighted Average	$1.2506 \pm 0.0051$	16.8/1
$p_T$	$\langle p_T \rangle$ [GeV/ $c$ ]	Histogram Mean	$1.2437 \pm 0.0032$	–
$\cos \theta_{GJ}$	$\lambda$	Global Fit	$-0.015 \pm 0.048$	18.9/10
$\cos \theta_{GJ}$	$\lambda$	Weighted Average	$-0.125 \pm 0.044$	20.9/11
$\phi_{GJ}$	Norm	Global Fit	–	26.2/9

**Table 4.10:** Fit parameters of  $J/\psi$  differential distributions for tungsten targets. The different fit methods are explained in the text.

Variable	Parameter	Method	Value	$\chi^2/n_{\text{dof}}$
$x_F$	$C$ (E705)	Global Fit	$5.44 \pm 0.21$	110.6/15
$x_F$	$C$ (E705)	Global Fit ( $x_F < 0$ )	$5.22 \pm 0.21$	46.3/11
$x_F$	$C$ (E705)	Weighted Average	$5.06 \pm 0.16$	0.4/8
$x_F$	Norm (NRQCD)	Global Fit	–	65.8/16
$p_T$	$\langle p_T \rangle$ [GeV/ $c$ ]	Global Fit	$1.3394 \pm 0.0058$	30.8/15
$p_T$	$\langle p_T \rangle$ [GeV/ $c$ ]	Weighted Average	$1.3367 \pm 0.0061$	34.4/9
$p_T$	$\langle p_T \rangle$ [GeV/ $c$ ]	Histogram Mean	$1.3348 \pm 0.0039$	–
$\cos \theta_{GJ}$	$\lambda$	Global Fit	$-0.092 \pm 0.055$	14.0/10
$\cos \theta_{GJ}$	$\lambda$	Weighted Average	$-0.063 \pm 0.054$	1.5/9
$\phi_{GJ}$	Norm	Global Fit	–	7.8/9

The maximum deviation of the three methods to extract  $C$  is taken as a rough estimate of the systematic uncertainty of  $C$  of  $\sigma_C = 0.8$ . Within two standard deviations of the statistical uncertainty, the fit values are comparable with each other and suggest that the  $x_F$  shape is not influenced significantly by effects related to the target material. However, due to the large uncertainties, no definite conclusions can be drawn.

If the  $x_F$  shape is compared to the results of other measurements, no clear picture emerges. The result on the  $x_F$  shape from the E705 experiment at  $\sqrt{s} = 23.8$  GeV of  $C = 4.8 \pm 0.3$  [Ant92] compares well with the result obtained in this analysis, suggesting that the parameter  $C$  is independent of the collision energy. However, the E789 result at  $\sqrt{s} = 38.3$  GeV [Sch95] is not well-described by the E705 parametrization. If the  $x_F$  shape measured by E789 is fitted with the E705 parametrization, a value of  $C = 7.79 \pm 0.50$  is obtained with a  $\chi^2$  probability of 0.0002.

### Transverse Momentum

Previous measurements of the transverse momentum distribution showed the effect of transverse momentum broadening, i.e. the increase of the average transverse momentum with increasing beam energy and atomic mass number. The HERA-B measurement of the transverse momentum broadening extends these measurements to a different beam energy.

The transverse momentum distribution is fitted with a parametrization of the functional form

$$\frac{dN}{dp_T^2} \propto \left[ 1 + \left( \frac{p_T}{p_0} \right)^2 \right]^n. \quad (4.16)$$

For exponents  $n \leq -3/2$ , the average transverse momentum of such a distribution is given by

$$\langle p_T \rangle = \frac{\pi}{2} \frac{\Gamma(-n - \frac{3}{2})}{\Gamma(-n - 1)} p_0, \quad (4.17)$$

where  $\Gamma(x) = \int_0^\infty t^{x-1} e^{-t} dt$  is the gamma function. Due to the strong correlation of the parameters  $p_0$  and  $n$ , a fit in which both parameters are left free leads to unstable results for  $p_0$  and  $n$ . In addition, the energy range covered by HERA-B does not allow to connect the power  $n$  with the asymptotic behavior of the cross sections as a function of  $p_T$ . Following the empirical parametrization suggested in [Kap78], the parameter  $n$  is fixed to  $n = -6$ . In this case, the average transverse momentum is given by  $\langle p_T \rangle = (35\pi/256) p_0$ .

The average transverse momentum can also be extracted without a fit to the spectrum, by calculating the mean value of the histogram of the distribution  $dN/dp_T$ . The histogram contains the transverse momentum range of 0–5 GeV/ $c$ . The uncertainty of the average transverse momentum is obtained from the standard deviation of the distribution, normalized to the square-root of the (uncorrected) total number of events which enter the distribution. The choice of the histogram binning and the cutoff at 5 GeV/ $c$  introduce a bias towards smaller average transverse momenta both for the fit and for the histogram mean value. In a MC simulation,  $1000 \times 10000$  events are generated according to the distribution (4.16) with  $n = -6$ , and the distribution of average transverse momenta is fitted with a Gaussian function. The mean of the Gaussian function

is shifted by approximately  $-0.01 \text{ GeV}/c$  for both approaches, however, the difference between the shifts is less than  $0.003 \text{ GeV}/c$ , smaller than the statistical uncertainties of the measurements.

All three methods of determining the average transverse momentum lead to stable results, which agree within the uncertainties. The fit quality is good for carbon targets. For tungsten targets, the variation of the single-period results is larger due to the larger amount of background, and consequently, the fit quality is deteriorated. To extract the final result on the average transverse momenta, the most stable and model-independent method is chosen, i.e. the method of histogram mean values.

By comparing the average transverse momenta of  $J/\psi$  produced on carbon and tungsten targets, the effect of transverse momentum broadening with increasing atomic mass number of the target is clearly visible:

$$\langle p_T \rangle = \begin{cases} (1.244 \pm 0.003(\text{stat.})) \text{ GeV}/c & \text{for carbon targets,} \\ (1.335 \pm 0.004(\text{stat.})) \text{ GeV}/c & \text{for tungsten targets.} \end{cases} \quad (4.18)$$

As an estimate of the systematic uncertainty of the result, the quadratic sum of largest variation between the three extraction methods and of the bias due to limited  $p_T$  range is chosen:  $\sigma_{\langle p_T \rangle} = 0.01 \text{ GeV}/c$ .

The results agree well with the values obtained in [Vuk04] extracted with the same method:

$$\langle p_T \rangle = \begin{cases} (1.244 \pm 0.003(\text{stat.}) \pm 0.034(\text{syst.})) \text{ GeV}/c & \text{for carbon targets,} \\ (1.336 \pm 0.004(\text{stat.}) \pm 0.041(\text{syst.})) \text{ GeV}/c & \text{for tungsten targets.} \end{cases} \quad (4.19)$$

The HERA-B results on the average transverse momentum at  $\sqrt{s} = 41.6 \text{ GeV}$  are compared to the results of previous experiments at  $\sqrt{s} = 38.3 \text{ GeV}$  and using target materials beryllium, silicon and gold:

$$\langle p_T \rangle = \begin{cases} (1.22 \pm 0.01(\text{stat.})) \text{ GeV}/c & \text{for beryllium targets [Gri00],} \\ (1.20 \pm 0.01(\text{stat.})) \text{ GeV}/c & \text{for silicon targets [Ale97],} \\ (1.289 \pm 0.009(\text{stat./syst.})) \text{ GeV}/c & \text{for gold targets [Sch95].} \end{cases} \quad (4.20)$$

The comparison shows that the average transverse momentum increases with the atomic mass number  $A$  and suggests that the transverse momentum broadening increases slowly with the collision energy. However, it is not known if and how biases in the mean transverse momentum are taken into account in the previous results.

### Angular Distributions and Polarization

Measuring the polarization of charmonia is an important test of charmonium production models. Previous fixed-target experiments report that  $J/\psi$  mesons are essentially unpolarized. This is expected in the CEM, in which all spin information is randomized by soft gluon emission. On the contrary, NRQCD predicts a large transverse  $J/\psi$  polarization.

The distribution of the polar angle  $\cos \theta_{\text{GJ}}$  is connected to the polarization parameter  $\lambda$  of the  $\text{J}/\psi$ :

$$\frac{dN}{d\cos \theta_{\text{GJ}}} \propto 1 + \lambda \cos^2 \theta_{\text{GJ}}, \quad (4.21)$$

where  $\lambda = 1$  stands for transverse polarization and  $\lambda = -1$  corresponds to longitudinal polarization. The polarization parameter is extracted from a fit to the differential distribution  $dN/d\cos \theta_{\text{GJ}}$ . For large positive and negative  $\cos \theta_{\text{GJ}}$ , the total efficiency decreases strongly, and the background is largest. Hence, the ‘‘lever arm’’ and therefore the sensitivity of a fit to the  $\cos \theta_{\text{GJ}}$  distribution is small. In this analysis, the fit to the  $\cos \theta_{\text{GJ}}$  distribution is restricted to  $-0.75 < \cos \theta_{\text{GJ}} < 0.75$ . As a consequence, the statistical uncertainty of the polarization measurement is large.

The distribution of the azimuthal angle  $\phi_{\text{GJ}}$  is assumed to be isotropic. Therefore, the  $\phi_{\text{GJ}}$  distribution is checked if it is constant. The assumption of constant  $\phi_{\text{GJ}}$  is only approximately true. There is a small correlation between the angular variables because the Gottfried-Jackson frame is an approximation of the reference frame of the parton-parton collision. The correlation is assumed to be small compared to the statistical uncertainties of the measurement and therefore neglected.

The differential distribution as a function of  $\phi_{\text{GJ}}$  is compatible with being constant with a  $\chi^2$  probability of 23% for tungsten targets. The agreement is worse for carbon targets (0.02%). The reason for this deviation is most probably due to imperfections of the MC description.

The values of the polarization parameter  $\lambda$  extracted from the global fit and the weighted average of fits to single calibration periods differ by more than one standard deviation. Since fit values of single periods show large fluctuations, the final result on  $\lambda$  is extracted from the global fit to all samples:

$$\lambda = \begin{cases} -0.015 \pm 0.048(\text{stat.}) & \text{for carbon targets,} \\ -0.092 \pm 0.055(\text{stat.}) & \text{for tungsten targets,} \\ -0.047 \pm 0.051(\text{stat.}) & \text{for carbon and tungsten targets.} \end{cases} \quad (4.22)$$

From the largest difference of the results obtained from the different fit methods, a systematic uncertainty of  $\sigma_\lambda = 0.1$  is estimated. All measurements are at variance with the large transverse polarization predicted by NRQCD and are compatible with unpolarized  $\text{J}/\psi$  within two standard deviations. The differential distributions show a small forward-backward asymmetry of 2–3%, while a symmetric distribution is expected for the parity-conserving electromagnetic decay  $\text{J}/\psi \rightarrow \mu^+ \mu^-$ . As in the case of the  $x_{\text{F}}$  and  $\phi_{\text{GJ}}$  distributions, the asymmetry points to small remaining imperfections in the MC description of the HERA–B detector and trigger.

The polarization parameter extracted from this analysis is in agreement with results of previous experiments, which are all compatible with no  $\text{J}/\psi$  polarization:

$$\lambda = \begin{cases} -0.11 \pm 0.12(\text{stat.}) \pm 0.09(\text{syst.}) & \text{for beryllium targets [Gri00],} \\ -0.09 \pm 0.12(\text{stat.}) & \text{for silicon targets [Ale97],} \\ 0.069 \pm 0.004(\text{stat.}) \pm 0.08(\text{syst.}) & \text{for copper targets [Cha03].} \end{cases} \quad (4.23)$$

The measurement presented in this thesis confirms the discrepancy between experimental results and the predictions of NRQCD.

## 4.5 Summary

In this chapter, the extraction of  $J/\psi$  signals in the HERA–B data has been described. As a first step, data-taking runs are selected which provide good data quality. Using a set of standard cuts, events with  $J/\psi$  candidates are collected for further analysis. With additional cuts, a clean sample of  $J/\psi$  events is selected, and every event is assigned to one of the target wires.

The number of  $J/\psi$  as a function of the kinematic variables is determined from fits to the invariant mass spectra. The raw spectra obtained from the fits are corrected with the total efficiencies to detect a  $J/\psi$  in a certain bin of the kinematic distribution. The efficiencies are taken from a detailed MC simulation of the HERA–B detector and trigger. By applying the efficiency correction, the differential distributions for the production of  $J/\psi$  are obtained. The differential distributions are presented as a function of the variables  $x_F$ ,  $p_T$ ,  $y$ ,  $\cos \theta_{GJ}$ , and  $\phi_{GJ}$ . Within the uncertainties, the shape parameters of all differential distributions agree well with previous measurements. The measured  $J/\psi$  polarization favors the CEM and is not within the predictions of NRQCD.



---

# Luminosity and Target Rate Sharing

---

The measurement of nuclear effects in  $J/\psi$  production at HERA-B is based on a measurement of the  $J/\psi$  cross section ratio for two different materials. The ratio of luminosities is one of the ingredients for the determination of the cross section ratio. To reduce the systematic uncertainties of the measurement, data was taken simultaneously with two targets of different materials. The target steering mechanism provided a dynamical adjustment of the sharing of the number of proton-nucleus interactions among the wires. Since the beam conditions and the target calibration varied over time, a precise measurement of the luminosity ratio cannot be obtained from target-related information alone. Therefore, algorithms to determine the luminosity ratio from the data are required.

This chapter commences with a description of the vertex counting method, which is the standard method used by the HERA-B collaboration to extract luminosities and luminosity ratios from the data. In the vertex counting method, the number of interactions at the targets is calculated from the number of reconstructed primary vertices. The chapter is concluded with a detailed study of the systematic uncertainties of the luminosity ratio calculation, including a comparison to a method with different systematic uncertainties, which is based on the average number of reconstructed tracks per event.

## 5.1 Luminosity Measurements at HERA-B

In the HERA-B experiment, the luminosity is measured by counting events which are produced in processes with a known cross section, the “minimum-bias” cross section. The total cross section of proton-nucleus interactions is composed of an elastic and an inelastic contribution. The inelastic cross section can be further divided into a minimum-bias part and a diffractive part. Minimum-bias events can be detected in the acceptance of the HERA-B spectrometer. Most of the diffractive interactions, i.e. interactions in which either the beam or the target particle or both of them remain intact, produce particles which leave the interaction region through the beam-pipe. Therefore, only the minimum-bias part of the cross section is used for the luminosity calculation.

**Table 5.1:** Minimum-bias cross sections  $\sigma^{\text{MB}}$  for carbon and tungsten targets, together with the nuclear suppression parameter  $\alpha^{\text{MB}}$  for a compilation of experimental results (first line) and a preliminary result of a theoretical calculation (second line).

$\sigma^{\text{MB}}$ [mb] (Carbon)	$\sigma^{\text{MB}}$ [mb] (Tungsten)	$\alpha^{\text{MB}}$	Reference
$237.4 \pm 3.4$	$1710 \pm 17$	$0.724 \pm 0.005$	[Car03]
241.7	1575.1	0.687	[Kop04]

The luminosity  $\mathcal{L}$  is determined by counting the number  $N^{\text{MB}}$  of minimum-bias events and normalizing  $N^{\text{MB}}$  by the efficiency  $\epsilon^{\text{MB}}$  to detect a minimum-bias event and the known cross section  $\sigma^{\text{MB}}$  for minimum-bias interactions:

$$\mathcal{L} = \frac{N^{\text{MB}}}{\sigma^{\text{MB}} \epsilon^{\text{MB}}}. \quad (5.1)$$

For the analysis of two-wire runs, the minimum-bias cross section  $\sigma^{\text{MB}}$  is needed for both target materials. Therefore, also the dependence of  $\sigma^{\text{MB}}$  on nuclear effects is required. A common parametrization of nuclear effects in the minimum-bias cross section is the power-law parametrization

$$\sigma_{\text{pA}}^{\text{MB}} = \sigma_{\text{pN}}^{\text{MB}} A^{\alpha^{\text{MB}}}. \quad (5.2)$$

Here,  $A$  is the atomic mass number of the target nucleus. The nuclear dependence of  $\sigma^{\text{MB}}$  is parametrized by the exponent  $\alpha^{\text{MB}}$ . If  $\sigma^{\text{MB}}$  is proportional to the geometrical cross section of the nucleus, a value of  $\alpha^{\text{MB}} = 2/3$  is expected (see Section 3.3.3). A fit to a compilation of previous measurements of the minimum-bias cross section yields  $\alpha^{\text{MB}} = 0.724 \pm 0.005$  [Car03]. A theoretical calculation of nuclear effects in inelastic proton-nucleus interactions results in a preliminary value of  $\alpha^{\text{MB}} = 0.687$  [Kop04]. An overview of the results of both analyses of the minimum-bias cross section is shown in Table 5.1.

The random trigger is used to record events for the luminosity determination. This trigger selects one of the 220 HERA bunches at random. During the data-taking, a variable fraction of events was recorded with the random trigger, in parallel to the dilepton trigger.

## 5.2 Vertex Counting Method

The basic idea of the vertex counting method is to determine the number of interactions by counting the number of reconstructed primary vertices on a wire. To infer the number of interactions from the number of reconstructed vertices, knowledge of the vertexing efficiency is required. The luminosity is obtained by normalizing the number of interactions by the minimum-bias cross section.



### 5.2.1 Vertexing Efficiency

The reconstruction of primary vertices in both, real data and MC-simulated events, is performed using Grover [Abt04a], which is the standard vertexing package for HERA-B. In the standard luminosity calculation, MC events with a varying number of superimposed interactions are reconstructed to extract the average reconstruction efficiency. The number of superimposed interactions follows a Poisson distribution with a mean value similar to the interaction rate at which the data were recorded. However, to allow for variations in the interaction rates and non-Poissonian distributions of primary interactions, a more flexible method of efficiency corrections is developed. The method is based on the full response of the HERA-B detector to minimum-bias interactions and describes both, effects which increase and effects which decrease the number of reconstructed vertices.

- Inefficiencies in the vertex detector (VDS) lead to a reduced number of reconstructed primary vertices.
- If the “beam spot”, i.e. the area on the target wire where the interactions occur, is small, two or more simultaneous interactions on a single wire cannot be separated. The corresponding primary vertices are merged to one vertex, thus the number of reconstructed vertices is reduced.
- Vertices with a large number of particles are split by the reconstruction algorithm with a certain probability. In this case, the number of reconstructed primary vertices is larger than the true number of interactions.

A MC simulation is employed to determine the resulting “smeared” vertexing efficiency. In a sample of 10,000 MC events, a fixed number of  $i = 1 \dots 5$  inelastic interactions is superimposed, and the events are reconstructed with the same primary vertex algorithm employed also for the real data. The resulting number of reconstructed primary vertices as a function of the number of superimposed events can be represented by the matrix equation

$$\vec{n}^{\text{rec}} = M \vec{n}^{\text{true}} \quad (5.3)$$

with the “response matrix”  $M$ . An element  $M_{ij}$  of the response matrix contains the probability to reconstruct  $j$  vertices if  $i$  events have been superimposed. The components  $n_i^{\text{true}}$  of the vector  $\vec{n}^{\text{true}}$  hold the number of events with  $i$  true interactions, and  $\vec{n}^{\text{rec}}$  is the vector of the number of reconstructed primary vertices. Due to the larger track multiplicity for the tungsten wire, the vertexing efficiency for the tungsten wire is larger than the efficiency obtained for the carbon wire. Examples of the response matrices for the carbon wire Below I and the tungsten wire Inner I for the calibration period of November 2002 are depicted in Table 5.2.

To infer the true number of interactions from the number of reconstructed primary vertices, Eq. (5.3) has to be solved for  $\vec{n}^{\text{true}}$ . The solution can be formally written as

$$\vec{n}^{\text{true}} = M^{-1} \vec{n}^{\text{rec}}. \quad (5.4)$$

**Table 5.2:** Vertexing efficiencies for the tungsten wire Inner I (top table) and for the carbon wire Below I (bottom table) for the calibration period of November 2002. In every table row, the fraction of events with 0...5 reconstructed vertices is shown for a given number of generated vertices. The table is based on 10,000 MC events each for 1...5 superimposed interactions.

Generated Vertices	Reconstructed Vertices					
	0	1	2	3	4	5
<b>Inner I (Tungsten)</b>						
<b>0</b>	1.0000	0.0000	0.0000	0.0000	0.0000	0.0000
<b>1</b>	0.0877	0.8855	0.0262	0.0006	0.0000	0.0000
<b>2</b>	0.0049	0.4962	0.4637	0.0331	0.0020	0.0001
<b>3</b>	0.0013	0.2141	0.5546	0.1998	0.0284	0.0017
<b>4</b>	0.0010	0.0811	0.4493	0.3569	0.0925	0.0172
<b>5</b>	0.0015	0.0297	0.3017	0.4135	0.1879	0.0556
<b>Below I (Carbon)</b>						
<b>0</b>	1.0000	0.0000	0.0000	0.0000	0.0000	0.0000
<b>1</b>	0.1998	0.7965	0.0037	0.0000	0.0000	0.0000
<b>2</b>	0.0291	0.6785	0.2888	0.0036	0.0000	0.0000
<b>3</b>	0.0036	0.4357	0.5013	0.0580	0.0013	0.0001
<b>4</b>	0.0002	0.2428	0.5830	0.1632	0.0105	0.0003
<b>5</b>	0.0001	0.1333	0.5513	0.2804	0.0329	0.0019

The total number of true and reconstructed vertices is given by the sum of the vector components, weighted with the corresponding number of interactions:

$$N^{\text{true,rec}} = \sum_{i=1}^5 i \cdot n_i^{\text{true,rec}}. \quad (5.5)$$

In the following section, a method to solve Eq. (5.3) and to calculate  $N^{\text{true}}$  is described.

## 5.2.2 Determination of the Number of Interactions

The method selected to solve Eq. (5.3) is the numerical inversion of the response matrix  $M$ . Since in general, matrix inversion is an ill-posed numerical problem, this method is not suited to obtain the true distribution of primary vertices. The matrix inversion introduces a strong correlation between the components of the solution vector  $\vec{n}^{\text{true}}$ , such that the distribution of primary vertices is not smooth and may contain negative numbers. These correlations are taken into account automatically in the evaluation of the sum in Eq. 5.5. Therefore, the total number of vertices is not affected by the above-mentioned numerical problems, and the straightforward method of numerical matrix inversion can be used to solve Eq. (5.3).

The matrix inversion is performed using the `TMatrix` class of the ROOT package [Bru97] in which a Gauß-Jordan elimination algorithm with pivoting is utilized. As a systematic check of the numerical matrix inversion, the number of primary interactions is also determined by an unfolding method, as it will be discussed in Section 5.3.1.

### 5.2.3 Luminosity Ratios for All Runs

To obtain the luminosity ratios for all runs analyzed in this thesis, the number of primary vertices in all random-triggered events of each run is extracted. The vertexing efficiency in the form of the response matrix is determined from MC simulations for all active wires of each calibration period. For each wire and period, five times 10,000 MC events with fixed numbers of  $i = 1 \dots 5$  superimposed inelastic interactions are reconstructed. The statistical uncertainty of the luminosity ratio is dominated by the uncertainties in the number of the reconstructed vertices per run. The statistical uncertainty of the response matrix obtained from 10,000 MC events per row is smaller than the average uncertainty in the number of vertices, therefore it is neglected.

The nuclear suppression parameter  $\alpha$  is measured by the ratio of the  $J/\psi$  yields  $N_1$  and  $N_2$ , the ratio of the efficiencies  $\varepsilon_1$  and  $\varepsilon_2$ , and the ratio of the luminosities  $\mathcal{L}_1$  and  $\mathcal{L}_2$  for two target materials with the atomic mass numbers  $A_1$  and  $A_2$ :

$$\alpha = \frac{1}{\log(A_2/A_1)} \log \left( \frac{N_2 \mathcal{L}_1 \varepsilon_1}{N_1 \mathcal{L}_2 \varepsilon_2} \right). \quad (5.6)$$

Therefore, the following function of the luminosities enter the measurement of  $\alpha$ :

$$\Delta\alpha^{\mathcal{L}} = \frac{1}{\log(A_2/A_1)} \log \left( \frac{\mathcal{L}_1}{\mathcal{L}_2} \right). \quad (5.7)$$

Since the luminosities are independent of the  $J/\psi$  kinematics, the ratio of luminosities results in a constant shift of  $\alpha$ . The values of  $\Delta\alpha^{\mathcal{L}}$  are listed in Appendix C together with their statistical uncertainties for all runs.

## 5.3 Systematic Uncertainties

As it can be seen from Eq. (5.6), uncertainties in the luminosity ratio enter the uncertainty of the nuclear dependence with the same weight as uncertainties in the ratio of  $J/\psi$  yields and the efficiency ratio. The systematic uncertainties of the luminosity ratio are studied in the following, separated into two categories. The first category comprises uncertainties within the framework of the vertex counting method. The second category of systematic checks is based on an alternative method to extract the efficiency ratio with different systematic influences.

### 5.3.1 Uncertainties of the Vertex Counting Method

#### Response Matrix

The main systematic uncertainty of the vertex counting method is the uncertainty of the response matrix. The probability of vertex merging and splitting is sensitive to the size of the beam spot. In the MC simulation, the beam spot is modelled by a Gaussian distribution of the primary vertices with a width of  $500\ \mu\text{m}$  and a fixed position on the wire. The beam position along the wire is known to change during a run, and a fit of the beam profile along the wire with a Gaussian function shows that a beam width of  $450\ \mu\text{m}$  is more appropriate for some runs. A smaller beam spot leads to an increased probability of vertex merging and hence to a smaller vertexing efficiency. The reduction of the vertexing efficiency is larger for carbon wires than for tungsten wires, due to the lower average track multiplicities in proton-carbon interactions. Therefore, the tungsten-to-carbon efficiency ratio is shifted to larger values by reducing the size of the beam spot. For a very small beam spot size of  $200\ \mu\text{m}$ , the average efficiency ratio is increased from 1.24 to 1.42. If this shift is interpolated linearly to a beam spot size of  $450\ \mu\text{m}$ , the efficiency ratio is increased from 1.24 to 1.27. The corresponding shift in the nuclear suppression parameter  $\alpha$  amounts to

$$\delta\alpha^{\text{response}} \approx 0.009. \quad (5.8)$$

This value of  $\delta\alpha^{\text{response}}$  is taken as the systematic uncertainty of the measurement of  $\alpha$  due to uncertainties of the vertexing efficiency.

#### Unfolding Method

The vertexing efficiency is applied to the number of reconstructed primary vertices by solving Eq. (5.3) via a numerical matrix inversion. As a cross-check for the unfolding method of matrix inversion, another method is used which is based on a Bayesian approach [D'A95]. The Bayesian unfolding method is equivalent to the iterative inversion of the response matrix described in [Mül87]. Contrary to the matrix inversion method, the unfolded distribution is smooth and non-negative. For the unfolding procedure, the program code provided by D'Agostini is used [D'A96]. A Poisson distribution with a mean value of 0.5 is chosen as the prior probability of the number of interactions. The unfolded number of primary vertices differs by less than 1% from the result of the matrix inversion method even for the runs with the smallest statistics. The average difference in the number of primary vertices amounts to approximately 0.5%, resulting in a small shift in the nuclear suppression parameter  $\alpha$  of approximately 0.001.

### 5.3.2 Luminosity Ratios from the Track Counting Method

The vertex counting method relies on the correct description of the primary vertex reconstruction in the MC simulation. As a test of the influence of the luminosity determination method on the luminosity ratio, the luminosities are calculated with an alternative method [Som00]. The method is based on counting the number of reconstructed tracks. It is therefore influenced by different systematic effects than the vertex counting method.

### Basic Idea

In the track counting method, the average track multiplicity in a run is used as a measure of the interaction rate. The interaction rate  $\lambda$  is related to the luminosity as follows,

$$\mathcal{L} \propto \frac{\lambda}{\sigma^{\text{MB}}}. \quad (5.9)$$

For the calculation of luminosity ratios, no absolute normalization of Eq. (5.9) is required. Assuming that the average track multiplicity  $\langle N \rangle$  per event is linearly proportional to the interaction rate, the interaction rate can be determined from the average track multiplicity, normalized to the average track multiplicity in events with exactly one interaction,  $\langle N \rangle^{(1)}$ :

$$\lambda = \frac{\langle N \rangle}{\langle N \rangle^{(1)}}. \quad (5.10)$$

Since the true number of interactions is unknown in the data, a tagging criterion is needed to identify events with at least one interaction. The corresponding tagging efficiency  $\varepsilon^{(1)}$  is determined from a MC simulation. If runs with a low interaction rate are considered, the probability to observe more than one interaction in an event is very low. Assuming a Poisson distribution of the number of interactions, the probability to observe more than one interaction in runs recorded at an interaction rate of 1 MHz is approximately  $6 \times 10^{-3}$ . In this “zero-rate limit”,  $\langle N \rangle^{(1)}$  is related to the number of tagged events in these runs by

$$\langle N \rangle^{(1)} = \varepsilon^{(1)} \langle N \rangle^{\text{tagged}}. \quad (5.11)$$

The luminosity acquired in a run is thus related to the average number of tracks in the run by

$$\mathcal{L} \propto \frac{\langle N \rangle}{\sigma^{\text{MB}} \varepsilon^{(1)} \langle N \rangle^{\text{tagged}}}. \quad (5.12)$$

In the derivation of these formulae in [Som00] it is assumed that the number of primary interactions is Poisson-distributed.

### Implementation

In order to use the track counting method in HERA–B, several options are available for the track selection, the track-vertex assignment, the tagging criteria, and the selection of runs to determine  $\langle N \rangle^{(1)}$ :

- To be considered in the track counting method, a track must consist at least of a reconstructed track segment in the VDS.
- The assignment of a track to a wire is performed by a function provided by the Grover package. Tracks are assigned to a wire if the  $\chi^2$  distance between the track and the wire is smaller than three (see Section 4.2.3).
- Two alternative methods are used to tag events with at least one interaction. In one of the methods, two or more tracks have to be assigned to a wire. The other method uses a criterion also employed for the interaction trigger: the number of photons in the ring-imaging Čerenkov counter (RICH) must be greater than 30.

- The average number of tracks in tagged events in the zero-rate limit is extracted from several runs with low interaction rates. Runs 20478 (Inner II), 20480 (Inner I), and 20490 (I1B1) were taken in November 2002 using the interaction trigger at an interaction rate of 1.0 MHz. During the runs 20700 (Below I) and 20701 (Inner I) taken in December 2002 at interaction rates of 0.8 MHz and 1.3 MHz, the interaction trigger was operated in a transparent mode, i.e. the data sample consists of random-triggered events.
- The average number of tracks is determined as the truncated mean of the track distribution: Events with 50 or more tracks assigned to a wire are discarded in the mean value calculation in order to suppress pile-up events and background contributions, for example due to beam–gas interactions.

### Results and Comparison to the Vertex Counting Method

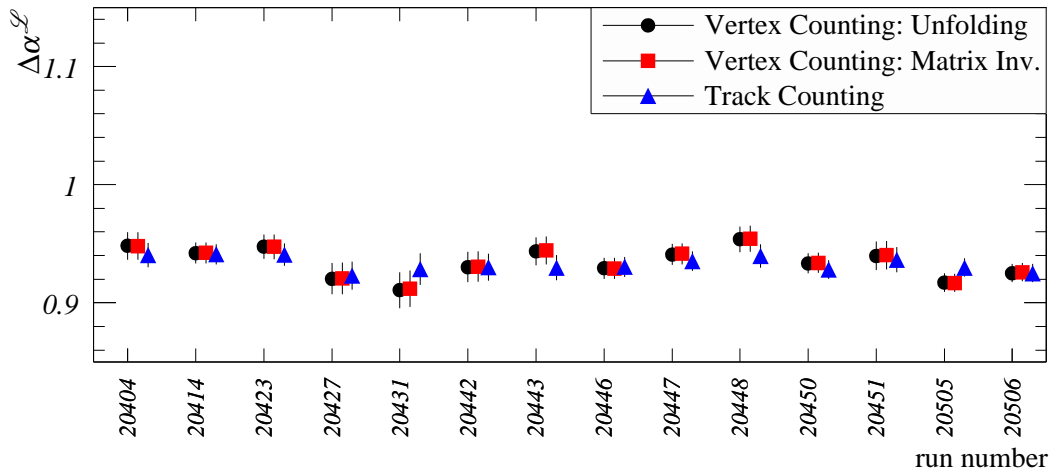
The list of possible options shows the main problem of the track counting method: there is no unique choice of the free parameters. The computation of the luminosity ratio is performed for the track-based and for the RICH-based tagging criterion. To determine the number of tracks in single interactions, both, runs taken with the interaction trigger and the random trigger are tested. The resulting average shifts  $\Delta\alpha^{\mathcal{L},\text{track}}$  in the nuclear suppression parameter  $\alpha$  vary by up to 0.07. This variation reflects the uncertainty of the track counting method in the normalization of the luminosity ratio. In contrast to the track counting method, the vertex counting method relies heavily on Grover, a well-tested vertexing tool in which the free parameters have already been tuned.

The parameters of the track counting method have been chosen such that the values of  $\Delta\alpha^{\mathcal{L}}$  in the track counting method and the vertex counting method are the same if averaged over all runs in the calibration period. The systematic uncertainty is derived from the per-run difference between the luminosities obtained from the two methods. Comparisons of the values of  $\Delta\alpha^{\mathcal{L}}$  obtained from the track counting and from the vertex counting method for the wire combinations I1I2 and I1B1 in November 2002 are shown in Fig. 5.1. The comparisons show that the fluctuations in the luminosity ratio are smaller for I1I2 than for I1B1. In addition, the fluctuations are more pronounced in the vertex counting method than in the track counting method. A measure of the difference between the two methods is the standard deviation of the shifts  $\Delta\alpha$  for  $n$  runs:

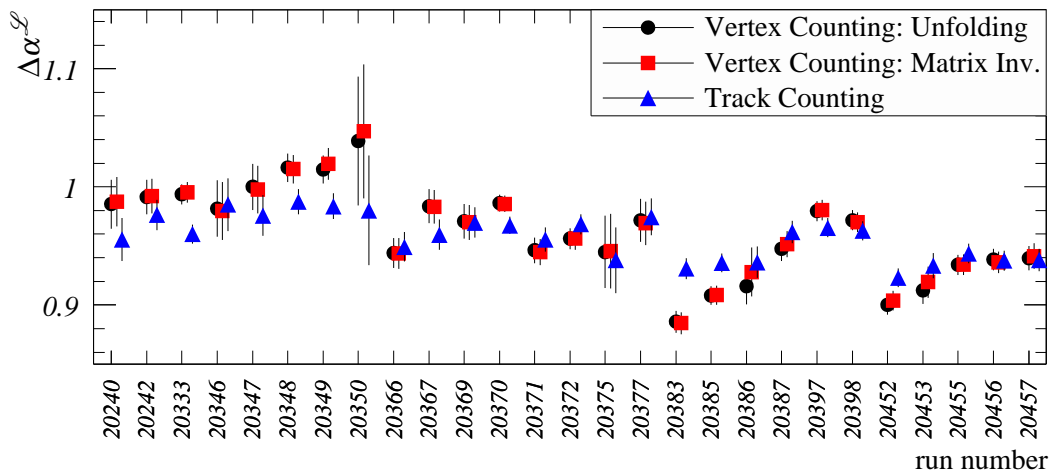
$$s = \sqrt{\frac{1}{n-1} \sum_{i=1}^n (\Delta\alpha^{\mathcal{L},\text{track}} - \Delta\alpha^{\mathcal{L},\text{vertex}})^2}. \quad (5.13)$$

The standard deviation of the two methods amounts to 0.009 for the wire combination I1I2 and 0.024 for I1B1. For the final analysis, results from all wire configurations are combined. Therefore, as an estimate of the systematic uncertainty in  $\Delta\alpha^{\mathcal{L}}$  from the method of luminosity determination, the arithmetic mean of the standard deviations of the two wire configurations is chosen:

$$\delta\alpha^{\text{method}} = 0.017. \quad (5.14)$$



(a)



(b)

**Figure 5.1:** Comparison of the luminosity ratios obtained by the vertex counting method and the track counting method. The figures show the shift in the nuclear suppression parameter  $\alpha$  for luminosities determined by the methods of matrix inversion and Bayesian unfolding and for luminosities determined by the track counting method. (a) Runs taken with the wire combination III2 in the calibration period of November 2002. (b) Runs taken with the wire combination in I1B1 in November 2002.

**Table 5.3:** Systematic uncertainties of the luminosity ratio. The total uncertainty is obtained by adding the individual uncertainties in quadrature. Values in parentheses are not included in the total systematic uncertainty.

Systematic Uncertainty	$\Delta\alpha$
Minimum-Bias Cross Section	(−0.037)
Variation of Response Matrix	$\pm 0.009$
Alternative Unfolding Method	$\pm 0.001$
Track Counting Method	$\pm 0.017$
<b>Total</b>	<b><math>\pm 0.019</math></b>

### 5.3.3 Uncertainty of the Minimum-Bias Cross Section

For both the vertex counting method and the track counting method, the nuclear dependence of the minimum-bias cross section is required as an input parameter. Thus, both methods are affected by the uncertainty of the nuclear dependence in the same way. The minimum-bias cross sections obtained in two different analyses [Car03, Kop04] are summarized in Table 5.1. For the determination of the luminosity ratios, the minimum-bias cross sections for the carbon and the tungsten wires are taken from [Car03]. Using the minimum-bias cross sections as predicted in [Kop04], the suppression parameter  $\alpha$  is shifted by

$$\delta\alpha^{\sigma^{\text{MB}}} = 0.687 - 0.724 = -0.037. \quad (5.15)$$

This shift in  $\Delta\alpha^{\mathcal{L}}$  is the single largest systematic uncertainty in the measurement of the luminosity ratio. As an uncertainty in the overall normalization of the nuclear dependence, it is not included in the combination of systematic effects but rather taken into account by reporting the nuclear dependence of  $J/\psi$  production relative to the nuclear dependence of the minimum-bias cross section, i.e. as the difference  $\alpha^{J/\psi} - \alpha^{\text{MB}}$ .

### 5.3.4 Combination of Systematic Uncertainties

A summary of all systematic uncertainties studied in this section can be found in Table 5.3. The systematic uncertainties are combined by adding the individual contributions to the shift of the nuclear suppression parameter in quadrature. The dominant systematic effect is the uncertainty in the choice of the luminosity determination method. The resulting uncertainty in  $\Delta\alpha^{\mathcal{L}}$ ,

$$\delta\alpha^{\mathcal{L}} = 0.019, \quad (5.16)$$

will be included in the total systematic uncertainty of the measurement of nuclear effects presented in Chapter 6.



## 5.4 Summary

The ratio of luminosities is one of the three main ingredients of the measurement of nuclear effects in the production of  $J/\psi$  mesons. The standard method used in HERA-B for the determination of luminosities is based on counting the number of primary vertices in random-triggered events. The vertex counting method is also employed for calculations of the ratios of luminosities. As an augmentation of the standard method to calculate vertexing efficiencies, the method of unfolding by a response matrix is introduced. The response matrix is obtained from a MC simulation. The luminosity ratios are determined for all two-wire runs used in the analysis of nuclear effects. The resulting shifts of the nuclear suppression parameter  $\alpha$  are documented in Appendix C.

The consistency of the luminosity ratios obtained from the vertex counting method is tested by several systematic studies. The main systematic uncertainty originates from the choice of the method of luminosity determination. The total uncertainty of the nuclear suppression parameter  $\alpha$  due to the ratio of luminosities amounts to 0.019. An additional normalization uncertainty of 0.037 arises from uncertainties in the nuclear dependence of the minimum-bias cross section. Therefore, the nuclear suppression parameter  $\alpha$  will also be reported relative to  $\alpha^{\text{MB}}$ .

The results presented in this chapter will be used in the following chapter to extract the nuclear dependence of  $J/\psi$  production in proton-nucleus interactions.



---

# Measurement of Nuclear Effects

---

In this chapter, the results of the previous chapters are collected, and the main result of this thesis is presented, a measurement of the nuclear dependence of  $J/\psi$  production. The nuclear dependence is derived from the ratio of  $J/\psi$  production cross sections for different target materials. To determine the cross section ratio, the ratio of  $J/\psi$  yields from carbon and tungsten targets is measured. The yield ratio is corrected by the corresponding ratio of detector and trigger efficiencies, and by the ratio of luminosities.

The first part of the chapter deals with the determination of the ratios of the  $J/\psi$  yields and efficiencies and their dependence on the  $J/\psi$  kinematics. Detailed studies of the systematic influences on both ratios are discussed next. The nuclear dependence of  $J/\psi$  production is presented in the power-law parametrization by determining the nuclear suppression parameter  $\alpha$ . In addition, the nuclear absorption cross section is extracted from the  $\langle\rho L\rangle$  parametrization of the Glauber model. The chapter concludes with a discussion of the analysis results and a comparison to theoretical predictions and the results of previous experiments.

## 6.1 Ratios of $J/\psi$ Yields

The ratio of  $J/\psi$  yields from two different target wires is calculated from the “raw” ratio of reconstructed  $J/\psi$  per wire. The ratio of reconstructed  $J/\psi$  is corrected by the ratio of the  $J/\psi$  detection efficiencies. In contrast to the luminosity ratio discussed in Chapter 5, both ratios depend on the  $J/\psi$  kinematics. Therefore, they are studied as functions of Feynman’s scaling variable  $x_F$ , the transverse momentum  $p_T$ , and the rapidity  $y$ . Throughout this chapter, the binning of the kinematic variables with large bin sizes is employed, introduced as binning II in Section 4.3.4. The efficiency ratio is determined from a detailed Monte Carlo (MC) simulation of the HERA-B detector and trigger, as it is detailed in Appendix A. Systematic uncertainties are separated into uncertainties which only affect the efficiency ratio and uncertainties which are connected to both, the efficiency ratio and the yield ratio.

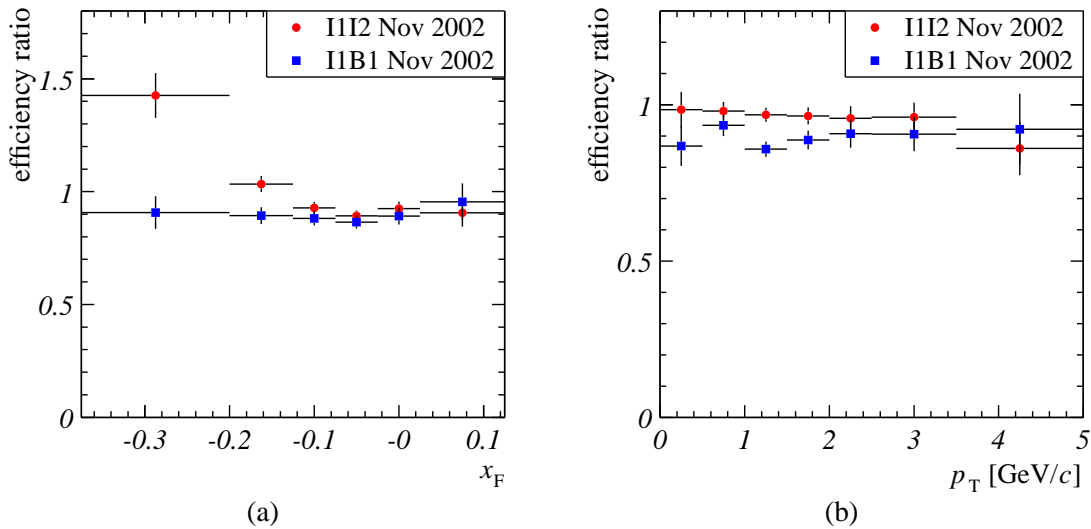


**Figure 6.1:** Comparison of efficiency ratios for the wire combinations I1I2 and I1B1 from the calibration period of November 2002 as functions of (a)  $x_F$  and (b)  $p_T$ . The large difference between the efficiency ratios as a function of  $x_F$  is caused by the trigger chain.

### 6.1.1 Efficiency Ratios

To calculate the efficiency ratios, the MC efficiencies to reconstruct  $J/\psi$  mesons are first determined separately for each of the target wires. In a second step, the efficiency ratios are calculated, bin by bin in the kinematic variables. At the time, when the measurement of nuclear effects in  $J/\psi$  production at HERA-B was proposed, it was expected that all detector efficiencies cancel out if ratios of the measured quantities are calculated, and only the difference in the geometrical acceptance between the two wires remains. By comparing the MC simulation and data from the data-taking period 2002/2003, it was observed later that this assumption is not valid. Large efficiency variations are introduced by the different treatment of the two wires in the trigger chain.

A comparison of the efficiency ratios for the wire combinations I1I2 and I1B1 in the calibration period of November 2002 as a function of  $x_F$  and  $p_T$  is shown in Fig. 6.1. The  $p_T$  distributions of the efficiency ratios are approximately constant for both wire combinations. For the wire combination I1B1, in which two wires from the same target station are employed, the efficiency ratio in  $x_F$  is also approximately constant. For I1I2, a combination of wires from both stations, the efficiency for the wire from station II is decreased by up to 50% for large negative  $x_F$ . The dependence of the efficiency ratio on the wire combination is caused by the limited size of the SLT target box. In the SLT algorithm, a target constraint is calculated from the size of the target box. The constraint was wrongly chosen such that a significant fraction of the tracks with large slopes which originate from the wire in station II was rejected. To incorporate the target box constraint in the analysis, the efficiency ratio is calculated from MC events in which the influence of both wires is taken into account in the trigger simulation. The systematic uncertainties of the efficiency ratios connected with the SLT target box will be discussed in Section 6.1.3.

Variations of the efficiency ratios are also observed if the same wire combination is used in different calibration periods. The variations reflect changes in the detector and trigger performance between the calibration periods which are implemented in the MC simulation. The largest variations of this kind are observed in the “Missing Quadrant” period, in which parts of the trigger were defective. The efficiency ratio as a function of  $x_F$ ,  $p_T$ , and  $y$  is summarized in Appendix D, Fig. D.12 for all wire combinations in all calibration periods.

### 6.1.2 Strategies to Extract Systematic Uncertainties

Contrary to the case of statistical uncertainties, no commonly accepted prescription is available to evaluate the systematic uncertainties of a measurement. In the following, the strategy chosen for this analysis is described.

#### Quantitative Evaluation of Systematic Uncertainties

One approach to quantify the influence of systematic uncertainties on a measured quantity  $x$  is to add the changes in  $x$  caused by changes in the analysis chain in quadrature. However, if the statistical uncertainty of  $x$  is larger than the systematic uncertainties, no conclusion on the significance of the systematic effects can be drawn. In particular, systematic uncertainties evaluated for a subset of the data cannot be assigned to the full data set with the same magnitude. The problem of low statistics is present in this analysis. Due to large amount of computing time required to generate and reconstruct MC-simulated events, the size of the MC data sets is limited to approximately twice the size of the real data samples. As a consequence, the MC data sets are not large enough to neglect the statistical uncertainties of the MC efficiency ratios and the yield ratios.

Following the prescription of [Bar02], systematic studies which show only insignificant effects are ignored in the calculation of the systematic uncertainties. All significant uncertainties are collected and added in quadrature. To quantify deviations from the nominal values of  $x$  in  $n$  bins of some kinematic variable, the  $\chi^2$  statistic of the deviation is calculated:

$$\chi^2 = \sum_{i=1}^n \frac{(x_i - \bar{x}_i)^2}{\sigma_i^2}. \quad (6.1)$$

Here,  $\bar{x}_i$  is the nominal value in a bin  $i$ , obtained from the standard analysis, and  $x_i$  is the value obtained from the study of one particular systematic effect. The statistical uncertainty of  $x_i$  is denoted by  $\sigma_i$ . The expectation value of  $\chi^2$  is  $n - 1$ . Systematic effects are insignificant compared to the statistical uncertainties, if they result in  $\chi^2$  values much smaller than the expectation value. Consequently, these systematic effects are neglected.

#### Choice of Data Sets

The evaluation of systematic uncertainties is performed based on two of the ten subsamples of the 2002/2003 data-taking period, the target wire combinations I1I2 and I1B1 from the calibration period of November 2002. This choice of subsamples covers two different types of two-wire setups. I1B1 is a setup with wires from the same

target station, and in I1I2, wires from different target stations are utilized. The effects of systematic variations are illustrated for the wire combination I1B1 unless indicated otherwise.

Significant systematic effects are re-evaluated using the full analysis chain for the entire data set to quantify their influence on the combined result of the analysis. For some of the studies, an extension to the entire data set was not possible for technical reasons. In this case, the arithmetic mean of the uncertainties for I1I2 and I1B1 is taken as the final systematic uncertainty. This strategy is chosen because the combined result of the analysis is calculated by averaging results of subsets of the data as well.

### 6.1.3 Systematic Uncertainties of the Efficiency Ratios

#### Kinematic Weights

In order to check the influence of the shape of the kinematic distributions on the efficiency ratio, the kinematic weights used in the MC generator are varied. The efficiency as a function of a single kinematic variable is largely independent of the MC model used for the same variable. However, a change of the MC model may affect the efficiency as a function of other kinematic variables in the case of correlations between the efficiencies. Therefore, visible effects of reweighting one of the variables are expected in the efficiency as a function of the other variables.

Since the weights for  $x_F$  and  $p_T$  used in the HERA-B MC simulation factorize by construction, each of the weights is varied independently. To modify the transverse momentum distribution, the parameter  $p_0$  of the  $p_T$  parametrization in Eq. (4.9) is varied. Four different combinations are chosen, in which the default values of  $p_0 = 2.9 \text{ GeV}/c$  for carbon wires and  $p_0 = 3.1 \text{ GeV}/c$  for tungsten wires are varied by  $\pm 0.1 \text{ GeV}/c$ . The distribution of  $x_F$  is modified by varying the asymptotic slope  $C$  of the  $x_F$  shape, defined in Eq. (4.8). Motivated by the large uncertainty of the  $x_F$  shape observed in the analysis of differential distributions, the value of  $C$  is varied by  $\pm 1$ . The changes of the efficiency ratio as a function of  $p_T$  by varying the  $x_F$  weights and vice versa are illustrated in Fig. 6.2 (a) and (b). The  $p_T$  shape is practically unaffected by changes in the  $x_F$  shape. The largest systematic deviations in the  $x_F$  shape are observed for the two extreme choices of the transverse momentum parameter,  $p_0 = 3.0 \text{ GeV}/c$  for both wires, and  $p_0 = 2.8 \text{ GeV}/c$  for carbon wires and  $p_0 = 3.2 \text{ GeV}/c$  for tungsten wires. However, both effects are small if they are compared to the statistical uncertainties.

#### Spatial Variation of Detector and Trigger Efficiencies

The efficiency of the FLT to find events with at least two tracks identified by the SLT is parametrized by the FLT efficiency map. The two-dimensional projection of the efficiency map to the detector layer TC2 (see Fig. A.6) shows large spatial variations of the efficiency. To estimate the influence of the efficiency variations in the FLT on the efficiency ratio, the FLT efficiency is replaced by a uniform efficiency of 0.5. The largest effect of this variation is seen in the efficiency ratio as a function of  $x_F$ , as depicted in Fig. 6.2 (c). The result of the study suggests that the efficiency ratio becomes flatter

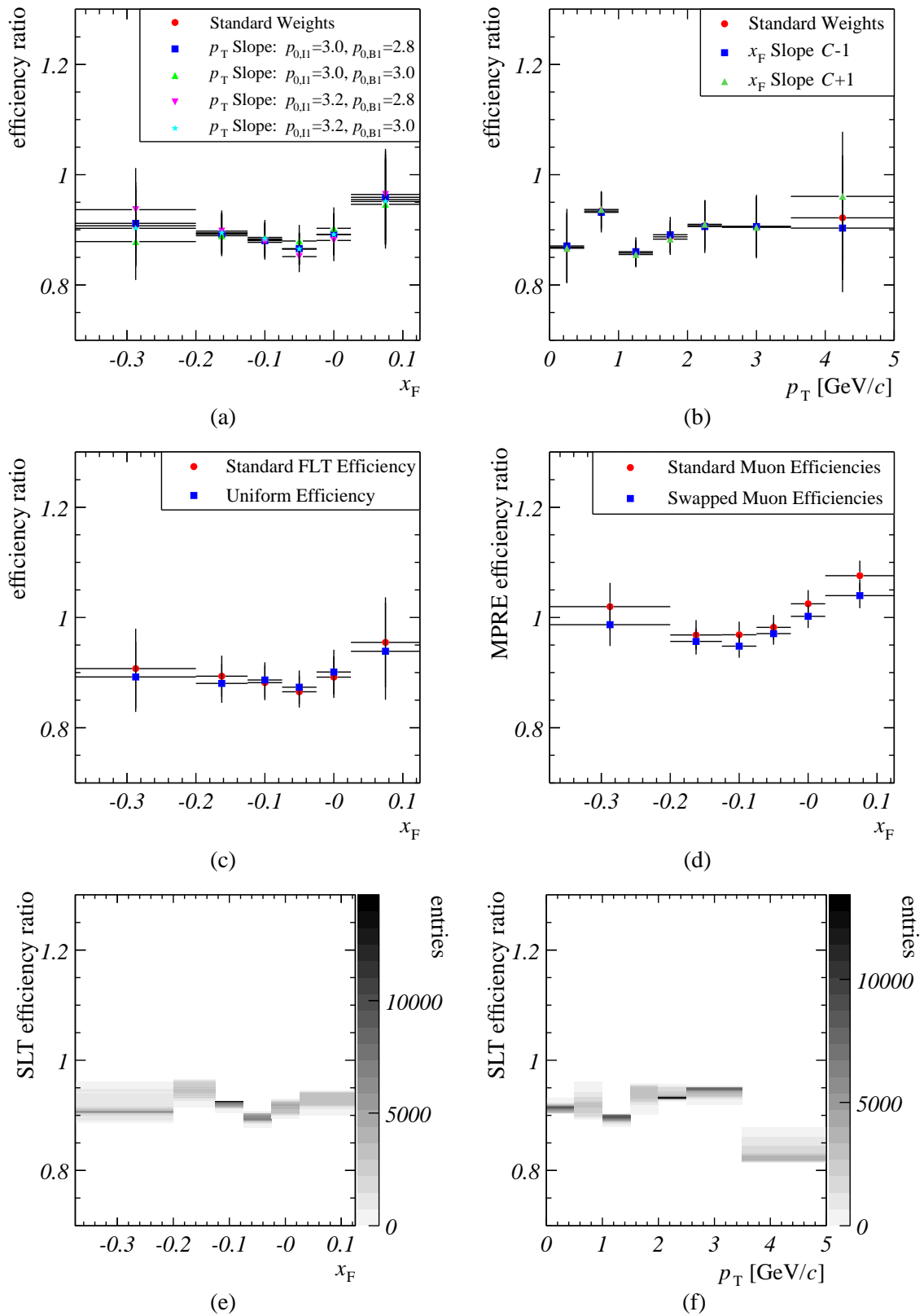


**Figure 6.2:** Summary of systematic uncertainties in the efficiency ratio for the wire combination I1B1 in the calibration period of November 2002. (a) Variation of the  $p_T$  kinematic weights. (b) Variation of the  $x_F$  kinematic weights. (c) Comparison of realistic and uniform FLT efficiencies. (d) Variation of muon detector and pretrigger efficiencies. (e)–(f) Variation of target box parameters. The scales on the y-axes are zero-suppressed.

by using a uniform FLT efficiency. However, the effect is insignificant compared to the statistical uncertainties.

The muon pretrigger is the first step in the trigger chain for muon pairs. Therefore, already small variations in the muon pretrigger efficiency are visible in the  $xy$ -distribution of triggered tracks. The muon pretrigger efficiency depends on the efficiencies of the muon pad cells and the Pretrigger Optical Links (POL). Therefore, the systematic influence of spatial variations in the pad and POL efficiencies on the ratios of muon pretrigger efficiencies is evaluated. The ratio of muon pretrigger efficiencies is determined from the muon pretrigger simulation. The muon pretrigger efficiency ratio obtained from the standard pad and POL efficiencies for the calibration period of November 2002 is compared with a simulation, in which the efficiencies are taken from the calibration period of October 2002. Samples of 100,000 MC events from each of the wires are passed through the muon detector hit preparation and the muon pretrigger simulation both for the standard and for the “swapped” efficiencies. The ratio of efficiencies as a function of  $x_F$  is compared to the standard efficiency ratio in Fig. 6.2 (d). The muon pretrigger efficiency ratio is shifted significantly by changing the efficiencies of the muon pad cells and the POLs.

For the study of systematic effects in the muon pretrigger efficiency ratio, only the first step of the trigger chain is simulated. The final efficiency ratio depends linearly on the muon pretrigger efficiency ratio. To calculate the influence of the systematic uncertainties on the final ratio of efficiencies, the size of the uncertainties is scaled by the ratio of the final efficiency ratio to the muon pretrigger efficiency ratio. The resulting systematic uncertainties of the efficiency ratios for the wire combinations I1B1 and I1I2 are averaged before they are applied to the final result of the analysis.

### Target Box Simulation

For wire combinations from both target stations, a change of up to 50% is observed in the efficiency ratio as a function of  $x_F$ . The origin of the variation is the target box constraint used in the SLT. A simulation of the target box is included in the SLT simulation program. However, due to the large variation of the efficiency ratios, a systematic study of the uncertainty connected with the target box is desirable.

Four parameters influence the target box calculation: the positions of the two wires in their moving directions,  $w_1$  and  $w_2$ , and the  $x$ - and  $y$ -components of the beam position,  $b_x$  and  $b_y$ . The estimated maximum uncertainty for each of the four parameters is 1 mm. In order to allow for systematic studies of target-box-related effects, the steps of the SLT simulation which depend on the target box are simulated for different target box parameters. Beginning with the L2Magnet algorithm, the last steps of the SLT simulation are carried out for 32 different combinations of shifts in one or two of the parameters by 1 mm. The influence of combinations of shifts on the efficiency can be evaluated by expanding the efficiency around the nominal efficiency [Med04a]. Using the notations  $\vec{x} \equiv (x_1, x_2, x_3, x_4) \equiv (w_1, w_2, b_x, b_y)$  and  $\Delta\vec{x} = (\Delta x_1, \Delta x_2, \Delta x_3, \Delta x_4)$ , a Taylor expansion of the efficiency  $\varepsilon$  up to second derivatives reads:

$$\varepsilon(\vec{x}_0 + \Delta\vec{x}) = \varepsilon(\vec{x}_0) + \sum_{i=1}^4 \left. \frac{\partial \varepsilon(\vec{x})}{\partial x_i} \right|_{\vec{x}_0} \Delta x_i + \frac{1}{2} \sum_{i=1}^4 \sum_{j=1}^4 \left. \frac{\partial^2 \varepsilon(\vec{x})}{\partial x_i \partial x_j} \right|_{\vec{x}_0} \Delta x_i \Delta x_j. \quad (6.2)$$



The partial derivatives are replaced by finite differences between the values at equidistant sampling points with the distance  $h_i = 1$  mm, given by the different combinations of shifts in  $\vec{x}$ :

$$\frac{\partial \varepsilon(\vec{x})}{\partial x_i} = \frac{\varepsilon(\dots, x_i + h_i, \dots) - \varepsilon(\dots, x_i - h_i, \dots)}{2h_i}, \quad (6.3)$$

$$\frac{\partial^2 \varepsilon(\vec{x})}{\partial x_i^2} = \frac{\varepsilon(\dots, x_i + h_i, \dots) + \varepsilon(\dots, x_i - h_i, \dots) - 2\varepsilon(\dots, x_i, \dots)}{h_i^2}, \quad (6.4)$$

$$\left. \frac{\partial^2 \varepsilon(\vec{x})}{\partial x_i \partial x_j} \right|_{i \neq j} = \frac{\varepsilon(\dots, x_i + h_i, \dots, x_j + h_j, \dots) + \varepsilon(\dots, x_i - h_i, \dots, x_j - h_j, \dots)}{4h_i h_j} - \frac{\varepsilon(\dots, x_i - h_i, \dots, x_j + h_j, \dots) + \varepsilon(\dots, x_i + h_i, \dots, x_j - h_j, \dots)}{4h_i h_j}. \quad (6.5)$$

The wire positions are continuously monitored during the data-taking. The uncertainty of the wire position from this measurement is approximately  $\Delta w_{1,2} = 0.1$  mm. The estimated accuracy of the beam position amounts to  $\Delta b_{x,y} = 1$  mm [Med04b]. The SLT efficiency is evaluated as a function of the kinematic variables  $x_F$  and  $p_T$ , which are calculated from the true MC momentum of the J/ψ. Using the formulae above, 100,000 random combinations of beam and wire shifts within the uncertainty ranges are generated for each bin in  $x_F$  and  $p_T$ . The systematic uncertainty of the efficiency ratio in a bin is obtained from the standard deviation of the efficiency ratio distributions in the bin.

Systematic uncertainties of the target box simulation are evaluated for the same-station wire combinations I1B1 in the calibration period of November 2002 and the two-station combination B1O2 in January 2003 (II)<sup>1</sup>. The largest effect related to the target box constraint is observed for I1B1. The variation of the SLT efficiency ratio for I1B1 as a function of  $x_F$  and  $p_T$  is shown in Fig. 6.2 (e) and (f). The uncertainty of the efficiency ratio is smaller than 1.7% for all bins of all samples and scales approximately linearly with the largest uncertainty of the input parameters. By assuming an uncertainty of the beam position of 0.5 mm, the target box uncertainty is less than 1% for all bins. The uncertainties of the SLT efficiency ratio can be applied to the final efficiency ratio without further scaling, because the final efficiency ratio is practically unaffected by the remaining step of the trigger chain, namely the FLT efficiency map. The systematic uncertainty of the target box is small compared to the statistical uncertainty.

#### 6.1.4 Systematic Uncertainties of J/ψ Yield Ratios

To evaluate the systematic uncertainties in the determination of the ratio of J/ψ yields, the number of J/ψ in all runs of a calibration period are added in order to ensure sufficient statistical precision of the measurement. The ratio of the number of J/ψ is corrected by the efficiencies valid for the calibration period. In all systematic studies, the quantity

$$R_j^{J/\psi} = \frac{\varepsilon_j^C}{\varepsilon_j^W} \cdot \frac{\sum_i N_i^W}{\sum_i N_i^C} \quad (6.6)$$

<sup>1</sup>For technical reasons, the MC simulation of the wire combination I1I2 in November 2002 could not be used for the study of systematic effects due to the SLT target box.

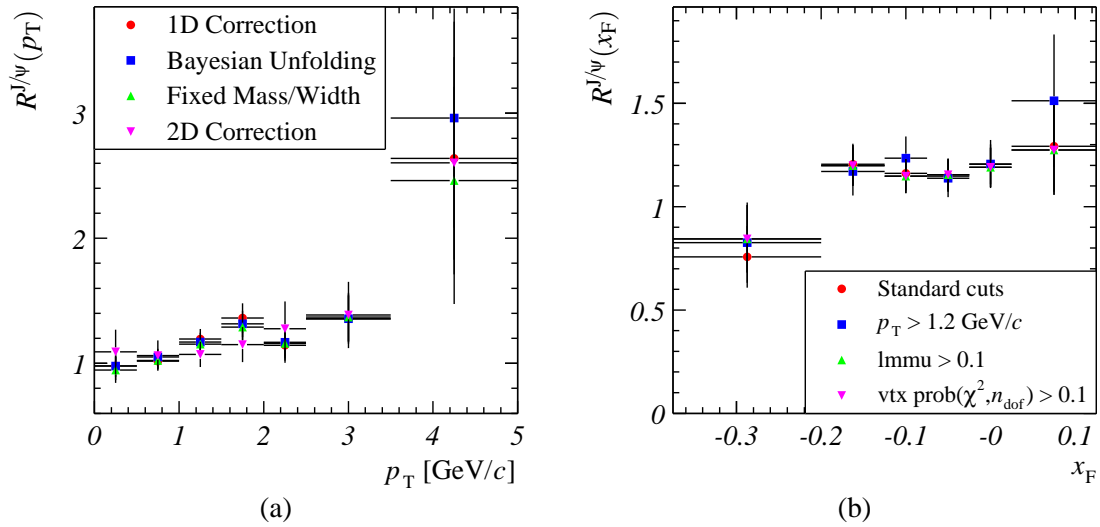


**Figure 6.3:** Systematic checks of  $J/\psi$  yield ratios for the wire combination I1B1 in the calibration period of November 2002. (a) Yield ratio as a function of  $p_T$ , variation of efficiency correction method. (b) Yield ratio as a function of  $x_F$ , variation of event selection cuts.

is calculated as a function of the kinematic variables. Here,  $N_i^W$  and  $N_i^C$  are the raw number of  $J/\psi$  reconstructed on the tungsten and the carbon wire in a run  $i$  within a calibration period  $j$ , and  $\varepsilon_j^C$  and  $\varepsilon_j^W$  are the corresponding MC efficiencies for the calibration period.

### Invariant Mass Fit

The determination of  $J/\psi$  yields is based on fits to the invariant mass spectra. Fits to mass spectra with a low number of  $J/\psi$  in the presence of background events are more stable if the number of free parameters is reduced. As discussed in Section 4.4.1, the reconstructed mass and width of the  $J/\psi$  signal in the data depend only weakly on the kinematic variables. Therefore, a systematic study is performed in which the  $J/\psi$  mass and width in the data are fixed to the average values of  $\mu = 3093 \text{ MeV}/c^2$  and  $\sigma = 39.6 \text{ MeV}/c^2$ . The  $J/\psi$  mass and width in the MC simulation show a stronger dependence on the kinematic variables, therefore, they remain free parameters for fits to MC-simulated invariant mass spectra. The influence of fixing the mass and width on the  $J/\psi$  yield ratio is negligible, as can be seen from Fig. 6.3 (a).

### Efficiency Correction Method

The standard method to obtain the efficiency-corrected distribution of  $J/\psi$  from the raw number of  $J/\psi$  is a one-dimensional correction, i.e. a correction performed bin by bin in a single kinematic variable. This method is easy to implement and robust. However, correlations between the kinematic variables are neglected. In order to test the influence of the method of efficiency correction on  $R_j^{J/\psi}$ , the  $J/\psi$  yield ratios obtained by two alternative efficiency correction methods are compared with the result of the one-dimensional bin-by-bin correction.

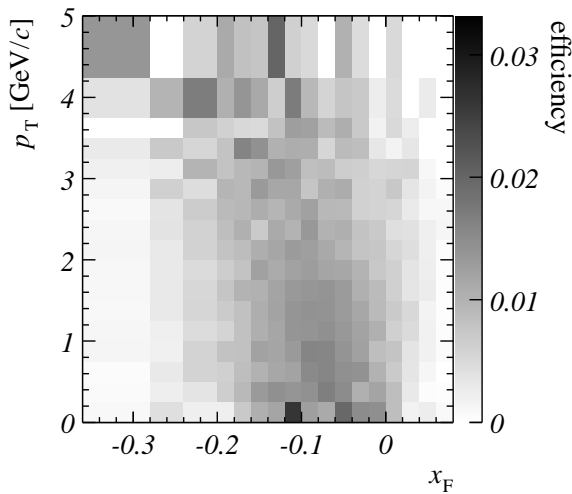


**Figure 6.4:** Correlation of the  $x_F$  and  $p_T$  efficiencies. The efficiency is calculated as the ratio of reconstructed to generated MC events for a matrix of  $17 \times 17$  bins in  $x_F$  and  $p_T$ . The simulation is performed for the wire combination I1B1 in the calibration period of November 2002.

The method of Bayesian unfolding [D’A95] (see also Section 5.3.1) is applied for a single kinematic variable. In the unfolding algorithm, more information from the MC simulation is utilized than in the one-dimensional efficiency correction by taking into account the probability for an event to “migrate” between different bins of the kinematic distributions. The resulting J/ψ yield ratio as a function of  $p_T$  is compared to the result of the standard analysis in Fig. 6.3 (a). The influence on the J/ψ yield ratio is small if it is compared to the statistical uncertainties.

If the bin-by-bin correction is performed only in a single kinematic variable, it is assumed that all other variables and their correlations are properly modelled in the MC simulation. The HERA-B MC simulation does not include correlations between  $x_F$  and  $p_T$ . However, as can be seen from Fig. 6.4, the  $x_F$  and  $p_T$  efficiencies are correlated. For large transverse momenta, the  $x_F$  range covered by the HERA-B experiment is extended to larger negative  $x_F$  values. As it is shown in Section 4.3.5, the description of the  $x_F$  distribution of J/ψ in the MC simulation and the data reveals discrepancies for large negative  $x_F$  and values of  $x_F > 0$ . To check the influence of the discrepancies in  $x_F$  on the  $x_F$  and  $p_T$  distributions, a two-dimensional efficiency correction is performed. The efficiency is obtained from a MC simulation in which the number of generated and reconstructed J/ψ is determined for two-dimensional intervals in  $x_F$  and  $p_T$ . For both variables, the same binning as in the one-dimensional case is used, hence the events are distributed over  $6 \times 7$  bins. To avoid instabilities of the invariant mass fits due to the low average number of J/ψ in single bins, the J/ψ mass and width are fixed to their average values of  $\mu = 3093 \text{ MeV}/c^2$  and  $\sigma = 39.6 \text{ MeV}/c^2$ . In addition, the determination of the amount and the shape of the background in the invariant mass spectrum is complicated by low statistics. Therefore, no background is added to the MC signal before the invariant mass fit. The resulting change in the J/ψ yield ratio is shown in Fig. 6.3 (a), for which the two-dimensional matrix of yield ratios is projected on  $p_T$ . The two-dimensional correction method shows a systematic influence on the transverse momentum distribution of J/ψ yields which is of the same size as the statistical uncertainties.

### Event Selection Criteria

Further systematic changes in the ratio of  $J/\psi$  yields could arise from employing different criteria to select events with  $J/\psi$  candidates. By imposing stronger cuts on the quality of the tracks and vertices, a cleaner sample is obtained, albeit with a lower number of events. In order to test the influence of the  $J/\psi$  selection on the  $J/\psi$  yield ratio, the following three additional cuts are applied:

- The average transverse momenta of muons from the two-body decay  $J/\psi \rightarrow \mu^+ \mu^-$  follows a distribution with a maximum at half the  $J/\psi$  mass. The transverse momenta of background events are mostly smaller than  $1 \text{ GeV}/c$ . Therefore, background is suppressed by increasing the standard cut of  $p_T > 0.7 \text{ GeV}/c$  to  $p_T > 1.2 \text{ GeV}/c$ .
- The standard cut on the muon likelihood of  $l_{\text{mu}} > 0.01$  selects almost all tracks in an event which are matched to hits in the muon detector. By increasing the cut to a value of  $l_{\text{mu}} > 0.1$ , a cleaner set of muons is selected.
- Pairs of muons are fitted to two-prong vertices. A larger fraction of random combinations of background muons is suppressed if the minimum  $\chi^2$  probability of the vertex fit is increased from  $10^{-5}$  to  $0.1$ .

The resulting  $J/\psi$  yield ratios as a function of  $p_T$  are shown in Fig. 6.3 (b). The influence of the stricter muon likelihood cut is small compared to the statistical uncertainties. However, the transverse momentum cut and the vertex probability cut show sizable effects.

### 6.1.5 Summary of Systematic Uncertainties

The results of the systematic studies on the MC efficiency ratio and the ratio of  $J/\psi$  yields are summarized in Tables 6.1 and 6.2. For all bins of the  $x_F$  and the  $p_T$  distributions, the  $\chi^2$  values of the deviations from the standard analysis are calculated according to Eq. (6.1) and compared to the expectation value of  $n - 1$  for  $n$  bins.

The largest influence on the efficiency ratio, both as a function of  $x_F$  and  $p_T$ , originates from the variation of the muon pad cell and POL efficiencies. The uncertainty of the  $J/\psi$  yield ratio is dominated by the effect of changing the one-dimensional to a two-dimensional efficiency correction. Less important but still sizable is the influence of the transverse momentum cut and the vertex probability cut. All these uncertainties will be included in the evaluation of systematic uncertainties of the final result. All other systematic uncertainties are much smaller than the statistical uncertainty and will therefore be neglected. The largest value of  $\chi^2/(n - 1)$  neglected for the final evaluation of the systematic uncertainties corresponds to a probability of 97% that the distribution of efficiency ratios or yield ratios obtained from the systematic study is compatible with the nominal distribution.

**Table 6.1:** Summary of systematic uncertainties of the efficiency ratio for the wire combination I1B1 in the calibration period of November 2002. The cumulative effects of the systematic studies for  $n$  bins in  $x_F$  or  $p_T$  are quoted as  $\chi^2/(n-1)$ .

Systematic Study	$x_F : \chi^2/(n-1)$	$p_T : \chi^2/(n-1)$
$x_F$ Slope $C-1$	0.050/5	0.056/6
$x_F$ Slope $C+1$	0.050/5	0.155/6
$p_T$ Slope $p_{0,11} = 3.0 \text{ GeV}/c, p_{0,B1} = 2.8 \text{ GeV}/c$	0.009/5	0.091/6
$p_T$ Slope $p_{0,11} = 3.0 \text{ GeV}/c, p_{0,B1} = 3.0 \text{ GeV}/c$	0.543/5	0.053/6
$p_T$ Slope $p_{0,11} = 3.2 \text{ GeV}/c, p_{0,B1} = 2.8 \text{ GeV}/c$	0.520/5	0.092/6
$p_T$ Slope $p_{0,11} = 3.2 \text{ GeV}/c, p_{0,B1} = 3.0 \text{ GeV}/c$	0.011/5	0.038/6
Uniform FLT Efficiency	0.379/5	0.340/6
Swapped Muon Efficiencies	5.974/5	13.540/6
SLT Target Box	0.225/5	0.358/6

**Table 6.2:** Summary of systematic uncertainties of the J/ψ yield ratio for the wire combination I1B1 in the calibration period of November 2002. The cumulative effects of the systematic studies for  $n$  bins in  $x_F$  or  $p_T$  are quoted as  $\chi^2/(n-1)$

Systematic Study	$x_F : \chi^2/(n-1)$	$p_T : \chi^2/(n-1)$
Bayesian Unfolding	0.344/5	0.762/6
Fixed J/ψ Mass/Width	0.882/5	0.951/6
Two-Dimensional Correction	1.273/5	4.749/6
Muon $p_T > 1.2 \text{ GeV}/c$	1.185/5	1.432/6
Muon Likelihood $1_{\text{mu}} > 0.1$	0.357/5	0.099/6
Vertex $\text{prob}(\chi^2, n_{\text{dof}}) > 0.1$	1.301/5	1.794/6

## 6.2 Nuclear Effects in J/ψ Production

In the previous section, the methods to extract the J/ψ yield ratios and to correct the J/ψ yield by the ratio of efficiencies have been described. Before the combined result of the measurement of nuclear effects in J/ψ production is presented, the methods available to combine the results of all calibration periods are introduced. The full analysis chain is applied first to a control sample, in which no nuclear effects can be extracted from the ratio of cross sections. Finally, the combined results of this analysis are presented and compared with results of previous experiments and with theoretical predictions.

## 6.2.1 Combination of Data Samples

### Weighted Average of Single Results

Results obtained from different subsets of the data are combined by the method of uncertainty-weighted averages:

$$\alpha = \frac{\sum_{i=1}^n w_i \alpha_i}{\sum_{i=1}^n w_i}, \quad \text{with } w_i = \frac{1}{\sigma_i^2}. \quad (6.7)$$

Here,  $\alpha$  is the combined result,  $n$  is the number of subsets,  $\alpha_i$  are the subset results, and  $\sigma_i$  are the uncertainties of the subset results. If the subsets are independent of each other, the uncertainty of  $\alpha$  is obtained by Gaussian error propagation:

$$\sigma_\alpha^2 = \frac{1}{\sum_{i=1}^n w_i}. \quad (6.8)$$

The consistency of the average results within the uncertainties can be tested by evaluating the  $\chi^2$  statistic:

$$\chi^2 = \sum_{i=1}^n w_i (\alpha_i - \alpha)^2, \quad (6.9)$$

which has the expectation value  $n - 1$  if the uncertainties of the single results follow a Gaussian distribution. Eq. (6.9) allows an a-posteriori test of the size of the uncertainties assigned to the single measurements. The uncertainties are correctly determined if a value of  $\chi^2/(n - 1) \approx 1$  is obtained.

### Measurement Principle

In the HERA-B experiment, the nuclear suppression parameter  $\alpha$  is determined in runs with two wire targets operated simultaneously by measuring the following three ratios;

- the ratio of  $J/\psi$  yields on the carbon and the tungsten wire,  $N^C$  and  $N^W$ ,
- the ratio of the efficiencies  $\varepsilon^C$  and  $\varepsilon^W$ , and
- the ratio of the luminosities  $\mathcal{L}^C$  and  $\mathcal{L}^W$ :

$$\alpha \propto \log \left( \frac{N^W}{N^C} \cdot \frac{\varepsilon^C}{\varepsilon^W} \cdot \frac{\mathcal{L}^C}{\mathcal{L}^W} \right). \quad (6.10)$$

The advantage of such a relative measurement is that all  $J/\psi$  are influenced in the same way by systematic effects of the detector and trigger, regardless on which of the target wires they are produced. All time variations of the efficiencies cancel out by calculating ratios of the measured quantities. However, Eq. (6.10) cannot be applied directly. It has to be translated into a measurement prescription which preserves the ‘‘cancellation mechanism’’ and allows to extract a meaningful result from data samples with limited statistical precision at the same time. The choice of the measurement prescription is restricted by the following aspects.

- The number of  $J/\psi$  is determined from fitting the number of signal and background events in the invariant mass spectrum of muon pairs. With this method, a minimum number of  $J/\psi$  is required to obtain stable fits to the spectrum and to separate the  $J/\psi$  signal from the background.

- The detector and trigger efficiencies derived from the MC simulation are averaged over calibration periods. Hence, they are only valid if the efficiency corrections are applied to all data from the entire calibration period.
- The luminosity is determined from events recorded with the random trigger, which is operated in parallel to the dilepton trigger. The luminosity determination is based on counting primary vertices. The statistical precision of this procedure requires a minimum number of vertices. Therefore, luminosities are evaluated on a run-by-run basis.

In the following, two alternative methods of extracting a combined result on  $\alpha$  for all runs in all calibration periods are discussed.

### Method I: Combination of Calibration Periods

Using the method of combining entire calibration periods, the final nuclear suppression parameter  $\alpha$  is obtained in two steps. For all calibration periods  $j$ , the suppression parameter  $\alpha_j$  is calculated separately, and  $\alpha$  is given by the weighted average of all  $\alpha_j$ . This strategy is motivated by the fact that the efficiencies derived from the MC simulation are average efficiencies for entire calibration periods. To obtain  $\alpha_j$ , the events of all runs in a period are summed, and the J/ψ yield is determined from a fit to the sum of the invariant mass spectra. The J/ψ yield is corrected by the MC efficiencies  $\varepsilon_j^{C,W}$  and by the sum of the single-run luminosities. If the luminosities of different runs are combined, a correction for the varying random trigger rates is required. Due to the low trigger rates of the order of 100 Hz compared to the interaction rate of 5 MHz, the probability for an event to be triggered by the random and the dilepton trigger at the same time is negligible. Therefore, the total number of events in a run is given by the sum of the number of random-triggered and dilepton-triggered events to a good approximation. Hence, an appropriate correction factor is the ratio  $r^{\text{trig}}$  of dilepton triggers to random triggers:

$$r^{\text{trig}} = \frac{\text{number of dilepton triggers}}{\text{number of random triggers}}. \quad (6.11)$$

By correcting the luminosity with  $r^{\text{trig}}$ , the fraction of luminosity acquired in random-triggered events is scaled to the luminosity fraction acquired with the dilepton trigger. Thus, the “trigger density” of all runs is equalized. The values of  $r^{\text{trig}}$  for all runs analyzed for this thesis are extracted from the database of the HERA–B data acquisition system and listed in Appendix C. In summary, the prescription to extract  $\alpha_j$  reads:

$$\alpha_j \propto \log \left( \frac{\varepsilon_j^C}{\varepsilon_j^W} \cdot \frac{\sum_i N_i^W}{\sum_i N_i^C} \cdot \frac{\sum_i r_i^{\text{trig}} \mathcal{L}_i^C}{\sum_i r_i^{\text{trig}} \mathcal{L}_i^W} \right), \quad (6.12)$$

where the run index  $i$  is restricted to all runs in the calibration period  $j$ . If the method of combining entire calibration periods is used, the number of J/ψ and the luminosities can be determined with good precision. However, the sum of ratios in Eq. (6.10) is replaced by a ratio of sums, and no explicit cancellation of efficiencies is achieved.

### Method II: Combination of Single Runs

A method which preserves the cancellation of efficiencies must be based on the evaluation of  $\alpha$  for short time intervals. A compromise between short time intervals and good statistical precision of the individual results is found in the evaluation of  $\alpha$  on a run-by-run basis:

$$\alpha_{ij} \propto \log \left( \frac{\epsilon_j^C}{\epsilon_j^W} \cdot \frac{N_i^W}{N_i^C} \cdot \frac{\mathcal{L}_i^C}{\mathcal{L}_i^W} \right). \quad (6.13)$$

The luminosity weight  $r^{\text{trig}}$  required for the method of combining calibration periods cancels out in this approach. The combined result on  $\alpha$  is obtained from the weighted average of the results for all runs  $i$  in all calibration periods  $j$ . The ratio of efficiencies obtained from the MC simulation is averaged over all runs in a calibration period. Therefore, it can be applied as an average correction if all runs in the period are analyzed, although the correction may not be appropriate for single runs. Due to the small number of  $J/\psi$  in some runs, the method of combining single runs introduces uncertainties in the determination of the number of  $J/\psi$  by a fit to the invariant mass spectrum. To stabilize the fit, the  $J/\psi$  mass and width are fixed to their average values of  $\mu = 3093 \text{ MeV}/c^2$  and  $\sigma = 39.6 \text{ MeV}/c^2$ .

### Comparison of the Methods

Both methods of combining single data sets are tested on data from the wire combination I1B1 in the calibration period of November 2002. A comparison of the resulting nuclear suppression parameter  $\alpha$  as a function of  $x_F$  and  $p_T$  is shown in Fig. 6.5. The difference between the methods is very small compared to the statistical uncertainties of the measurement. The method of averaging single runs has the advantage that due to the relatively short time period of single runs, the cancellation mechanism is preserved to a good approximation. In addition, slightly better statistical uncertainties of the combined results are achieved. Furthermore, no additional correction factors are required, as for the luminosity ratio in the method of averaging entire calibration periods. Therefore, the method of averaging single runs is chosen to present combined results of the nuclear suppression parameter  $\alpha$  in the following.

### 6.2.2 Control Sample

To establish the effects of nuclear suppression in  $J/\psi$  production, the analysis applied to data collected in two-wire runs with carbon and tungsten targets is also applied to a control sample in which no nuclear effects can be measured. For this purpose, a data sample of comparable size to the carbon-tungsten samples was recorded with the carbon-carbon combination B1I2 during the calibration period of January 2003 (II). By analyzing the control sample, the uncertainties of the absolute normalization and the kinematic dependence of nuclear suppression are quantified. The ratio of cross sections on the two wires in a run  $i$ ,

$$R_i^{\text{CC}} = \frac{\sigma_i^{\text{B1}}}{\sigma_i^{\text{I2}}} = \frac{N_i^{\text{B1}}}{N_i^{\text{I2}}} \cdot \frac{\epsilon^{\text{I2}}}{\epsilon^{\text{B1}}} \cdot \frac{\mathcal{L}_i^{\text{I2}}}{\mathcal{L}_i^{\text{B1}}}, \quad (6.14)$$



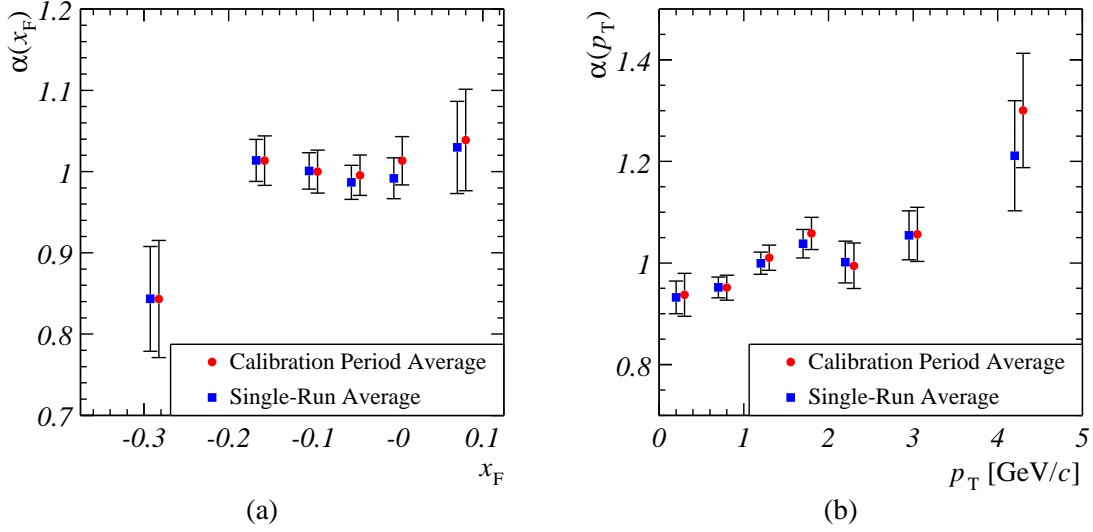


**Figure 6.5:** Comparison of methods to combine data sets for the wire combination I1B1 in November 2002. (a)  $x_F$  distribution. (b)  $p_T$  distribution. The data points are shifted from the bin centers for better visibility. The scales on the y-axes are zero-suppressed.

is determined for all runs of the wire combination B1I2, and the weighted average  $R^{\text{CC}}$  is calculated. The cross section ratio is expected to have a value  $R^{\text{CC}} = 1$  and to be independent of the kinematic variables. The observed distributions of  $R^{\text{CC}}$  as a function of  $x_F$  and  $p_T$  are depicted in Fig. 6.6, together with the fit results. Within the statistical uncertainties, all distributions are compatible with a value of  $R^{\text{CC}} = 1$ .

The analysis of the control sample shows that the influence of systematic effects on the shape and the normalization of the nuclear suppression measurement is small. However, the shapes of the  $x_F$  and  $p_T$  distributions of  $R^{\text{CC}}$  suggest that  $R^{\text{CC}}$  is systematically overestimated around  $x_F = -0.1$  and underestimated for large  $p_T$ . The control sample contains only a single wire combination from a single calibration period, and different uncertainties could be present in other subsamples of the full data set. At the time of writing this thesis, a small remaining discrepancy between the data and the MC simulation exists, as discussed in Section 4.3. However, there are no indications for large uncertainties.

### 6.2.3 Nuclear Suppression Parameter

#### Combined Result

The central result of this thesis, a measurement of the nuclear suppression parameter  $\alpha$ , is presented in this section. The final result on  $\alpha$  is obtained from a combination of all two-wire runs by the method of averaging single runs. In Fig 6.7, the combined result for  $\alpha$  is presented as a function of the kinematic variables  $x_F$ ,  $p_T$ , and  $y$ . The numerical values of  $\alpha$  as a function of  $x_F$ ,  $p_T$ , and  $y$  are summarized in Tables 6.3, 6.4, and 6.5, together with their statistical and systematic uncertainties. The measured distributions of  $\alpha$ —separately for each wire configuration and calibration period—are shown in Appendix D, Figs. D.13, D.14, and D.15.

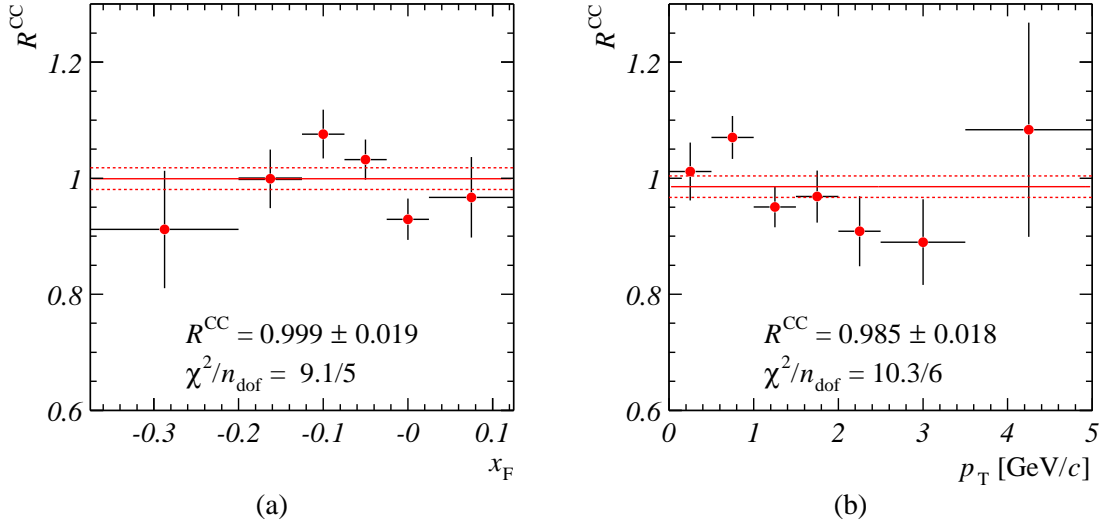


**Figure 6.6:** Average cross section ratio  $R^{\text{CC}}$  measured in the control sample from the wire combination B112 in the calibration period of January 2003 (II). (a)  $x_F$  dependence. (b)  $p_T$  dependence. The lines indicate the central values and statistical uncertainties of fits to the distributions with a constant. The y-scales are zero-suppressed.

The measurement of  $\alpha(x_F)$  extends existing measurements of nuclear effects in  $J/\psi$  hadroproduction at fixed-target energies to the previously unexplored region of  $-0.375 < x_F < -0.1$ . The observed nuclear suppression in this region is very similar to the suppression for  $x_F \gtrsim -0.1$ , where  $\alpha(x_F)$  can be compared with previous results. The nuclear suppression parameter increases with increasing  $p_T$ . For large transverse momenta, values of  $\alpha > 1$  are observed, i.e. an enhancement of  $J/\psi$  production. This behavior of  $\alpha(p_T)$  is a consequence of transverse momentum broadening, as described in Section 3.4.1. The rapidity distribution of the nuclear suppression is strongly correlated with the  $x_F$  distribution. Therefore, the measurement of  $\alpha(y)$  serves as a cross-check of  $\alpha(x_F)$  with better resolution in the kinematic range of  $x_F \approx 0$ . The distribution of  $\alpha(y)$  shows a slightly increasing  $\alpha$  with decreasing  $y$ . However, within the uncertainties, this effect is not significant.

As a test of the consistency of the uncertainties assigned to the measurement, the  $\chi^2$  statistic of the weighted average is evaluated. As shown in Tables 6.3, 6.4, and 6.5, the values of  $\chi^2/n_{\text{dof}}$  are smaller than unity for almost all bins of the kinematic variables. Therefore, the size of the statistical uncertainties assigned to the measurement is realistic.

### Systematic Uncertainties

The total systematic uncertainty of the measurement of the nuclear suppression parameter  $\alpha$  is calculated from all significant effects observed in the previous studies of systematic uncertainties. Systematic uncertainties found in the efficiency ratio, in the  $J/\psi$  yield ratio, and in the ratio of luminosities are combined. For each bin of the  $x_F$ ,  $p_T$ ,

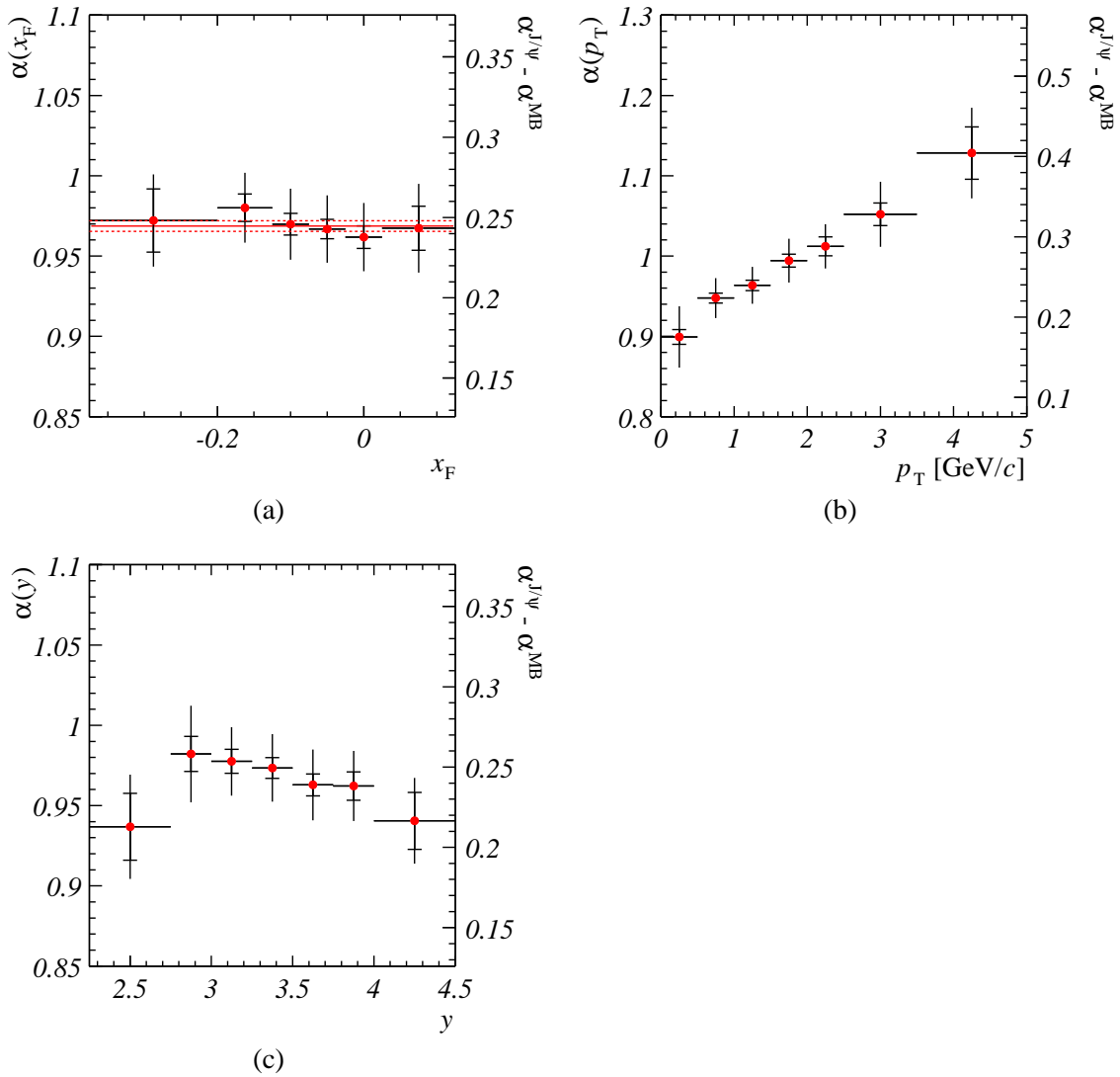


**Figure 6.7:** Nuclear suppression parameter  $\alpha$  as a function of  $x_F$ ,  $p_T$ , and  $y$ . In addition to the absolute value of  $\alpha$ , the value of  $\alpha$  is shown relative to the nuclear suppression parameter for the minimum-bias cross section,  $\alpha^{MB}$ . (a)  $x_F$  distribution, average value of  $\alpha(x_F)$  (solid line), and uncertainty of average (dashed lines). (b)  $p_T$  distribution. (c)  $y$  distribution. The error bars indicate the statistical uncertainties and the quadratic sum of the statistical and the systematic uncertainties. The scales on the y-axes are zero-suppressed.

**Table 6.3:** Nuclear suppression parameter  $\alpha$  as a function of  $x_F$ . For all bins of the  $x_F$  distribution, the measured values of  $\alpha(x_F)$  are presented together with their statistical and systematic uncertainties and the quality of the weighted average.

Bin Number	Minimum $x_F$	Maximum $x_F$	$\alpha(x_F)$	$\chi^2/n_{\text{dof}}$	Systematic Uncertainty
1	-0.375	-0.200	$0.972 \pm 0.020$	77.3/140	0.021
2	-0.200	-0.125	$0.980 \pm 0.009$	121.0/140	0.020
3	-0.125	-0.075	$0.970 \pm 0.007$	117.7/140	0.021
4	-0.075	-0.025	$0.967 \pm 0.006$	146.0/140	0.020
5	-0.025	0.025	$0.962 \pm 0.007$	125.7/140	0.020
6	0.025	0.125	$0.967 \pm 0.014$	103.1/140	0.024

**Table 6.4:** Nuclear suppression parameter  $\alpha$  as a function of  $p_T$ . For all bins of the  $p_T$  distribution, the measured values of  $\alpha(p_T)$  are presented together with their statistical and systematic uncertainties and the quality of the weighted average.

Bin Number	Minimum $p_T$ [GeV/c]	Maximum $p_T$ [GeV/c]	$\alpha(p_T)$	$\chi^2/n_{\text{dof}}$	Systematic Uncertainty
1	0.0	0.5	$0.899 \pm 0.009$	109.5/140	0.037
2	0.5	1.0	$0.948 \pm 0.006$	127.3/140	0.024
3	1.0	1.5	$0.964 \pm 0.007$	153.6/140	0.022
4	1.5	2.0	$0.994 \pm 0.008$	117.8/140	0.026
5	2.0	2.5	$1.012 \pm 0.012$	103.1/140	0.025
6	2.5	3.5	$1.052 \pm 0.014$	77.0/140	0.038
7	3.5	5.0	$1.128 \pm 0.033$	45.9/140	0.046

**Table 6.5:** Nuclear suppression parameter  $\alpha$  as a function of  $y$ . For all bins of the  $y$  distribution, the measured values of  $\alpha(y)$  are presented together with their statistical and systematic uncertainties and the quality of the weighted average.

Bin Number	Minimum $y$	Maximum $y$	$\alpha(y)$	$\chi^2/n_{\text{dof}}$	Systematic Uncertainty
1	2.25	2.75	$0.937 \pm 0.021$	72.0/140	0.025
2	2.75	3.00	$0.982 \pm 0.011$	119.8/140	0.028
3	3.00	3.25	$0.978 \pm 0.007$	153.7/140	0.020
4	3.25	3.50	$0.973 \pm 0.007$	132.8/140	0.020
5	3.50	3.75	$0.963 \pm 0.007$	115.2/140	0.021
6	3.75	4.00	$0.962 \pm 0.009$	119.2/140	0.020
7	4.00	4.50	$0.941 \pm 0.018$	92.5/140	0.020

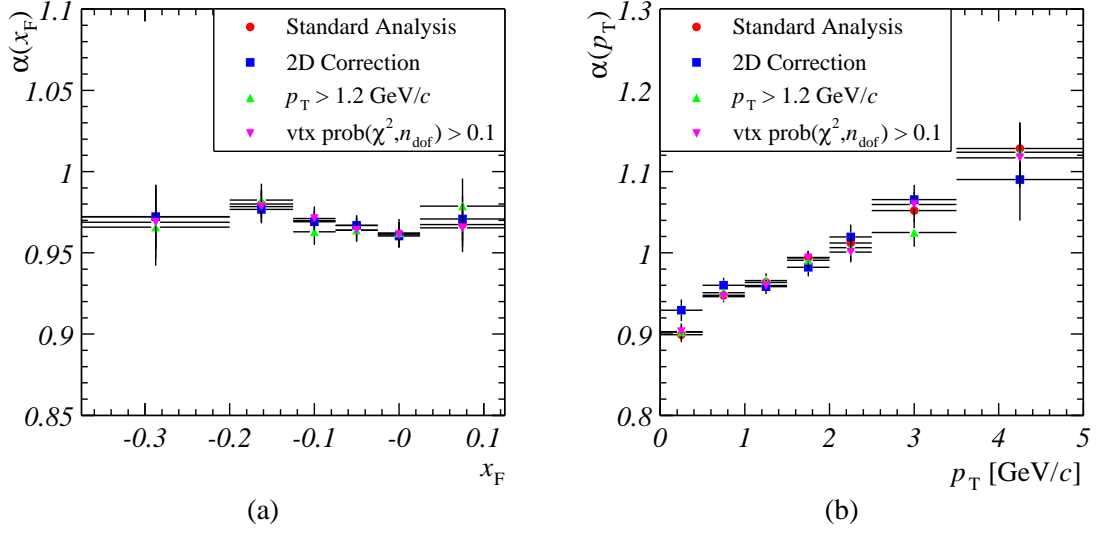


**Figure 6.8:** Systematic uncertainties of the nuclear suppression parameter  $\alpha$ . (a)  $x_F$  distributions. (b)  $p_T$  distributions. The standard analysis is compared to modified versions of the analysis, in which two-dimensional efficiency corrections and stricter cuts on the transverse momenta of the muons and on the probability of the vertex fit are performed. The scales on the y-axes are zero-suppressed.

and  $y$  distributions, the systematic uncertainties are added in quadrature. The following main sources of systematic effects are identified.

- *Selection criteria for  $J/\psi$  candidates.* As an alternative to the standard selection, transverse momenta larger than 1.2 GeV/c are required during the selection of muons, and dimuon vertices are accepted if their  $\chi^2$  probability is greater than 0.1.
- *Method of efficiency correction.* The efficiency correction is performed using a two-dimensional matrix of efficiencies as a function of  $x_F$  and  $p_T$  instead of one-dimensional corrections in  $x_F$  and  $p_T$  separately.
- *Efficiencies of the muon detector and the muon pretrigger.* The efficiency ratio of the muon pretrigger is calculated for muon pad cell and POL efficiencies from a different calibration period.
- *Method of luminosity determination.* The luminosity ratio is extracted from a track-counting method instead of the standard method of counting primary vertices.

The systematic uncertainties due to additional analysis cuts are determined from a comparison of the final value of the nuclear suppression parameter obtained from the standard analysis with the value obtained by using the additional cuts. Similarly, the one-dimensional efficiency correction is replaced by a two-dimensional correction for the entire data set. The resulting projections of the nuclear suppression parameter  $\alpha(x_F, p_T)$  on  $x_F$  and  $p_T$  are compared to the results of the standard analysis. The results of these comparisons are depicted in Fig. 6.8. The estimate of the uncertainty due to the efficiency of the muon detector and the muon pretrigger is obtained from applying the efficiencies valid for the calibration period of October 2002 to data taken in November 2002. The deviations observed for the wire combinations I1I2 and I1B1 are scaled to the

full efficiency ratio, averaged, and utilized as the systematic uncertainty, as discussed in Section 6.1.3. The determination of systematic uncertainties in the measurement of the luminosity ratio is described in Section 5.3.

All significant systematic uncertainties of the nuclear suppression parameter  $\alpha$  are summarized in Table 6.6. The dominant source of systematic uncertainties is the luminosity determination which accounts for uncertainties of 0.019 for all bins of the kinematic distributions. The systematic effect due to the muon detector and muon pre-trigger efficiencies is smaller than 0.01 for most kinematic bins. The efficiency correction method has little influence on  $\alpha(x_F)$ . However, uncertainties of 0.01 and larger are found for  $\alpha(p_T)$ . The systematic influence of changing the  $J/\psi$  selection criteria is the smallest of the effects under study.

## 6.2.4 Comparison to Previous Experiments

One of the most important motivations to perform a measurement of nuclear effects in  $J/\psi$  production at HERA-B is the possibility to extend the kinematical range of the nuclear suppression parameter  $\alpha(x_F)$  to negative values of  $x_F$ . This analysis covers the range of  $-0.375 < x_F < 0.125$ . In the entire range, the nuclear suppression parameter is approximately constant. Therefore, as a first step, an average value  $\bar{\alpha}$  is calculated by fitting a constant to the  $x_F$  distribution of  $\alpha$ :

$$\bar{\alpha} = 0.969 \pm 0.003(\text{stat.}) \pm 0.021(\text{syst.}) \quad \text{for } -0.375 \leq x_F < 0.125. \quad (6.15)$$

The statistical uncertainty of the average is taken from the fit, and the systematic uncertainty is the arithmetic mean of the systematic uncertainties of all data points. The result of this analysis is in agreement with a previous analysis within the HERA-B collaboration, which is based on data taken during the HERA-B commissioning run in 2000 [Bru02b]:

$$\begin{aligned} \alpha(J/\psi \rightarrow \mu^+ \mu^-) &= 1.02 \pm 0.04(\text{stat.}) \pm 0.02(\text{syst.}) \quad \text{for } -0.105 < x_F < 0.017, \\ \alpha(J/\psi \rightarrow e^+ e^-) &= 0.93 \pm 0.07(\text{stat.}) \pm 0.02(\text{syst.}) \quad \text{for } -0.056 < x_F < 0.032. \end{aligned}$$

The estimate of the systematic uncertainties of the previous analysis is smaller than the value assumed for this analysis, because an uncertainty of approximately 0.01 is assigned to the luminosity determination, whereas this analysis finds a value of 0.019.

The value obtained for  $\bar{\alpha}$  is compared to results of previous experiments which cover a kinematic range close to  $x_F = 0$ :

$$\bar{\alpha} = \begin{cases} 0.955 \pm 0.010 & \text{for } -0.1 \leq x_F < 0.1 \quad \text{averaged from E866 [Lei00],} \\ 0.925 \pm 0.015 & \text{for } -0.1 \leq x_F < 0.1 \quad \text{NA50 [Ale04].} \end{cases} \quad (6.16)$$

Both values of  $\bar{\alpha}$  include statistical and systematic uncertainties. The value of  $\bar{\alpha}$  is compatible with the result of the E866 experiment. The average nuclear suppression parameters measured in this analysis and in E866 are slightly larger than value measured in the NA50 experiment.

In addition to the average value, also the shape of the nuclear suppression parameter  $\alpha$  is compared to previous experiments. Comparisons of the  $x_F$  and the  $p_T$  distributions

**Table 6.6:** Summary of systematic uncertainties on the nuclear suppression parameter  $\alpha$  as a function of the  $J/\psi$  kinematics. The uncertainties due to stricter cuts on the transverse momenta of the muons and on the vertex probability, due to the method of efficiency corrections, due to the ratio of muon efficiencies, and due to the ratio of luminosities are shown for all bins of the  $x_F$ ,  $p_T$ , and  $y$  distributions. The bin numbering is the same as in Tables 6.3, 6.4, and 6.5.

Bin Number	Transv. Momentum $p_T > 1.2 \text{ GeV}/c$	Vertex Prob. $> 0.1$	2D Efficiency Correction	Muon Efficiencies	Luminosity Ratio
$\alpha(x_F)$					
1	0.006	0.003	$< 0.001$	0.007	0.019
2	0.002	0.002	0.003	0.003	0.019
3	0.007	0.001	0.001	0.006	0.019
4	0.003	0.003	$< 0.001$	0.005	0.019
5	$< 0.001$	0.001	0.002	0.007	0.019
6	0.011	0.002	0.003	0.008	0.019
$\alpha(p_T)$					
1	0.003	0.004	0.030	0.007	0.019
2	0.003	0.002	0.013	0.007	0.019
3	0.002	0.004	0.005	0.008	0.019
4	0.004	0.001	0.012	0.012	0.019
5	0.006	0.011	0.008	0.008	0.019
6	0.027	0.008	0.013	0.010	0.019
7	0.005	0.011	0.038	0.011	0.019
$\alpha(y)$					
1	0.003	0.008	–	0.014	0.019
2	0.013	0.011	–	0.011	0.019
3	0.007	0.002	–	0.001	0.019
4	0.006	0.003	–	0.002	0.019
5	0.002	0.001	–	0.009	0.019
6	0.001	0.006	–	0.003	0.019
7	0.005	0.002	–	0.002	0.019

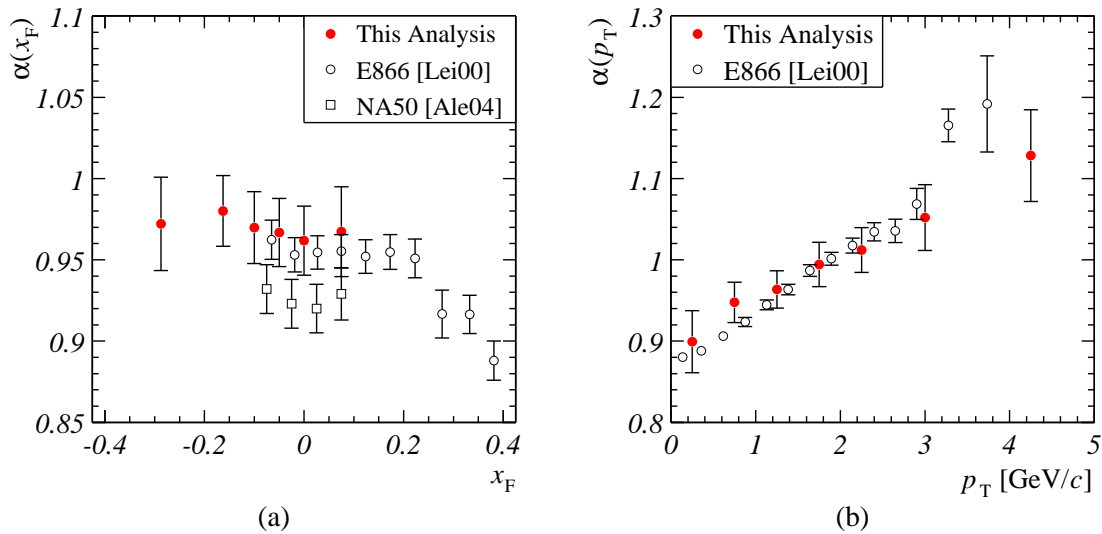


**Figure 6.9:** Nuclear suppression parameter  $\alpha$  compared to results of previous experiments. (a)  $x_F$  distribution compared to E866 [Lei00] and NA50 [Ale04]. (b)  $p_T$  distribution compared to the SXF (small- $x_F$ ) setup of E866. The error bars indicate the quadratic sum of the statistical and the systematic uncertainties. The scales on the y-axes are zero-suppressed.

of  $\alpha$  are shown in Fig. 6.9. The transverse momentum distribution of  $\alpha$  agrees well with the distribution measured by the E866 experiment for the SXF (small- $x_F$ ) configuration. In the overlap region of  $\alpha(x_F)$ , i.e. for  $x_F > -0.1$ , the result of this analysis is compatible with the E866 result, and both results are slightly larger than the result of the NA50 experiment. All three distributions follow the same “U”-shaped trend. However, the trend is insignificant if compared to the uncertainties of the results.

Note that the result of this analysis includes a normalization uncertainty due to the nuclear dependence of the minimum-bias cross section, which is not included in the systematic uncertainties. If the minimum-bias cross sections calculated in [Kop04] are used, the average value of  $\alpha$  would be shifted by  $-0.037$ .

### 6.2.5 Scaling with the Momentum Fraction of the Target Parton

The nuclear suppression can be presented as a function of the scaling variable  $x_2$ , which describes the momentum fraction of the target parton involved in the  $J/\psi$  production process. If nuclear suppression is dominated by effects related to the target parton distribution functions, the suppression pattern as a function of  $x_2$  is identical in experiments with different center-of-mass energies  $\sqrt{s}$ , i.e. the suppression “scales with  $x_2$ ”.

In Fig. 6.10, the nuclear suppression parameter  $\alpha(x_2)$  measured in this analysis at  $\sqrt{s} = 41.6$  GeV is compared to previous results of the NA3 experiment at  $\sqrt{s} = 19.4$  GeV and of the E866 experiment at  $\sqrt{s} = 38.8$  GeV. Already the comparison of the NA3 and the E866 results shows that the nuclear suppression for small  $x_2$  cannot be dominated by effects which depend on  $x_2$ . This experimental evidence is confirmed by the result of this analysis. Although HERA-B covers a range in  $x_2$  in



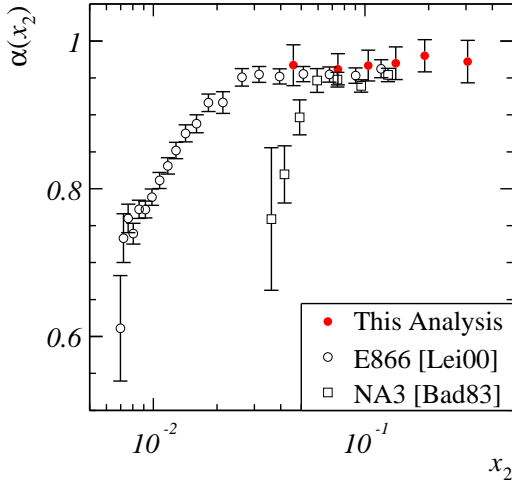


**Figure 6.10:** Scaling of the nuclear suppression parameter with  $x_2$ . The suppression parameter  $\alpha(x_2)$  measured at the HERA-B center-of-mass energy of  $\sqrt{s} = 41.6$  GeV is compared to results of the NA3 and the E866 experiments at  $\sqrt{s} = 19.4$  GeV and  $\sqrt{s} = 38.8$  GeV respectively. The error bars include statistical and systematic uncertainties.

which no strong suppression is observed, there is a small overlap with the region of strong suppression in NA3. The suppression measured in this analysis follows the trend of E866 rather than the one of NA3 in the overlap region.

### 6.2.6 Comparison to Theoretical Predictions

In Fig. 6.11, the  $x_F$  distribution of the nuclear suppression parameter  $\alpha$  is compared to theoretical predictions. In order to cover different approaches of calculating the nuclear suppression, a prediction in which nuclear suppression is due to final state absorption effects [Vog02], and a prediction of the Reggeon-based BCKT model [Bor03] are confronted with the HERA-B data. Both approaches have been introduced in Section 3.4. The model based on final state absorption predicts approximately constant suppression, slightly stronger for  $x_F < -0.2$  due to the different absorption of color-singlet and color-octet states. The BCKT model predicts antiscreening, i.e.  $\alpha > 1$ , for large negative  $x_F$  due to a redistribution of the longitudinal parton momenta. Further theoretical predictions are either already excluded experimentally or do not cover the full  $x_F$  range of HERA-B. Therefore, they are not included in the comparison.

The parameters of the BCKT model are tuned to the nuclear suppression observed in the E866 experiment. As shown in Fig 3.10, the prediction for  $\alpha$  in the region of  $x_F \approx 0$  is below the value measured by E866. Similarly, the absolute normalization of the  $\alpha(x_F)$  measured in this analysis is not described by the model. On the other hand, the predicted shape of the  $x_F$  distribution agrees well with the results of this analysis. However, the  $x_F$  range covered by HERA-B is too small to test the hypothesis of increasing antiscreening for negative  $x_F$ .

The final state absorption model is in good agreement with the nuclear suppression measured in this analysis. However, the precision of the data does not allow to distinguish the suppression of the color-octet pre-resonance  $c\bar{c}$  state from the suppression of the fully formed  $J/\psi$ . Therefore, this analysis is not sensitive to the rather subtle effects related to the time development of the  $J/\psi$  formation process.

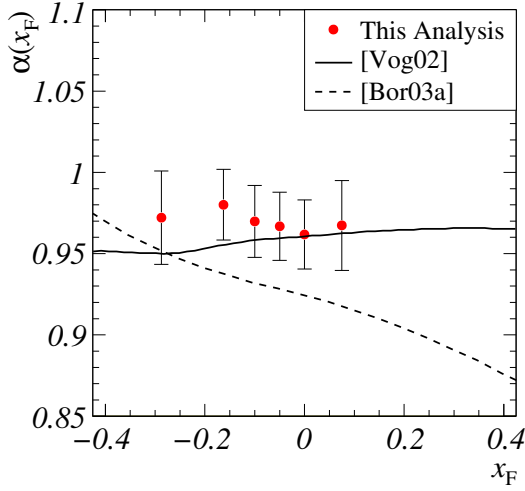


**Figure 6.11:** Nuclear suppression parameter  $\alpha(x_F)$  compared to a prediction of a model based on final state absorption [Vog02] (solid line), and a prediction of the BCKT model [Bor03] (dashed line). The error bars include statistical and systematic uncertainties.

## 6.2.7 Absorption Cross Section in the Glauber Model

An alternative representation of nuclear suppression is given by the  $\langle \rho L \rangle$  parametrization derived from the Glauber model. Assuming that the observed nuclear suppression is due to the absorption of the pre-resonance  $c\bar{c}$  state or the fully formed  $J/\psi$  in the nuclear matter, the cross section  $\sigma^{\text{abs}}$  for the absorption process can be extracted (see Section 3.3.5):

$$\sigma^{\text{abs}} = \frac{\log(R^S)}{\langle \rho L \rangle^C - \langle \rho L \rangle^W} = \frac{(1 - \alpha) \log(A^W/A^C)}{\langle \rho L \rangle^W - \langle \rho L \rangle^C}, \quad (6.17)$$

where  $R^S = (\sigma^W/\sigma^C)/(A^W/A^C)$  is the ratio of suppression factors for the two materials. The values of the parameters  $\langle \rho L \rangle^{C,W}$  depend on the model chosen to describe the nuclear density distributions of the target. The values of  $\langle \rho L \rangle^{C,W}$  used for this analysis are listed in Table 3.3. The resulting absorption cross section as a function of  $x_F$  is shown in Fig. 6.12.

The measured absorption cross section is lower than the values obtained by the NA50 experiment, which reported an average value of  $\bar{\sigma}^{\text{abs}} = 4.4 \pm 0.7$  mb [Ale04]. For some  $x_F$  bins, the uncertainties of the measurement even allow for unphysical absorption cross sections of  $\bar{\sigma}^{\text{abs}} < 0$ . However, the result of this analysis has a large uncertainty in the overall normalization, because  $\sigma^{\text{abs}}$  is proportional to  $1 - \alpha$ . The values shown in Fig. 6.12 are extracted using the value of  $\alpha^{\text{MB}} = 0.724 \pm 0.005$  for the nuclear dependence of the minimum-bias cross section. If the values of the minimum-bias cross section from [Kop04] are used, the absorption cross section is increased to  $\bar{\sigma}^{\text{abs}} \approx 3.3$  mb, closer to the result of NA50. The average value of  $\sigma^{\text{abs}}$  for the result of this analysis is obtained from a fit with a constant function:

$$\bar{\sigma}^{\text{abs}} = (1.45 \pm 0.15(\text{stat.})_{-1.0}^{+2.1}(\text{syst.})) \text{ mb}. \quad (6.18)$$

The statistical uncertainty of  $\bar{\sigma}^{\text{abs}}$  is obtained from the fit, and the systematic uncertainty is the quadratic sum of the scaled uncertainty of the nuclear suppression parameter and of the normalization uncertainty due to the nuclear dependence of the minimum-bias cross section.

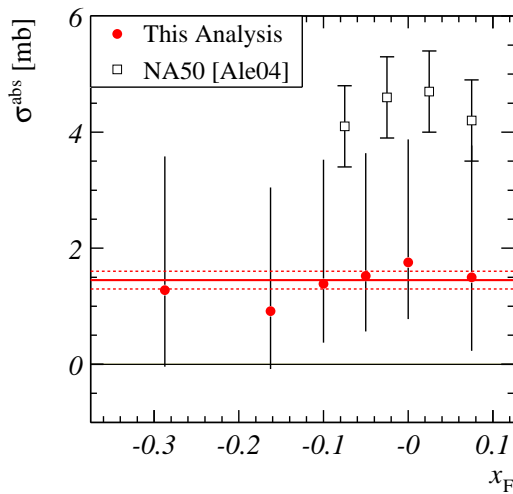


**Figure 6.12:** Nuclear absorption cross section in the  $\langle \rho L \rangle$  parametrization. The absorption cross section  $\sigma^{\text{abs}}$  as a function of  $x_F$  is compared to the results of the NA50 experiment. The central value and the statistical uncertainty of the average absorption cross section is indicated by the solid line and dashed lines. The error bars include statistical, systematic, and normalization uncertainties.

### 6.3 Summary

In this chapter, the main result of this thesis is derived, the nuclear dependence of  $J/\psi$  production. As a first step, the ratio of the  $J/\psi$  detection efficiencies for two target wires is calculated as a function of the kinematic variables. The ratio of the number of reconstructed  $J/\psi$  is corrected by the efficiency ratio and the luminosity ratio, and the nuclear suppression parameter  $\alpha$  is derived. The value of  $\alpha$  is first calculated separately for each run. The combined result of  $\alpha$  for all runs is given by the weighted average of the single-run results.

Detailed studies are performed to determine the systematic uncertainties connected with the measurement of the efficiency ratio and the  $J/\psi$  yield ratios. The largest uncertainties arise from the description of the muon detector and pretrigger efficiencies and from the choice of the method of efficiency corrections. The dominant systematic uncertainty of the nuclear suppression parameter is due to uncertainties in the determination of the luminosity ratio.

The value of the nuclear suppression parameter measured in this analysis is in good agreement with previous results of HERA-B and other experiments in the overlapping kinematic ranges of  $x_F$  and  $p_T$ . The measurement of  $\alpha$  is extended to  $x_F = -0.375$ , a kinematic range previously inaccessible to fixed-target experiments. The nuclear suppression measured in this range is approximately constant. By comparing  $\alpha(x_2)$  with experiments at center-of-mass energies different from the HERA-B center-of-mass energy, the hypothesis of  $x_2$  scaling of the nuclear suppression is disfavored.

The measurement of the nuclear suppression parameter is compared with two different theoretical predictions. A prediction based on final state absorption agrees well with the measurement. However, due to the limited precision of the measurement, no statement with respect to the validity of the theoretical models can be made.

In summary, the measurement of the nuclear dependence of  $J/\psi$  production presented in this chapter shows a small constant suppression of  $J/\psi$  production with a suppression parameter of  $\alpha \approx 0.97$  in the kinematic range of  $-0.375 < x_F < 0.1$ .



---

# Summary and Conclusions

---

In this thesis, a measurement of nuclear effects in the production of  $J/\psi$  mesons at a center-of-mass energy of 41.6 GeV is performed. The data analyzed for the measurement were collected with the HERA-B detector, a fixed-target spectrometer at the HERA storage ring at DESY. In the HERA-B detector,  $J/\psi$  mesons are produced in the interactions of protons with thin wire targets. Nuclear effects are measured by operating two target wires made of different materials simultaneously.

In the HERA-B experiment, leptonic decays of  $J/\psi$  mesons are enriched by a multi-level trigger system. The  $J/\psi$  mesons analyzed in this thesis are reconstructed in the decay channel  $J/\psi \rightarrow \mu^+\mu^-$ . During a five-month data-taking period from October 2002 to February 2003, a sample of approximately 170,000  $J/\psi \rightarrow \mu^+\mu^-$  decays was recorded, approximately 90,000 of which in runs using a carbon and a tungsten target in parallel.

Nuclear effects in interactions of protons with nuclear target materials of atomic mass number  $A$  are commonly represented by a power-law parametrization of the production cross section:  $\sigma_{pA} = \sigma_{pN}A^\alpha$ . The nuclear suppression parameter  $\alpha$  assumes values of  $\alpha < 1$  in the case of nuclear suppression of  $J/\psi$  production and values of  $\alpha > 1$  in the case of enhanced production. In general,  $\alpha$  depends on the kinematics of the  $J/\psi$  production process. In this thesis,  $\alpha$  is measured as a function of Feynman's scaling variable  $x_F$ , the transverse momentum  $p_T$ , and the rapidity  $y$ .

The measurement of the nuclear suppression parameter presented in this thesis is a relative measurement, namely the measurement of the ratio of  $J/\psi$  production cross sections on the two target wires operated simultaneously. By measuring the ratio rather than the absolute values of the cross sections, the influence of many systematic effects is reduced. The measurement of the cross section ratio is based on the determination of three ratios. The ratio of  $J/\psi$  produced on the two target wires is corrected by the ratio of efficiencies and by the ratio of luminosities recorded on the wires.

Events with  $J/\psi$  candidates are selected by a set of standard criteria. Muons from the decay  $J/\psi \rightarrow \mu^+\mu^-$  are identified by the vertex detector, the main tracker, and the muon detector. Pairs of muons are combined to secondary vertices. Dimuon vertices which

are reconstructed close to the target are assigned to one of the target wires. The number of  $J/\psi$  is determined from a fit to the invariant mass spectrum of dimuon vertices.

The efficiency to reconstruct  $J/\psi$  mesons is calculated from a detailed Monte Carlo (MC) simulation of the HERA-B detector and trigger. A reweighting of the kinematical distributions of  $J/\psi$  mesons obtained from the MC event generator is required to match the  $J/\psi$  differential distributions in the MC simulation to the data. The detector and trigger simulation includes realistic efficiencies and masking of defective channels for all detector systems, bit-level simulations of the pretriggers and the Second Level Trigger (SLT), and a parametrization of the efficiency of the First Level Trigger. The different treatment of the two target wires in the SLT is modelled in the MC simulation to a good precision. The overall agreement between the data and the MC simulation is satisfactory. However, small imperfections in the MC description persist.

The MC efficiencies are employed to measure the differential distributions of  $J/\psi$  mesons as a function of the momentum-related kinematic variables  $x_F$ ,  $p_T$ , and  $y$ , and as a function of the angular variables in the Gottfried-Jackson frame,  $\cos \theta_{GJ}$  and  $\phi_{GJ}$ . The shape of the  $x_F$  distribution is rather well described by the shape predicted by NRQCD. For the  $p_T$  distribution, the effect of transverse momentum broadening is observed, i.e. the increase of the average transverse momentum with the atomic mass number of the target. The average transverse momentum for carbon targets is  $\langle p_T \rangle = (1.244 \pm 0.003(\text{stat.})) \text{ GeV}/c$ , and a value of  $\langle p_T \rangle = (1.334 \pm 0.004(\text{stat.})) \text{ GeV}/c$  is measured for tungsten targets. The polarization of the  $J/\psi$  is extracted from the distribution of  $\cos \theta_{GJ}$ . Averaged over data from both, carbon and tungsten targets, a polarization parameter of  $\lambda = -0.047 \pm 0.051(\text{stat.})$  is determined, consistent with no  $J/\psi$  polarization. This finding confirms results of previous experiments and is at variance with the predictions of NRQCD.

The sharing of luminosities among the target wires is determined from the number of reconstructed primary vertices per wire. The number of interactions on a wire is calculated from the observed number of vertices, using vertexing efficiencies determined from a MC simulation. The luminosities are obtained by normalizing the number of interactions to the minimum-bias cross section for the target material. Thus, via the ratio of luminosities, the measurement of nuclear effects in  $J/\psi$  production depends on the nuclear dependence of the minimum-bias cross section.

Detailed studies are performed in order to determine systematic uncertainties of the nuclear dependence measurement. The largest systematic influence on the measurement originates from the method of determining the luminosity ratio. Furthermore, the MC description of the muon detector and pretrigger efficiencies, the method of efficiency corrections and the exact choice of the event selection criteria are identified as important sources of systematic uncertainties. With further improvements of the luminosity determination and the MC description of the HERA-B detector and trigger, and a larger sample of MC-simulated events, a reduction of the systematic uncertainties is feasible.

The central result of this thesis is a measurement of the nuclear suppression parameter  $\alpha$  as a function of  $x_F$ ,  $p_T$ , and  $y$ . The kinematic distributions of  $\alpha$  obtained from a combination of all data samples is presented in Fig. 6.7. Numerical values can be found in Tables 6.3, 6.4, and 6.5. As a function of  $x_F$ , a small constant suppression is observed in the kinematic range covered by the HERA-B experiment. The average value of the

nuclear suppression parameter  $\alpha$  in the range of  $-0.375 < x_F < 0.125$  is

$$\bar{\alpha} = 0.969 \pm 0.003(\text{stat.}) \pm 0.021(\text{syst.}).$$

The  $p_T$  distribution of  $\alpha$  is in good agreement with previous measurements by the E866 collaboration. The measured dependence of  $\alpha$  on  $x_F$  agrees well with the results of previous experiments in the overlap region of  $x_F > -0.1$  and with theoretical predictions based on nuclear absorption of the final state  $c\bar{c}$  pair and the fully formed  $J/\psi$  meson. Theoretical models which predict a strong suppression of  $J/\psi$  production for negative  $x_F$  or the scaling of nuclear effects with  $x_2$  are disfavored. The available  $J/\psi$  statistics and the accuracy of the measurement do not allow to impose further restrictions on theoretical models. For the first time, the nuclear suppression parameter  $\alpha$  is measured for negative values of  $x_F$  smaller than  $-0.1$ .





# Monte Carlo Simulation of the HERA–B Detector and Trigger

---

In this appendix, the main aspects of the HERA–B Monte Carlo (MC) simulation chain are presented, as it is utilized for analyzing data taken during the 2002/2003 run with the dimuon trigger. The simulation of a  $J/\psi$  event in HERA–B comprises of the following steps: First, the event is generated by the physics generators PYTHIA and FRITIOF. In the GEANT detector simulation, interactions of the produced particles with the detector are modelled. The electronic signals produced by interactions in the detector are simulated in the digitization and hit preparation step. The simulation of the HERA–B trigger chain comprises bit-level simulations of the pretriggers and the SLT and a parametrization of the FLT efficiency. The data flow between the different parts of the simulation chain and the points where detector and trigger efficiencies enter the simulation, are explained in detail, using the data flow in the muon detector and trigger simulation as an example. The data flow is summarized in a flow chart in Fig. A.1.

## A.1 Physics Generators

In HERA–B, the physics generator packages PYTHIA 5.7 and JETSET 7.4 [Sjö94] are used to generate events containing heavy quarkonia, employing the standard PYTHIA model of charmonium production. As an alternative to the PYTHIA production model, a model based on the nonrelativistic QCD matrix elements calculated in [Ben96] has been introduced to the MC generator [Igo01, Igo02].

Since PYTHIA is only capable of simulating proton-nucleon interactions, the FRITIOF 7.02 package [Pi92] is employed in connection with PYTHIA. FRITIOF is a physics generator to simulate inelastic proton-nucleus interactions, including a self-consistent treatment of the transition between the regimes of soft scattering and hard parton scattering. A charmonium event is generated as follows: the complete PYTHIA decay chain of the charmonium is kept, and all other particles in the event are discarded. The remaining energy is passed to FRITIOF to generate the underlying inelastic proton-nucleus interaction. All particles of the FRITIOF event are Lorentz-transformed such

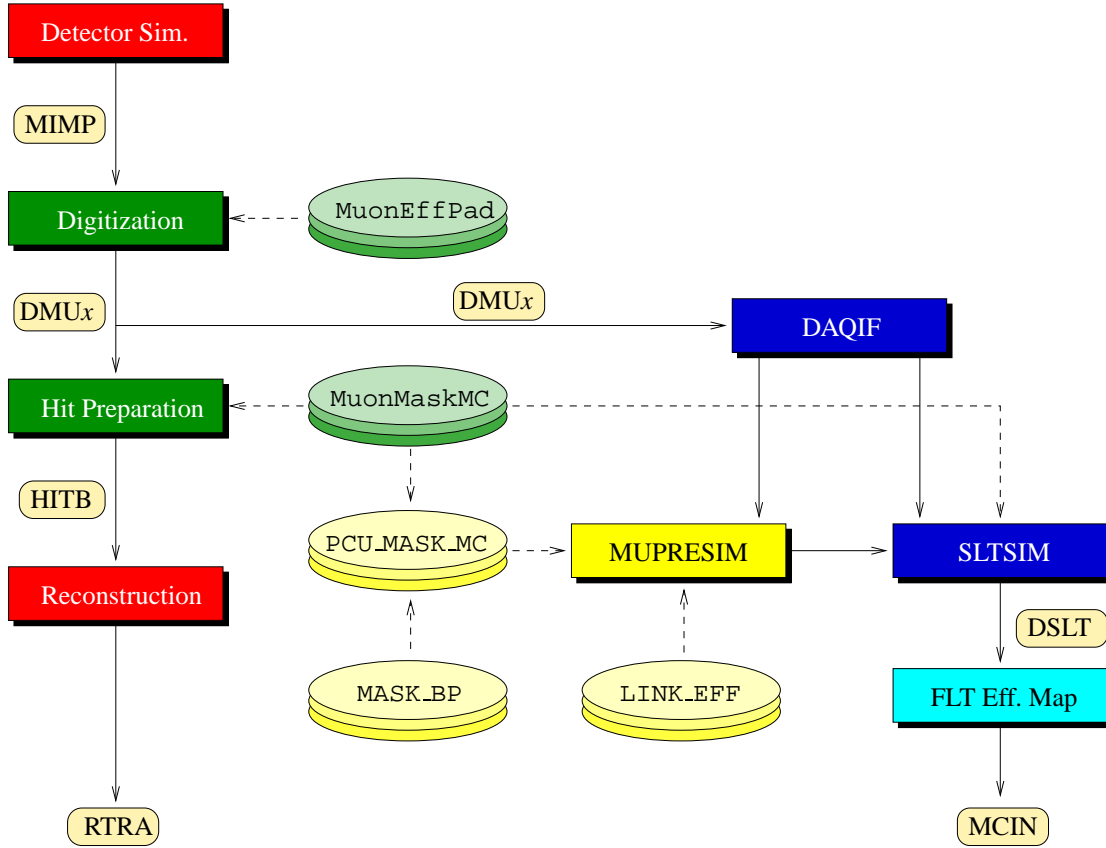


**Figure A.1:** Flow chart of the detector and trigger simulations in the muon detector. Rectangular boxes correspond to parts of the simulation code, boxes with round edges stand for the ARTE tables used in exchanging data between the parts of the simulation code, and ellipses represent database tables. Data exchange is symbolized by solid lines, while dashed lines depict access to the database. The simulation steps are explained in the text.

that energy and momentum of the complete event are conserved. Finally, a list of tracks from the generated event is passed to the HERA-B detector simulation.

### A.1.1 Reweighting of Kinematic Distributions

The differential distributions of  $J/\psi$  and  $\Upsilon$  mesons obtained from PYTHIA do not agree well with the distributions measured in previous experiments. Especially the  $p_T$  spectrum is distorted by a low- $p_T$  cutoff of  $1 \text{ GeV}/c$  on the parton level. Therefore, event weights are needed adjust the  $x_F$  and  $p_T$  spectra such that they match their “desired” shapes. An early version of these weights is discussed in [Iva99], in which the desired shapes are parametrizations of the spectra measured in the E789 experiment in proton-gold collisions [Sch95]:

$$\frac{dN}{dx_F} \propto (1 - |x_F|)^C \quad \text{with } C = 4.91, \quad (\text{A.1})$$

$$\frac{dN}{dp_T^2} \propto \left[ 1 + \left( \frac{p_T}{p_0} \right)^2 \right]^{-6} \quad \text{with } p_0 = 3.0 \text{ GeV}/c. \quad (\text{A.2})$$

In general, the weights are calculated as the ratio of the desired to the PYTHIA-generated kinematic distribution:

$$w = \frac{\text{desired number of events}}{\text{number of events generated by PYTHIA}}. \quad (\text{A.3})$$

Comparisons of the spectra reweighted with the early version of weights to the HERA-B data showed two problems: The  $x_F$  distribution is not well-described by the non-differentiable function (A.1), and the parameter  $p_0$  of the  $p_T$ -parametrization (A.2) depends on the target material. Therefore, a new set of event weights has been introduced, taking into account the current best knowledge of the shape of the differential distributions.

Comparing the available theoretical models of charmonium production with the measured  $x_F$  distribution in HERA-B, the best description of the data is obtained using the prediction of nonrelativistic QCD (NRQCD) shown in Fig. 3.3 [Vuk04]. Therefore, the  $x_F$  distribution is weighted such that the reweighted distribution follows the desired shape from NRQCD. The functional form of the NRQCD prediction is approximated by the empirical parametrization [Kol04]

$$\frac{dN}{dx_F} \propto \frac{f(x_F; x_1, C)}{x_F^2 + x_0^2} \quad \text{with } f(x_F; x_1, C) = \begin{cases} \exp\left[-\frac{x_F^2}{2\sigma^2}\right] & \text{for } |x_F| \leq x_1, \\ A(1 - |x_F|)^C & \text{for } |x_F| > x_1, \end{cases} \quad (\text{A.4})$$

where the parameters  $\sigma$  and  $A$  are fixed by requiring the parametrization to be continuously differentiable at  $x_F = x_1$ :

$$\sigma^2 = \frac{x_1(1 - x_1)}{C}, \quad A = \exp\left[-\frac{x_1^2}{2\sigma^2}\right] (1 - |x_1|)^{-C}.$$

The parameters obtained from the fit are

$$x_0 = 0.356, \quad x_1 = 0.110, \quad C = 5.07.$$

The  $x_F$  weight is calculated from the ratio of the NRQCD prediction and the  $x_F$  distribution generated by PYTHIA. The ratio of 100,000 random events generated according to the desired  $x_F$  distribution and the  $x_F$  distribution of  $J/\psi$  mesons generated by PYTHIA for the same number of MC events is fitted to the empirical function

$$w(x_F) = \begin{cases} a_0 + a_1 x_F^2 & \text{for } x_F \leq x_1, \\ D + a_2 x_F + a_3 x_F^2 & \text{for } x_F > x_1, \end{cases} \quad (\text{A.5})$$

where the boundary is fixed to  $x_1 = 0.18$ , and the relative normalization is obtained by requiring that  $w(x_F)$  is continuous at  $x_F = x_1$ :

$$D = a_0 - a_2 x_1 - (a_3 - a_1) x_1^2.$$

The fit resulted in the following values:

$$a_0 = 0.9905, \quad a_1 = -1.002, \quad a_2 = -2.122, \quad a_3 = 5.985.$$

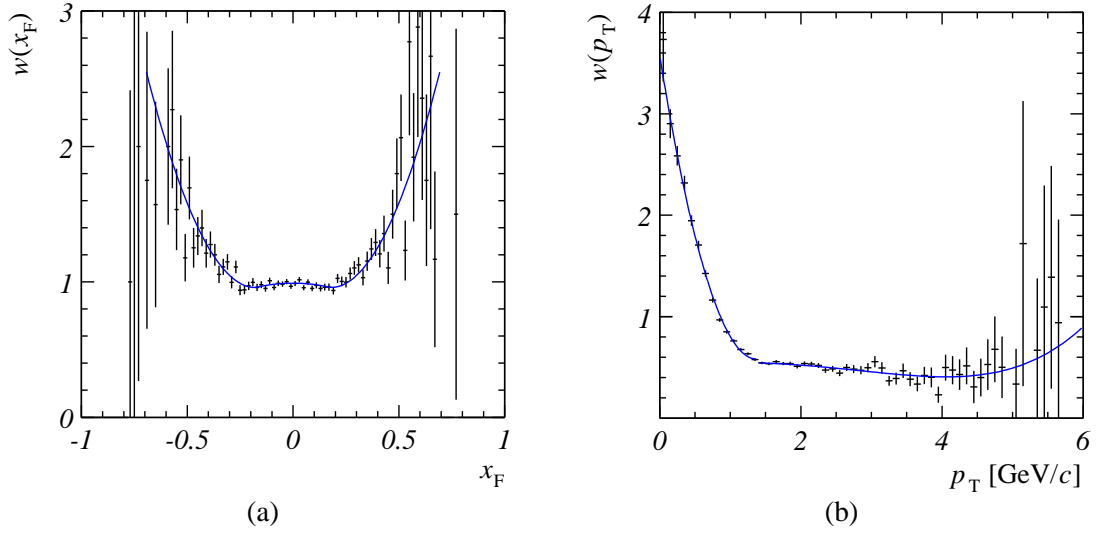


**Figure A.2:** Weighting functions used for the reweighting of (a) the  $x_F$  distribution and (b) the  $p_T$  distribution for carbon targets (solid lines), and examples of the ratio of the desired distribution and the distribution generated by PYTHIA for 100,000 MC events. The functional form of the weights are given in the text.

An example of the ratio of the PYTHIA and the NRQCD predictions for 100,000 MC events is shown in Fig. A.2 (a), together with the weighting function  $w(x_F)$ .

The desired shape of the  $p_T$  distribution is material-dependent. The  $p_T$  distribution of  $J/\psi \rightarrow \mu^+ \mu^-$  decays in HERA-B for the two main target materials carbon and tungsten is approximately described by the following shape:

$$\frac{dN}{dp_T^2} \propto \left[ 1 + \left( \frac{p_T}{p_0} \right)^2 \right]^{-6} \quad \text{with } p_0 = \begin{cases} 2.9 \text{ GeV}/c & \text{for carbon targets,} \\ 3.1 \text{ GeV}/c & \text{for tungsten targets.} \end{cases} \quad (\text{A.6})$$

The  $p_T$  weights are calculated from the ratio of the desired distribution, given in A.6, and the PYTHIA-generated  $p_T$  distribution. The ratio of the desired and the PYTHIA distributions for 100,000 random events is fitted with a function similar to the one used in [Iva99]:

$$w(p_T) = \begin{cases} \exp[b_0 + b_1 p_T] (b_2 + b_3 p_T + b_4 p_T^2) & \text{for } p_T \leq p_{\text{thr}}, \\ b_0 + b_1 p_T + b_2 p_T^2 + b_3 p_T^3 + b_4 p_T^4 & \text{for } p_T > p_{\text{thr}}, \end{cases} \quad (\text{A.7})$$

where  $p_T$  is measured in  $\text{GeV}/c$ . The value of  $p_{\text{thr}}$  is fixed to  $1.375 \text{ GeV}/c$ , and the values for the parameters  $b_i$  obtained from the fit are summarized in Table A.1. The  $p_T$  weighting function is shown in Fig. A.2 (b).

The final weight is obtained from the product of the  $x_F$  and the  $p_T$  weights, and a normalization factor:

$$w(x_F, p_T) = N w(x_F) w(p_T), \quad (\text{A.8})$$

where the normalization  $N$  is chosen such that the number of events is the same before

**Table A.1:** Parameters for the calculation of  $p_T$  weights for carbon and tungsten targets after Eq. (A.7).

Parameter	Carbon		Tungsten	
	$p_T \leq p_{\text{thr}}$	$p_T > p_{\text{thr}}$	$p_T \leq p_{\text{thr}}$	$p_T > p_{\text{thr}}$
$b_0$	9.54	0.557	9.54	0.753
$b_1 \times 10^3$	10.8	-15.5	80.1	-440
$b_2 \times 10^3$	0.257	25.6	0.238	363
$b_3 \times 10^3$	-0.314	-18.9	-0.289	-111
$b_4 \times 10^3$	0.114	2.77	0.106	11.3

and after the reweighting [Iva99]:

$$N = \frac{\int w(x_F)^{-1} \frac{dN}{dx_F} dx_F}{\int \frac{dN}{dx_F} dx_F} \cdot \frac{\int w(p_T)^{-1} \frac{dN}{dp_T^2} dp_T}{\int \frac{dN}{dp_T^2} dp_T}. \quad (\text{A.9})$$

Here, the distributions  $dN/dx_F$  and  $dN/dp_T^2$  are the distributions obtained after the reweighting, as given by Eq. (A.4) and Eq. (A.6). Note that the statistical uncertainty of the weighted events is also influenced by the spread of the weights: In HERA-B, the weighted MC events are used to calculate the detector efficiency  $\varepsilon$  for a class of events, e.g. for all events in a given  $x_F$  bin, from the number of generated events,  $N_{\text{gen}}$ , and the number of reconstructed events,  $N_{\text{rec}}$ :

$$\varepsilon = \frac{N_{\text{rec}}}{N_{\text{gen}}}.$$

The statistical uncertainty  $\sigma_\varepsilon$  for  $\varepsilon \neq 0, 1$  is given by the variance of the binomial distribution,  $\varepsilon(1 - \varepsilon)$ , divided by the number of generated events:

$$\sigma_\varepsilon^2 = \frac{\varepsilon(1 - \varepsilon)}{N_{\text{gen}}}. \quad (\text{A.10})$$

In the case of weighted events, the efficiency reads

$$\varepsilon = \frac{\sum_i w_i \varepsilon_i}{\sum_i w_i},$$

where  $\varepsilon_i$  and  $w_i$  are the efficiency and the weight of the  $i$ -th event. Since the events are independent of each other, the uncertainty of  $\varepsilon$  is obtained by Gaussian error propagation:

$$\sigma_\varepsilon^2 = \sum_i \left( \frac{\partial \varepsilon}{\partial \varepsilon_i} \right)^2 \sigma_{\varepsilon_i}^2 = \frac{\sum_i w_i^2 \varepsilon_i (1 - \varepsilon_i)}{(\sum_i w_i)^2}. \quad (\text{A.11})$$

Assuming that all single-event efficiencies are equal to  $\varepsilon$ , the equivalent number of unweighted events is obtained from a comparison of Eq. (A.10) and Eq. (A.11):

$$N_{\text{eff}} = \frac{(\sum_i w_i)^2}{\sum_i w_i^2}. \quad (\text{A.12})$$

An efficiency determination using  $N_{\text{eff}}$  unweighted events would result in the same statistical uncertainty as an efficiency determination from the weighted events. Note that  $N_{\text{eff}}$  decreases with increasing spread of the weights.

### A.1.2 Multiplicity Reweighting for the Underlying Event

The number of particles in the underlying event found in real data is larger than the number of particles generated by FRITIOF by a factor of approximately 1.4. The reason for this mismatch is a bias effect which is not taken into account by the FRITIOF generator [Bru02b]: The probability to produce  $J/\psi$  mesons or any other particle with a small production probability is proportional to the number of proton-nucleon sub-collisions in the event. Since each of these sub-collisions is a source of particles, the average track multiplicity of events which contain a  $J/\psi$  is enhanced compared to normal inelastic interactions. In order to model this effect, the track multiplicity of the underlying inelastic event is reweighted by an accept-reject Monte Carlo method [Hus01b]: After generating the FRITIOF event, a quantity  $n$  that is proportional to the track multiplicity is compared with a random number  $r \in [0; 1]$ . The event is discarded, and a new inelastic event is generated if  $r > n$ . By default, the reweighting is based on the number of tracks  $N_{\text{tr}}$  from charged particles in the acceptance of the HERA-B detector. The slopes of these tracks are required to be larger than 10 mrad and smaller than 220 mrad in either the  $x$ - or the  $y$ -direction. The quantity  $n$  is given by

$$n = \frac{N_{\text{tr}}}{N_{\text{tr,max}}} = \frac{N_{\text{tr}}}{30 + 10 \log(A)}, \quad (\text{A.13})$$

where an ad-hoc measure of the maximum track multiplicity as a function of the atomic mass number  $A$  is used as a normalization. Note that as long as  $n \in [0; 1]$ , the reweighted track multiplicity does not depend on the choice of the normalization. However, the execution speed of the event generator is decreased with decreasing  $n$ , since in this case, more events are rejected. Alternatively, the number of gluons in the event can be used for the reweighting. Here,  $n$  is given by

$$n = \frac{N_{\text{g}}}{N_{\text{g,max}}} = \frac{N_{\text{g}}}{10 + 3 \log(A)}. \quad (\text{A.14})$$

## A.2 Detector Simulation and Hit Preparation

### A.2.1 GEANT Simulation

The response of the HERA-B detector to particles crossing the detector volume is simulated using the GEANT 3.21 package [CER94]. In GEANT, all particles produced by the event generators are tracked through the detector material, and interactions with the materials are simulated. A detailed description of the distribution of active and passive material in the detector is provided by the detector geometry [Now03]. In the GEANT simulation, a particle can for example produce new particles or lose energy by multiple scattering. Long-lived particles such as  $K_S^0$  or  $\Lambda$  are declared stable during the event

generator step, and their decays are handled by GEANT. Whenever a sensitive volume of the detector is crossed, the track leaves so-called Monte Carlo impact points (MIMP) both at the entry and the exit points of the volume.

During the data-taking, events which contain charmonia are superimposed with inelastic proton-nucleus interactions. The number of simultaneous interactions in a single bunch crossing is approximately Poisson-distributed:

$$P(N; \lambda) = \frac{\lambda^N}{N!} \exp[-\lambda]. \quad (\text{A.15})$$

Here  $P$  is the probability to observe  $N$  interactions at an average number of  $\lambda$  interactions. To account for superimposed events, MIMPs from additional inelastic events, i.e. generated only by FRITIOF, can be mixed with the MIMPs from the charmonium event before the detector simulation. The number of mixed inelastic events is either a fixed number per event or distributed randomly according to a Poisson distribution with a given mean value  $\lambda$ . A realistic description of the measured detector occupancies in two-wire runs at the typical interaction rate of 5 MHz is reached by mixing inelastic interactions from both wires with  $\lambda = 0.5$  each.

## A.2.2 Hit Preparation in the Muon Detector

In the hit preparation procedure, MIMPs are translated into three-dimensional space points and stored in the ARTE table HITB (HITB: Hit Bank). In the following, the hit preparation in the outer muon detector is described as an example.

### Digitization and Cell Efficiencies

In a first step, the MIMPs are digitized, i.e. assigned to a given wire or pad of the muon detector. The efficiencies of the individual detector cells are taken into account by an accept-reject MC method. For a cell with an efficiency  $\varepsilon$ , a random number  $r \in [0; 1]$  is drawn, and the MIMP is rejected if  $r > \varepsilon$ . The efficiencies of the muon pad detector are determined from dedicated efficiency runs during the data-taking, in which a specialized algorithm was employed in the Second Level Trigger (SLT). This algorithm is based on a very clean sample of reference tracks which require hits in all superlayers of the muon detector except the superlayer for which the efficiency is measured [Fom03]. The resulting efficiencies are stored in the database table /MUON\_NEW/MuonEffPad. The efficiencies of the sensitive drift volumes of the tube detector cells are assumed to be unity, since efficiencies of at least 99% have been demonstrated in test beam studies [Tit00]. The single-cell efficiency is therefore only given by its geometrical acceptance of 85%, which is calculated as the ratio the width of the drift volume of 13.9 mm and the cell size of 16.4 cm. The width of the sensitive volume has been further decreased by 2 mm, reducing the geometrical acceptance to 73%, to account for hits which are registered only in the following bunch crossing [Ego04]. Due to the double-layer structure of the tube detector, inefficient areas of the tube cells in a single layer are covered by the other layer. The digitized detector hits are stored in the ARTE tables DMUP (DMUP: Digitized Muon Pad Hits) for the pad detectors and DMUT (DMUT: Digitized Muon Tube Hits) for the tube detectors.

The simulation programs for pretriggers and SLT can be operated on real data as well as on MC simulated data, requiring identical input for both cases, i.e. the raw data stored in the FED records. The DAQIF tool translates digitized detector hits to this format. In the case of the muon detector, the translation reduces to copying the DMUP and DMUT tables to the corresponding FED record structures. Thus, the input data for the pretrigger and SLT simulations contain cell efficiencies for the digitization. Note that all further steps of the event processing in the pretriggers and the SLT are independent of the remaining parts of the hit preparation procedure.

### Reconstruction of Space Points, Alignment, and Masking

The second step of the hit preparation comprises the translation of detector hits into space points. The space points are stored in the ARTE table HITB, which serves as a starting point for the track reconstruction. In this step, the detector geometry together with alignment corrections is used to determine the geometrical position of a detector hit. In the detector geometries used for the MC simulation, GEOM/VERS 02.1205 and newer, corrections of the muon detector positions due to misalignment during the data-taking period 2002/2003 are already taken into account, hence no additional alignment corrections are needed. In addition, defective channels are masked before the reconstruction of space points.

Masks for hot channels are determined by comparing the measured hit occupancy of a given detector channel with a reference occupancy determined from the data. The reference occupancy is scaled linearly to the interaction rate measured during the run, and the occupancies of defective reference channels are interpolated. The masking was checked and updated approximately once per month, usually in the first runs after maintenance work in the muon detector. A small number of additional hot channels emerging after the update of the masking were tolerated in order to limit the number of data-taking periods with different masking conditions. The influence of these additional hot channels on the muon identification algorithm was found to be negligible [Sip04b].

Hot channels were identified by the following algorithm: For every detector channel, the occupancy was compared the maximum allowed occupancy, which was defined as the minimum of the following three limits: 10 times the reference occupancy, a superlayer-specific maximum occupancy (between 50% for the tube chambers in MU1 and 6% for the tube chambers in MU3), and a cutoff occupancy of 70%. The 16 channels of a single readout cable were excluded from the hot channel search, if less than 150 hits were found. In the tube system, the entire cable was masked if 40% or more of the channels in the cable were hot. The resulting hot channel masks were cross-checked by hand and stored in the database table /MUON\_NEW/MuonMask for further use during the data-taking. The hot channel masks applied in the MC simulation are identical to those utilized during the data-taking.

While masking of dead channels is not needed during the data-taking, it is important in the MC simulation in order to correctly describe the detector efficiency. To identify dead channels, the correlation between the channel occupancies in real data,  $O_{RD}$ , and in an ideal MC simulation,  $O_{MC}$ , was used. Even if the absolute number of hits is different in data and MC, the occupancies of working channels show a strong correlation. From the slope of a straight-line fit to the distribution of the real data occupancy versus



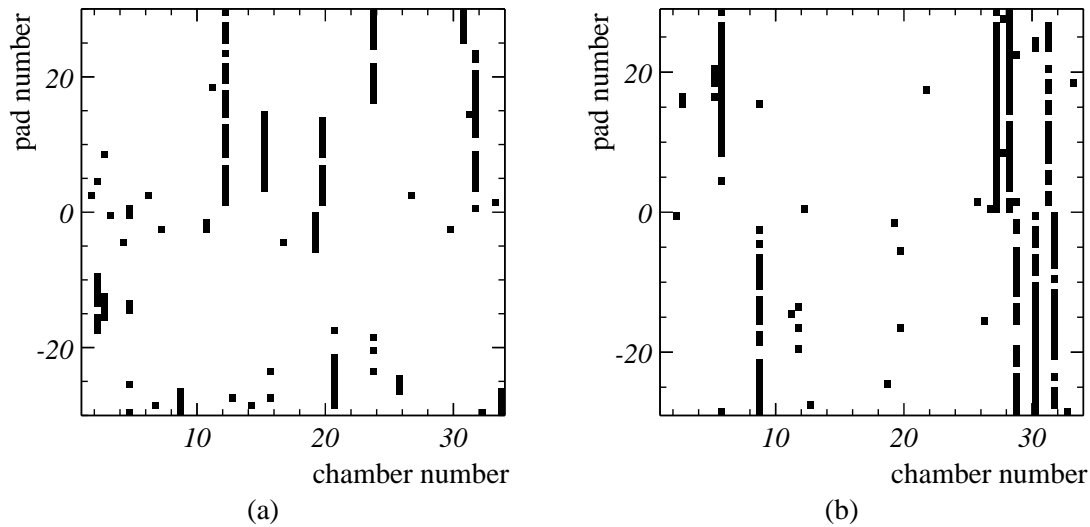


**Figure A.3:** Masks for defective channels in the muon pad system for the November 2002 calibration period for (a) MU3 and (b) MU4. The shaded areas represent pads masked in the MC simulation. The chambers are numbered according to the scheme described in [Har99].

the MC occupancy, an approximate scaling factor  $S$  between the two occupancy levels was obtained. For the tube chambers, a value of  $S = 1.58$  was used, while  $S = 0.63$  was employed for the pad chambers. A channel was considered dead if the observed occupancy was less than 10% of the expected value, i.e.  $O_{RD} < 0.1 S \cdot O_{MC}$ . See [Vuk04] for a detailed description of this method. The list of dead channels was added to the list of hot channels and stored in the database table `/MUON_NEW/MuonMaskMC`. A graphical representation of the masking used in the muon pad system for the calibration period of November 2002 is shown in Fig. A.3.

Several channels in the muon pad detector have been detected, which were connected to wrong front-end driver (FED) channels [Zai04], or which showed wrong connections between the FED channels and the muon pretrigger. In the MC simulation, these cabling mistakes are taken into account in the mapping of detector channels to FEDs, both in the muon hit preparation and in the muon pretrigger simulation. In addition, one pair of swapped optical links was identified in the muon pretrigger and implemented in the simulation. A list of all known swapped connections is given in Table A.2.

### A.3 Trigger Simulation

The HERA-B trigger simulation chain has been subject to many changes over the last years. In this section, the most recent status of the simulation is presented. Many of the systematic studies leading to the localization of problems and the improvements of the simulation are summarized in [Vuk04].

The main strategy of the trigger simulation is shown in Fig. 4.7. Similar to the implementation of the real trigger chain, described in Section 2.3, the trigger messages of the muon pretrigger simulation and the ECAL pretrigger simulation are stored in a struc-

**Table A.2:** List of swapped connections in the muon pad detector and the muon pretrigger. The positions of swapped connections are given by the corresponding readout cable names, as defined in [Har99].

Cable Name	Swapped with	Connection	Period
Mp3.1-19 A	Mp3.1-19 C	Detector→FED	October 2002
Mp4.2-26 A/B	Mp4.2-26 C/D	Detector→FED	October 2002
Mp4.1-05 A/B	Mp4.1-06 C/D	Detector→FED	All
Mp4.1-31 C	Mp4.1-31 D	Detector→FED	All
Mp4.2-16 A/B	Mp4.2-16 C/D	Detector→FED	All
Mp4.2-28 C	Mp4.2-28 D	Detector→FED	All
Mp4.1-17 A/B	Mp4.1-17 C/D	FED→Muon Pretrigger	All
Mp4.1-20 C/D	Mp4.1-21 C/D	FED→Muon Pretrigger	All
Mp3.2-17 A/B	Mp3.2-17 C/D	Pretrigger Optical Link	before January 21, 2003

ture that corresponds to the FED record of the second Trigger Decision Unit (TDU) of the First Level Trigger (FLT). The simulation of the Second Level Trigger (SLT) reads these data and performs the same trigger algorithm as during the data-taking. The SLT track parameters are passed to the FLT efficiency map, a parametrization of the FLT efficiency relative to the SLT efficiency. This exchange of FLT and SLT in the trigger chain is justified by the trigger mode utilized in the data-taking, in which the SLT algorithm uses the pretrigger messages as starting points. Hence, the trigger decisions of the FLT and the SLT are independent, and their ordering can be exchanged [Bal03b].

### A.3.1 Muon Pretrigger and RICH Multiplicity Veto

#### MUPRESIM

The muon pretrigger simulation tool MUPRESIM [Ada01] is a C++ class library that provides a bit-level simulation of all steps of the muon pretrigger algorithm. In MUPRESIM, configuration information identical to the information used for the muon pretrigger hardware is utilized to ensure a realistic simulation of the muon pretrigger setup. The flexible modular design of MUPRESIM allows operating the simulation both in stand-alone applications and in the trigger simulation chain for the 2002/2003 data-taking period. The pretrigger messages generated by MUPRESIM are stored in the FLT FED record of the 2<sup>nd</sup> TDU for further processing by the SLT simulation.

#### Muon Pretrigger Masking

Due to the 1-to-6 coincidence algorithm of the muon pretrigger, a MU4 pad is used in the coincidence calculation for three different MU3 pads, hence the pad masks used in the hit preparation and the SLT must be translated to specialized muon pretrigger masks. Masks for defective channels in the muon pretrigger are derived from two sources.

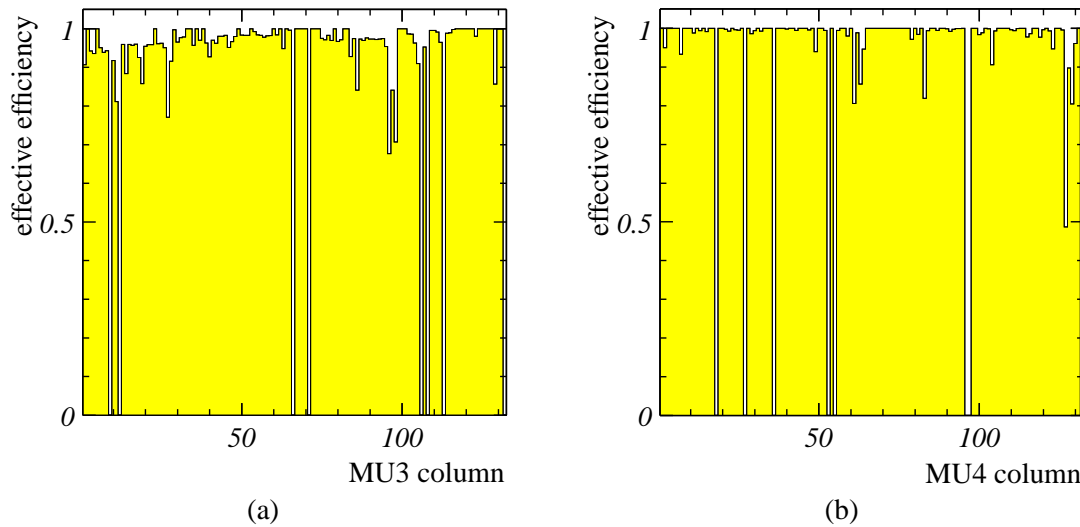


**Figure A.4:** Effective muon pretrigger optical link efficiencies averaged over all runs taken during the calibration period of November 2002 as a function of the muon pretrigger column number: (a) MU3 links. (b) MU4 links. The column numbers 1–66 correspond to pad columns in the upper detector half, and the column numbers 67–132 represent the lower detector half.

A “blueprint” mask, stored in the database table `/MUON_MPRE/MASK_BP`, contains channels with known hardware problems in the muon pretrigger. This mask is combined with a pretrigger mask generated from the list of defective channels in the muon detector, taken from the database table `/MUON_NEW/MuonMaskMC` by a logical OR. The combined mask is finally stored in the database table `/MUON_MPRE/PCU_MASK_MC`. The blueprint masks are identical to those used during the data-taking, and the masks for defective channels in the muon detector are derived from the hot channel masks employed during the data-taking and additional dead channel masks, as described in Section A.2.2.

### Optical Link Efficiency

Due to irreparable problems with the optical links used in HERA–B, the optical data transmission between the Pretrigger Link Boards and the Pretrigger Coincidence Units was unstable during the data-taking [Sch01]. Thus, the efficiencies of the optical links are modelled in the MC simulation by an accept-reject MC simulation: The optical link efficiency  $\varepsilon$  is compared with a random number  $r \in [0; 1]$ , and all hits in the detector channels served by the optical links are deleted if  $r > \varepsilon$ . The link efficiencies—see Fig. A.4 for an example—are stored in the database table `/MUON_MPRE/LINK_EFF`.

During the data-taking, the optical links were continuously monitored by the muon pretrigger online software. From the monitoring data, the uptime of all links in physics runs can be calculated. However, if the optical link efficiencies derived from this source are used in the MC simulation, the agreement between real data and simulation is non-satisfactory. Therefore, the link efficiencies were treated as a free parameter and determined from the triggered data itself: The data stream contains both the FED hits in

the muon detector and the original pretrigger messages. MUPRESIM is operated using the FED hits as an input while employing a configuration designed for the MC simulation. The link efficiencies are derived from a comparison of the original messages with the MUPRESIM-simulated messages. Differences between messages from these two sources can only originate from the pretrigger chain, i.e. starting from the splitting of the data-paths in the FED daughter boards of the muon detector and ending in the one of the TDUs of the FLT. The link efficiencies are effective efficiencies in the sense that they are biased by the trigger, and all discrepancies between the data and the simulation which affect entire columns of pads are included.

The time-dependent link efficiencies are averaged for every MC calibration period. The data sets used for the determination of the link efficiencies for a given calibration period consists of preselected events from all runs in the period which are accepted for physics analysis. The pre-selection is done according to the event classification bit #24, i.e. selecting events which contain a dimuon vertex with an invariant mass in the range of  $2.3\text{--}20\text{ GeV}/c^2$ . The comparison of messages comprises the messages parameters  $\xi$  and  $\eta$ , which correspond to the  $xy$ -position of the message in MU3, and the MU4 pattern of the message, coded in the parameter  $d\xi$ .

Since the message parameters are non-continuous binned quantities, the parameter values obtained from the data and the simulation must be identical. However, in the data, 2–3% of the events include the messages with  $\xi$  and  $d\xi$  values not allowed by the binning. The influence of these messages on the invariant mass spectrum of muon pairs is checked. Excluding events with less than two valid messages, the  $J/\psi$  signal is reduced by 1.6%, and no significant influence on the differential distributions is observed. Therefore, messages unmatched in  $\xi$  or  $d\xi$  are excluded from the link efficiency analysis. In addition, messages from unmasked “warm” pretrigger channels in the data are ignored.

The link efficiencies are determined by simultaneously adjusting the total number of messages per column, i.e. for a given  $\xi$  value, and the  $d\xi$  values in the column. Due to the coincidence algorithm, every optical link in MU4 contributes to the neighboring columns with the same efficiency. Thus, inconsistent MU4 efficiencies in neighboring columns are used to identify wrong cable connections in the muon pretrigger.

In some columns, the number of messages in the real data exceeded the number found by the simulation by a factor of 2–3 [Sip04b]. Most of the affected channels are localized on a single Pretrigger Message Generator. This excess would result in an “efficiency” larger than unity, which cannot be simulated in an accept-reject MC. However, the spurious messages are found to be uncorrelated with the other messages and distributed approximately equally in all channels. Therefore, these messages are expected to be filtered out by the higher trigger levels. This hypothesis is supported by fact that the number of muon tracks from  $J/\psi$  decays in these channels is not significantly different from the number of muons from  $J/\psi$  decays in the neighboring channels.

In some data-taking runs, a mis-synchronization of two readout crates was observed. The crates covered the muon pad detector columns 1–30 in the superlayers MU3 and MU4, i.e. roughly one quadrant of the muon pad detector. Due to the coincidence algorithm of the muon pretrigger, the trigger rate in these columns was reduced to the level of random coincidences. Runs in which this “missing quadrant problem” was

detected are marked in the run list in Appendix C. On average, approximately 30% of the events in “missing quadrant” runs are affected by the synchronization problem. To incorporate this effect in the MC simulation, a special calibration period has been created in which the efficiencies of the optical links in the MU3 columns 1–30 are reduced by 30%.

### Total Muon Pretrigger Efficiency

The “intrinsic” efficiency of the muon pretrigger hardware during the 2002/2003 data-taking period is evaluated in detail in [Sip04b]. For approximately 80% of the muon pretrigger channels, efficiencies greater than 99% are found. In order to determine the total efficiency of the muon pretrigger for  $J/\psi \rightarrow \mu^+\mu^-$  decays, the intrinsic efficiency has to be multiplied with the acceptance of the system. The acceptance is composed of several contributions. A study based on a MC simulation of approximately 100,000 decays  $J/\psi \rightarrow \mu^+\mu^-$  is performed to determine the individual contributions to the acceptance. Simulation results utilizing the latest available settings for realistic masking and efficiencies of the muon detector and pretrigger are compared to simulations using “ideal” settings to disentangle the different contributions to the acceptance.

For the study, the geometrical acceptance of the muon pad system for muon pairs is defined as the fraction of events in which both muons from the  $J/\psi$  decay cross the sensitive areas of the muon pad system both in the superlayer MU3 and MU4. All further acceptances are based on the fraction of events in which two muon pretrigger messages are generated by MUPRESIM, and the  $xy$ -positions of the messages are matched to the simulated muon tracks within  $\pm 10$  cm both in  $x$  and  $y$ . If all efficiencies are set to unity and no masking of hot or dead channels is applied, the resulting acceptance describes the efficiency of the setup of muon detector and pretrigger. This acceptance includes the efficiency of the pretrigger algorithm,  $0.975 \pm 0.006$  [Ada01], and known cabling problems during the data-taking which are modelled in the MC simulation. The total efficiency is further reduced by simulating the measured efficiencies of the muon pad detector and by introducing masks for hot and dead channels both in the muon detector and the muon pretrigger. An additional reduction originates from the efficiency of the optical data transmission.

The resulting total efficiencies for the main periods of the 2002/2003 data-taking period are summarized in Table A.3. The most important factors are the limited geometrical acceptance of the muon pad system for muon pairs and the efficiencies of the pad detector. Since two hit coincidences are required by the muon pretrigger, the single-pad efficiencies of 80–85% enter at their fourth power. The correction of a cabling error between the January 2003 (I) and the January 2003 (II) periods results in higher efficiencies of the setup and pad efficiencies. The successful repair work of the optical links results in higher optical link efficiencies for all 2003 data samples. The “missing quadrant problem” is parametrized by lower optical link efficiencies in the quadrant. In summary, the average total efficiency of the muon pretrigger chain amounts to approximately 10%.

**Table A.3:** Total efficiency of the muon pretrigger for muon pairs from  $J/\psi$  decays in all calibration periods of the 2002/2003 data-taking. The contributions to the efficiency are explained in the text.

Period	Geometrical	Setup	Pad Eff.	Masking	Link Eff.	Total
October 2002	$0.445 \pm 0.005$	$0.768 \pm 0.002$	$0.420 \pm 0.004$	$0.837 \pm 0.003$	$0.779 \pm 0.004$	$0.094 \pm 0.003$
November 2002	$0.445 \pm 0.005$	$0.776 \pm 0.002$	$0.377 \pm 0.004$	$0.857 \pm 0.003$	$0.709 \pm 0.005$	$0.079 \pm 0.003$
December 2002	$0.445 \pm 0.005$	$0.776 \pm 0.002$	$0.372 \pm 0.004$	$0.870 \pm 0.003$	$0.703 \pm 0.005$	$0.079 \pm 0.003$
January 2003 (I)	$0.445 \pm 0.005$	$0.776 \pm 0.002$	$0.442 \pm 0.004$	$0.858 \pm 0.003$	$0.888 \pm 0.003$	$0.117 \pm 0.003$
January 2003 (II)	$0.445 \pm 0.005$	$0.838 \pm 0.002$	$0.445 \pm 0.004$	$0.866 \pm 0.003$	$0.895 \pm 0.003$	$0.129 \pm 0.003$
February 2003	$0.445 \pm 0.005$	$0.838 \pm 0.002$	$0.444 \pm 0.004$	$0.871 \pm 0.003$	$0.875 \pm 0.003$	$0.126 \pm 0.003$
“Missing Quadrant”	$0.445 \pm 0.005$	$0.776 \pm 0.002$	$0.377 \pm 0.004$	$0.857 \pm 0.003$	$0.556 \pm 0.006$	$0.062 \pm 0.002$

### RICH Multiplicity Veto Simulation

The RICH multiplicity veto has been employed in most of the data-taking runs in 2002/2003. In a part of the RICH detectors, the number of photon hits was compared with a threshold, and the muon pretrigger was stopped if the RICH multiplicity was too large. A threshold of 300 hits was used throughout the data-taking, corresponding to 2,000–3,000 hits in the entire RICH. In the hardware of the RICH multiplicity veto, no masks have been applied, and the efficiency of the device has been determined to 99.9991% [Brü02a]. Therefore, the simulation of the device assumes 100% efficiency. The number of photon hits is read from the RICH FED records and summed in the same way as in the hardware, i.e. discarding the least significant bit in each Base Sum Card. The number of hits is stored in the ARTE table EVRC (EVRC: Event Reconstruction Information) to be applied in the offline analysis.

### A.3.2 Second Level Trigger Simulation

The simulation of the SLT for a given calibration period is based on a SLT executable that is identical to the one used during the data-taking in that period. With DAQIF, digitized MC data are translated to FED records and transferred from ARTE to the SLT simulation via a piping mechanism. Masking of defective channels in the muon detector is implemented in the muon part of the SLT algorithm, reading the same database table as the hit preparation code, `/MUON_NEW/MuonMaskMC`. The output of the SLT simulation is stored in the ARTE table DSLT (DSLIT: Digitized SLT Data).

For analyses which are sensitive to the acceptances of the SLT for the different target wires, it is essential to properly simulate the relative positions of proton beam, target wires and detector. In the SLT algorithm, a target constraint is used, the so-called “target box”, depending on the beam and target positions. A track is accepted by the algorithm if it crosses a rectangle in the  $z = 0$  plane, the size and position of which is calculated for every track individually. The track slope is calculated from the  $xy$ -position of the track at the center of the magnet and the average position of all active target wires. Boxes around the positions of the target wires are projected to the  $z = 0$  plane in the direction of the track slope. The size of the box for a single wire is calculated from the size of the wire and the current beam position and width. The final target box is the minimum

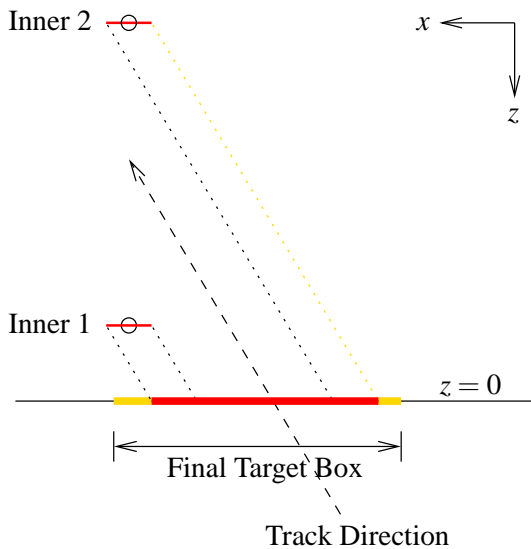


**Figure A.5:** Illustration of the SLT target box calculation for the target wires Inner 1 and Inner 2 (plan view). Rectangles (“boxes”) around the active wires are projected to the  $z = 0$  plane. The final box encloses the single-wire boxes and is enlarged (not to scale) to account for displaced vertices from B mesons.

box enclosing all single-wire boxes. To account for displaced vertices from B mesons, the box is enlarged by a constant offset in the track direction and an additional slope-dependent offset in the direction opposite to the track both in the  $x$ - and  $y$ -views. See Fig. A.5 for an illustration. In the SLT algorithm, the size of the target box is used to calculate the actual size of the target constraint by scaling the size with an empirical multiplier which was subject to optimization during the course of the data-taking.

During the data-taking, the beam and target positions changed even within single runs. From events within runs accepted for the analysis, the set of beam and wire positions used in the SLT are extracted and stored in a database. For every MC event to be simulated, the beam and target positions are selected randomly from the database. The probability to select a set of beam and target positions is proportional to the number of SLT input events [Med04b].

### A.3.3 Efficiency Map of the First Level Trigger

The FLT network—as the muon pretrigger—relies on optical data transmission. Due to the unstable behavior of the optical links, the FLT efficiencies derived from a bit-level simulation of the FLT differ by approximately 20% from the values measured in dedicated efficiency runs. In addition, the  $xy$ -projection of the FLT efficiencies are not reproduced by the simulation. Therefore, a parametrization of the FLT efficiency relative to the SLT is used instead, namely the FLT efficiency map [Bal03b]. Since in the 1 FLT/2 SLT\* mode, only one FLT track is required, one of the SLT tracks is unbiased by the FLT and can be used as a reference track to determine the FLT efficiency.

To suppress the influence of fake tracks on the efficiency determination, a clean set of SLT reference tracks is selected. The SLT track is matched with a reconstructed track with a muon likelihood probability of 0.05 for muons or a bremsstrahlung photon in the case of electrons. The efficiency is then derived from a geometrical matching of FLT tracks to the SLT reference tracks, according to the distance measure

$$\Delta r = \frac{1}{4} \left( |\Delta x_{PC1}| + \frac{|\Delta y_{PC1}|}{4} + |\Delta y_{TC2}| + \frac{|\Delta y_{TC2}|}{8} \right), \quad (\text{A.16})$$

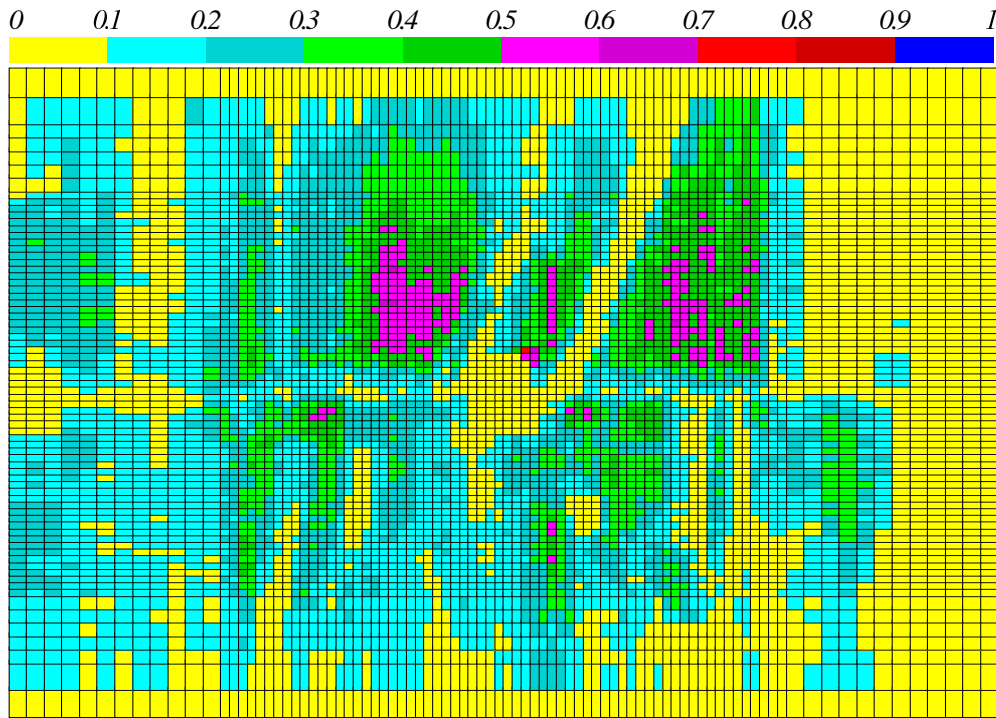


**Figure A.6:** Projection of the average FLT efficiency map for November 2002 to the  $xy$  plane at the  $z$ -position of the OTR superlayer TC2 (generated with [Bal03a]).

i.e. a resolution-weighted sum of the differences in the  $x$ - and  $y$ -positions of the tracks in the OTR superlayers PC1 and TC2. Three different efficiency maps are calculated for the matching criteria  $\Delta r < 2$  cm,  $\Delta r < 5$  cm, and  $\Delta r < 10$  cm. The parameter space of the FLT is completely described by three parameters, chosen to be the position of the track in the OTR superlayer TC2,  $x_{TC2}$  and  $y_{TC2}$ , and a parameter related to the track momentum,  $0.865x_{TC2} - 1.854x_{PC1}$ , where  $x_{PC1}$  is the  $x$ -position of the track in PC1. The efficiency is measured on a run-by-run basis in  $88 \times 74 \times 10$  bins within the parameter space, and efficiencies of neighboring bins with low statistics are merged. Average efficiencies for entire calibration periods are determined as the mean values of the weighted single-run efficiencies, where the weight is given by the number of analyzed SLT tracks in the run. The FLT efficiency map for November 2002, projected to the  $xy$  plane at the  $z$ -position of TC2, is shown in Fig. A.6.

During the MC simulation, the SLT track parameters behind the magnet are fed into the FLT efficiency maps for the three matching criteria. The matched FLT tracks and their efficiencies are stored in the ARTE table FTRA (FTRA: FLT Tracks). From the single-track efficiencies, the efficiency for an event to contain at least one FLT-triggered track is derived and stored in the ARTE table MCIN (MCIN: Monte Carlo Input Data), again with three entries for the three matching criteria.

The efficiency values obtained from the FLT efficiency map can only be used in comparing the MC simulation to data if the same criteria for the matching of FLT and SLT tracks are applied to both, the MC and the data. Therefore, events without a FLT-SLT match are removed from the analysis.



---

# Kinematic Variables in Fixed-Target Experiments

---

The kinematics of a particle decay into a two-body state is described completely by a set of eight variables for the four-momenta of the two outgoing particles. If the masses of these particles are known and assuming that the mother particle is produced isotropically in the azimuthal angle, the number of independent variables is reduced to five. A common choice for these variables consists of the invariant mass  $M$  of the decaying particle, two variables describing the longitudinal and transverse momenta of the decaying particle with respect to the beam direction, and two variables for the directions of the outgoing particles with respect to the mother particle. As an example, the production of a  $J/\psi$  meson in fixed-target proton-nucleus collisions and its subsequent decay into a muon pair are discussed in the following.

### B.1 Transverse and Longitudinal Momentum

The momentum  $p$  of the  $J/\psi$  is commonly parametrized by a longitudinal and transverse component, i.e. components parallel and perpendicular to the beam direction, chosen as the  $z$ -axis of the coordinate system:  $p^2 = p_L^2 + p_T^2 = p_z^2 + (p_x^2 + p_y^2)$ . Since  $p_T$  is transverse to the relative movement of the laboratory frame and the center-of-mass frame, it is a Lorentz-invariant quantity.

A common choice for the longitudinal momentum variable is Feynman's scaling variable  $x_F$ , defined as the fractional longitudinal momentum carried by the particle, evaluated in the center-of-mass frame of the proton-nucleus interaction:

$$x_F \equiv \frac{p_L^*}{p_{L,\max}^*}. \quad (\text{B.1})$$

In this thesis, the maximum longitudinal momentum,  $p_{L,\max}^*$ , is approximated by half the available center-of-mass energy,  $\sqrt{s}/2$ . The exact definition of  $p_{L,\max}^*$  includes

corrections due to the non-zero final state masses and the minimum mass of the recoil system, i.e. twice the proton mass  $m_p$  [Kow94]:

$$p_{L,\max}^* = \frac{1}{2\sqrt{s}} \sqrt{[s - (M_{\mu^+\mu^-} + 2m_p)^2] [s + (M_{\mu^+\mu^-} + 2m_p)^2]}. \quad (\text{B.2})$$

Given the HERA-B center-of-mass energy of  $\sqrt{s} \approx 41.6$  GeV, the difference between the two expressions is negligible:  $p_{L,\max}^* = 0.992\sqrt{s}/2$ , justifying the choice of  $p_{L,\max}^* = \sqrt{s}/2$ . Performing the Lorentz transformation to the hadronic center-of-mass frame explicitly,  $x_F$  can be written by laboratory frame variables as follows:

$$x_F = \frac{1}{m_p} \left( p_L - E \sqrt{\frac{E_{\text{beam}} - m_p}{E_{\text{beam}} + m_p}} \right). \quad (\text{B.3})$$

Here  $p_L$  and  $E$  are the laboratory frame energy and longitudinal momentum of the particle under consideration, and  $E_{\text{beam}}$  is the beam energy,  $E_{\text{beam}} = 920$  GeV for the HERA proton ring.

In the formalism of the quark-parton model,  $x_F$  of a newly produced particle can also be written as

$$x_F = x_1 - x_2, \quad (\text{B.4})$$

where  $x_1$  and  $x_2$  are defined as the momentum fractions carried by the interacting partons inside the beam proton and the target nucleon in a reference frame in which the proton carries infinite momentum. At a given center-of-mass energy,  $x_1$  and  $x_2$  are related to the mass  $M$  of the produced particle by

$$M^2 = x_1 x_2 s. \quad (\text{B.5})$$

For studies of the time evolution of particle production, it is useful to relate the Lorentz boost factor  $\beta\gamma$  to the observable  $x_F$ . For a particle with momentum  $|\vec{p}|$ , mass  $M$  and the velocity  $\beta = v/c$ ,  $\beta\gamma$  is given by

$$\beta\gamma = \frac{\beta}{\sqrt{1 - \beta^2}} = \frac{|\vec{p}|}{M} \quad (\text{B.6})$$

In the laboratory frame, the four-momenta  $p_1$  and  $p_2$  of the colliding partons inside the beam proton and the target nucleon are

$$p_1 \approx (x_1 E_{\text{beam}}, 0, 0, x_1 E_{\text{beam}}), \quad (\text{B.7})$$

$$p_2 \approx (x_2 m_N, 0, 0, 0). \quad (\text{B.8})$$

Here  $E_{\text{beam}}$  is the beam energy and  $m_N$  is the mass of target nucleon. The mass of the beam proton is neglected. The mass and energy of the produced particle are then obtained as

$$M^2 = (p_1 + p_2)^2 \approx 2x_1 x_2 m_N E_{\text{beam}}, \quad (\text{B.9})$$

$$|\vec{p}| = x_1 E_{\text{beam}}, \quad (\text{B.10})$$

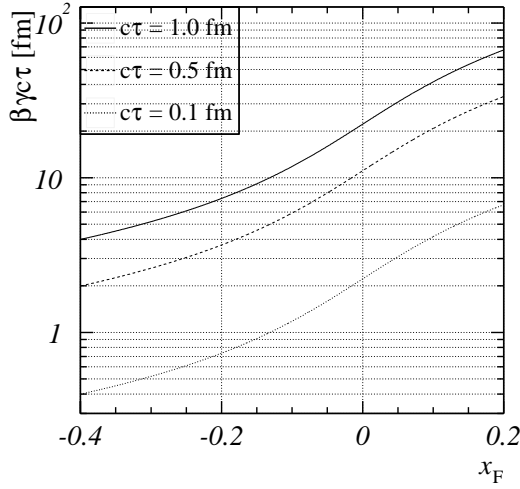


**Figure B.1:** Laboratory frame travelling distance  $\beta\gamma c\tau$  as a function of  $x_F$  for  $\sqrt{s} = 41.6$  GeV. The curves depict the  $x_F$  dependence of the travelling distance for three different proper times:  $c\tau = 1.0$  fm (solid line),  $c\tau = 0.5$  fm (dashed line), and  $c\tau = 0.1$  fm (dotted line).

where again masses have been neglected. The boost factor then reads

$$\beta\gamma(x_F) = \frac{|\vec{p}|}{M} \approx \frac{Mx_1 E_{\text{beam}}}{2x_1x_2 m_N E_{\text{beam}}} = \frac{1}{2x_2} \frac{M}{m_N} = \frac{1}{-x_F + \sqrt{x_F^2 + 4M^2/s}} \frac{M}{m_N}, \quad (\text{B.11})$$

where in the last step, Eq. (B.4) and Eq. (B.5) have been solved for  $x_2$ . For the  $x_F$  range covered by the HERA-B experiment,  $\beta\gamma c\tau(x_F)$  is plotted for three different proper times  $c\tau$  in Fig. B.1.

Another measure of the longitudinal momentum is the rapidity  $y$ , defined as

$$y = \tanh^{-1} \left( \frac{p_L}{E} \right) = \frac{1}{2} \log \left( \frac{E + p_L}{E - p_L} \right). \quad (\text{B.12})$$

The central region of the primary interaction, i.e. the region around  $x_F = 0$ , is better resolved by  $y$  than by  $x_F$ . The shape of the rapidity distribution is Lorentz-invariant, such that a Lorentz transformation between the laboratory frame and the center-of-mass frame with the relative velocity  $\beta$  results in a shift of the rapidity distribution by  $-\tanh^{-1} \beta$ .

## B.2 Angular Distributions

The angular distributions of the two muons with respect to the  $J/\psi$  are defined in the rest frame of the  $J/\psi$ . A schematic drawing of the decay in this frame is shown in Fig. B.2. If the  $J/\psi$  carries a non-vanishing transverse momentum, the angle  $2\alpha$  between the flight directions of the proton and the nucleus is given by  $\tan \alpha = p_T/M$ . Three different choices for the definition of the  $z$ -axis in this frame are used in the literature. In the Gottfried-Jackson frame [Got64], the  $z$ -axis is parallel to the proton beam. The  $z$ -axis is anti-parallel to the flight direction of the  $J/\psi$  in the  $u$ -channel frame. The Collins-Soper frame [Col77] constitutes a compromise between these extreme choices, using the bisector between the proton flight direction and the negative of the flight direction of the  $J/\psi$  as the  $z$ -axis.

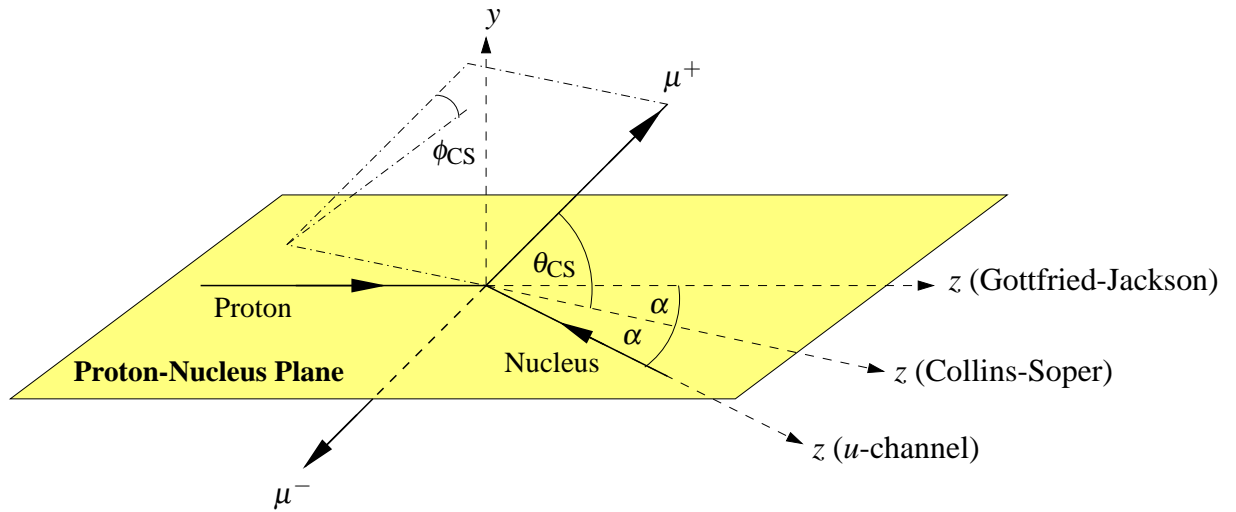


**Figure B.2:** Definitions of angular variables in the decay  $J/\psi \rightarrow \mu^+\mu^-$ , given in the rest frame of the  $J/\psi$  (after [Con89]). The different choices for the coordinate system are described in the text.

The  $y$ -axis is chosen perpendicular to the plane defined by the flight directions of the proton and the  $J/\psi$ , and the  $x$ -axis is added such that  $x$ ,  $y$ , and  $z$  form a right-handed coordinate system. The angular variables  $\cos \theta$  and  $\phi$  correspond to the conventional polar and azimuthal angles of the positive muon in this coordinate system. The angle  $\theta$  is the angle of flight direction of the positive muon with respect to the  $z$ -axis, and  $\phi$  is the angle between the projection of the positive muon to the  $xy$ -plane and the  $x$ -axis.

To distinguish the three choices for the decay angles, in this thesis, they are marked with the subscripts “GJ” for the Gottfried-Jackson frame, “CS” for the Collins-Soper frame, and “UC” for the  $u$ -channel frame, e.g.  $\cos \theta_{CS}$  and  $\phi_{CS}$  for the Collins-Soper frame.

---

# Run Selection

---

In this appendix, a list of all two-wire runs used in this thesis is provided. The interaction rates are given by the average interaction rates measured by the target hodoscope counters. The number of events is defined as the total number of events recorded by the data acquisition system, containing both dilepton-triggered and random-triggered events. The number of  $J/\psi$  is given separately for the two wires. “Wire 1” and “Wire 2” denote the first and second wire of the combination respectively, e.g. Inner I and Below I for the combination I1B1.  $J/\psi$  candidates are selected according to the event classification bit #24. The assignment of  $J/\psi$  candidates to wires is described in Section 4.2.3. All fits to invariant mass spectra are performed with an unbinned maximum likelihood fit employing the functional form introduced in Section 4.2.1. The luminosity ratio is represented by the shift in the nuclear suppression parameter  $\Delta\alpha^{\mathcal{L}} = \log(\mathcal{L}^{\text{C}}/\mathcal{L}^{\text{W}})/\log(A^{\text{W}}/A^{\text{C}})$ , where the superscript “C” denotes the carbon wire; and “W” denotes the tungsten wire, the titanium wires, or the second carbon wire (see Section 5.2.3). The trigger ratio, defined as the ratio of the number of dilepton-triggered and random-triggered events in a run, is used to weight single-run luminosities if all runs from a calibration period are added (see Section 6.2.1).

**Table C.1:** List of two-wire runs used in the analysis. Run numbers marked with daggers (†) indicate “Missing Quadrant” runs. Runs in which the wire Below II is a titanium wire are marked with asterisks (\*). All uncertainties given in the table are the statistical uncertainties of the quantities.

Run	Date	IA Rate [MHz]	# Events	Number of $J/\psi$		$\Delta\alpha^{\mathcal{L}}$	Trigger Ratio
				Wire 1	Wire 2		
<b>Wire Combination IIB1 (Tungsten–Carbon)</b>							
20225	2002-11-03	2.62	730,444	–	–	0.916±0.017	51.06±0.44
20226	2002-11-03	2.47	2,619,685	–	–	0.946±0.010	48.48±0.21
20229	2002-11-03	3.56	3,811,826	1432±52	1675±50	0.935±0.008	39.71±0.13
20239	2002-11-04	3.85	1,344,443	467±28	380±24	0.993±0.010	33.32±0.17
20240	2002-11-05	4.43	232,545	84±12	55±10	0.987±0.021	41.57±0.59
20242	2002-11-05	4.20	510,012	166±17	135±15	0.992±0.015	36.12±0.32
20333†	2002-11-07	4.76	974,713	262±23	142±16	0.995±0.009	12.57±0.05
20346†	2002-11-08	2.92	30,964	9±3	5±2	0.979±0.024	5.49±0.09
20347†	2002-11-08	3.68	65,501	14±4	17±5	0.998±0.020	8.27±0.11
20348†	2002-11-08	4.87	252,214	16±6	32±7	1.015±0.012	11.76±0.09
20349†	2002-11-08	4.80	246,408	26±7	43±8	1.019±0.013	11.26±0.09
20366†	2002-11-10	2.93	116,457	51±9	49±9	0.944±0.013	4.73±0.04
20367†	2002-11-10	4.91	130,594	51±9	41±7	0.983±0.014	9.88±0.10
20369†	2002-11-10	4.90	126,883	63±9	34±9	0.970±0.015	9.77±0.10
20370†	2002-11-11	4.83	2,090,779	1068±44	843±36	0.986±0.007	8.38±0.02
20371†	2002-11-11	4.91	256,088	125±15	85±12	0.945±0.011	9.07±0.06
20372†	2002-11-11	4.86	525,306	248±22	196±18	0.956±0.009	8.65±0.04
20375†	2002-11-11	4.38	44,461	40±8	18±5	0.946±0.032	15.89±0.33
20377†	2002-11-11	4.79	144,517	58±12	65±10	0.969±0.018	18.89±0.24
20383†	2002-11-11	5.61	565,815	147±17	113±14	0.885±0.009	13.08±0.07
20385†	2002-11-12	5.78	1,286,396	519±32	468±27	0.908±0.008	14.39±0.05
20386	2002-11-12	5.43	132,463	54±11	60±10	0.928±0.021	12.94±0.14
20387†	2002-11-12	4.75	415,289	196±19	195±18	0.952±0.011	10.58±0.06
20397	2002-11-13	5.15	918,124	580±35	614±33	0.980±0.009	9.82±0.04
20398	2002-11-13	4.47	845,268	580±34	679±32	0.970±0.008	9.55±0.04
20452	2002-11-18	4.45	1,152,089	903±42	786±35	0.904±0.008	11.14±0.04
20453	2002-11-18	4.54	261,889	163±18	193±16	0.919±0.013	10.32±0.07
20455	2002-11-18	5.25	821,336	558±32	558±29	0.934±0.009	10.90±0.04
20456	2002-11-18	5.85	691,994	429±29	432±25	0.936±0.009	12.54±0.06
20457†	2002-11-18	5.80	437,029	247±22	239±19	0.941±0.011	11.29±0.06
<b>Wire Combination III2 (Tungsten–Carbon)</b>							
20076	2002-10-19	4.41	150,162	247±21	245±19	0.956±0.027	12.53±0.12
20079	2002-10-20	4.39	126,318	176±18	149±15	0.954±0.016	8.26±0.08
20160	2002-10-26	2.68	125,818	62±11	75±11	0.901±0.025	21.52±0.30
20161	2002-10-26	2.76	39,425	22±6	15±4	0.894±0.043	20.08±0.48
20215	2002-11-02	2.85	8,988	2±2	–	0.722±0.169	55.48±4.51
20216	2002-11-02	2.84	245,329	66±10	45±8	0.769±0.027	54.86±0.84
20217	2002-11-02	2.36	1,434,292	343±25	271±20	0.875±0.017	47.09±0.28
20218	2002-11-02	2.03	472,424	156±16	121±13	0.779±0.019	39.14±0.37
20220	2002-11-02	1.97	1,590,736	523±31	369±22	0.794±0.012	36.07±0.18
20404	2002-11-14	4.52	228,281	183±18	190±17	0.948±0.012	9.62±0.07
20414	2002-11-14	2.32	696,179	584±32	573±29	0.942±0.009	9.30±0.04
20423	2002-11-15	4.30	331,538	202±22	222±18	0.947±0.010	8.89±0.05
20427	2002-11-15	4.07	146,464	116±14	99±13	0.921±0.013	7.71±0.06
20431	2002-11-16	4.67	106,999	5±3	7±3	0.912±0.015	9.65±0.11
20442	2002-11-16	4.59	204,738	130±15	109±13	0.931±0.013	11.19±0.09
20443	2002-11-16	4.54	249,845	204±19	154±16	0.944±0.012	10.57±0.08
20446	2002-11-17	4.31	465,900	294±23	306±21	0.929±0.009	7.43±0.03
20447	2002-11-17	4.39	468,890	326±24	305±22	0.941±0.009	7.09±0.03
20448	2002-11-17	4.41	223,774	144±17	153±15	0.954±0.011	7.50±0.05
20450	2002-11-17	4.53	580,156	383±27	364±23	0.934±0.008	7.18±0.03
20451	2002-11-17	4.49	353,972	290±22	255±19	0.940±0.012	16.69±0.12
20505	2002-11-23	4.21	1,266,145	850±41	781±34	0.917±0.008	9.61±0.03
20506	2002-11-23	2.37	1,127,673	964±42	925±37	0.926±0.008	7.02±0.02
20612	2002-12-07	3.34	14,670	11±4	10±4	0.914±0.027	3.02±0.06
20614	2002-12-07	4.57	554,587	–	–	0.915±0.009	10.54±0.05
20616	2002-12-07	1.62	89,990	95±12	82±11	0.918±0.015	2.63±0.02
20617	2002-12-07	1.45	69,403	34±8	108±12	1.251±0.019	2.45±0.02

*continued on next page*

*continued from previous page*

Run	Date	IA Rate [MHz]	# Events	Number of J/ψ		$\Delta\alpha^{\mathcal{L}}$	Trigger Ratio
				Wire 1	Wire 2		
20623	2002-12-07	3.59	321,137	81±12	70±10	1.000±0.010	7.07±0.04
20630	2002-12-08	1.87	31,593	18±7	23±6	0.964±0.026	4.11±0.06
20631	2002-12-08	1.87	20,749	14±6	17±6	0.980±0.032	4.33±0.08
20633	2002-12-08	1.98	239,720	190±18	172±16	0.979±0.011	4.32±0.02
20636	2002-12-08	1.89	233,551	161±17	253±19	0.967±0.011	4.01±0.02
20637	2002-12-08	1.88	507,660	389±28	505±27	0.983±0.009	3.97±0.01
20638	2002-12-08	4.67	1,027,138	665±34	735±33	0.967±0.008	12.78±0.05
20639	2002-12-08	4.62	962,596	535±32	620±31	0.978±0.008	11.72±0.05
20644	2002-12-08	2.19	28,921	33±7	18±5	0.988±0.023	2.66±0.04
20645	2002-12-09	1.86	711,450	586±33	645±31	0.968±0.008	3.34±0.01
20650	2002-12-09	1.83	21,051	29±8	15±4	0.942±0.027	2.83±0.04
Wire Combination B1I2 (Carbon–Carbon)							
21047	2003-02-02	4.77	1,146,956	1229±43	950±38	0.083±0.008	9.81±0.03
21049	2003-02-02	4.76	492,299	496±27	390±24	0.075±0.012	10.98±0.06
21050	2003-02-02	4.09	314,238	369±23	205±18	0.194±0.011	9.97±0.06
21051	2003-02-02	4.71	510,377	583±30	368±24	0.159±0.010	11.08±0.06
21052	2003-02-02	4.66	200,804	167±17	142±14	0.094±0.012	10.54±0.08
21053	2003-02-02	4.76	1,310,713	1416±47	1084±41	0.098±0.008	11.14±0.04
21054	2003-02-03	4.75	1,288,926	1331±46	1012±39	0.074±0.008	10.96±0.04
21056	2003-02-03	4.82	126,945	125±14	106±13	0.067±0.014	11.12±0.11
21057	2003-02-03	4.84	1,013,508	1110±42	845±35	0.084±0.009	11.26±0.04
21058	2003-02-03	4.69	1,040,989	1051±41	950±37	0.053±0.009	9.58±0.03
21077	2003-02-04	4.77	140,384	144±16	157±14	0.071±0.014	10.88±0.11
21079	2003-02-04	4.68	482,971	550±29	497±27	0.077±0.011	9.93±0.05
21087	2003-02-04	4.62	43,892	38±8	31±7	0.078±0.021	8.82±0.14
21100	2003-02-04	4.90	614,173	730±33	565±28	0.084±0.009	10.51±0.05
21102	2003-02-05	4.86	1,238,707	1409±45	1145±41	0.044±0.009	11.55±0.04
21104	2003-02-05	4.80	93,240	115±13	63±10	0.063±0.016	9.51±0.11
Wire Combination B1O2 (Carbon–Tungsten)							
20881	2003-01-18	2.88	1,535,081	76±10	345±23	0.336±0.008	8.19±0.02
20899	2003-01-19	2.71	31,556	–	–	0.327±0.018	0.71±0.01
20905	2003-01-19	2.78	39,860	–	–	0.316±0.016	0.67±0.01
20912	2003-01-19	3.92	681,443	275±19	230±20	0.910±0.009	11.99±0.06
20913	2003-01-19	3.71	762,931	403±24	299±22	0.942±0.009	11.71±0.05
20914	2003-01-20	3.58	674,334	250±19	249±22	0.815±0.009	10.79±0.05
20915	2003-01-20	3.56	610,099	298±21	308±24	0.819±0.010	11.77±0.06
20916	2003-01-20	3.53	781,140	221±19	300±23	0.818±0.009	10.05±0.04
20917	2003-01-20	3.14	571,304	158±15	280±22	0.611±0.011	9.20±0.04
20918	2003-01-20	3.38	562,305	160±16	326±23	0.620±0.010	9.59±0.05
20919	2003-01-20	3.23	83,607	18±7	50±9	0.662±0.023	8.99±0.11
20920	2003-01-20	3.56	1,171,056	559±29	749±37	0.720±0.008	10.15±0.03
20921	2003-01-20	3.62	577,159	298±22	315±24	0.799±0.010	10.29±0.05
20922	2003-01-20	3.77	542,380	302±21	316±24	0.830±0.010	12.28±0.06
20923	2003-01-20	3.97	219,798	142±16	127±16	0.824±0.015	13.44±0.12
20924	2003-01-20	3.84	389,812	186±18	228±19	0.810±0.011	10.77±0.06
20926	2003-01-21	3.67	1,134,765	602±30	824±37	0.768±0.009	13.50±0.05
20927	2003-01-21	3.75	1,039,072	493±28	726±35	0.765±0.008	12.30±0.05
20928	2003-01-22	3.82	273,370	84±13	190±17	0.734±0.013	13.97±0.11
20929	2003-01-22	3.87	596,485	230±19	410±28	0.701±0.010	14.10±0.07
20932	2003-01-22	3.74	317,989	148±14	221±19	0.765±0.012	13.54±0.10
20933	2003-01-22	3.68	1,005,252	446±26	636±33	0.769±0.009	12.42±0.05
20934	2003-01-22	3.48	411,988	204±18	304±24	0.760±0.011	11.48±0.07
20938	2003-01-22	4.44	350,861	134±15	196±19	0.767±0.012	15.53±0.11
20939	2003-01-22	4.35	361,081	130±13	190±18	0.766±0.012	15.21±0.11
20940	2003-01-23	4.19	1,517,754	732±33	780±37	0.838±0.008	13.64±0.04
20941	2003-01-23	4.19	484,234	230±19	201±19	0.835±0.010	13.51±0.08
20942	2003-01-23	4.18	158,383	93±11	102±13	0.845±0.016	13.98±0.14
20944	2003-01-23	4.20	601,964	238±19	294±22	0.792±0.010	12.26±0.06
20945	2003-01-23	4.12	63,509	39±8	29±7	0.759±0.024	12.08±0.19
20948	2003-01-23	4.07	136,750	83±12	77±11	0.778±0.017	12.23±0.13
20950	2003-01-23	3.75	261,746	177±16	172±18	0.814±0.012	8.49±0.06
20951	2003-01-23	3.95	360,011	216±18	206±18	0.843±0.011	9.58±0.06
20952	2003-01-23	4.61	451,534	252±19	275±23	0.839±0.010	10.87±0.06
20953	2003-01-23	4.46	188,955	84±14	91±13	0.800±0.013	10.80±0.09
20954	2003-01-23	4.27	228,704	119±13	103±14	0.808±0.012	10.12±0.08

*continued on next page*

*continued from previous page*

Run	Date	IA Rate [MHz]	# Events	Number of $J/\psi$		$\Delta\alpha^{\mathcal{L}}$	Trigger Ratio
				Wire 1	Wire 2		
20955	2003-01-23	4.11	746,153	403±25	481±29	0.826±0.009	12.27±0.06
20956	2003-01-23	4.31	189,391	114±13	113±14	0.825±0.014	13.10±0.12
20957	2003-01-24	4.42	332,351	158±16	163±18	0.786±0.012	13.36±0.09
20959	2003-01-24	2.56	15,860	4±3	11±4	0.770±0.046	5.91±0.14
20963	2003-01-24	4.62	144,860	83±11	72±11	0.885±0.016	12.38±0.13
20964	2003-01-24	4.12	783,430	297±21	348±26	0.793±0.009	9.59±0.04
20967	2003-01-24	4.05	593,821	115±14	132±15	0.824±0.009	8.49±0.04
20969	2003-01-25	4.09	781,267	347±23	426±27	0.813±0.008	9.18±0.04
20970	2003-01-25	4.15	2,281,066	1165±42	1361±48	0.831±0.007	10.80±0.03
20972	2003-01-25	3.15	489,105	230±20	243±21	0.827±0.010	9.54±0.05
20973	2003-01-25	3.81	158,941	–	–	0.818±0.014	8.40±0.07
20974	2003-01-25	3.61	107,765	–	–	0.849±0.016	7.43±0.07
20975 <sup>†</sup>	2003-01-25	4.13	830,895	376±24	422±28	0.836±0.009	12.11±0.05
20977	2003-01-25	3.85	220,260	95±11	133±15	0.875±0.013	10.69±0.08
20978	2003-01-26	4.11	2,256,352	1007±39	1127±45	0.845±0.007	9.67±0.02
20979	2003-01-26	4.18	1,675,992	881±36	1007±41	0.828±0.008	11.82±0.03
20980 <sup>†</sup>	2003-01-26	4.12	134,529	–	–	0.808±0.015	9.54±0.09
20987	2003-01-27	5.56	51,285	39±7	29±8	0.895±0.030	16.29±0.32
20988	2003-01-28	4.76	4,284,053	2264±59	3268±75	0.742±0.007	17.65±0.04
20989	2003-01-28	4.57	2,176,392	1001±38	1346±48	0.728±0.008	14.52±0.04
21300	2003-03-01	1.85	275,988	124±16	196±19	0.646±0.011	2.53±0.01
21301	2003-03-01	1.87	289,224	155±17	211±18	0.695±0.010	2.73±0.01
21302	2003-03-01	1.90	250,898	113±13	190±19	0.658±0.011	2.86±0.01
21303	2003-03-01	4.08	693,443	381±25	331±25	0.922±0.010	7.53±0.03
21304	2003-03-01	4.20	1,260,359	820±36	535±31	1.001±0.008	7.60±0.02
<b>Wire Combination B1B2 (Carbon–Tungsten/Titanium*)</b>							
20231*	2002-11-04	4.20	1,660,757	661±32	499±27		
20233*	2002-11-04	4.10	149,987	80±10	41±8		
21157	2003-02-11	4.76	253,981	143±14	229±19	0.683±0.011	2.38±0.01
21159	2003-02-11	4.74	54,832	8±3	17±5	0.710±0.028	11.35±0.18
21160	2003-02-11	4.58	402,277	41±16	68±11	0.645±0.015	10.98±0.06
21161	2003-02-11	4.24	223,152	19±5	27±6	0.701±0.026	9.59±0.07
21170	2003-02-12	4.61	1,799,738	97±12	164±17	0.684±0.009	10.77±0.03
21171	2003-02-12	4.75	274,006	17±5	27±9	0.666±0.019	10.99±0.08
21172	2003-02-12	4.92	696,274	34±13	53±11	0.692±0.015	8.99±0.04
21183	2003-02-13	4.82	250,674	9±3	34±8	0.708±0.021	12.49±0.10
21187	2003-02-13	4.82	652,544	181±17	308±24	0.704±0.017	13.13±0.07
21191	2003-02-14	4.83	656,000	186±17	337±24	0.690±0.015	16.52±0.09
21192	2003-02-14	4.33	646,322	180±16	292±22	0.685±0.014	13.75±0.07
21194	2003-02-14	3.95	105,550	36±7	43±11	0.680±0.035	N/A
21195	2003-02-14	3.87	1,441,025	646±32	1065±44	0.723±0.011	11.01±0.03
21196	2003-02-14	3.83	316,874	130±15	203±19	0.707±0.015	11.90±0.08
21197	2003-02-14	4.88	503,053	153±15	243±21	0.739±0.017	16.72±0.11
21200	2003-02-15	4.84	410,371	126±14	255±21	0.705±0.016	16.50±0.12
21201	2003-02-15	4.86	335,464	93±12	194±19	0.709±0.016	16.36±0.13
21202	2003-02-15	4.85	203,242	72±11	102±14	0.658±0.023	14.12±0.13
21203	2003-02-15	4.65	166,726	50±8	78±12	0.685±0.019	13.01±0.13
21204	2003-02-15	4.92	782,594	318±22	430±28	0.782±0.014	17.41±0.09
21206	2003-02-15	4.87	961,613	366±24	586±33	0.741±0.013	15.70±0.07



## Appendix D

---

# Plots and Tables

---

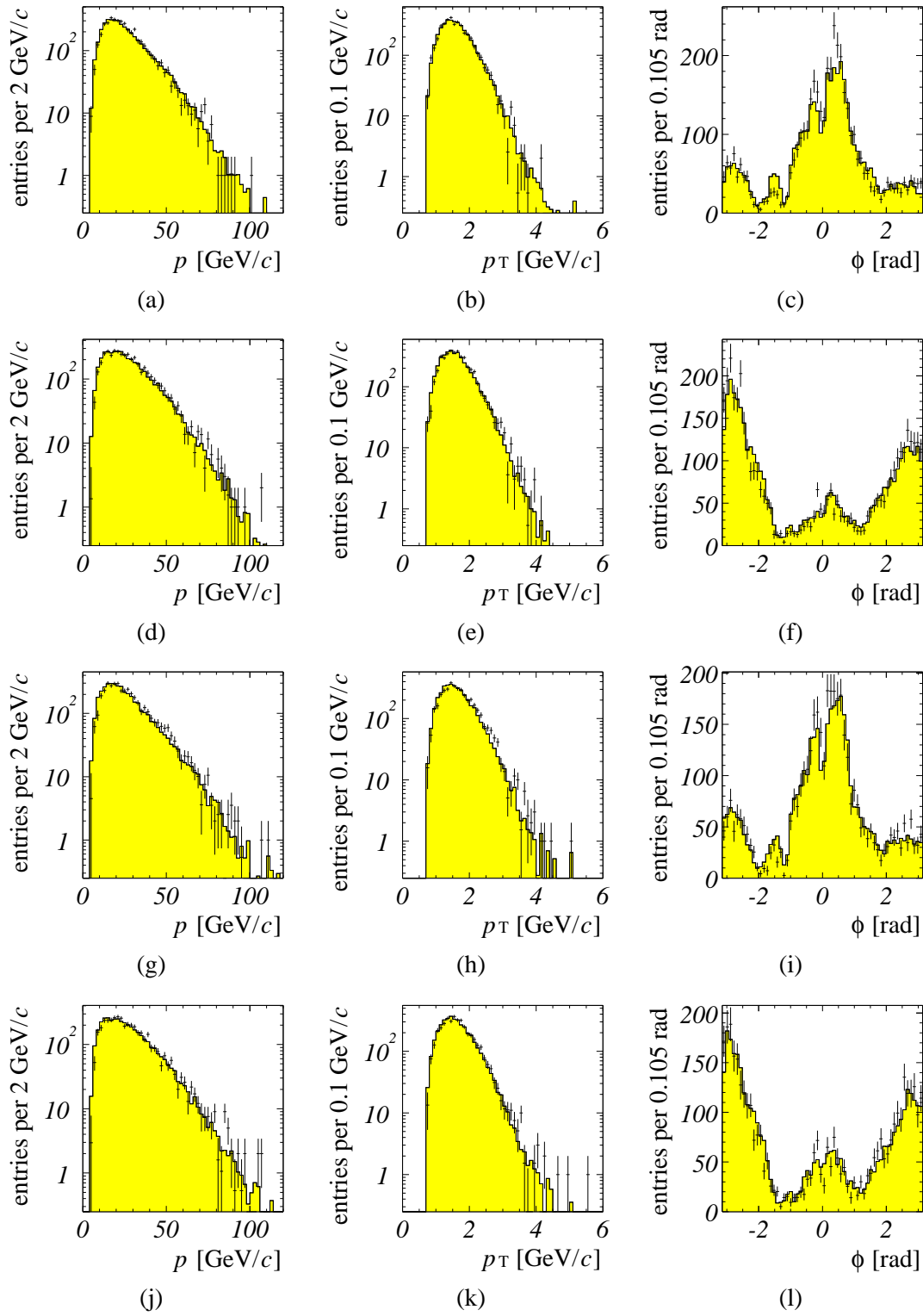


**Figure D.1:** Kinematics of muons from  $J/\psi$  decays in data (points) and MC simulation (histogram) for the wire combination III2. (a)–(c)  $p$ ,  $p_T$ , and  $\phi$  of  $\mu^+$  produced on the wire Inner II. (d)–(f)  $p$ ,  $p_T$ , and  $\phi$  of  $\mu^-$  produced on the wire Inner II. (g)–(i)  $p$ ,  $p_T$ , and  $\phi$  of  $\mu^+$  produced on the wire Inner I. (j)–(l)  $p$ ,  $p_T$ , and  $\phi$  of  $\mu^-$  produced on the wire Inner I. Background is removed via sideband subtraction, and the MC distributions are scaled to the integral of the data distributions.

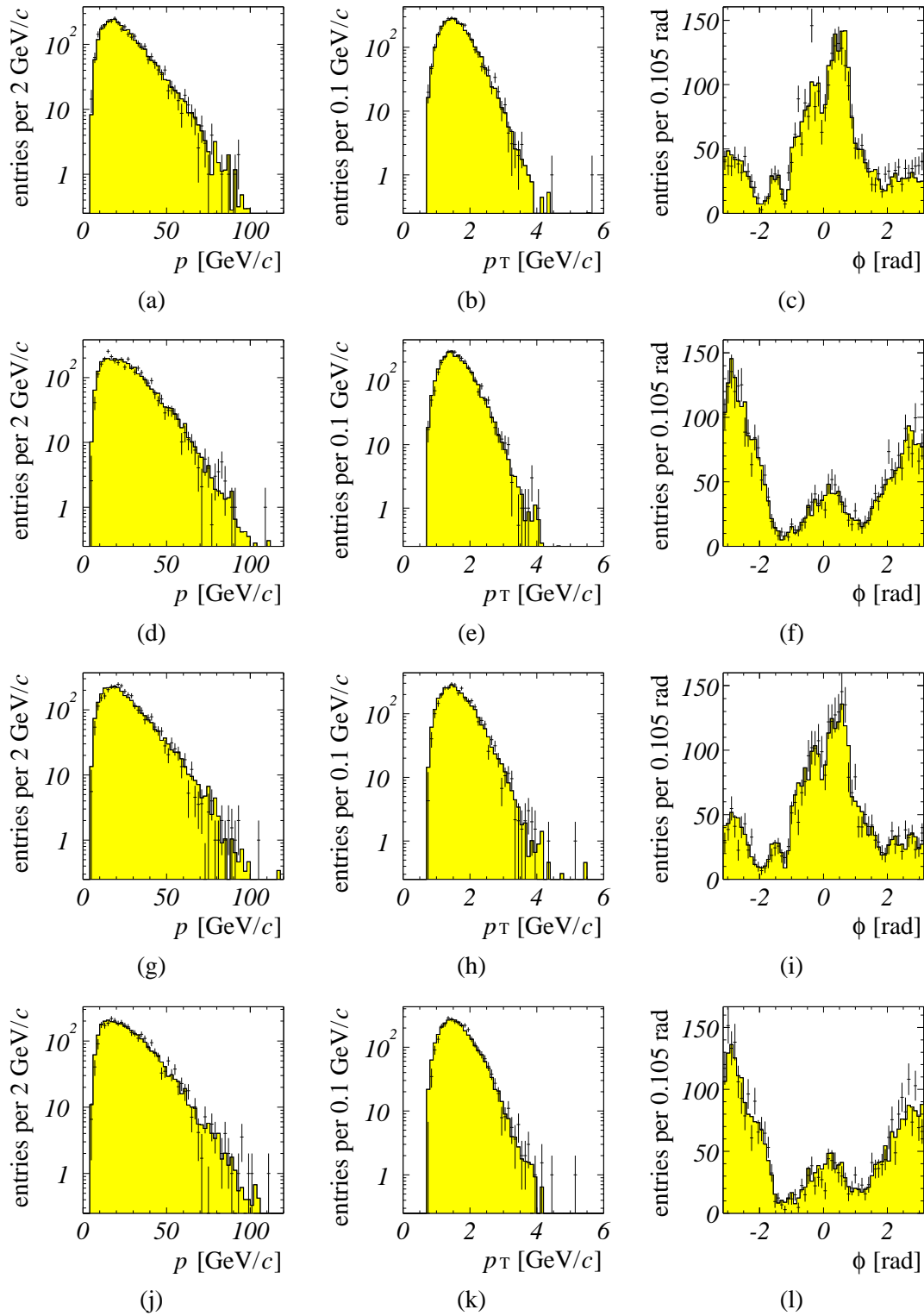


**Figure D.2:** Kinematics of muons from  $J/\psi$  decays in data (points) and MC simulation (histogram) for the wire combination I1B1. (a)–(c)  $p$ ,  $p_T$ , and  $\phi$  of  $\mu^+$  produced on the wire Inner II. (d)–(f)  $p$ ,  $p_T$ , and  $\phi$  of  $\mu^-$  produced on the wire Inner II. (g)–(i)  $p$ ,  $p_T$ , and  $\phi$  of  $\mu^+$  produced on the wire Inner I. (j)–(l)  $p$ ,  $p_T$ , and  $\phi$  of  $\mu^-$  produced on the wire Inner I. Background is removed via sideband subtraction, and the MC distributions are scaled to the integral of the data distributions.

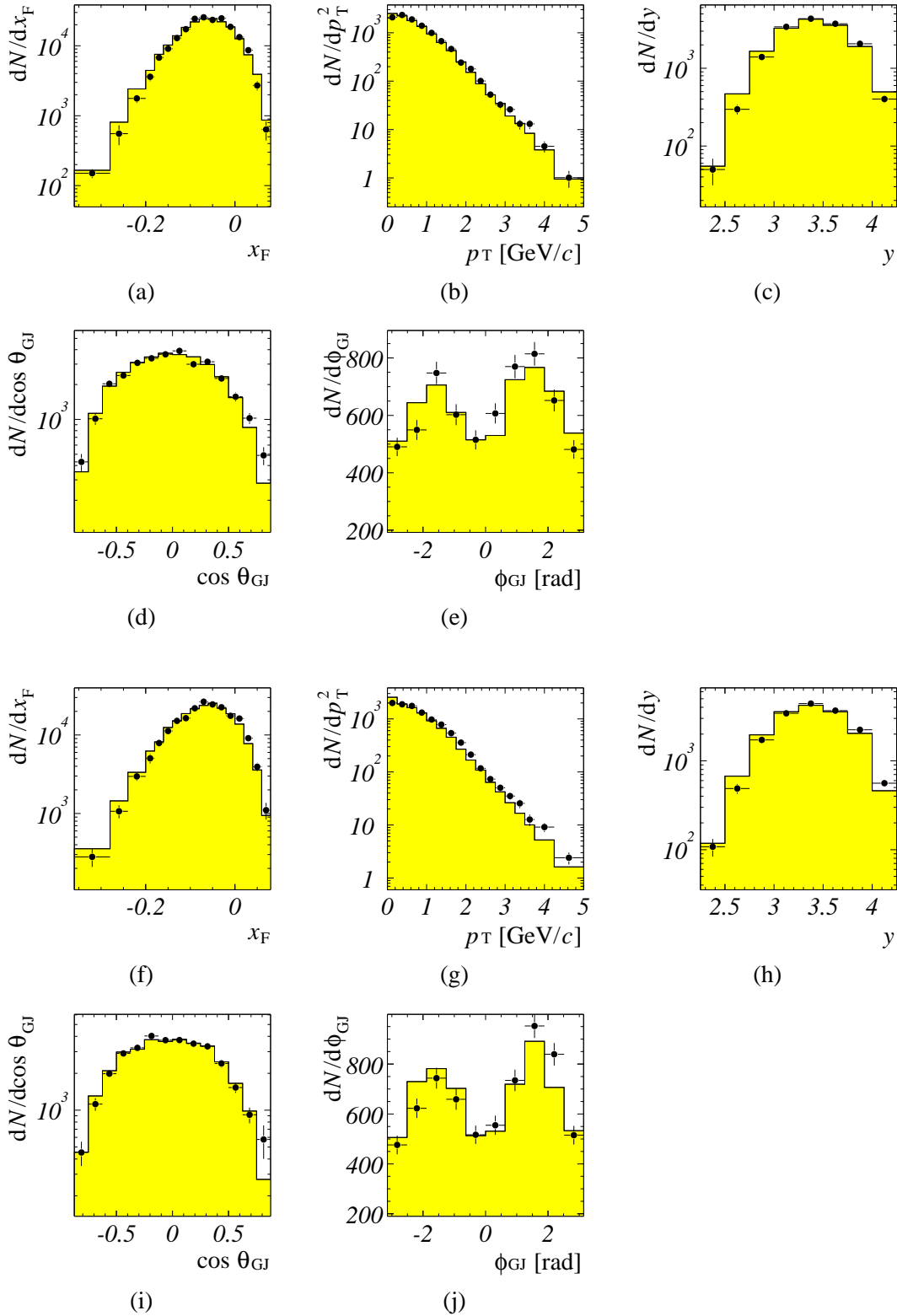


**Figure D.3:**  $J/\psi$  kinematics in data (points) and MC simulation (histograms) for the wire combination I1I2. (a)–(e)  $x_F$ ,  $p_T$ ,  $y$ ,  $\cos\theta_{GJ}$ , and  $\phi_{GJ}$  for  $J/\psi$  produced on the wire Inner II. (f)–(j)  $x_F$ ,  $p_T$ ,  $y$ ,  $\cos\theta_{GJ}$ , and  $\phi_{GJ}$  for  $J/\psi$  produced on the wire Inner I. The MC distributions are scaled to the integral of the data distributions.

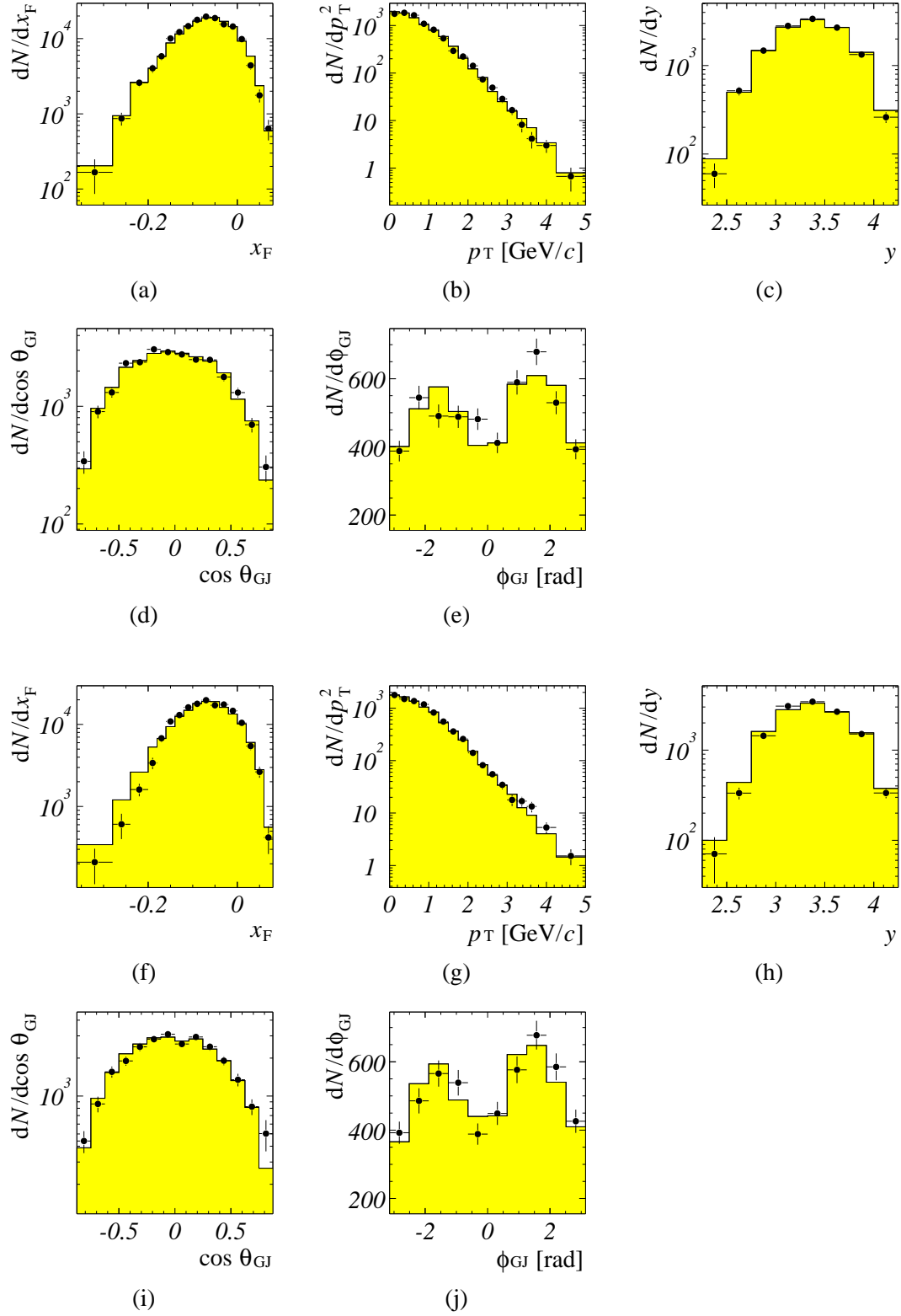


**Figure D.4:**  $J/\psi$  kinematics in data (points) and MC simulation (histograms) for the wire combination I1B1. (a)–(e)  $x_F$ ,  $p_T$ ,  $y$ ,  $\cos\theta_{GJ}$ , and  $\phi_{GJ}$  for  $J/\psi$  produced on the wire Inner II. (f)–(j)  $x_F$ ,  $p_T$ ,  $y$ ,  $\cos\theta_{GJ}$ , and  $\phi_{GJ}$  for  $J/\psi$  produced on the wire Inner I. The MC distributions are scaled to the integral of the data distributions.

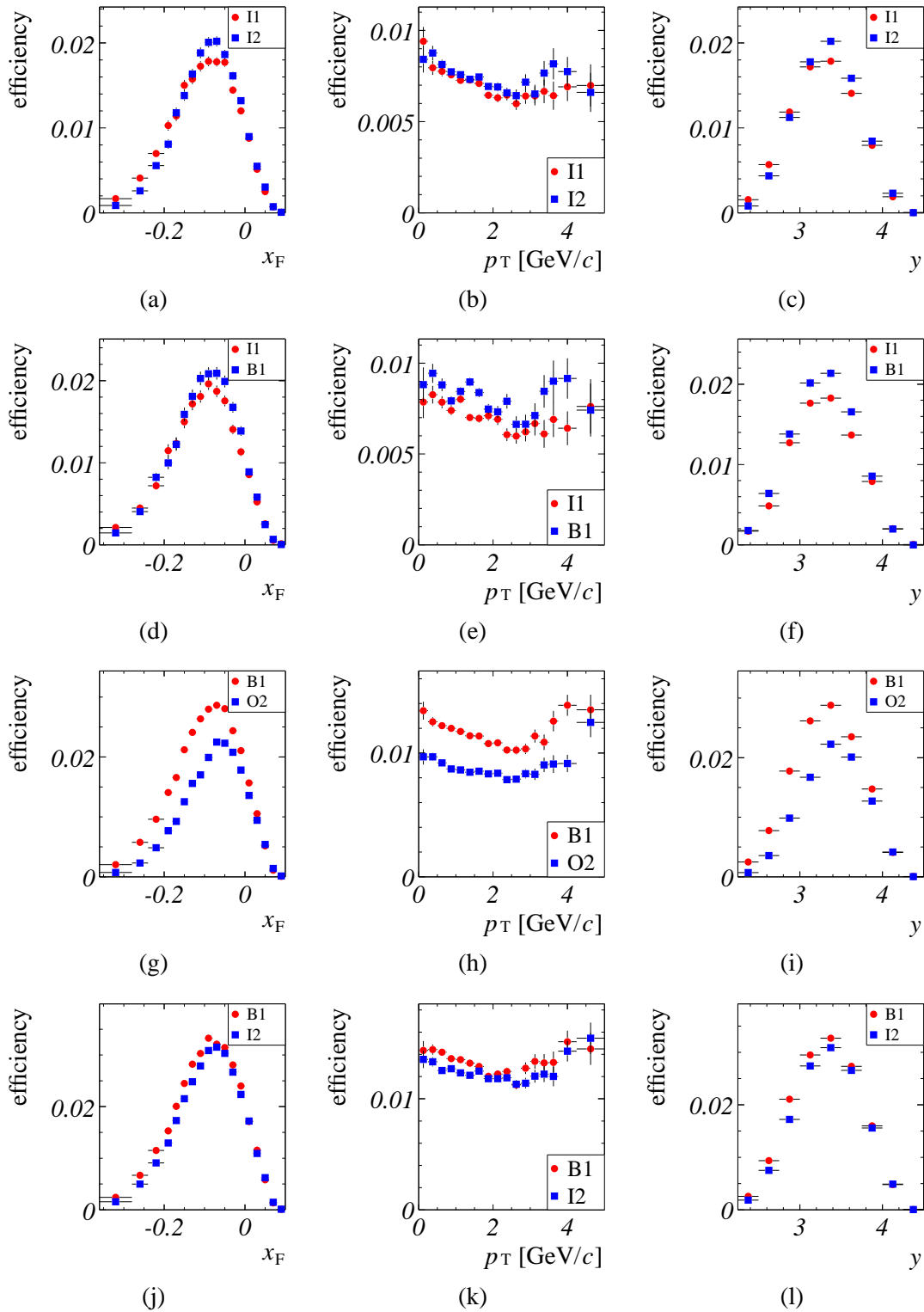


**Figure D.5:** Total efficiency as a function of the kinematic variables  $x_F$ ,  $p_T$ , and  $y$  for several calibration periods and wire combinations. (a)–(c) I1I2 November 2002. (d)–(f) I1B1 November 2002. (g)–(i) B1O2 January 2003 (II). (j)–(l) B1I2 January 2003 (II).

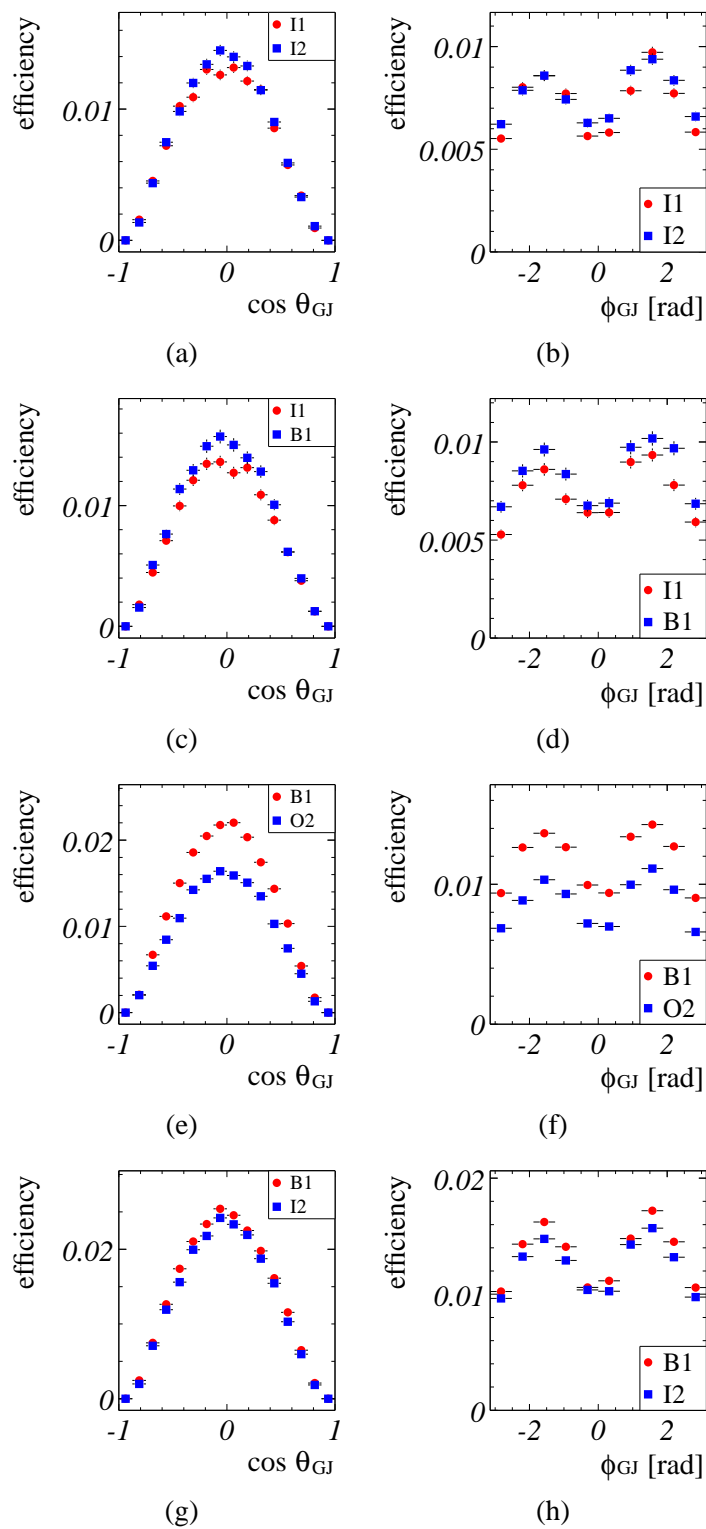


**Figure D.6:** Total efficiency as a function of the kinematic variables  $\cos \theta_{GJ}$  and  $\phi_{GJ}$  for several calibration periods and wire combinations. (a)–(b) I1I2 November 2002. (c)–(d) I1B1 November 2002. (e)–(f) B1O2 January 2003 (I). (g)–(h) B1I2 January 2003 (II).

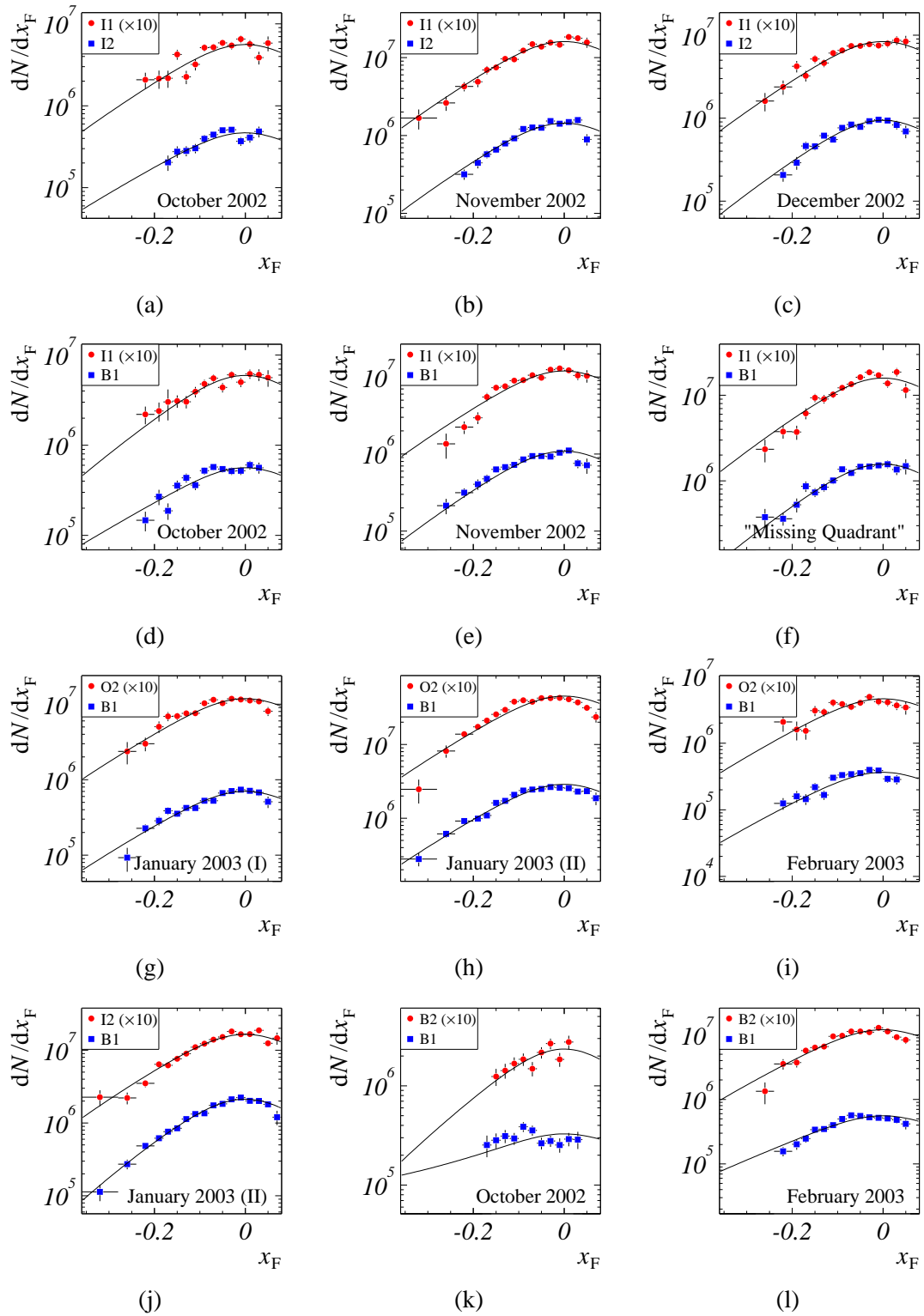


**Figure D.7:** Differential distributions:  $dN/dx_F$  for all two-wire combinations in all calibration periods. (a) I1I2 October 2002. (b) I1I2 November 2002. (c) I1I2 December 2002. (d) I1B1 October 2002. (e) I1B1 November 2002. (f) I1B1 “Missing Quadrant”. (g) B1O2 January 2003 (I). (h) B1O2 January 2003 (II). (i) B1O2 February 2003. (j) B1I2 January 2003 (II). (k) B1B2 October 2003. (l) B1B2 February 2003. The solid lines indicate fits to the spectra. The fit results are summarized in Table D.1.



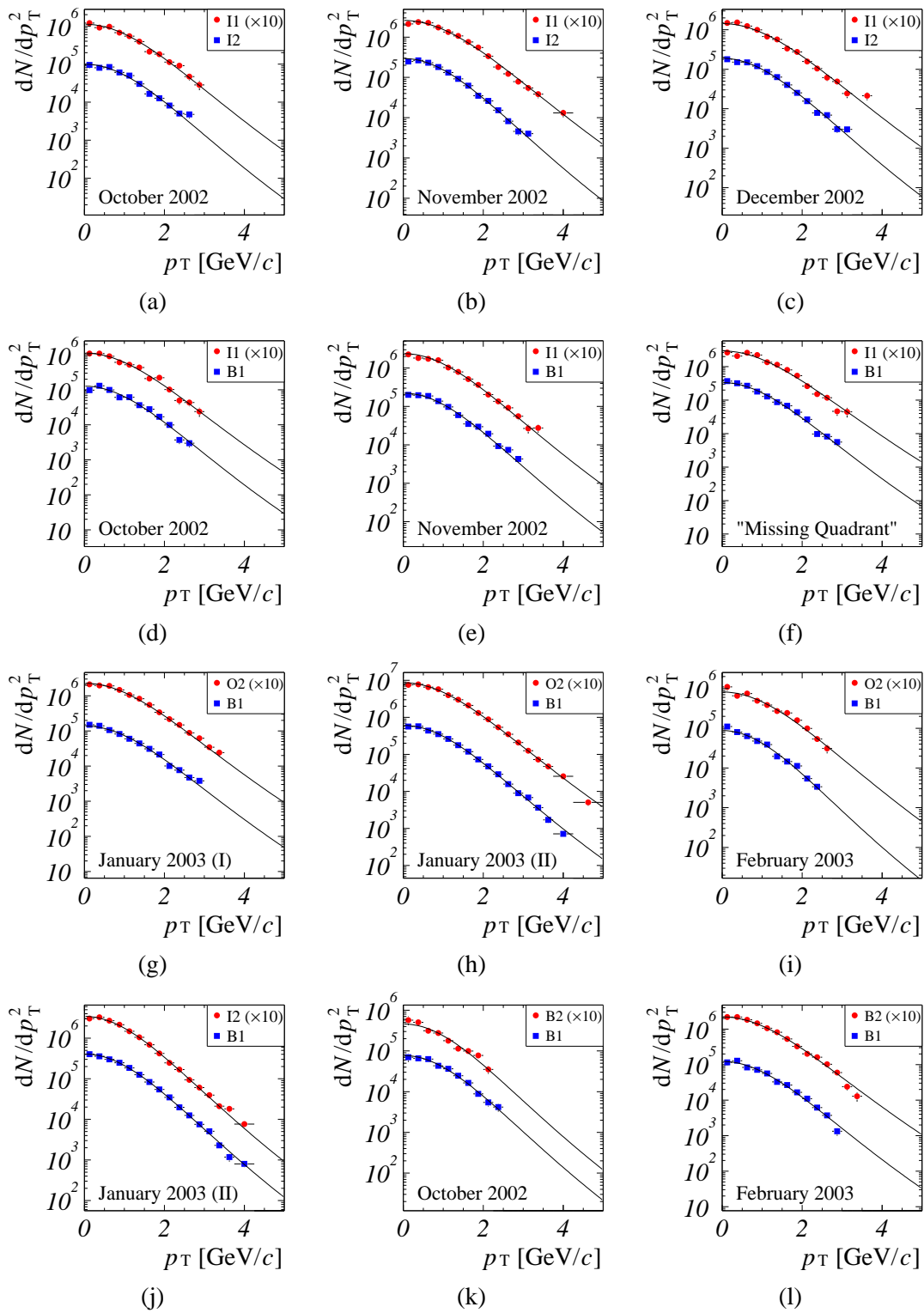


**Figure D.8:** Differential distributions:  $dN/dp_T^2$  for all two-wire combinations in all calibration periods. (a) I1I2 October 2002. (b) I1I2 November 2002. (c) I1I2 December 2002. (d) I1B1 October 2002. (e) I1B1 November 2002. (f) I1B1 “Missing Quadrant”. (g) B1O2 January 2003 (I). (h) B1O2 January 2003 (II). (i) B1O2 February 2003. (j) B1I2 January 2003 (II). (k) B1B2 October 2002. (l) B1B2 February 2003. The solid lines indicate fits to the spectra. The fit results are summarized in Table D.2.

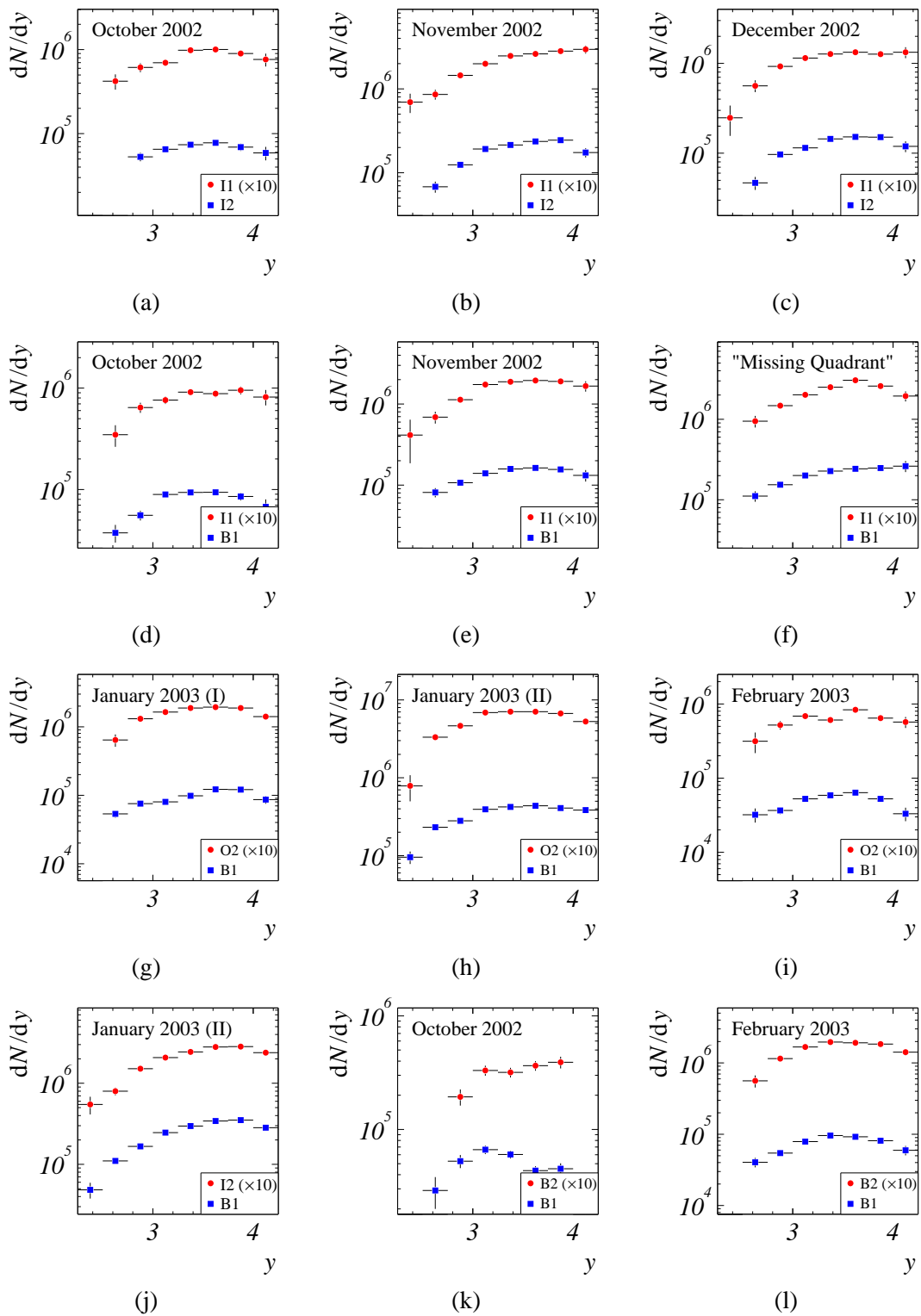


**Figure D.9:** Differential distributions:  $dN/dy$  for all two-wire combinations in all calibration periods. (a) III2 October 2002. (b) III2 November 2002. (c) I1I2 December 2002. (d) I1B1 October 2002. (e) I1B1 November 2002. (f) I1B1 “Missing Quadrant”. (g) B1O2 January 2003 (I) (h) B1O2 January 2003 (II) (i) B1O2 February 2003. (j) B1I2 January 2003 (II). (k) B1B2 October 2003. (l) B1B2 February 2003.

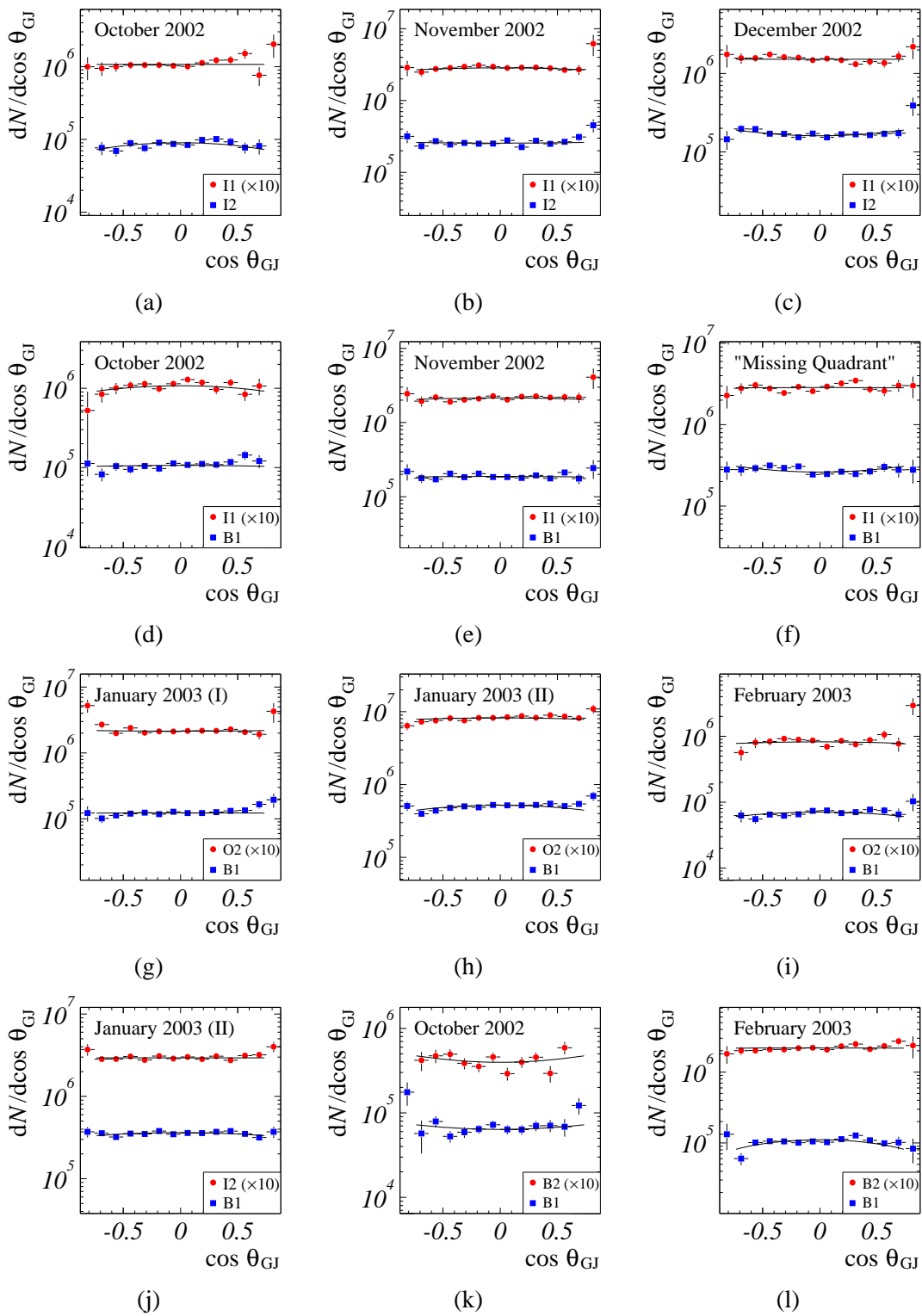


**Figure D.10:** Differential distributions:  $dN/d\cos \theta_{GJ}$  for all two-wire combinations in all calibration periods. (a) I1I2 October 2002. (b) I1I2 November 2002. (c) I1I2 December 2002. (d) I1B1 October 2002. (e) I1B1 November 2002. (f) I1B1 “Missing Quadrant”. (g) B1O2 January 2003 (I). (h) B1O2 January 2003 (II). (i) B1O2 February 2003. (j) B1I2 January 2003 (II). (k) B1B2 October 2003. (l) B1B2 February 2003. The solid lines indicate fits to the spectra. The fit results are summarized in Table D.3.

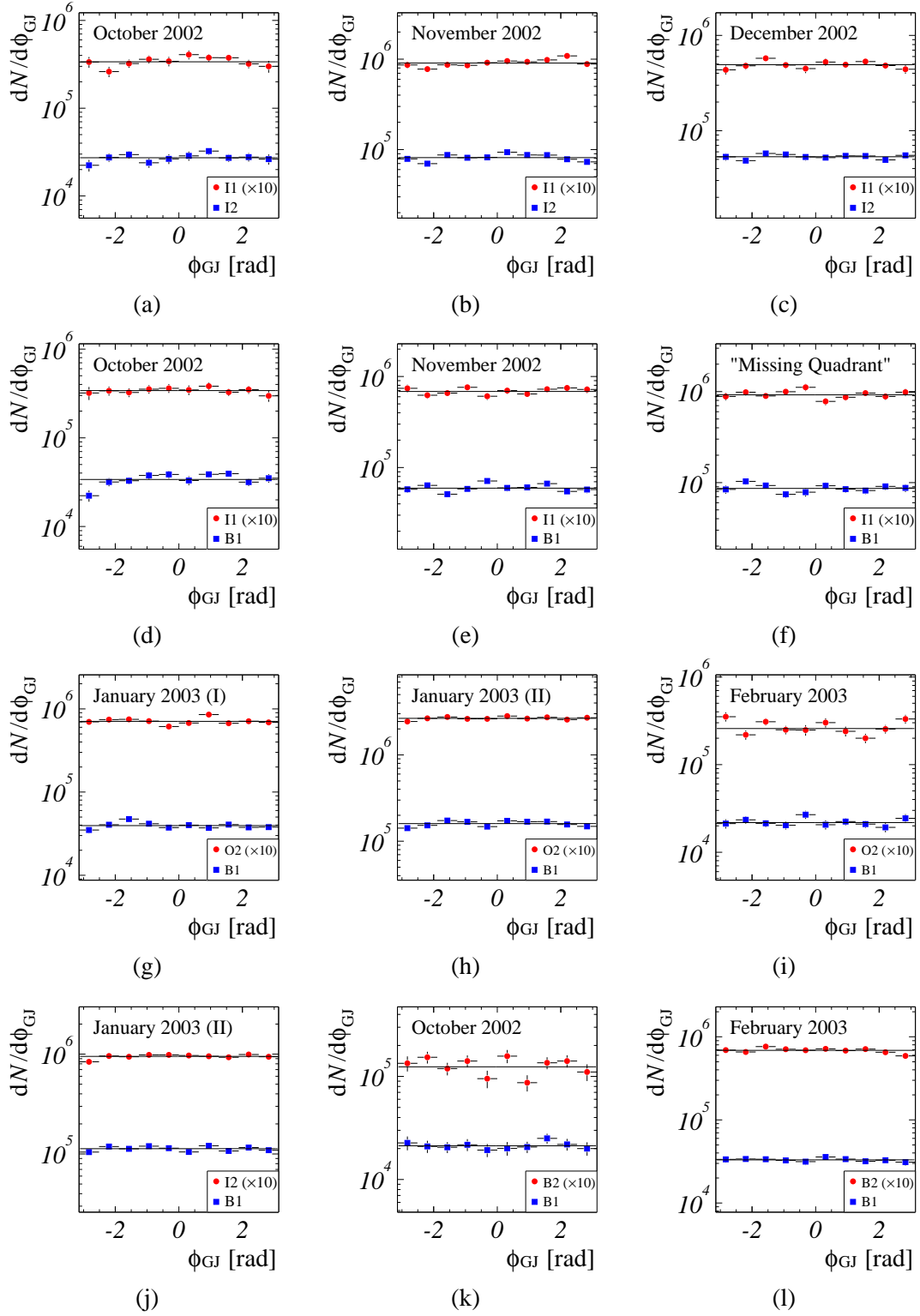


**Figure D.11:** Differential distributions:  $dN/d\phi_{GJ}$  for all two-wire combinations in all calibration periods. (a) III2 October 2002. (b) III2 November 2002. (c) III2 December 2002. (d) IIB1 October 2002. (e) IIB1 November 2002. (f) IIB1 “Missing Quadrant”. (g) B1O2 January 2003 (I). (h) B1O2 January 2003 (II). (i) B1O2 February 2003. (j) B1I2 January 2003 (II). (k) B1B2 October 2003. (l) B1B2 February 2003. The solid lines indicate fits to the spectra. The fit results are summarized in Table D.4.

**Table D.1:** Fits to the  $x_F$  differential distributions. The number of  $J/\psi$  as a function of  $x_F$  is fitted to a function proposed by the E705 collaboration [Ant92]  $\propto [(1-x_1)(1-x_2)]^C/\sqrt{x_F^2+4M^2/s}$  and to the  $x_F$  shape predicted by NRQCD [Vog04]. The table shows the fit result for the parameter  $C$  and the fit quality of the E705-inspired and the NRQCD fits. For the wire combinations B1I2 and B1B2 (October 2002), the actual materials of the “Tungsten Wire” column are carbon and titanium.

Wires	Period	Carbon Wire			Tungsten Wire		
		E705: $C$	E705: $\chi^2/n_{\text{dof}}$	NRQCD: $\chi^2/n_{\text{dof}}$	E705: $C$	E705: $\chi^2/n_{\text{dof}}$	NRQCD: $\chi^2/n_{\text{dof}}$
I1I2	October 2002	$3.65\pm 1.02$	12.2/9	11.1/10	$4.53\pm 0.88$	26.8/12	26.4/13
I1I2	November 2002	$5.05\pm 0.56$	20.7/12	31.3/13	$4.89\pm 0.47$	15.1/14	24.3/15
I1I2	December 2002	$5.05\pm 0.68$	15.2/12	18.4/13	$4.64\pm 0.65$	11.4/13	9.4/14
I1B1	October 2002	$3.05\pm 0.72$	19.9/11	16.7/12	$4.89\pm 1.33$	10.8/12	9.1/13
I1B1	November 2002	$5.29\pm 0.68$	22.5/13	13.7/14	$4.89\pm 0.55$	29.9/13	40.4/14
I1B1	“Missing Quadrant”	$5.04\pm 0.73$	9.6/13	11.2/14	$4.77\pm 0.58$	27.8/13	37.8/14
B1O2	January 2003 (I)	$4.40\pm 0.60$	14.9/13	17.0/14	$4.56\pm 0.59$	23.8/13	19.8/14
B1O2	January 2003 (II)	$4.69\pm 0.36$	57.6/15	38.7/16	$4.81\pm 0.32$	114.9/15	98.0/16
B1O2	February 2003	$4.49\pm 0.73$	21.9/11	19.2/12	$4.89\pm 1.44$	17.3/12	14.5/13
B1I2	January 2003 (II)	$6.85\pm 0.35$	17.4/15	109.6/16	$5.11\pm 0.34$	31.9/15	62.7/16
B1B2	October 2002	$0.00\pm 0.29$	19.2/9	33.4/10	$5.04\pm 2.36$	9.6/7	9.2/8
B1B2	February 2003	$3.13\pm 0.66$	18.1/12	14.7/13	$4.75\pm 0.56$	31.9/13	32.1/14

**Table D.2:** Fits to the  $p_T$  differential distributions. The number of  $J/\psi$  as a function of  $p_T^2$  is fitted to a function  $\propto (1 + (35\pi p_T)^2 / (256\langle p_T \rangle)^2)^{-6}$ , separately for the carbon and the tungsten wire. The table shows the fit result for the parameter  $\langle p_T \rangle$ , the fit quality and  $\langle p_T \rangle$  calculated from the mean value and the standard deviation of the  $p_T$  distribution. For the wire combinations B1I2 and B1B2 (October 2002), the actual materials of the “Tungsten Wire” column are carbon and titanium.

Wires	Period	Carbon Wire			Tungsten Wire		
		Fit: $\langle p_T \rangle$ [GeV/c]	$\chi^2/n_{\text{dof}}$	Histo: $\langle p_T \rangle$ [GeV/c]	Fit: $\langle p_T \rangle$ [GeV/c]	$\chi^2/n_{\text{dof}}$	Histo: $\langle p_T \rangle$ [GeV/c]
I1I2	October 2002	1.263±0.035	10.2/9	1.265±0.022	1.334±0.037	7.8/10	1.338±0.021
I1I2	November 2002	1.264±0.018	6.7/11	1.264±0.012	1.428±0.020	12.8/13	1.398±0.012
I1I2	December 2002	1.275±0.020	11.1/11	1.267±0.013	1.406±0.028	14.8/12	1.365±0.016
I1B1	October 2002	1.230±0.028	20.1/9	1.242±0.019	1.305±0.034	14.9/10	1.318±0.022
I1B1	November 2002	1.236±0.023	18.0/10	1.231±0.013	1.301±0.023	10.2/12	1.335±0.014
I1B1	“Missing Quadrant”	1.211±0.025	13.4/10	1.199±0.015	1.337±0.024	32.1/11	1.327±0.014
B1O2	January 2003 (I)	1.289±0.022	11.4/10	1.271±0.014	1.311±0.019	8.1/12	1.323±0.013
B1O2	January 2003 (II)	1.238±0.009	14.7/14	1.233±0.007	1.323±0.009	19.8/15	1.325±0.006
B1O2	February 2003	1.189±0.032	9.6/8	1.182±0.019	1.356±0.038	10.5/9	1.318±0.020
B1I2	January 2003 (II)	1.265±0.010	8.2/14	1.263±0.008	1.251±0.012	11.7/14	1.246±0.009
B1B2	October 2002	1.256±0.042	2.9/8	1.281±0.026	1.248±0.060	8.6/7	1.276±0.031
B1B2	February 2003	1.251±0.022	18.1/10	1.238±0.015	1.339±0.018	16.2/12	1.301±0.012

**Table D.3:** Fits to  $\cos \theta_{GJ}$  differential distributions. The number of  $J/\psi$  as a function of  $\cos \theta_{GJ}$  is fitted to a function  $\propto (1 + \lambda \cos^2 \theta_{GJ})$ . The table shows the fit result for the parameter  $\lambda$ , the fit quality, and the asymmetry in the number of  $J/\psi$  with positive and negative  $\cos \theta_{GJ}$ , separately for the carbon and the tungsten wires. For the wire combinations B1I2 and B1B2 (October 2002), the actual materials of the ‘‘Tungsten Wire’’ column are carbon and titanium.

Wires	Period	Carbon Wire			Tungsten Wire		
		$\lambda$	$\chi^2/n_{\text{dof}}$	Asymmetry	$\lambda$	$\chi^2/n_{\text{dof}}$	Asymmetry
I1I2	October 2002	$-0.365 \pm 0.238$	6.6/10	0.046	$0.000 \pm 0.271$	9.7/10	0.057
I1I2	November 2002	$0.044 \pm 0.167$	11.2/10	0.032	$-0.112 \pm 0.140$	3.5/10	-0.009
I1I2	December 2002	$0.340 \pm 0.202$	4.2/10	-0.030	$0.000 \pm 0.206$	7.7/10	-0.044
I1B1	October 2002	$-0.049 \pm 0.231$	10.6/10	0.088	$-0.274 \pm 0.252$	8.8/10	0.026
I1B1	November 2002	$-0.032 \pm 0.186$	6.0/10	-0.003	$-0.088 \pm 0.199$	4.3/10	0.025
I1B1	‘‘Missing Quadrant’’	$0.334 \pm 0.245$	8.1/10	-0.037	$-0.014 \pm 0.208$	13.3/10	0.040
B1O2	January 2003 (I)	$-0.018 \pm 0.179$	8.8/10	0.067	$0.039 \pm 0.180$	7.1/10	-0.022
B1O2	January 2003 (II)	$-0.271 \pm 0.088$	19.7/10	0.055	$-0.077 \pm 0.093$	15.1/10	0.041
B1O2	February 2003	$-0.262 \pm 0.240$	5.8/10	0.057	$-0.102 \pm 0.272$	10.1/10	0.012
B1I2	January 2003 (II)	$-0.150 \pm 0.102$	8.0/10	0.006	$0.000 \pm 0.118$	8.9/10	0.015
B1B2	October 2002	$0.248 \pm 0.406$	9.7/10	0.088	$0.361 \pm 0.438$	14.6/9	-0.120
B1B2	February 2003	$-0.495 \pm 0.164$	15.3/10	0.060	$-0.006 \pm 0.167$	10.1/10	0.055

**Table D.4:** Fits to the  $\phi_{GJ}$  differential distributions. The number of  $J/\psi$  as a function of  $\phi_{GJ}$  is fitted to a constant function. The table shows the quality of the fits separately for the carbon and the tungsten wires. For the wire combinations B1I2 and B1B2 (October 2002), the actual materials of the “Tungsten Wire” column are carbon and titanium.

Wires	Period	Carbon: $\chi^2/n_{\text{dof}}$	Tungsten: $\chi^2/n_{\text{dof}}$
I1I2	October 2002	7.2/9	10.7/9
I1I2	November 2002	15.4/9	16.8/9
I1I2	December 2002	5.0/9	8.9/9
I1B1	October 2002	21.6/9	3.0/9
I1B1	November 2002	14.1/9	8.7/9
I1B1	“Missing Quadrant”	10.1/9	10.7/9
B1O2	January 2003 (I)	11.8/9	12.6/9
B1O2	January 2003 (II)	27.5/9	8.0/9
B1O2	February 2003	6.7/9	21.5/9
B1I2	January 2003 (II)	13.1/9	7.0/9
B1B2	October 2002	3.1/9	15.1/9
B1B2	February 2003	2.1/9	8.3/9



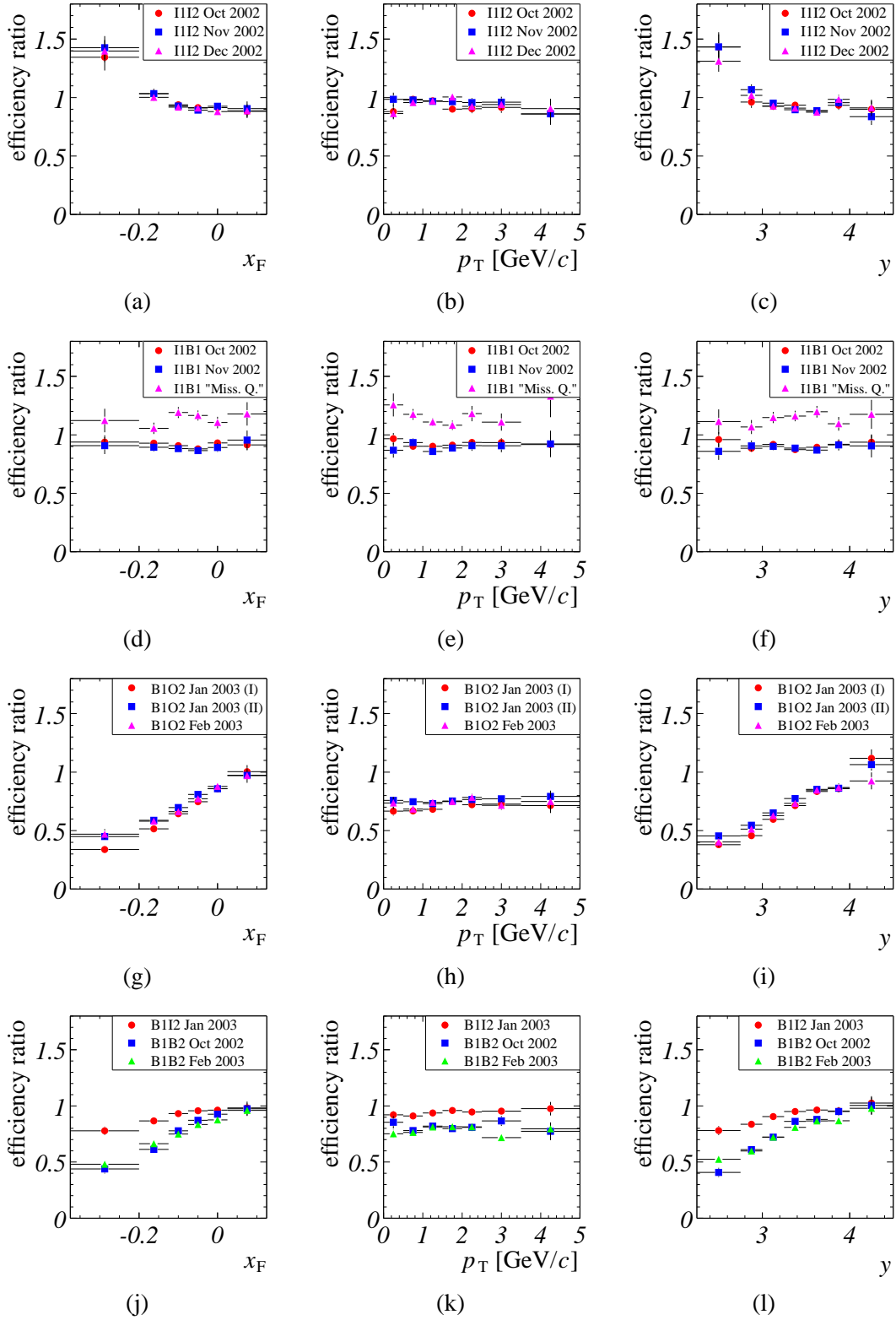


**Figure D.12:** Efficiency ratios as a function of  $x_F$ ,  $p_T$ , and  $y$  for all wire combinations and calibration periods. (a)–(c)  $\epsilon^{I1}/\epsilon^{I2}$  for the calibration periods of October 2002, November 2002, and December 2002. (d)–(f)  $\epsilon^{I1}/\epsilon^{B1}$  for October 2002, November 2002, and “Missing Quadrant”. (g)–(i)  $\epsilon^{O2}/\epsilon^{B1}$  for January 2003 (I), January 2003 (II), and February 2003. (j)–(l)  $\epsilon^{I2}/\epsilon^{B1}$  for January 2003 (II) and  $\epsilon^{B2}/\epsilon^{B1}$  for October 2002 and February 2003.

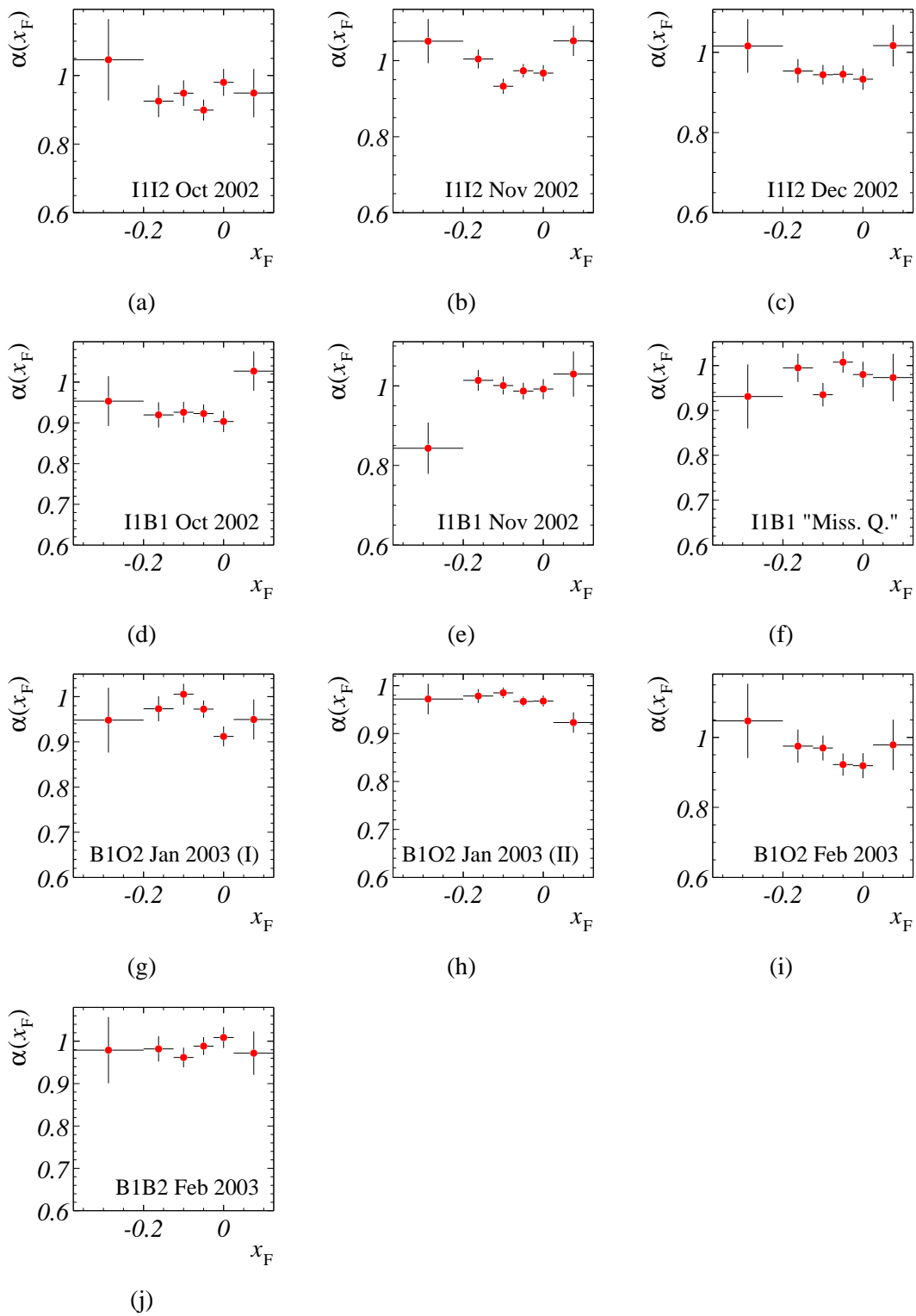


**Figure D.13:** Nuclear suppression parameter  $\alpha$  as a function of  $x_F$  for all carbon-tungsten wire combinations in all calibration periods. The error bars include only statistical uncertainties. (a) III2 October 2002. (b) III2 November 2002. (c) III2 December 2002. (d) IIB1 October 2002. (e) IIB1 November 2002. (f) IIB1 "Missing Quadrant". (g) B1O2 January 2003 (I). (h) B1O2 January 2003 (II). (i) B1O2 February 2003. (j) B1B2 February 2003.

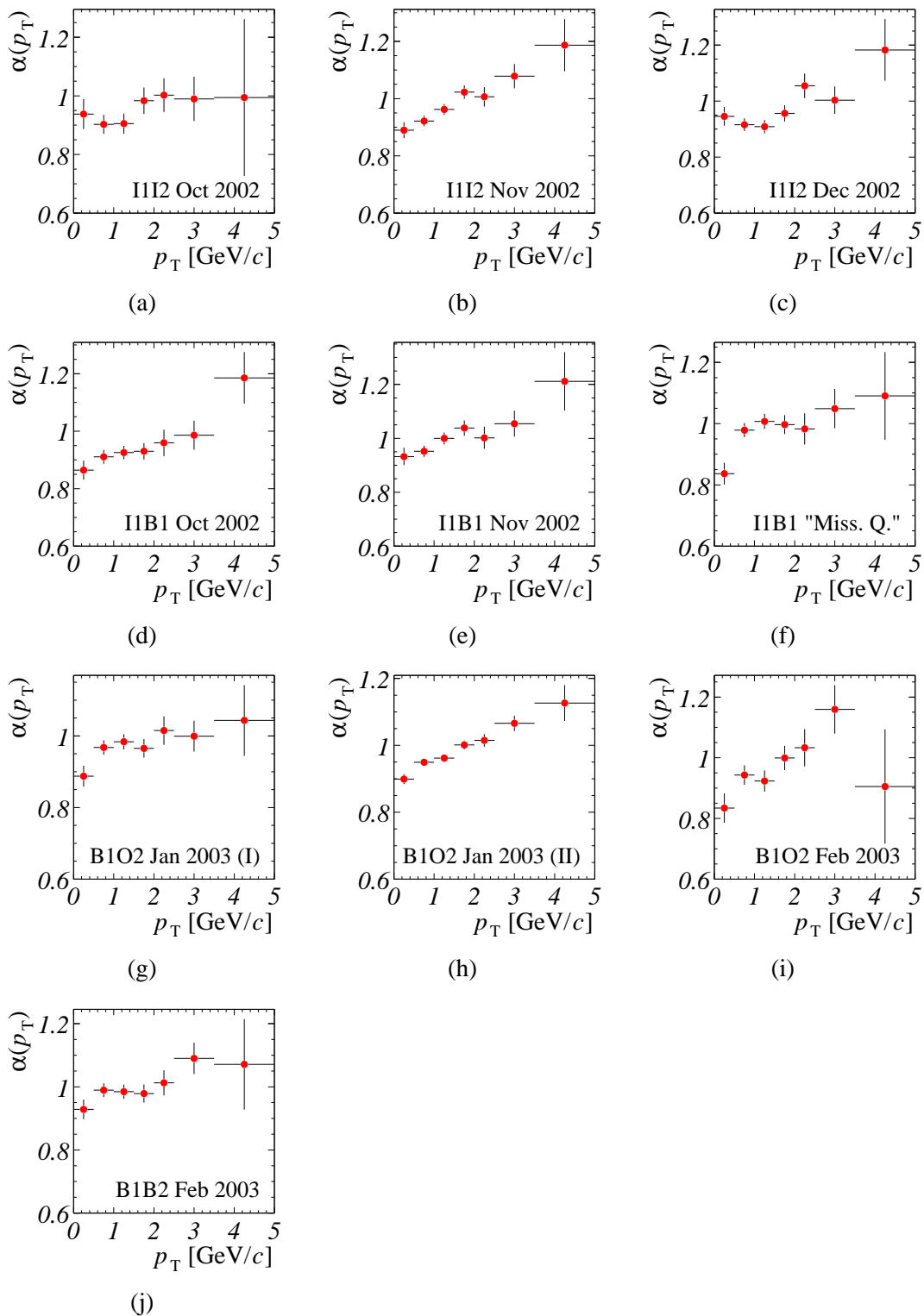


**Figure D.14:** Nuclear suppression parameter  $\alpha$  as a function of  $p_T$  for all carbon-tungsten wire combinations in all calibration periods. The error bars include only statistical uncertainties. (a) I1I2 October 2002. (b) I1I2 November 2002. (c) I1I2 December 2002. (d) I1B1 October 2002. (e) I1B1 November 2002. (f) I1B1 “Missing Quadrant”. (g) B1O2 January 2003 (I). (h) B1O2 January 2003 (II). (i) B1O2 February 2003. (j) B1B2 February 2003.

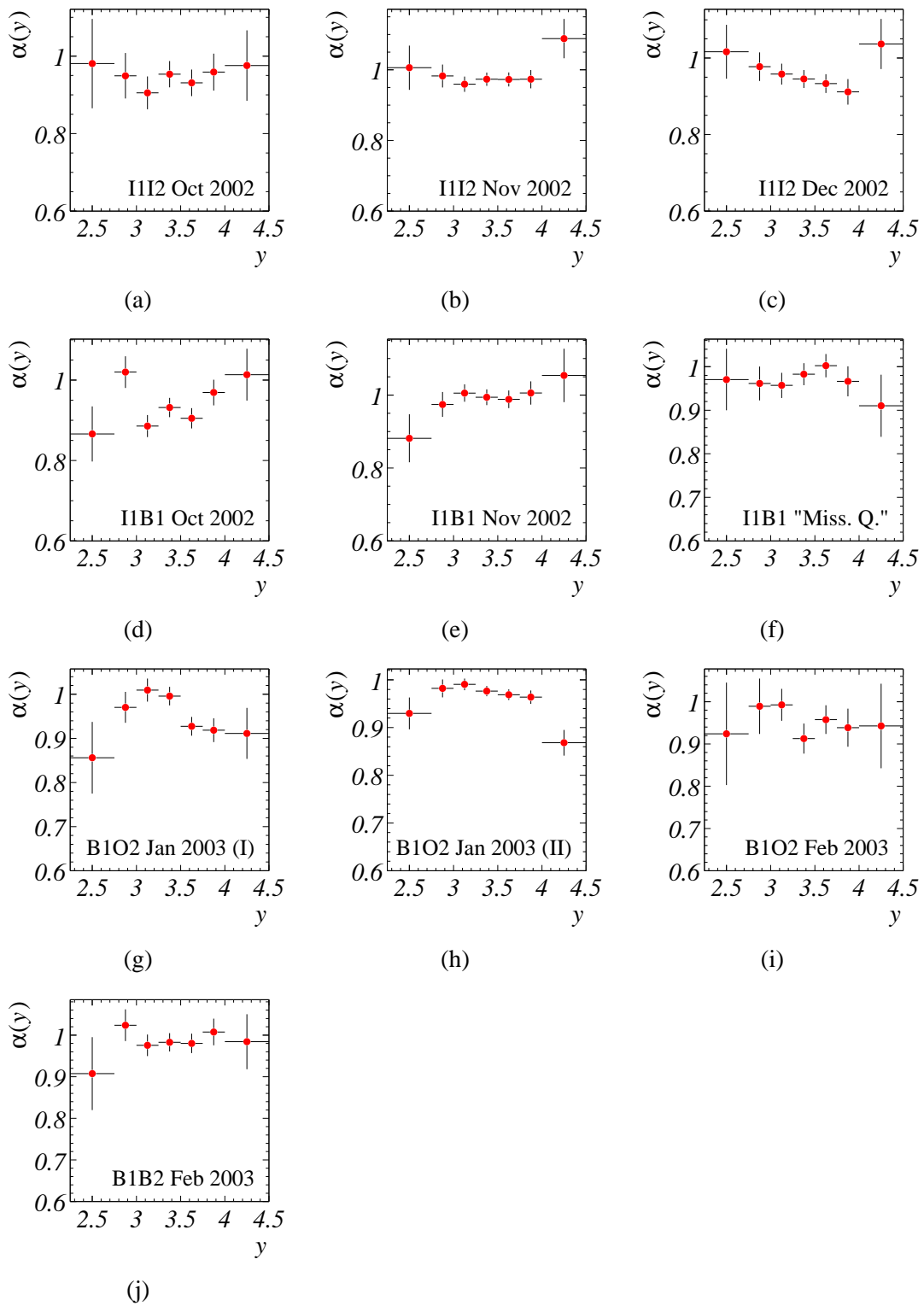


**Figure D.15:** Nuclear suppression parameter  $\alpha$  as a function of  $y$  for all carbon-tungsten wire combinations in all calibration periods. The error bars include only statistical uncertainties. (a) III2 October 2002. (b) III2 November 2002. (c) III2 December 2002. (d) IIB1 October 2002. (e) IIB1 November 2002. (f) IIB1 "Missing Quadrant". (g) B1O2 January 2003 (I) (h) B1O2 January 2003 (II) (i) B1O2 February 2003. (j) B1B2 February 2003.

# List of Figures

2.1	Sketch of the HERA storage ring . . . . .	8
2.2	Schematic views of the HERA-B detector . . . . .	9
2.3	Sketch of the target wire configuration . . . . .	10
2.4	Schematic drawing of the VDS . . . . .	12
2.5	Illustration of the honeycomb drift cells of the OTR . . . . .	13
2.6	Sketch of a GEM-MSGC detector of the ITR . . . . .	14
2.7	Schematic drawing of the RICH, and Čerenkov angle as a function of $p$ . . . . .	15
2.8	Illustration of the shashlik calorimeter used in the ECAL . . . . .	15
2.9	Sketch of the muon detector . . . . .	16
2.10	Muon pretrigger coincidence schemes . . . . .	18
2.11	The network of FLT processors . . . . .	20
3.1	Invariant mass spectrum of charmonium states . . . . .	33
3.2	Contributions of $\mathcal{O}(\alpha_S^3)$ to charmonium production in the CSM . . . . .	36
3.3	Sketch of a color-octet contribution to $J/\psi$ production . . . . .	40
3.4	$x_F$ distribution of $J/\psi$ production in NRQCD and in the CEM . . . . .	41
3.5	Schematic illustration of a proton-nucleus collision in the Glauber model . . . . .	42
3.6	Illustrations of charmonium suppression by nuclear structure functions . . . . .	49
3.7	Charmonium energy loss at 800 GeV in NRQCD . . . . .	50
3.8	Nuclear suppression by final state absorption at 920 GeV . . . . .	53
3.9	Nuclear suppression by a combination of nuclear effects at 800 GeV . . . . .	54
3.10	$J/\psi$ suppression in the BCKT model . . . . .	54
3.11	$J/\psi$ suppression in the light-cone Green function approach . . . . .	55
3.12	Schematic drawing of the CERN NA50 experiment . . . . .	57
3.13	Schematic drawing of the FNAL Meson East spectrometer . . . . .	58
3.14	Previous measurements of $\alpha$ as a function of $x_F$ . . . . .	60
3.15	Previous measurements of $\alpha$ as a function of $p_T$ . . . . .	61
4.1	Influence of track selection cuts . . . . .	70
4.2	Influence of vertex selection cuts . . . . .	71
4.3	Fiducial cuts in the OTR superlayer PC1 . . . . .	72
4.4	Fits to the invariant mass spectra in the data and in the MC simulation . . . . .	76
4.5	Illustration of wire separation methods . . . . .	78
4.6	Comparison of the PYTHIA-generated and reweighted kinematic distributions . . . . .	82
4.7	Sketch of the trigger simulation chain . . . . .	83

4.8	Efficiencies of the trigger simulation steps . . . . .	83
4.9	Detector resolutions in the kinematic variables $x_F$ , $p_T$ , and $y$ . . . . .	86
4.10	Comparison of muon momenta in the data and the MC simulation . . . . .	87
4.11	Comparison of $J/\psi$ kinematic distributions: data vs. MC simulation . . . . .	88
4.12	Total efficiency as a function of $x_F$ and $p_T$ . . . . .	90
4.13	Mass and width of $J/\psi$ signal, and background slope . . . . .	93
4.14	$J/\psi$ differential distributions summed over all data sets . . . . .	95
4.15	Fit parameters for the $x_F$ , $p_T$ , and $\cos \theta_{GJ}$ distributions for all data samples . . . . .	96
5.1	Comparison of luminosity ratios: vertex counting versus track counting . . . . .	111
6.1	Comparison of efficiency ratios as a function of $x_F$ and $p_T$ . . . . .	116
6.2	Summary of systematic uncertainties in the efficiency ratio . . . . .	119
6.3	Systematic checks of $J/\psi$ yield ratios . . . . .	122
6.4	Correlation of the $x_F$ and $p_T$ efficiencies . . . . .	123
6.5	Comparison of methods to combine data sets. . . . .	129
6.6	Average cross section ratio $R^{CC}$ in the control sample . . . . .	130
6.7	Nuclear suppression parameter $\alpha$ as a function of $x_F$ , $p_T$ , and $y$ . . . . .	131
6.8	Systematic uncertainties of the nuclear suppression parameter $\alpha$ . . . . .	133
6.9	Nuclear suppression parameter $\alpha$ compared to E866 and NA50 . . . . .	136
6.10	Scaling of the nuclear suppression parameter with $x_2$ . . . . .	137
6.11	Nuclear suppression parameter $\alpha(x_F)$ compared to theoretical predictions . . . . .	138
6.12	Nuclear absorption cross section in the $\langle \rho L \rangle$ parametrization . . . . .	139
A.1	Flow chart of the detector and trigger simulations in the muon detector. . . . .	146
A.2	Weighting functions used for $x_F$ and $p_T$ reweighting . . . . .	148
A.3	Masks for defective channels in the muon pad system for November 2002 . . . . .	153
A.4	Effective muon pretrigger optical link efficiencies for November 2002 . . . . .	155
A.5	Illustration of SLT target box calculation . . . . .	159
A.6	Projection of the average FLT efficiency map for November 2002 . . . . .	160
B.1	Laboratory frame travelling distance $\beta\gamma c\tau$ as a function of $x_F$ . . . . .	163
B.2	Definitions of angular variables in the decay $J/\psi \rightarrow \mu^+\mu^-$ . . . . .	164
D.1	I1I2: kinematics of muons from $J/\psi$ decays in data and MC simulation . . . . .	170
D.2	I1B1: kinematics of muons from $J/\psi$ decays in data and MC simulation . . . . .	171
D.3	I1I2: $J/\psi$ kinematics in data and MC simulation . . . . .	172
D.4	I1B1: $J/\psi$ kinematics in data and MC simulation . . . . .	173
D.5	Total efficiency as a function of the kinematic variables $x_F$ , $p_T$ , and $y$ . . . . .	174
D.6	Total efficiency as a function of the kinematic variables $\cos \theta_{GJ}$ and $\phi_{GJ}$ . . . . .	175
D.7	Differential distributions: $dN/dx_F$ . . . . .	176
D.8	Differential distributions: $dN/dp_T^2$ . . . . .	177
D.9	Differential distributions: $dN/dy$ . . . . .	178
D.10	Differential distributions: $dN/d\cos \theta_{GJ}$ . . . . .	179
D.11	Differential distributions: $dN/d\phi_{GJ}$ . . . . .	180
D.12	Efficiency ratios for all wire combinations and calibration periods . . . . .	185
D.13	Nuclear suppression parameter $\alpha$ as a function of $x_F$ . . . . .	186
D.14	Nuclear suppression parameter $\alpha$ as a function of $p_T$ . . . . .	187
D.15	Nuclear suppression parameter $\alpha$ as a function of $y$ . . . . .	188

# List of Tables

1.1	The fundamental fermions in the Standard Model of particle physics . . .	2
1.2	Theories in the Standard Model of particle physics . . . . .	3
2.1	Target wire configurations during the data-taking period 2002/2003 . . .	11
3.1	Lowest order processes contributing to $J/\psi$ production at fixed-target energies . . . . .	40
3.2	NRQCD matrix elements for fixed-target $J/\psi$ production . . . . .	41
3.3	Summary of nuclear parameters for carbon and tungsten . . . . .	47
3.4	Compilation of $J/\psi$ $A$ -dependence measurements in pA collisions . . . .	63
4.1	Classification of dimuon candidate events . . . . .	67
4.2	Selection criteria for muon candidates . . . . .	69
4.3	Selection criteria for dimuon vertices . . . . .	71
4.4	List of fiducial volume cuts . . . . .	73
4.5	Run statistics for different wire configurations . . . . .	77
4.6	Definition of calibration periods during the 2002/2003 data-taking . . .	80
4.7	Summary of Monte Carlo simulated events . . . . .	81
4.8	Detector resolutions in the kinematic variables . . . . .	84
4.9	Carbon targets: fit parameters of $J/\psi$ differential distributions . . . . .	97
4.10	Tungsten targets: fit parameters of $J/\psi$ differential distributions . . . . .	97
5.1	Minimum-bias cross sections $\sigma^{\text{MB}}$ for carbon and tungsten targets . . .	104
5.2	Vertexing efficiencies for the wires Inner I and Below I . . . . .	106
5.3	Systematic uncertainties of the luminosity ratio . . . . .	112
6.1	Summary of systematic uncertainties of the efficiency ratio . . . . .	125
6.2	Summary of systematic uncertainties of the $J/\psi$ yield ratio . . . . .	125
6.3	Nuclear suppression parameter $\alpha$ as a function of $x_F$ . . . . .	132
6.4	Nuclear suppression parameter $\alpha$ as a function of $p_T$ . . . . .	132
6.5	Nuclear suppression parameter $\alpha$ as a function of $y$ . . . . .	132
6.6	Summary of systematic uncertainties on $\alpha$ . . . . .	135
A.1	Parameters for the calculation of $p_T$ weights . . . . .	149
A.2	List of swapped connections in the muon pad detector and the muon pretrigger . . . . .	154
A.3	Total efficiency of the muon pretrigger for muon pairs from $J/\psi$ decays .	158
C.1	List of two-wire runs used in the analysis . . . . .	166

D.1	Fits to the $x_F$ differential distributions . . . . .	181
D.2	Fits to the $p_T$ differential distributions . . . . .	182
D.3	Fits to $\cos \theta_{GJ}$ differential distributions . . . . .	183
D.4	Fits to the $\phi_{GJ}$ differential distributions . . . . .	184



# List of Acronyms

---

<b>Acronym</b>	<b>Explanation</b>
4LT	Fourth Level Trigger
ARTE	Analysis and Reconstruction Tool
BNL	Brookhaven National Laboratory
CARE	Calorimeter Reconstruction
CATS	Cellular Automaton for Tracking in Silicon
CDF	Collider Detector at Fermilab
CEM	Color Evaporation Model
CERN	Conseil Européen pour la Recherche Nucléaire (European Organization for Nuclear Research)
CSM	Color Singlet Model
DAQ	Data Acquisition
DESY	Deutsches Elektronen-Synchrotron
DMUP	Digitized Muon Pad Hits (ARTE table)
DMUT	Digitized Muon Tube Hits (ARTE table)
DSLIT	Digitized SLT Data (ARTE table)
DSP	Digital Signal Processor
DST	Data Summary Tape
ECAL	Electromagnetic Calorimeter
EEL	ECAL Energy Inhibit
EVRC	Event Reconstruction Information (ARTE table)
FED	Front-End Driver
FCS	Fast Control System
FLT	First Level Trigger
FNAL	Fermi National Accelerator Laboratory (Fermilab)
FTRA	First Level Trigger Tracks (ARTE table)
FWHM	Full Width at Half-Maximum
GEM	Gas Electron Multiplier
Grover	Generic Reconstruction of Vertices
HERA	Hadron-Elektron-Ringanlage
HITB	Hit Bank (ARTE table)

---

*continued on next page*

*continued from previous page*

<b>Acronym</b>	<b>Explanation</b>
ITR	Inner Tracker
LEP	Large Electron-Positron Collider
LHC	Large Hadron Collider
MC	Monte Carlo
MCIN	Monte Carlo Input Data (ARTE table)
MC $n$	Outer Tracker Magnet Chamber $n$
MF $n$	Muon Filter $n$
ML	Maximum Likelihood
MIMP	Monte Carlo Impact Point (ARTE table)
MINI	Mini Data Summary Tape
MSGC	Micro-Strip Gaseous Chamber
MU $n$	Muon Detector Superlayer $n$
MWPC	Multi-Wire Proportional Chamber
NRQCD	Nonrelativistic Quantum Chromodynamics
OTR	Outer Tracker
PC $n$	Outer Tracker Pattern Recognition Chamber $n$
PCU	Pretrigger Coincidence Unit
PDF	Parton Distribution Function
POL	Pretrigger Optical Link
QCD	Quantum Chromodynamics
QED	Quantum Electrodynamics
RHIC	Relativistic Heavy-Ion Collider
RICH	Ring-Imaging Čerenkov Counter
RoI	Region of Interest
RTRA	Reconstructed Tracks (ARTE table)
SLAC	Stanford Linear Accelerator Center
SLB	Second Level Buffer
SLT	Second Level Trigger
SPS	Super Proton Synchrotron
TC $n$	Outer Tracker Trigger Chamber $n$
TDU	Trigger Decision Unit
TFU	Track Finding Unit
TLT	Third Level Trigger
TPU	Track Parameter Unit
TRD	Transition Radiation Detector
VDS	Vertex Detector System
WWW	World Wide Web
XML	Extensible Markup Language

# Bibliography

- [Aba02] A. Abashian et al., *The Belle detector*, Nucl. Instrum. Meth. **A479** (2002), 117–232.
- [Abe97] F. Abe et al. (CDF Collaboration), *J/ψ and ψ(2S) production in p $\bar{p}$  collisions at  $\sqrt{s} = 1.8$  TeV*, Phys. Rev. Lett. **79** (1997), 572–577.
- [Abr74] G. S. Abrams et al., *Discovery of a Second Narrow Resonance in e<sup>+</sup>e<sup>-</sup> Annihilation*, Phys. Rev. Lett. **33** (1974), 1453–1455.
- [Abr97a] M. C. Abreu et al. (NA50 Collaboration), *Anomalous J/ψ suppression in Pb-Pb interactions at 158 GeV/c per nucleon*, Phys. Lett. **B410** (1997), 337–343.
- [Abr97b] M. C. Abreu et al. (NA50 Collaboration), *J/ψ and Drell-Yan cross-sections in Pb-Pb interactions at 158 GeV/c per nucleon*, Phys. Lett. **B410** (1997), 327–336.
- [Abr98a] M. C. Abreu et al. (NA38 Collaboration), *Charmonia production in 450-GeV/c proton induced reactions*, Phys. Lett. **B444** (1998), 516–522.
- [Abr98b] M. C. Abreu et al. (NA51 Collaboration), *J/ψ, ψ' and Drell-Yan production in pp and pd interactions at 450 GeV/c*, Phys. Lett. **B438** (1998), 35–40.
- [Abt97] I. Abt et al. (H1 Collaboration), *The H1 detector at HERA*, Nucl. Instrum. Meth. **A386** (1997), 310–347.
- [Abt02a] I. Abt et al., *CATS: a Cellular Automaton for Tracking in Silicon for the HERA-B Vertex Detector*, Nucl. Instrum. Meth. **A489** (2002), 389–405.
- [Abt02b] I. Abt et al., *The cellular automaton and Kalman filter based track search in the HERA-B pattern tracker*, Nucl. Instrum. Meth. **A490** (2002), 546–558.
- [Abt03a] I. Abt et al. (HERA-B Collaboration), *Inclusive V<sup>0</sup> production cross sections from 920 GeV fixed target proton nucleus collisions*, Eur. Phys. J. **C29** (2003), 181–190.
- [Abt03b] I. Abt et al. (HERA-B Collaboration), *J/ψ production via χ<sub>c</sub> decays in 920 GeV pA interactions*, Phys. Lett. **B561** (2003), 61–72.

- [Abt03c] I. Abt et al. (HERA-B Collaboration), *Measurement of the  $b\bar{b}$  production cross section in 920 GeV fixed-target proton-nucleus collisions*, Eur. Phys. J. **C26** (2003), 345–355.
- [Abt03d] I. Abt et al., *Update on the performance of the HERA-B vertex detector system*, Nucl. Instrum. Meth. **A511** (2003), 24–31.
- [Abt04a] I. Abt et al., *Grover – the vertexing package for the HERA-B experiment*, to be published in Nucl. Instrum. Meth. **A**.
- [Abt04b] I. Abt et al. (HERA-B Collaboration), *Limits for the central production of  $\Theta^+$  and  $\Xi^{--}$  pentaquarks in 920 GeV pA collisions*, Phys. Rev. Lett. **93** (2004), 212003.
- [Abt04c] I. Abt et al. (HERA-B Collaboration), *Search for the flavor-changing neutral current decay  $D^0 \rightarrow \mu^+\mu^-$  with the HERA-B detector*, Phys. Lett. **B596** (2004), 173–183.
- [Acc03] A. Accardi et al., *Hard probes in heavy ion collisions at the LHC: PDFs, shadowing and pA collisions*, hep-ph/0308248.
- [Ack98] K. Ackerstaff et al. (HERMES Collaboration), *The HERMES spectrometer*, Nucl. Instrum. Meth. **A417** (1998), 230–265.
- [Ada99] M. Adams et al., *The Muon Pretrigger System of the HERA-B Experiment*, IEEE Trans. Nucl. Sci. **46** (1999), 1982–1988.
- [Ada01] M. Adams, *Entwicklung eines Simulationsprogrammes für das Myon-Pretrigger-System des HERA-B Experimentes und Untersuchungen zum Systemverhalten*, Ph.D. thesis, Universität Dortmund, Germany, 2001.
- [Alb97] V. Alberico et al., *The reconstruction for the electromagnetic calorimeter of the HERA-B experiment*, Proc. 7th International Conference on Calorimetry in High Energy Physics (ICCHEP97) (E. Cheu, T. Embry, J. Rutherford, and R. Wigmans, eds.), World Scientific, 1997, pp. 429–438.
- [Alb03] H. Albrecht et al., *Aging Studies for the Large Honeycomb Drift Tube System of the Outer Tracker of HERA-B*, Nucl. Instrum. Meth. **A515** (2003), 155–165.
- [Ald91] D. M. Alde et al. (E772 Collaboration), *A-dependence of  $J/\psi$  and  $\psi'$  production at 800 GeV/c*, Phys. Rev. Lett. **66** (1991), 133–136.
- [Ale97] T. Alexopoulos et al. (E771 Collaboration), *Differential cross sections of  $J/\psi$  and  $\psi'$  in 800 GeV/c p-Si interactions*, Phys. Rev. **D55** (1997), 3927–3932.
- [Ale99] T. Alexopoulos et al. (E771 Collaboration), *A measurement of the  $b\bar{b}$  cross section in 800 GeV/c proton-silicon interactions*, Phys. Rev. Lett. **82** (1999), 41–44.

- [Ale04] B. Alessandro et al. (NA50 Collaboration), *Charmonium production and nuclear absorption in p-A interactions at 450 GeV*, Eur. Phys. J. **C33** (2004), 31–40.
- [And84] L. Anderson et al. (NA10 Collaboration), *A High Resolution Spectrometer for the Study of High Mass Muon Pairs Produced by Intense Hadron Beams*, Nucl. Instr. Meth. **A223** (1984), 26.
- [Ant92] L. Antoniazzi et al. (E705 Collaboration), *Measurement of  $J/\psi$  and  $\psi'$  production in 300-GeV/c proton, antiproton and  $\pi^\pm$  interactions with nuclei*, Phys. Rev. **D46** (1992), 4828–4835.
- [Apa98] L. Apanasevich et al. (Fermilab E706 Collaboration), *Evidence for Parton  $k_T$  Effects in High- $p_T$  Particle production*, Phys. Rev. Lett. **81** (1998), 2642–2645.
- [App75] T. Appelquist and H. D. Politzer, *Heavy Quarks and  $e^+e^-$  annihilation*, Phys. Rev. Lett. **34** (1975), 43–45.
- [Are01] A. Arefev et al., *A gaseous muon detector at the HERA-B experiment*, IEEE Trans. Nucl. Sci. **48** (2001), 1059–1064.
- [Ari04] I. Ariño et al., *The HERA-B ring imaging Cherenkov counter*, Nucl. Instrum. Meth. **A516** (2004), 445–461.
- [Arl00] F. Arleo, P. B. Gossiaux, T. Gousset, and J. Aichelin, *Charmonium suppression in pA collisions*, Phys. Rev. **C61** (2000), 054906.
- [Arn94] M. Arneodo, *Nuclear effects in structure functions*, Phys. Rept. **240** (1994), 301–393.
- [ART03] *ARTE versions*, June 15, 2003,  
<http://www-hera-b.desy.de/subgroup/software/arte/ARTE>  
(retrieved: April 4, 2004).
- [Aub74] J. J. Aubert et al., *Experimental observation of a heavy particle J*, Phys. Rev. Lett. **33** (1974), 1404–1406.
- [Aub83] J. J. Aubert et al. (European Muon Collaboration), *The ratio of the nucleon structure functions  $F_2^N$  for iron and deuterium*, Phys. Lett. **B123** (1983), 275.
- [Aub02] B. Aubert et al. (BABAR Collaboration), *The BABAR detector*, Nucl. Instrum. Meth. **A479** (2002), 1–116.
- [Aug74] J. E. Augustin et al., *Discovery of a narrow resonance in  $e^+e^-$  annihilation*, Phys. Rev. Lett. **33** (1974), 1406–1408.
- [Avo01] G. Avoni et al., *The electromagnetic calorimeter of the HERA-B experiment*, Nucl. Instrum. Meth. **A461** (2001), 332–336.

- [Bab78] J. Babcock, D. W. Sivers, and S. Wolfram, *Quantum-chromodynamic estimates for heavy-particle production*, Phys. Rev. **D18** (1978), 162–181.
- [Bad80] J. Badier et al. (Saclay–CERN–College de France–Ecole Poly-Orsay Collaboration), *A Large Acceptance Spectrometer to Study High-Mass Muon Pairs*, Nucl. Instrum. Meth. **175** (1980), 319.
- [Bad83] J. Badier et al. (NA3 Collaboration), *Experimental J/ψ hadronic production from 150 GeV/c to 280 GeV/c*, Z. Phys. **C20** (1983), 101–116.
- [Bag89] C. Baglin et al. (NA38 Collaboration), *The production of J/ψ in 200 GeV/c/nucleon oxygen uranium interactions*, Phys. Lett. **B220** (1989), 471–478.
- [Bag02] Y. Bagaturia et al., *Studies of aging and HV break down problems during development and operation of MSGC and GEM detectors for the inner tracking system of HERA–B*, ICFA Instrum. Bull. **24** (2002), 54–84.
- [Bai81] R. Baier and R. Rückl, *Hadronic production of ψ and Υ: Transverse momentum distributions*, Phys. Lett. **B102** (1981), 364.
- [Bai97] R. Baier, Y. L. Dokshitzer, A. H. Mueller, S. Peigne, and D. Schiff, *Radiative energy loss and p<sub>T</sub>-broadening of high energy partons in nuclei*, Nucl. Phys. **B484** (1997), 265–282.
- [Bal00] V. Balagura et al., *High-p<sub>T</sub> trigger for HERA–B experiment*, Nucl. Instrum. Meth. **A453** (2000), 412–416.
- [Bal03a] V. Balagura, *Efficiency Map Viewer*, 2003, [/hb/flt/balagura/eff\\_map\\_viewer/viewer](http://hb/flt/balagura/eff_map_viewer/viewer) (retrieved: October 19, 2004).
- [Bal03b] V. Balagura, *FLT Efficiency Maps*, HERA–B Internal Note 03-024, 2003.
- [Bar77] R. C. Barrett and D. F. Jackson, *Nuclear Sizes and Structure*, Oxford University Press, 1977.
- [Bar02] R. Barlow, *Systematic errors: Facts and fictions*, Proc. Advanced Statistical Techniques in Particle Physics, Durham, UK, 18–22 March, 2002, hep-ex/0207026.
- [Bau03] C. Bauer et al., *Performance of the HERA–B vertex detector system*, Nucl. Instrum. Meth. **A501** (2003), 39–48.
- [Bec01] P. Bechtle, *Inbetriebnahme des HERA–B Myon-Pretrigger-Systems*, Diploma thesis, Universität Dortmund, Germany, 2001.
- [Bel02] A. Bel’kov et al., *Study of Muon Misidentification in the HERA–B Experiment*, HERA–B Internal Note 02-036, 2002.

- [Ben96] M. Beneke and I. Z. Rothstein, *Hadro-production of Quarkonia in Fixed Target Experiments*, Phys. Rev. **D54** (1996), 2005–2016, erratum *ibid.* **D54** (1996) 7082.
- [Ben97] M. Beneke, *Nonrelativistic Effective Theory for Quarkonium Production in Hadron Collisions*, Proc. 24th SLAC Summer Institute on Particle Physics, August 19–30, 1996: The Strong Interaction, From Hadrons to Partons, (J. Chan, L. DePorcel, and L. Dixon, eds.), 1997, SLAC-R-508.
- [Ber81] E. L. Berger and D. L. Jones, *Inelastic photoproduction of  $J/\psi$  and  $\Upsilon$  by gluons*, Phys. Rev. **D23** (1981), 1521–1530.
- [Bet34] H. Bethe and W. Heitler, *On the stopping of fast particles and on the creation of positive electrons*, Proc. Roy. Soc. Lond. **A146** (1934), 83–112.
- [Bla89] J. P. Blaizot and J.-Y. Ollitrault, *On the  $A$ -dependence of hadroproduction of  $J/\psi$  on nuclei and the  $E_T$  dependence of  $J/\psi$  suppression in nucleus-nucleus collisions*, Phys. Lett. **B217** (1989), 386–391.
- [Böc01] M. Böcker et al., *The muon pretrigger system of the HERA-B experiment*, IEEE Trans. Nucl. Sci. **48** (2001), 1270–1275.
- [Böc04] M. Böcker, *Messung der transversalen  $\Lambda$ -Polarisation mit dem HERA-B-Detektor*, Ph.D. thesis, Universität Siegen, Germany, 2004.
- [Bod95] G. T. Bodwin, E. Braaten, and G. P. Lepage, *Rigorous QCD analysis of inclusive annihilation and production of heavy quarkonium*, Phys. Rev. **D51** (1995), 1125–1171, erratum *ibid.* **D55** (1997), 5853.
- [Bod96] G. T. Bodwin, D. K. Sinclair, and S. Kim, *Quarkonium decay matrix elements from quenched lattice QCD*, Phys. Rev. Lett. **77** (1996), 2376–2379, hep-lat/9605023.
- [Bod03] G. T. Bodwin, *Inclusive quarkonium production and the NRQCD-factorization approach*, Talk given at 2nd International Conference on Flavor Physics (ICFP 2003), Seoul, Korea, 6–11 Oct 2003, 2003, hep-ph/0312173.
- [Bog04] A. Bogatyrev et al. (HERA-B Collaboration), *Open and hidden charm production with the HERA-B experiment*, to appear in Proc. 39th Rencontres de Moriond, QCD and High Energy Hadronic Interactions, La Thuile, Italy, March 20 – April 4, 2004, hep-ex/0405058.
- [Bon98] R. Bonciani, S. Catani, M. L. Mangano, and P. Nason, *NLL resummation of the heavy-quark hadroproduction cross-section*, Nucl. Phys. **B529** (1998), 424–450.
- [Bor93] K. Boreskov, A. Capella, A. Kaidalov, and J. Tran Thanh Van, *Heavy quark and lepton pair production on nuclei*, Phys. Rev. **D47** (1993), 919–932.

- [Bor03] K. G. Boreskov and A. B. Kaidalov, *Screening and anti-screening effects in  $J/\psi$  production on nuclei*, JETP Lett. **77** (2003), 599–602.
- [Brä01] M. Bräuer, *Die Alignierung des HERA–B Vertexdetektors*, Ph.D. thesis, Universität Heidelberg, Germany, 2001.
- [Brä03] M. Bräuer, *Status of Data Quality*, Talk given at the HERA–B Collaboration Meeting, January 20–24, 2003, HERA–B Internal Note 03-006, 2003.
- [Bra04] N. Brambilla et al., *Heavy quarkonium physics*, hep-ph/0412158.
- [Bro93] S. J. Brodsky and P. Hoyer, *A Bound on the Energy Loss of Partons in Nuclei*, Phys. Lett. **B298** (1993), 165–170.
- [Bru97] R. Brun and F. Rademakers, *ROOT: An object oriented data analysis framework*, Nucl. Instrum. Meth. **A389** (1997), 81–86, throughout this thesis, ROOT version 03.03/09 is employed.
- [Brü02a] M. Brüggemann, *Untersuchungen zum RICH-Vetosystem des HERA–B Experiments*, Diploma thesis, Universität Dortmund, Germany, 2002.
- [Bru02b] M. Bruinsma,  *$J/\psi$  in pA: Performance of the first level trigger of HERA–B and nuclear effects in  $J/\psi$  production*, Ph.D. thesis, Universiteit Utrecht, The Netherlands, 2002.
- [Buc81] W. Buchmüller and S. H. H. Tye, *Quarkonia and quantum chromodynamics*, Phys. Rev. **D24** (1981), 132–156.
- [Buc99] M. Buchler et al., *Design and operation of front end electronics for the HERA–B muon detector*, IEEE Trans. Nucl. Sci. **126** (1999), 126–132.
- [Bur03] G. Burdman and I. Shipsey,  *$D^0\bar{D}^0$  mixing and rare charm decays*, Ann. Rev. Nucl. Part. Sci. **53** (2003), 431.
- [Car03] J. Carvalho, *Compilation of cross sections for proton nucleus interactions at the HERA energy*, Nucl. Phys. **A725** (2003), 269–275.
- [Cas86] W. E. Caswell and G. P. Lepage, *Effective Lagrangians for bound state problems in QED, QCD, and other field theories*, Phys. Lett. **B167** (1986), 437–442.
- [CER94] CERN, *GEANT 3.21 detector description and simulation tool*, CERN Library Long Writeup W5013, CERN, Genève, 1994.
- [Cha03] T. H. Chang et al. (E866/NuSea Collaboration),  *$J/\psi$  polarization in 800-GeV  $p$ -Cu interactions*, Phys. Rev. Lett. **91** (2003), 211801.
- [Cho96a] P. L. Cho and A. K. Leibovich, *Color octet quarkonia production*, Phys. Rev. **D53** (1996), 150–162.



- [Cho96b] P. L. Cho and A. K. Leibovich, *Color-octet quarkonia production II*, Phys. Rev. **D53** (1996), 6203–6217.
- [Col77] J. C. Collins and D. E. Soper, *Angular distribution of dileptons in high-energy hadron collisions*, Phys. Rev. **D16** (1977), 2219–2225.
- [Con89] J. S. Conway et al. (Chicago-Iowa-Princeton Collaboration), *Experimental study of muon pairs produced by 252-GeV pions on tungsten*, Phys. Rev. **D39** (1989), 92.
- [Cru98] C. Cruse, *Entwicklung und Untersuchung von Komponenten zur Datenübertragung für den Myon-Pretrigger des HERA-B Experimentes*, Diploma thesis, Universität Dortmund, Germany, 1998.
- [Cru02] C. Cruse, *Das RICH-Multiplizitätsveto-System für das HERA-B Experiment*, Ph.D. thesis, Universität Dortmund, Germany, 2002.
- [D'A95] G. D'Agostini, *A multidimensional unfolding method based on Bayes' theorem*, Nucl. Instrum. Meth. **A362** (1995), 487–498.
- [D'A96] G. D'Agostini, *Bayesian unfolding*, April 12, 1996, [http://www-zeus.roma1.infn.it/~agostini/bayes\\_distr.txt](http://www-zeus.roma1.infn.it/~agostini/bayes_distr.txt) (retrieved: December 7, 2004).
- [Dam04] M. Dam et al., *HERA-B data acquisition system*, Nucl. Instrum. Meth. **A525** (2004), 566–581.
- [Dan01] M. Danilov et al., *Aging studies of large area proportional chambers under high-rate irradiation with CF<sub>4</sub> based mixtures*, ITEP-15-01-PART-1, hep-ex/0111078.
- [DES00] DESY, Abteilung Presse und Öffentlichkeitsarbeit, Hamburg, 2000.
- [DJ87] C. W. De Jager, H. De Vries, and C. De Vries, *Nuclear charge and magnetization density distribution parameters from elastic electron scattering*, Atom. Data Nucl. Data Tabl. **36** (1987), 495–536.
- [DR75] A. De Rújula and S. L. Glashow, *Is Bound Charm Found?*, Phys. Rev. Lett. **34** (1975), 46–49.
- [Ego04] V. Egorytchev et al., *Muon Likelihood*, Talk given at the HERA-B Collaboration Meeting, October 5–8, 2004.
- [Eic78] E. Eichten, K. Gottfried, T. Kinoshita, K. D. Lane, and T.-M. Yan, *Charmonium: The Model*, Phys. Rev. **D17** (1978), 3090–3117, erratum *ibid.* **D21** (1980) 313.
- [Eic80] E. Eichten, K. Gottfried, T. Kinoshita, K. D. Lane, and T.-M. Yan, *Charmonium: Comparison With Experiment*, Phys. Rev. **D21** (1980), 203–233.

- [Eid04] S. Eidelman et al. (Particle Data Group Collaboration), *Review of particle physics*, Phys. Lett. **B592** (2004), 1.
- [Eig01] V. Eiges et al., *The muon detector at the HERA-B experiment*, Nucl. Instrum. Meth. **A461** (2001), 104–106.
- [Ein75] M. B. Einhorn and S. D. Ellis, *Hadronic production of the new resonances: Probing gluon distributions*, Phys. Rev. **D12** (1975), 2007–2014.
- [Esk99] K. J. Eskola, V. J. Kolhinen, and C. A. Salgado, *The scale dependent nuclear effects in parton distributions for practical applications*, Eur. Phys. J. **C9** (1999), 61–68.
- [Fel99] J. Felix, *On theoretical studies of  $\Lambda^0$  polarization*, Mod. Phys. Lett. **A14** (1999), 827–842.
- [Fla01] J. Flammer, *Entwicklung der Simulation des ECAL Pretrigger Systems für das Experiment HERA-B und Analyse der Effizienzen des Zerfalls  $J/\psi \rightarrow e^+e^-$* , Ph.D. thesis, Universität Hamburg, Germany, 2001.
- [Fom00] B. Fominykh, *Study of muon identification program (MuonID.C) on di-muon SLT triggered events*, Talk given at the HERA-B Collaboration Meeting, October 2–4, 2000, in HERA-B Internal Note 00-171.
- [Fom03] B. Fominykh, *Muon detector: alignment, masks, efficiency*, Talk given at the HERA-B Collaboration Meeting, January 2003.
- [Fom04] B. Fominykh, Private communication, March 2004.
- [Fri77] H. Fritzsch, *Producing heavy quark flavors in hadronic collisions – a test of Quantum Chromodynamics*, Phys. Lett. **B67** (1977), 217–221.
- [Frü87] R. Frühwirth, *Application of Kalman filtering to track and vertex fitting*, Institut für Hochenergiephysik der Österreichischen Akademie der Wissenschaften, Wien, HEPHY-PUB-87-503.
- [Ful99] T. Fuljahn, *Aufbau und Charakterisierung des schnellen Kontrollsystems für das Experiment HERA-B*, Ph.D. thesis, Universität Hamburg, Germany, 1999.
- [Gag98] C. A. Gagliardi et al., *Hardware trigger system for Fermilab E866*, Nucl. Instrum. Meth. **A418** (1998), 322–331.
- [Gav88] S. Gavin and M. Gyulassy, *Transverse momentum dependence of  $J/\psi$  production in nuclear collisions*, Phys. Lett. **B214** (1988), 241–246.
- [Gav92] S. Gavin and J. Milana, *Energy loss at large  $x_F$  in nuclear collisions*, Phys. Rev. Lett. **68** (1992), 1834–1837.
- [Gei91] W. M. Geist, *Atomic mass dependence in soft and hard pA collisions*, Nucl. Phys. **A525** (1991), 149c–164c.

- [Ger92] C. Gerschel and J. Hüfner, *Comparison of  $J/\psi$  suppression in photon, hadron and nucleus nucleus collisions: Where is the quark gluon plasma?*, *Z. Phys.* **C56** (1992), 171–174, The authors give a value for  $L$ . Note that in this work, a different definition of  $\rho_0$  is used.
- [Ger99] C. Gerschel and J. Hüfner, *Charmonium suppression in heavy-ion collisions*, *Ann. Rev. Nucl. Part. Sci.* **49** (1999), 255–301.
- [Ger00] L. Gerland, L. Frankfurt, M. Strikman, H. Stoecker, and W. Greiner, *Charmonium suppression: Interplay of hadronic and partonic degrees of freedom*, *Nucl. Phys.* **A663** (2000), 1019–1022.
- [Gia04] B. Giacobbe et al., *A New Measurement of the  $b\bar{b}$  Production Cross Section at HERA-B*, HERA-B Internal Note 04-036, 2004.
- [Gla59] R. J. Glauber, *High-energy collision theory*, Lectures in theoretical physics: Proc. 1. Annual Summer Institute, Boulder, USA, June 16-August 22, 1958 (W. E. Brittin and L. G. Dunham, eds.), vol. 1, Interscience, New York, 1959, pp. 315–414.
- [Gla70a] S. L. Glashow, J. Iliopoulos, and L. Maiani, *Weak Interactions with Lepton-Hadron Symmetry*, *Phys. Rev.* **D2** (1970), 1285–1292.
- [Gla70b] R. J. Glauber and G. Matthiae, *High-energy scattering of protons by nuclei*, *Nucl. Phys.* **B21** (1970), 135–157.
- [Glü78] M. Glück, J. F. Owens, and E. Reya, *Gluon contribution to hadronic  $J/\psi$  production*, *Phys. Rev.* **D17** (1978), 2324–2331.
- [GM64] M. Gell-Mann, *A schematic model of baryons and mesons*, *Phys. Lett.* **8** (1964), 214–215.
- [Gor04] I. Gorbounov, *Pattern Recognition in the Inner Tracking System of HERA-B and Measurement of the  $V^0$  Production Cross Section in pN Collisions*, Ph.D. thesis, Universität Siegen, Germany, 2004.
- [Got64] K. Gottfried and J. D. Jackson, *On the connection between production mechanism and decay of resonances at high-energies*, *Nuovo Cim.* **33** (1964), 309–330.
- [Gri00] A. Gribushin et al., *Production of  $J/\psi$  mesons in pBe collisions at 530 and 800 GeV/c*, *Phys. Rev.* **D62** (2000), 012001.
- [Hal77] F. Halzen, *CVC for gluons and hadroproduction of quark flavors*, *Phys. Lett.* **B69** (1977), 105.
- [Har95] E. Hartouni et al. (HERA-B Collaboration), *HERA-B – An Experiment to Study CP Violation in the B System Using an Internal Target at the HERA Proton Ring*, Technical Design Report, DESY-PRC 95/01, January 1995.

- [Har99] R. Harr, *Muon Chamber and Channel Numbering*, HERA-B Internal Note 99-117, 1999.
- [HER00a] HERA-B Collaboration, *HERA-B Report on Status and Prospects*, DESY-PRC 00/04, October 2000.
- [HER00b] HERA-B Collaboration, *HERA-B Physics in 2001/2002*, Letter to the DESY directorate, December 2000.
- [HER01] HERA-B Collaboration, *Update of Status and Plans for 2001/2*, HERA-B Internal Note 01-064, 2001.
- [Her03] J. M. Hernández, V. Rybnikov, and F. Sánchez, *Offline mass data processing using online computing resources at HERA-B*, Nucl. Instrum. Meth. **A502** (2003), 471–474.
- [HER04] HERA-B Collaboration, *The HERA-B Detector*, paper in preparation, 2004.
- [Hir01] M. Hirai, S. Kumano, and M. Miyama, *Determination of nuclear parton distributions*, Phys. Rev. **D64** (2001), 034003.
- [Hoa02] A. Hoang, *Heavy Quarkonium Dynamics*, Handbook of QCD (M. Shifman, ed.), vol. 4, World Scientific, Singapore, 2002.
- [Hol93] U. Holm et al. (ZEUS Collaboration), *ZEUS: A Detector for HERA – Status Report*, ZEUS-STATUS-REPT-1993, DESY-PRC 93/05, 1993.
- [Hüf88] J. Hüfner, Y. Kurihara, and H. J. Pirner, *Gluon multiple scattering and the transverse momentum dependence of  $J/\psi$  production in nucleus-nucleus collisions*, Phys. Lett. **B215** (1988), 218–222.
- [Hul02] W. D. Hulsbergen, *A Study of Track Reconstruction and Massive Dielectron Production in HERA-B*, Ph.D. thesis, Universiteit van Amsterdam, The Netherlands, 2002.
- [Hus01a] U. Husemann, *Prospects of Drell-Yan Physics with the HERA-B Detector*, Diploma thesis, Universität Dortmund, Germany, 2001.
- [Hus01b] U. Husemann, *MC Multiplicity Tuning: The Implementation*, Talk given at the HERA-B Analysis Meeting, October 30, 2001.
- [Hus03] U. Husemann et al., *A RICH multiplicity veto for the HERA-B experiment*, IEEE Trans. Nucl. Sci. **50** (2003), 1059–1066.
- [Hus04] U. Husemann et al. (HERA-B Collaboration), *Open and hidden charm production in 920 GeV proton-nucleus collisions*, to appear in Proc. 6th International Conference on Hyperons, Charm and Beauty Hadrons (BEACH 2004), Chicago, IL, June 27–July 3, 2004.

- [Igo98] O. Igonkina, *MARPLE: matching of the ARTE reconstruction packages*, HERA-B Internal Note 98-129, 1998, <http://www-hera-b.desy.de/subgroup/software/arte/MARPLE> (retrieved: March 17, 2004).
- [Igo01] O. Igonkina, *Implementation of CSM and COM models for  $J/\psi$  production in PYTHIA*, HERA-B Internal Note 01-067, 2001.
- [Igo02] O. Igonkina, *Implementation of CSM and NRQCD for the simulation of charmonium production in PYTHIA*, Update of HERA-B Internal Note 01-067, 2002.
- [Iiz66] J. Iizuka, *Systematics and phenomenology of meson family*, Prog. Theor. Phys. Suppl. **37** (1966), 21–34.
- [Ish04] K.-I. Ishikawa, *Hadron spectrum from dynamical lattice QCD simulations*, Talk given at the XXII International Symposium on Lattice Field Theory (Lattice 2004), FNAL, Batavia, IL, 21–26 June, 2004, hep-lat/0410050.
- [Iva99] J. Ivarsson, P. Kreuzer, and T. Lohse, *PYTHIA and FRITIOF: Event Generators of HERA-B*, HERA-B Internal Note 99-067, 1999.
- [Jaf89] D. E. Jaffe et al., *High-transverse-momentum single-hadron production in pp and pd collisions at  $\sqrt{s} = 27.4$  and 38.8 GeV*, Phys. Rev. **D40** (1989), 2777.
- [Jam75] F. James and M. Roos, *MINUIT – a system for function minimization and analysis of the parameter errors and correlations*, Comput. Phys. Commun. **10** (1975), 343–367.
- [Jan95] D. M. Jansen et al. (E789 Collaboration), *Measurement of the Bottom-Quark Production Cross Section in 800 GeV/c Proton-Gold Collisions*, Phys. Rev. Lett. **74** (1995), 3118–3121.
- [Kap78] D. M. Kaplan et al., *Study of the High-Mass Dimuon Continuum in 400-GeV Proton-Nucleus Collisions*, Phys. Rev. Lett. **40** (1978), 435–438.
- [Kar88] F. Karsch, M. T. Mehr, and H. Satz, *Color screening and deconfinement for bound states of heavy quarks*, Z. Phys. **C37** (1988), 617.
- [Kha93] D. Kharzeev and H. Satz, *Color confinement in hadron-nucleus collisions*, Z. Phys. **C60** (1993), 389–396.
- [Kid01] N. Kidonakis, E. Laenen, S. Moch, and R. Vogt, *Sudakov resummation and finite order expansions of heavy quark hadroproduction cross sections*, Phys. Rev. **D64** (2001), 114001.
- [Kla00] E. Klaus, *Untersuchungen zur Inbetriebnahme des HERA-B-Myon-Pretriggers und Monte-Carlo-Studien zum Zerfall  $B^0 \rightarrow K^{*0} \mu^+ \mu^-$* , Diploma thesis, Universität Dortmund, Germany, 2000.

- [Kli04] E. Klinkby,  $\Lambda/\bar{\Lambda}$  polarisation studies in proton nucleus collisions at 920 GeV proton beam energy, Master's thesis, Københavns Universitet, Denmark, 2004.
- [Kol04] H. Kolanoski, A. Spiridonov, and I. Vukotić, *How Should we Fit the Differential Cross Sections of  $J/\psi$  Production?*, HERA-B Internal Note 04-027, 2004.
- [Kop01] B. Z. Kopeliovich, A. Tarasov, and J. Hüfner, *Coherence phenomena in charmonium production off nuclei at the energies of RHIC and LHC*, Nucl. Phys. **A696** (2001), 669–714.
- [Kop04] B. Z. Kopeliovich and I. K. Potashnikova, *Large Rapidity Gap Events in Proton-Nucleus Collisions*, Paper in preparation, October 2004.
- [Kou02] D. Koudela, *Formationszeiteffekte in der Produktion von Charmonia in Proton-Kern-Kollisionen*, Diploma thesis, Universität Heidelberg, Germany, 2002.
- [Kou04] D. Koudela and C. Volpe, *Charmonium production in relativistic proton-nucleus collisions: What will we learn from the negative  $x_F$  region?*, Phys. Rev. **C69** (2004), 054904.
- [Kow94] M. S. Kowitt et al., *Production of  $J/\psi$  at large  $x_F$  in 800-GeV/c p-copper and p-beryllium collisions*, Phys. Rev. Lett. **72** (1994), 1318–1321.
- [Krä01] M. Krämer, *Quarkonium production at high-energy colliders*, Prog. Part. Nucl. Phys. **47** (2001), 141–201.
- [Lan48] L. D. Landau, *On the angular momentum of a system of two photons*, Dokl. Akad. Nauk SSSR **60** (1948), 208.
- [Lan53] L. D. Landau and I. Pomeranchuk, *Limits of applicability of the theory of bremsstrahlung electrons and pair production at high-energies*, Dokl. Akad. Nauk Ser. Fiz. **92** (1953), 535–536.
- [Lee99] W. M. Lee, *A Measurement of the nuclear dependence of  $J/\psi$  and  $\psi'$  production*, Ph.D. thesis, Georgia State University, Atlanta, GA, 1999, FERMILAB-THESIS-1999-30.
- [Lei95] M. J. Leitch et al. (E789 Collaboration), *Nuclear dependence of  $J/\psi$  production by 800-GeV/c protons near  $x_F = 0$* , Phys. Rev. **D52** (1995), 4251–4253.
- [Lei00] M. J. Leitch et al. (E866/NuSea Collaboration), *Measurement of  $J/\psi$  and  $\psi'$  suppression in pA collisions at 800-GeV/c*, Phys. Rev. Lett. **84** (2000), 3256–3260.
- [Loh94] T. Lohse et al. (HERA-B Collaboration), *HERA-B – An Experiment to Study CP Violation in the B System Using an Internal Target at the HERA Proton Ring*, Proposal, DESY-PRC 94/02, May 1994.

- [Mal99] F. Maltoni, *Quarkonium Phenomenology*, Ph.D. thesis, Università degli Studi di Pisa, Italy, 1999.
- [Man97] R. Mankel, *A Concurrent Track Evolution Algorithm for Pattern Recognition in the HERA-B Main Tracking System*, Nucl. Instrum. Meth. **A395** (1997), 169–184.
- [Mar98a] A. D. Martin, R. G. Roberts, W. J. Stirling, and R. S. Thorne, *Parton distributions: A new global analysis*, Eur. Phys. J. **C4** (1998), 463–496.
- [Mar98b] A. D. Martin, R. G. Roberts, W. J. Stirling, and R. S. Thorne, *Scheme dependence, leading order and higher twist studies of MRST partons*, Phys. Lett. **B443** (1998), 301–307.
- [Mat86] T. Matsui and H. Satz, *J/ψ suppression by quark-gluon plasma formation*, Phys. Lett. **B178** (1986), 416.
- [Mat04] I. Matchikhilian et al., *The Electromagnetic Calorimeter of the HERA-B Experiment*, to appear in Proc. XI International Conference on Calorimetry in High Energy Physics (CALOR04), Perugia, Italy, March 29 – April 2, 2004.
- [Med04a] M. Medinnis, Private communication, June 2004.
- [Med04b] M. Medinnis, *SLT work*, Talk given at the HERA-B Charmonium Analysis Meeting, November 16, 2004.
- [Mig56] A. B. Migdal, *Bremsstrahlung and pair production in condensed media at high-energies*, Phys. Rev. **103** (1956), 1811–1820.
- [Mül87] H. N. Mülthei and B. Schorr, *On an iterative method for the unfolding of spectra*, Nucl. Instr. Meth. **A257** (1987), 371.
- [New93] F. M. Newcomer et al., *A fast, low power amplifier, shaper and discriminator for high rate straw tracking systems*, IEEE Trans. Nucl. Sci. **40** (1993), 630.
- [Nör02] M. Nörenberg, *DQcheck*, July 17, 2002, <http://www-hera-b.desy.de/subgroup/DataQuality/herab/DQcheck/online/> (retrieved: October 27, 2004).
- [Nör03] M. Nörenberg, *Tracking Efficiency of the HERA-B First Level Trigger in the Single Lepton Mode*, Ph.D. thesis, Universität Hamburg, Germany, 2003.
- [Now03] S. Nowak, *Existing Geometry Versions*, May 22, 2003, <http://www-hera-b.desy.de/subgroup/software/geometry/welcome.html> (retrieved: April 9, 2004).
- [NPdV03] T. Núñez Pardo de Vera et al., *The Second Level Trigger Algorithm*, HERA-B Internal Note 03-021, 2003.

- [Oku63] S. Okubo, *Phi meson and unitary symmetry model*, Phys. Lett. **5** (1963), 165–168.
- [Pes01] R. Pestotnik, *Identification of Pions, Kaons and Protons in the HERA–B Spectrometer*, Ph.D. thesis, Univerza v Ljubljani, Slovenia, 2001.
- [Pi92] H. Pi, *An event generator for interactions between hadrons and nuclei: FRITIOF version 7.0*, Comput. Phys. Commun. **71** (1992), 173–192.
- [Ple01] M.-A. Pleier, *Cloneremove V1.0*, HERA–B Internal Note 01-062, 2001.
- [Ple03] M.-A. Pleier, *Cloneremoval and  $V^0$  selection*, Talk given at the HERA–B Minimum Bias Working Group Meeting, March 4, 2003.
- [Pri00] D. Pripstein et al. (E789 Collaboration), *Search for flavor-changing neutral currents and lepton-family-number violation in two-body  $D^0$  decays*, Phys. Rev. **D61** (2000), 032005.
- [Qui79] C. Quigg and J. L. Rosner, *Quantum mechanics with applications to quarkonium*, Phys. Rept. **56** (1979), 167–235.
- [Sch94] G. A. Schuler, *Quarkonium production and decays*, CERN-TH.7170/94, hep-ph/9403387.
- [Sch95] M. H. Schub et al. (E789 Collaboration), *Measurement of  $J/\psi$  and  $\psi'$  production in 800-GeV/c proton-gold collisions*, Phys. Rev. **D52** (1995), 1307–1315.
- [Sch97] B. Schwenninger, *Untersuchungen der Myon-Pretrigger-Elektronik für das HERA–B Experiment*, Diploma thesis, Universität Dortmund, Germany, 1997.
- [Sch00a] U. Schwanke, *Trigger and Reconstruction Farms in the HERA–B Experiment and Algorithms for a Third Level Trigger*, Ph.D. thesis, Humboldt-Universität zu Berlin, Germany, 2000.
- [Sch00b] B. Schwenninger et al., *The muon pretrigger of the HERA–B Experiment*, Proc. 6th Workshop on Electronics for LHC Experiments (LEB2000), Kraków, Poland, September 11–15, 2000, CERN 2000-010.
- [Sch01] B. Schwenninger, *Das Myon-Pretrigger-System für das HERA–B Experiment*, Ph.D. thesis, Universität Dortmund, Germany, 2001.
- [Sha01] R. Shahoyan,  *$J/\psi$  and  $\psi'$  production in 450 GeV pA interactions and its dependence on the rapidity and  $x_F$* , Ph.D. thesis, Universidade Técnica de Lisboa, Portugal, 2001.
- [Sip04a] V. Sipicã, *Data Quality Check of the Muon System in HERA–B*, HERA–B Internal Note 04-014, 2004.



- [Sip04b] V. Sipică, *Performance Studies of the HERA-B Muon Detector and Pretrigger Systems*, Master's thesis, Universität Siegen, Germany, 2004.
- [Sjö94] T. Sjöstrand, *High-energy physics event generation with PYTHIA 5.7 and JETSET 7.4*, Comput. Phys. Commun. **82** (1994), 74–90.
- [Som00] A. Somov, *Hard proton nucleus interactions and production of heavy flavours at HERA-B*, Ph.D. thesis, Humboldt-Universität zu Berlin, Germany, 2000.
- [Spe02] J. Spengler, *HERA-B detector components*, March 22, 2002, <http://www-hera-b.desy.de/subgroup/detector/> (retrieved: February 22, 2004).
- [Spi04a] A. Spiridonov, *Bremsstrahlung in Leptonic Onia Decays: Effects on Mass Spectra*, HERA-B Internal Note 04-016, 2004.
- [Spi04b] A. Spiridonov, *Joint fitting of  $J/\psi$  and  $\psi'$  and tests on repro 5*, Talk given at the HERA-B Charmonium Analysis Meeting, February 24, 2004.
- [Spi04c] A. Spiridonov, *Selection of  $J/\psi$  and  $\psi(2S)$  in Muon Mode on Repro 5*, Talk given at the HERA-B Charmonium Analysis Meeting, March 23, 2004.
- [Sym04] M. Symalla, *Produktion von  $\phi$ -Mesonen in inelastischen Proton-Kern-Wechselwirkungen*, Ph.D. thesis, Universität Dortmund, Germany, 2004.
- [Tar03] *HERA-B target mechanic page*, February 2003, [http://www-hera-b.desy.de/subgroup/detector/target/mechanic\\_page](http://www-hera-b.desy.de/subgroup/detector/target/mechanic_page) (retrieved: December 12, 2003).
- [Tit00] M. Titov et al., *The MUON system in the HERA-B experiment*, Nucl. Instrum. Meth. **A446** (2000), 355–365.
- [vE04] C. van Eldik,  *$K^{*0}$  production in proton-nucleus collisions*, Ph.D. thesis, Universität Dortmund, Germany, 2004.
- [Ver04] W. Verkerke and D. Kilby, *The RooFit Toolkit for Data Modelling*, April 4, 2004, <http://roofit.sourceforge.net> (retrieved: September 27, 2004).
- [Vog91] R. Vogt, S. J. Brodsky, and P. Hoyer, *Systematics of  $J/\psi$  production in nuclear collisions*, Nucl. Phys. **B360** (1991), 67–96.
- [Vog99] R. Vogt,  *$J/\psi$  production and suppression*, Phys. Rept. **310** (1999), 197–260.
- [Vog00] R. Vogt, *The  $x_F$  dependence of  $\psi$  and Drell-Yan production*, Phys. Rev. **C61** (2000), 035203.
- [Vog02] R. Vogt, *Are the  $J/\psi$  and  $\chi_c$  A-dependencies the same?*, Nucl. Phys. **A700** (2002), 539–554.

- [Vog04] R. Vogt, Private communication, August 2004.
- [vR67] R. van Royen and V. F. Weisskopf, *Hadron decay processes and the quark model*, Nuovo Cim. **A50** (1967), 617–645, erratum *ibid.* **A51** (1967), 583.
- [Vuk04] I. Vukotić, *Measurement of  $J/\psi$  and  $\psi(2S)$  Production in Proton-Nucleus Interactions using the HERA-B Experiment*, Ph.D. thesis, Humboldt-Universität zu Berlin, Germany, 2004.
- [Woo54] R. D. Woods and D. S. Saxon, *Diffuse Surface Optical Model for Nucleon-Nuclei Scattering*, Phys. Rev. **95** (1954), 577–578.
- [Yan50] C.-N. Yang, *Selection rules for the dematerialization of a particle into two photons*, Phys. Rev. **77** (1950), 242–245.
- [Zai04] Y. Zaitsev, Private communication, February 2004.
- [Zoc00] A. Zoccoli et al., *The electromagnetic calorimeter of the HERA-B experiment*, Nucl. Instrum. Meth. **A446** (2000), 246–252.
- [Zwe64a] G. Zweig, unpublished, 1964.
- [Zwe64b] G. Zweig, *An  $SU(3)$  Model for Strong Interaction Symmetry and its Breaking I & II*, CERN-8182-TH-401, CERN-8419-TH-412 (1964).

# Danksagung

Heiligabend 2004. Der Chef hat meine Arbeit mit in die Ferien genommen, und ich komme so langsam in Weihnachtsstimmung – genau richtig, um ein paar Zeilen des Dankes zu verfassen.

Mein herzlichster Dank gilt meinem Doktorvater Prof. Dr. Peter Buchholz, der in mich das Vertrauen gesetzt hat, „sein Mann am Experiment“ zu sein. Gleichzeitig hat er mir die Möglichkeit gegeben, mich in die verschiedensten Richtungen weiter zu entwickeln, von der Mitgestaltung unseres Umzuges von Dortmund nach Siegen bis hin zu Vorlesungen und Öffentlichkeitsarbeit. Prof. Dr. Claus Grupen danke ich sehr herzlich für die Übernahme des Koreferats, außerdem für seine legendären „Dean’s Speeches“ und so manches Tischtennisduell.

Weiterhin gilt mein Dank unserer Dortmunder/Siegener Myon-Pretrigger-Arbeitsgruppe für die hervorragende Zusammenarbeit. Vielen Dank an „unseren Jaust“ Marc Brüggemann für die westfälischen Momente in meinem Doktorandendasein und an Dr. Matthias Böcker für unsere gemeinsames „Kulturbüro“, sowie an unseren Masterstudenten Valentin Sipicã und „meine“ Sommerstudenten Sven Over und Lu Qiwen. Die gute Zusammenarbeit mit Dr. Markus Adams, Dr. Philip Bechtle, Dr. Carsten Cruise, Elmar Klaus und Dr. Björn Schwenninger werde ich in bester Erinnerung behalten. Dr. Wolfgang Walkowiak, obschon kein HERA-B-ler, hatte immer ein paar Minuten für Diskussionen – nicht nur über meine Arbeit – und für ausgedehnte Fahrradtouren übrig. Ich danke ihm und allen Kolleginnen und Kollegen der Experimentellen Teilchenphysik für die gute Atmosphäre am Lehrstuhl.

Stellvertretend für die HERA-B-Myongruppe möchte ich Prof. Dr. Yuri Zaitsev und Dr. Boris Fominykh für die gute Zusammenarbeit danken. Für das gute und produktive Arbeitsklima in der Charmonium-Analysegruppe danke ich den Gruppenleitern Dr. Maaijke Mevius und Dr. Torsten Zeuner, sowie unserem Physikkoordinator Prof. Dr. Antonio Zoccoli (we still have to finalize our litte project!). Unserem Sprecher Dr. Michael Medinnis danke ich für sein großes Engagement für die Charmoniumanalyse. Die enge Zusammenarbeit mit Dr. Wolfgang Gradl und Dr. Ilija Vukotić und die zuverlässige Monte-Carlo-Produktion durch Dmitri Goloubkov haben sehr zum Gelingen dieser Arbeit beigetragen.

Fürs Korrekturlesen meiner Arbeit und die wertvollen Kommentare zu meinen Entwürfen möchte ich mich herzlich bei Dr. Wolfgang Gradl, Nadir Omar Hashim und Dr. Wolfgang Walkowiak bedanken. Immer ein offenes Ohr für meine Fragen zur Analyse und zur Statistik fand ich bei Prof. Dr. Thomas Lohse und Prof. Dr. Günter Zech. Prof. Dr. Thomas Mannel danke ich für die Diskussionen über die Theorie der Charmoniumproduktion und „unclear effects“.

Ich denke sehr gern an meine Zeit in Hamburg zurück und danke ganz herzlich Sibylle von Dassel für die vielen interessanten Menschen, die ich in ihrem Haus kennenlernen durfte. Meinen Hamburger Kolleginnen und Kollegen Sonja, Wolfgang, Hartmut, Martin, Mino, Stefan, Iouri, Torsten, Carsten, Mitch, Christopher, Ana, Judy, Oxana, Jens und Roger. danke ich für viele gemeinsamen Aktionen – besonders außerhalb der Physik. Philip und Tania habe ich es zu verdanken, dass auch Essen und Trinken in Hamburg nie zu kurz kamen. Von meinem Siegener Mitbewohner Nadir Omar Hashim habe ich gelernt, die Welt auch mal aus afrikanischer Perspektive zu sehen. Asante sana!

Mein tiefster Dank gilt meinen Eltern. Sie haben es verstanden, meine kindliche Neugier auf die Natur und ihre Zusammenhänge zu fördern und haben mich auf meinem Lebensweg jederzeit bedingungslos unterstützt. Ihnen ist diese Arbeit gewidmet.

Diese Arbeit wurde mit Mitteln des Bundesministeriums für Bildung und Forschung unter dem Förderkennzeichen 05HB1PEA/7 gefördert.